Determination of the structure function F_2 at HERMES

DISSERTATION

zur Erlangung des Doktorgrades
des Department Physik
der Universität Hamburg

vorgelegt von
Dominik D. Gabbert
aus
Krefeld

Hamburg
2008

Gutachter der Dissertation:	Herr Prof. Dr. Eckhard Elsen Herr Prof. Dr. Joachim Meyer
Gutachter der Disputation:	Herr Prof. Dr. Eckhard Elsen Herr Dr. Wolf-Dieter Nowak
Datum der Disputation:	29. Oktober 2008
Vorsitzender des Prüfungsausschusses:	Herr Dr. Michael Martins
Vorsitzender des Promotionsausschusses:	Herr Prof. Dr. Joachim Bartels
Leiter des Department Physik:	Herr Prof. Dr. Robert Klanner
Dekan der Fakultät für Mathematik, Informatik und Naturwissenschaften:	Herr Prof. Dr. Arno Frühwald

Abstract

In this thesis we present the first measurement of inclusive proton and deuteron deep-inelastic scattering cross sections at the HERMES experiment. The measurement is performed using the 27.6 GeV lepton beam provided by the HERA storage ring in conjunction with hydrogen and deuterium gas targets internal to the beam pipe. The relevant systematic effects such as radiative corrections, detector smearing, acceptance, particle misidentification, misalignment, tracking related effects and trigger efficiencies are taken into account. Based on these results, the structure functions F_2^p and F_2^d are determined using the parameterization R_{1998} for the longitudinal-to-transverse virtual-photon absorption cross section R. A phenomenological fit of the proton deep-inelastic scattering cross section is performed based on all available data and using photoproduction data in order to pin down the low Q^2 region. A second fit is performed to the world data on the deuteron-to-proton cross section ratio in order to study its Q^2 evolution, the difference between higher twist contributions in proton and deuteron, and the difference between R as obtained from the two targets. It can be confirmed that R obtained for proton and deuteron is in agreement. The Gottfried integral is evaluated from the fit at different values of Q^2. The result at $Q^2 = 4\,\mathrm{GeV}^2$ agrees with previous measurements by NMC and no indication for a Q^2 dependence of the Gottfried integral is found.

Kurzfassung

In dieser Arbeit präsentieren wir die erste Bestimmung inklusiver Wirkungsquerschnitte in tief-inelastischer Streuung an Proton und Deuteron am HERMES-Experiment. Die Messung wurde am Leptonenstrahl des HERA-Speicherrings bei einer Energie von 27,6 GeV unter Verwendung von Wasserstoff- und Deuterium-Gas-Targets durchgeführt. Die relevanten systematischen Effekte wie Strahlungskorrekturen, Impuls- und Winkelauflösung, Akzeptanz, Teilchenidentifikation, Misalignment, Tracking-Effekte und Triggereffizienzen werden berücksichtigt. Auf der Grundlage dieser Ergebnisse werden die Struktur-Funktionen F_2^p und F_2^d bestimmt unter Verwendung der Parametrisierung R_{1998} für das Verhältnis R des Absorptionswirkungsquerschnittes longitudinaler und transversaler virtueller Photonen. Eine phänomenologische Parameterisierung des Wirkungsquerschnittes tief-inelastischer Streuung an Protonen erfolgt mittels der verfügbaren Weltdaten unter Einbeziehung von Photoproduktionsdaten zur Bestimmung der Region bei kleinen Werten für Q^2. Eine weitere Parameterisierung von Weltdaten wird durchgeführt für das Verhältnis aus Deuteron- und Proton-Wirkungsquerschnitten zur Untersuchung der Q^2-Abhängigkeit, der Differenz zwischen higher-twist Beiträgen in Proton und Deuteron und des Unterschiedes der beiden Targets hinsichtlich R. Es kann bestätigt werden, dass R für Proton und Deuteron übereinstimmt. Das Gottfried-Integral wird für verschiedene Werte von Q^2 ausgewertet. Das Ergebnis bei $Q^2 = 4\,\mathrm{GeV}^2$ stimmt mit früheren Messungen von NMC überein und es wurden darüber hinaus keine Anzeichen für eine Q^2-Abhängigkeit des Gottfried-Integrals gefunden.

Contents

Chapter 1

Introduction

Deep-inelastic lepton-nucleon scattering (DIS) has played a major role in the development of our modern understanding of the nucleon structure. Until today, leptons are regarded as point-like particles offering the cleanest way to probe the substructure of the nucleon. In lepton-nucleon scattering, a lepton l interacts with a nucleon N through the exchange of a virtual boson and, in the deep-inelastic scattering regime, causes it to breakup and fragment into the hadronic final state X:

$$l + N \rightarrow l' + X. \tag{1.1}$$

Measuring the kinematic distributions of the scattered lepton l' allows one to draw conclusions about the properties and a possible substructure of the nucleon.

The lepton-nucleon interaction is an electroweak process that is mediated either by the exchange of virtual $W^{\pm}$ bosons or by the exchange of virtual γ or Z^0 bosons. Due to the high masses of $W^{\pm}$ and Z^0, the electromagnetic interaction through the exchange of γ bosons is dominant for lepton energies below 300 GeV in the nucleon rest frame. The weak interaction is negligible for the kinematic conditions of the Hermes experiment.

The electromagnetic lepton-nucleon scattering in the Born (one-photon-exchange) approximation is depicted in Figure 1.1. The 4-momenta of the incoming lepton and the lepton scattered under the angle θ are denoted by $k = (E, \vec{k})$ and $k' = (E', \vec{k'})$, the 4-momentum of the initial nucleon and the virtual photon by $P = (M, \vec{0})$ and $q = (\nu, \vec{q})$ in the nucleon rest frame. The *inclusive* analysis involves the integration over the hadronic final state X

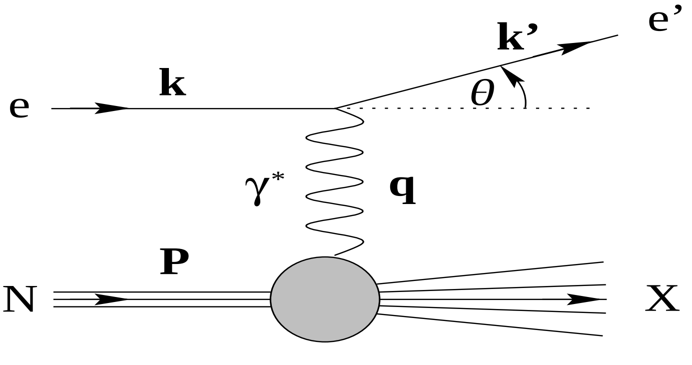

Figure 1.1: Deep-inelastic scattering process in the one-photon-exchange approximation.

and requires only the detection of the scattered lepton while in the *semi-inclusive* analysis at least one hadron is detected in addition.

The squared center-of-mass energy of the scattering process is given by

$$s = (P + k)^2 \overset{lab}{=} M^2 + 2ME, \tag{1.2}$$

where the lepton mass is neglected.

For a given center-of-mass energy, the scattering process in the inclusive analysis is completely characterized by two independent variables, for instance the Lorentz-invariant quantities Q^2 and ν:

$$Q^2 = -q^2 = (k - k')^2 \overset{lab}{=} 4EE' \cdot sin^2\frac{\theta}{2} \tag{1.3}$$

$$\nu = \frac{P \cdot q}{M} \overset{lab}{=} E - E'. \tag{1.4}$$

The photon's virtuality Q^2 is the negative squared four-momentum transfer between the lepton and the nucleon whereas ν is its energy. The invariant mass of the hadronic final state is given by

$$W^2 = (P + q)^2 = M^2 + 2M\nu - Q^2. \tag{1.5}$$

Alternatively, the Lorentz-invariant dimensionless variables x and y can be used:

$$x = \frac{Q^2}{2P \cdot q} = \frac{Q^2}{2M\nu} \tag{1.6}$$

$$y = \frac{P \cdot q}{P \cdot k} \overset{lab}{=} \frac{\nu}{E} \tag{1.7}$$

In the laboratory frame, y is the energy fraction of the vector boson with respect to that of the lepton in the initial state. The variable x is the *Bjørken scaling variable*, for which the elastic scattering process on the nucleon is at $x = 1$. In the naïve *Quark-parton model* which will be discussed in Section 1.2, x has the interpretation of the momentum fraction carried by the struck parton.

The spatial resolution of deep-inelastic scattering is given by the wavelength

$$\lambda = \frac{1}{|\mathbf{q}|} = \frac{1}{\sqrt{\nu^2 + Q^2}} \approx \frac{2Mx}{Q^2} \tag{1.8}$$

so that with larger Q^2 smaller structures can be resolved at fixed x.

Table 1.1 summarizes the important quantities used to describe deep-inelastic scattering.

E	Energy of incoming lepton
E'	Energy of scattered lepton
$\mathbf{k} = (E, \vec{k}),\ \ \mathbf{k'} = (E', \vec{k'})$	4-momenta of incoming and scattered lepton
$\mathbf{P} \overset{lab}{=} (M, \vec{0})$	4-momentum of target nucleon
$\mathbf{q} \overset{lab}{=} (\nu, \vec{q})$	4-momentum of virtual photon
θ	Polar scattering angle
$Q^2 = -q^2 \overset{lab}{=} 4EE'sin^2(\theta/2)$	Negative squared four-momentum transfer
$\nu = \frac{\mathbf{P} \cdot \mathbf{q}}{M} \overset{lab}{=} E - E'$	Energy of virtual photon
$x = \frac{Q^2}{2\mathbf{P} \cdot \mathbf{q}} = \frac{Q^2}{2M\nu}$	Bjørken scaling variable
$y = \frac{\mathbf{P} \cdot \mathbf{q}}{\mathbf{P} \cdot \mathbf{k}} \overset{lab}{=} \frac{\nu}{E}$	Fractional energy of virtual photon
$W^2 = (\mathbf{P} + \mathbf{q})^2 = M^2 + 2M\nu - Q^2$	Squared invariant mass of hadronic final state
$\sigma_{Mott} = \frac{\alpha_{em}^2 cos^2(\theta/2)}{4E^2 sin^4(\theta/2)}$	Mott cross section, describing lepton scattering off a spinless point-charge
$\alpha_{em} = \frac{1}{137.036}$	Fine structure constant
$\epsilon = \frac{\Gamma_L}{\Gamma_T}$	Virtual photon polarization parameter
$R = \frac{\sigma_L}{\sigma_T}$	Ratio of longitudinal to transverse virtual-photon absorption cross section

Table 1.1: Definition of the basic quantities in deep-inelastic scattering.

1.1 Structure Functions of the Nucleon

The differential cross section for charged lepton nucleon scattering in the one-photon exchange approximation is composed of a leptonic and a hadronic contribution [1]:

$$\frac{d^2\sigma}{d\Omega dE'} = \frac{\alpha_{em}^2}{2MQ^4}\frac{E'}{E}L_{\mu\nu}W^{\mu\nu}. \tag{1.9}$$

The leptonic tensor $L_{\mu\nu}$ [2] describes the photon radiation by the lepton and can be calculated exactly in Quantum Electrodynamics (QED). The hadronic tensor $W^{\mu\nu}$ [3] describes the interaction of the virtual photon with the nucleon and therefore depends on its a priori unknown, i.e. presently not calculable, inner structure that can be parameterized with structure functions as shown below.

Each tensor is composed of symmetric (S) and antisymmetric (A) terms under exchange of ν and μ, resulting in the following equation for the cross section:

$$\begin{aligned}\frac{d^2\sigma}{d\Omega dE'} &= \frac{\alpha_{em}^2}{2MQ^4}\frac{E'}{E}[L_{\mu\nu}^{(S)}W^{\mu\nu(S)} + L'^{(S)}_{\mu\nu}W^{\mu\nu(S)} && (1.10)\\ &\quad -L_{\mu\nu}^{(A)}W^{\mu\nu(A)} - L'^{(A)}_{\mu\nu}W^{\mu\nu(A)}]. && (1.11)\end{aligned}$$

The symmetric hadronic tensor $W^{\mu\nu(S)}$ can be parameterized by the two measurable structure functions W_1 and W_2 (or F_1 and F_2) observable in unpolarized scattering, whereas G_1 and G_2 (or g_1 and g_2) are the structure functions observable in polarized scattering which parameterize the antisymmetric hadronic tensor $W^{\mu\nu(A)}$.

Using the Mott cross section σ_{Mott}

$$\sigma_{Mott} = \frac{\alpha_{em}^2 cos^2(\theta/2)}{4E^2 sin^4(\theta/2)} \tag{1.12}$$

for electron scattering off a spinless point charge, the unpolarized DIS cross section is accordingly written [2] in the form:

$$\frac{d^2\sigma}{d\Omega\ dE'} = \sigma_{Mott}[W_2(\nu,Q^2) + 2W_1(\nu,Q^2)tan^2(\theta/2)]. \tag{1.13}$$

For the dimensionless structure functions F_1 and F_2, Bjørken [4] predicted a scaling behavior in the limit $Q^2 \to \infty$ for fixed Q^2/ν:

$$\begin{aligned} F_1(x,Q^2) &= MW_1(\nu,Q^2) \quad \to F_1(x), && (1.14)\\ F_2(x,Q^2) &= \nu W_2(\nu,Q^2) \quad \to F_2(x). && (1.15)\end{aligned}$$

Using Equations (1.14) and (1.15), the DIS cross section can be rewritten as:

$$\frac{d^2\sigma}{dx\ dQ^2} = \frac{4\pi\alpha_{em}^2}{Q^4}\left[y^2\cdot F_1(x,Q^2) + (1-y-\frac{My}{2E})\cdot F_2(x,Q^2)\right]. \tag{1.16}$$

The structure functions F_1 and F_2 are composed of longitudinal and transverse virtual-photon contributions:

$$F_1 = \frac{MK}{4\pi^2\alpha_{em}}\sigma_T \tag{1.17}$$

$$F_2 = \frac{\nu K(\sigma_L+\sigma_T)}{4\pi^2\alpha_{em}(1+\frac{Q^2}{4M^2x^2})}, \tag{1.18}$$

where σ_L and σ_T are the longitudinal (L) and transverse (T) virtual-photon absorption cross sections, respectively. Their ratio R in turn can be expressed by F_1 and F_2:

$$R = \frac{\sigma_L}{\sigma_T} = (1 + \frac{Q^2}{\nu^2})\frac{F_2}{2xF_1} - 1. \tag{1.19}$$

Using the Hand convention [5, 6] $K = \nu - \frac{Q^2}{2M}$ for the virtual-photon flux

$$\Gamma = \frac{\alpha_{em} K}{2\pi^2 Q^2}\frac{E'}{E}\frac{1}{1-\epsilon}, \tag{1.20}$$

the cross section, Equation (1.10), be written in the simple form

$$\frac{d^2\sigma}{d\Omega\ dE'} = \Gamma[\sigma_T(x,Q^2) + \epsilon\sigma_L(x,Q^2)], \tag{1.21}$$

where the virtual photon polarization parameter ϵ is the ratio of virtual photon fluxes for longitudinal and transverse polarizations. It can be expressed as a function of E, y, and Q^2:

$$\epsilon = \frac{4(1-y) - Q^2/E^2}{4(1-y) + 2y^2 + Q^2/E^2}. \tag{1.22}$$

Instead of using the two structure functions F_1 and F_2 to parameterize the hadronic structure, the cross section can be re-parameterized using F_2 together with the ratio of the longitudinal and transverse virtual photon absorption cross sections $R = \frac{\sigma_L}{\sigma_T}$:

$$\begin{aligned} \frac{d^2\sigma}{dx\ dQ^2} &= \frac{4\pi\alpha_{em}^2}{Q^4}\frac{F_2(x,Q^2)}{x} \\ &\quad \times \left[1 - y - \frac{Q^2}{4E^2} + \frac{y^2 + Q^2/E^2}{2[1+R(x,Q^2)]}\right]. \end{aligned} \tag{1.23}$$

The previous considerations only take into account the purely electromagnetic interaction. This is a reasonable approximation at low Q^2, where the weak interaction via the exchange of the massive Z^0 and $W^\pm$ bosons is suppressed due to the high boson masses in the propagator terms $Q^2/(Q^2 + M^2_{Z,W^\pm})$. However, for completeness it should be mentioned that due to the weak interaction at higher Q^2, a parity violating term in the product of hadronic and leptonic tensors occurs which is taken into account by a third structure function F_3.

The *neutral current* (NC) interaction is mediated by the exchange of Z^0, γ and the interference of both, while the *charged current* (CC) interaction is mediated by the exchange of $W^\pm$ bosons. Both interactions are relevant for the collider experiments H1 and ZEUS at HERA.

Among the experimental confirmations of the quark model a particularly noteworthy role was played by the neutrino experiments, beginning in the 1980s, which measured the charged current interaction. As an example, the charged current neutrino DIS cross section is to be given here:

$$\begin{aligned} \frac{d^2\sigma}{dx\ dQ^2} &= \frac{G^2}{2\pi} \\ &\times \left\{\frac{F_2(x,Q^2)}{x}\left[1 - y - \frac{Q^2}{4E^2} + \frac{y^2 + Q^2/E^2}{2[1+R(x,Q^2)]}\right] \pm 2(2y + y^2)F_3(x,Q^2)\right\} \end{aligned} \tag{1.24}$$

1.2 The Quark-Parton Model

The naïve Quark-Parton Model (QPM) provides a simple picture for the understanding of deep-inelastic scattering based on the description of lepton-nucleon interaction as the elastic lepton scattering off the non-interacting constituents of the nucleon, referred to as partons. The Parton Model [7] was suggested by Richard Feynman in 1969 in order to understand high energy collisions involving hadrons. Later, it was realized that the partons can be identified with the quarks that were postulated earlier by Murray Gell-Mann [8] and George Zweig [9] in 1964 to explain the hadron spectrum. The interaction of partons with one another by the exchange of gluons will be discussed in Section 1.3 in the context of the QCD-improved QPM.

In the limit $Q^2 \to \infty$ for a fixed value of x, referred to as the *Bjørken limit*, the time of the interaction is small compared to the lifetime of partonic states and thus the lepton interacts with a single parton of well-defined momentum. The Parton Model is defined in a fast-moving reference system, in which transverse momenta as well as masses can be neglected. The 4-momentum of the parton carrying the fraction ξ of the nucleon momentum $\mathbf{P}$ due to the interaction with the lepton is given by:

$$(\xi\mathbf{P} + \mathbf{q})^2 = 2\xi\mathbf{P}\cdot\mathbf{q} - Q^2 \approx 0. \tag{1.25}$$

Hence the momentum fraction $\xi \approx Q^2/(2\mathbf{P}\cdot\mathbf{q})$ can be identified with the Bjørken scaling variable x.

In the Bjørken limit, the relation (1.19) reduces to

$$R = \frac{\sigma_L}{\sigma_T} = \frac{F_2}{2xF_1} - 1. \tag{1.26}$$

In the limit of a fast-moving reference system, in which helicity is conserved, the absorption of a longitudinally polarized photon by spin 1/2 particles is not possible due to the required spin flip. With $R = 0$, Equation (1.26) results in the *Callan-Gross relation* [10]:

$$F_2 = 2xF_1. \tag{1.27}$$

In fact, due to quark-gluon interactions (see Section 1.3) by which quarks obtain transverse momentum, and due finite quark masses which weaken the helicity conservation, this relation is not strictly fulfilled. The violation of the Callan-Gross relation is usually expressed without the approximation of the Bjørken limit by the structure function $F_L = (1+\frac{Q^2}{\nu^2})F_2 - 2xF_1 \neq 0$.

However, in the naïve quark-parton model the structure functions are given by the simple equations

$$F_1 = \frac{1}{2}\sum_f e_f^2[q(x) + \bar{q}(x)] \tag{1.28}$$

$$F_2 = x\sum_f e_f^2[q(x) + \bar{q}(x)] \tag{1.29}$$

$$F_3 = x\sum_f e_f^2[q(x) - \bar{q}(x)], \tag{1.30}$$

and depend on x but are independent from Q^2. The x dependence is omitted in the following.

In this picture, deep-inelastic scattering corresponds to the incoherent superposition of lepton-parton interactions. The structure functions are composed of weighted probability distributions $q(x)$ and $\bar{q}(x)$ for scattering off quarks and anti-quarks with the different flavors: q=u,d,s,c,b,t.

The quantum numbers of the nucleon are carried by the valence quarks whereas the quark-antiquark pairs in the sea carry the quantum numbers of the vacuum. The t quark is too heavy to be accessed with the values of Q^2 currently reached with deep-inelastic scattering experiments. Hence the structure function $F_2^p \equiv F_2^{ep(\mu p)}$ in charged-lepton proton scattering can be written in the form:

$$F_2^p = x\left[\frac{4}{9}(u+\bar{u}) + \frac{1}{9}(d+\bar{d}) + \frac{1}{9}(s+\bar{s}) + \frac{4}{9}(c+\bar{c}) + \frac{1}{9}(b+\bar{b})\right]. \tag{1.31}$$

The structures of protons and neutrons are connected via *isospin symmetry.* The conception of isospin symmetry arose from the observation that several light baryons are so similar in terms of the strong interactions, that they can be treated as the same particle in different states. In the quark model this is expressed by the strong interaction seeing no difference between quark flavors and by the masses of u and d quarks being very similar. Following the quantum mechanical formalism of the spin, the isospin quantum number I is introduced with the component I_z in a predefined direction in the isospin space. The isospin of 1/2 is assigned for u and d quarks with different projections I_z of $+1/2$ and $-1/2$, respectively. In this model, neutrons ($I_z = -1/2$) and protons ($I_z = 1/2$) can be converted into each other by rotation in the isospin space. Such a rotation can be realized by exchange of u and d quarks:

$$\begin{aligned} u &\equiv u^p = d^n \qquad (1.32)\\ d &\equiv d^p = u^n \\ s &\equiv s^p = s^n \\ c &\equiv c^p = c^n \\ b &\equiv b^p = b^n. \end{aligned}$$

Hence the neutron structure function $F_2^n \equiv F_2^{en(\mu n)}$ can be written as:

$$F_2^n = x\left[\frac{4}{9}(d+\bar{d}) + \frac{1}{9}(u+\bar{u}) + \frac{1}{9}(s+\bar{s}) + \frac{4}{9}(c+\bar{c}) + \frac{1}{9}(b+\bar{b})\right]. \tag{1.33}$$

The structure function for an isoscalar nucleon is given by:

$$F_2^{eN(\mu N)} = x\frac{5}{18}\left[(u+\bar{u}) + (d+\bar{d})\right] + \frac{1}{9}(s+\bar{s}) + \frac{4}{9}(c+\bar{c}) + \frac{1}{9}(b+\bar{b}). \tag{1.34}$$

This can be compared to the nucleon averaged structure function in neutrino scattering where the charge factors are unity and one obtains:

$$F_2^{\nu N} = x\left[(u+\bar{u}) + (d+\bar{d}) + (s+\bar{s}) + (c+\bar{c}) + (b+\bar{b})\right]. \tag{1.35}$$

Based on the relations between the quark distributions and the structure functions, certain statements can be made known as *sum rules*:

Adler sum rule [11]

$$\begin{aligned}\int \frac{dx}{x}\left(F_2^{\bar{\nu}p} - F_2^{\nu p}\right) &= \int \frac{dx}{x}\left(F_2^{\nu n} - F_2^{\nu p}\right) \\ &= 2\int dx(u_v - d_v) = 2 \end{aligned} \tag{1.36}$$

Gross-Llewellyn Smith sum rule [12]

$$\begin{aligned}\int dx\left(F_3^{\bar{\nu}p} + F_3^{\nu p}\right) &= \int dx\left(F_3^{\nu n} + F_3^{\nu p}\right) \\ &= 2\int dx(u_v + d_v) = 6 \end{aligned} \tag{1.37}$$

Gottfried sum rule [13]

$$\begin{aligned}\int \frac{dx}{x}\left(F_2^{ep(\mu p)} - F_2^{en(\mu n)}\right) &= \frac{1}{3}\int dx\,(u_v - d_v) + \frac{2}{3}\int dx\,(\bar{u} - \bar{d}) \\ &\overset{\bar{u}=\bar{d}}{=} \frac{1}{3} \end{aligned} \tag{1.38}$$

All three sum rules are direct results of current algebra and make distinct statements about the basic structure of the nucleon. In particular the Adler sum rule and the Gross-Llewellyn Smith sum rule do not depend on the quark sea. The Gross-Llewellyn Smith sum rule is sensitive only to the total number of valence quarks while the Adler sum rule is sensitive only to the difference of the numbers of u and d valence quarks. In addition to the difference of u and d valence quarks, the Gottfried sum rule, which can be tested in charged lepton scattering, gives access to a possible sea quark flavor asymmetry $\bar{u} - \bar{d}$, see Section 1.8.

There are additional sum rules which play analogous roles for the spin-dependant structure function g_1: The Bjørken sum rule has a fundamental nature similar to that of the Gross-Llewellyn Smith sum rule and the Adler sum rule, whereas the Jaffe-Ellis sum rule requires assumptions on the sea quark distributions similar to the Gottfried sum rule.

Another important sum rule is the momentum sum rule that ensures that the momenta of all partons sum up to the total nucleon momentum.

1.3 Quantum Chromodynamics (QCD)

The parton model can be extended to the *QCD-improved* Quark-Parton Model by accounting for interactions between partons. Through its theoretical robustness and extensive experimental agreement, Quantum Chromodynamics is believed to provide the best description of these interactions. Its concept closely follows that of Quantum Electrodynamics, which describes the interaction between charged particles in the Abelian gauge theory SU(1). Quantum Chromodynamics describes the *strong interaction* between *color charges* within the non-Abelian gauge theory SU(3) mediated by the exchange of gluons. Gluons are the gauge bosons of QCD such as photons are the gauge bosons of QED. The gluons come in eight color combinations and experience the strong interaction themselves. Accordingly, color charges are carried by both, quarks and gluons.

The strength of the strong interaction is embodied in strong coupling constant $\alpha_s(Q^2)$, a function of Q^2 with values increasing towards lower Q^2 with a pole in the limit $Q^2 \to 0$.

The large coupling at low Q^2 prevents the existence of free quarks, a phenomenon known as *confinement*. In the high Q^2 limit, the coupling constant takes small values, leading to the asymptotic behavior of quarks as quasi-free particles, known as *asymptotic freedom*. In this limit, the Quark-Parton-Model with non-interacting quarks is approximately recovered.

In lowest order QCD, the DIS BORN cross section is corrected with terms proportional to α_s, due to radiation of gluons by quarks and the splitting of gluons into quark-anti-quark-pairs. A quark observed at a scale Q_0^2 and a fractional momentum x_0 can be resolved into more quarks and gluons at smaller fractional momenta $x_1 < x_0$ with larger $Q^2 > Q_0^2$. A descriptive picture of the Q^2 dependence of the structure functions is provided by the relation of Q^2 to the spatial resolution according to Equation (1.8). The higher the value of Q^2, the more partons can be resolved due the self-similarity implied by QCD (quarks and gluons consist of quarks and gluons, etc.), thus more partons with lower fractional momenta $\xi \sim x$ are resolved. This leads to a redistribution of quarks from high to low fractional momenta with increasing Q^2, a phenomenon known as *scaling violation*.

QCD corrections to the parton model are absorbed in a Q^2 dependence of the structure functions, which implies violation of Bjørken scaling, e.g.: $F_2(x) \rightarrow F_2(x, Q^2)$.

Deep-inelastic scattering can be interpreted using the factorization theorem [14] that is based on the separation of the cross-section into a *short-distance* and a *long-distance* part. The short-distance part is calculated in perturbative QCD using (ultraviolet) renormalization. The long-distance part cannot be calculated but it is described by the parton distributions which absorb the infrared divergences of QCD so that the structure function F_2 can be written as a convolution integral of parton density functions f_i with coefficient functions C_2^i:

$$F_2(x, Q^2) = \sum_i \int_x^1 \mathrm{d}z C_2^i \left(\frac{x}{z}, \frac{Q^2}{\mu_r^2}, \frac{\mu_f^2}{\mu_r^2}, \alpha_s(\mu_r^2) \right) f_i(z, \mu_r, \mu_f). \tag{1.39}$$

The coefficient functions C_2^i describe the hard photon-parton interaction and can be calculated in perturbative QCD in an α_s-expansion. The parton density functions f^i are probability distributions for finding a parton with a certain fractional momentum in the nucleon while they incorporate the soft contributions of the interaction. Coefficient functions and parton densities are independent from each other. The sum in Equation (1.39) covers all possible quark flavors and gluons.

The factorization scale μ_f separates the long-distance from the short-distance contribution. For example, soft gluon emission below this limit is incorporated in the parton density distributions. The renormalization scale μ_r accounts for ultraviolet divergences in higher orders of the perturbation theory.

Physics quantities like cross sections have to be independent on the arbitrary choice of the renormalization scheme, leading to scaling effects on α_s (running coupling constant) and F_2 (scaling violation). There exist several possible renormalization schemes. In the deep-inelastic scheme (DIS), $\mu_r = \mu_f = Q^2$ is chosen and the finite contributions are completely absorbed[1] by the parton distributions. In this scheme, F_2 has no explicit higher-order perturbative QCD corrections:

$$F_2(x, Q^2) = \sum_i e_i^2 x f_i(x, Q^2). \tag{1.40}$$

---

[1] Another common scheme is the $\overline{MS}$ scheme in which only minimal finite contributions are absorbed by the parton distributions.

The evolution in Q^2 of parton density distributions starting from a fixed Q^2 is described by the DGLAP evolution equation [15, 16, 17, 18] which can be derived from the scale independence of F_2. The DGLAP evolution is given by an integro-differential equation named after the authors Dokshitzer, Gribov, Lipatov, Altarelli, Parisi. The evolution of quark and gluon distributions can be written in the form:

$$\frac{\mathrm{d}q_i(x,Q^2)}{\mathrm{d}\ln Q^2} = \frac{\alpha_s(Q^2)}{2\pi}\int_x^1 \frac{\mathrm{d}z}{z}\left[\sum_j q_j(z,Q^2)P_{ij}\left(\frac{x}{z}\right) + g(z,Q^2)P_{ig}\left(\frac{x}{z}\right)\right] \tag{1.41}$$

$$\frac{\mathrm{d}g(x,Q^2)}{\mathrm{d}\ln Q^2} = \frac{\alpha_s(Q^2)}{2\pi}\int_x^1 \frac{\mathrm{d}z}{z}\left[\sum_j q_j(z,Q^2)P_{gj}\left(\frac{x}{z}\right) + g(z,Q^2)P_{gg}\left(\frac{x}{z}\right)\right] \tag{1.42}$$

The splitting functions $P_{\alpha\beta}$ can be calculated in perturbative QCD ordered by powers of α_s. The leading order ($\sim \alpha_s^1$) term $P^{(0)}_{\alpha\beta}(x/z)$ of the splitting function can be interpreted as a probability that a parton β at a fractional momentum of z emits a parton α with a fractional momentum x.

1.4 The low-Q^2 region

In the leading-log(Q^2) approximation of perturbative QCD, valid at large Q^2, F_2 is directly related to the quark and anti-quark distributions, as expressed by Equation (1.40). The mildly violated Bjørken scaling is described by the DGLAP evolution. However, in the next-to-leading-log(Q^2) approximation additional terms proportional to α_s are acquired by the DGLAP evolution as well as by F_2 which are attributed to quark-gluon-correlations. Formally, the corrections to the structure function F_2 can be calculated in operator product expansions (OPE) of the electromagnetic currents [19] which lead to expansions of F_2 in inverse powers of Q^2:

$$F_2(x,Q^2) = \sum_{n=0}^{\infty} \frac{C_n(x,Q^2)}{(Q^2)^n}. \tag{1.43}$$

The functions $C_n(x,Q^2)$ have only a small Q^2 dependence. The various terms in Equation (1.43) are referred to as leading-twist for $n = 0$ and higher-twist for $n > 0$. The twist number t is defined to be 2 for the leading-twist term and consecutive even integers correspond to the higher-twist terms.

Higher-twist corrections can become significant in the Q^2 region of a few GeV^2. However, it should be emphasized that the higher-twist terms are leading-order-corrections to the scaling at higher Q^2 (perturbative region), and they are not able to describe the very low Q^2 region of the structure function F_2. This can be seen from the unphysical pole of F_2 in the photoproduction region ($Q^2 \approx 0$) as implied by Equation (1.43). A model that aims to describe this Q^2 region and at the same time can be represented by Equation (1.43) in the limit of high Q^2, is the Vector Meson Dominance model (VMD) [20]. It is based on the experimental observation that the photon interactions are very similar to the ones with a hadron. In the VMD model, the structure function F_2 can be represented by:

$$F_2(x,Q^2) = \frac{Q^2}{4\pi}\sum_V \frac{M_V^4\sigma_V(s)}{\gamma_V^2(Q^2+M_V^2)^2}. \tag{1.44}$$

The sum includes all possible vector mesons V with masses M_V, into which the photon can convert. The total hadron-hadron cross section is given by σ_V and the quantity γ_V is related to the leptonic width of the meson [21]. As long as the sum includes only a finite number of vector mesons, then F_2 vanishes, $F_2 \to 0$, in the limit $Q^2 \to \infty$. Consequently, the leading-twist term is not covered. In order to reproduce scaling, an infinite number of vector mesons is included, as it is done in the Generalized Vector Meson Dominance (GVMD) model [21]. The heavy mesons are directly related to the structure function in the scaling region.

For practical reasons, the following parameterization is commonly used to account for higher-twist effects in a simplified way:

$$F_2(x, Q^2) = F_2^{LT}(x, Q^2)\left(1 + \frac{C(x)}{Q^2}\right), \tag{1.45}$$

where $F_2^{LT}(x, Q^2)$ is the leading-twist term. The small Q^2 dependence of the higher-twist coefficient function is thereby neglected as well as the higher-twist contributions beyond next-to-leading-twist.

1.5 Historical View

Experiment	Year	Reaction	Process	Beam Energy
SLAC	1968	ep, ed	NC	4.5-20 GeV
CDHS,CHARM	1984	ν_μFe	CC	<260 GeV
FMMF	<1988	ν_μN	CC	<500 GeV
CCFR	1979-1988	ν_μFe	CC	<600 GeV
BCDMS	1981-1985	μp, μd	NC	100-280 GeV
EMC	<1983	μp, μd	NC	<325 GeV
NMC	1986-1989	μp, μd	NC	90-280 GeV
E665	1987-1992	ep, ed	NC	90-470 GeV

Table 1.2: Fixed-target experiments prior to HERA, probing the structure of nucleons and nuclei by lepton scattering.

Deep-inelastic scattering has been measured in a variety of fixed-target experiments as well as by H1 and ZEUS at the HERA collider. Table 1.2 summarizes the fixed-target experiments prior to the HERA era. A large kinematic region is covered today by all measurements due to the different kinematic conditions of different experiments. This fact motivates global fits which were performed to obtain the world best knowledge on the nucleon structure, see Section 6.1.

In the development of the modern understanding of the nucleon structure, charged current neutrino scattering experiments contributed important information about the flavor composition of the nucleon. Based on the Gross-Llewellyn Smith sum rule, Equation (1.37), the number of valence quarks was determined to be three [22]. From the comparison of the nucleon structure functions obtained in neutrino and charged lepton scattering, it could also be shown that the mean charge square of u and d quarks is 5/18 [23, 24] as suggested by Equations (1.34) and (1.35).

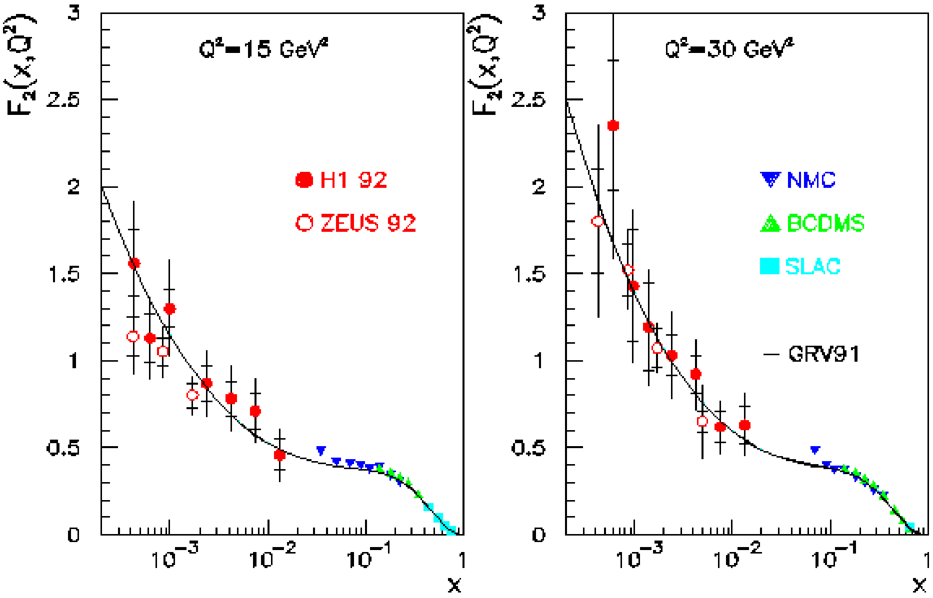

Figure 1.2: Rise of F_2 at small x as found by H1 and ZEUS.

The considerable success of QCD should not be taken to suggest that predictions are simple to make or that results are in line with naïve expectations. In the 80s, the European Muon Collaboration observed strong nuclear effects on the structure of nucleons known as the *EMC effect* [25], see Section 1.7. Furthermore, the same collaboration found experimental evidence for the violation [26] of the Ellis-Jaffe sum rule [27] in association with the finding that only little or nothing of the nucleon spin is carried by its quarks. The violation was confirmed by SMC [28] and initiated the *spin puzzle*.

Then, the violation of the Gottfried integral found by NMC [68] suggested for the first time a flavor asymmetry ($\bar{u} \neq \bar{d}$) in the sea. The HERA collider as it will be shortly discussed at the beginning of Chapter 2 opened a new kinematic region at very small x and very high Q^2, accessed by the two experiments H1 and ZEUS between 1992 and 2007. Already after the first year of operation, H1 [30] and ZEUS [31] reported on a rise of the structure function F_2 at small x, as shown in Figure 1.2. This behavior can be attributed to high densities of gluons and sea quarks at small momenta. It was found that the derivative $\mathrm{d}\ln(F_2)/\mathrm{d}\ln(x)$ is approximately independent from x in the region $x < 0.01$, in which the behavior of F_2 can consequently be described by the function $F_2 \sim x^{-\lambda}$, see Figure 1.3.

At very low x, a saturation of the rise of F_2 with decreasing x is expected due to unitarity bounds. Within the kinematic coverage of HERA, such a saturation could unfortunately not be found. The DGLAP evolution basically follows an ordering in $\alpha_s \log Q^2$, which may not be appropriate at high values of $\frac{\alpha_s}{x}$, therefore different evolution equations were suggested to describe the behavior of F_2 in the limit $x \to 0$. The BFKL evolution [32, 33, 34] which follows an ordering in x predicts a characteristic $x^{-\lambda}$ behavior for the gluon density. As the gluon density strongly drives the sea-quark densities at low x, a rise in F_2 can be expected. However, the parton dynamics for all world data on inclusive deep-inelastic scattering available until today can still be described by the DGLAP evolution.

In addition to the possibility of probing the structure of protons in deep-inelastic scat-

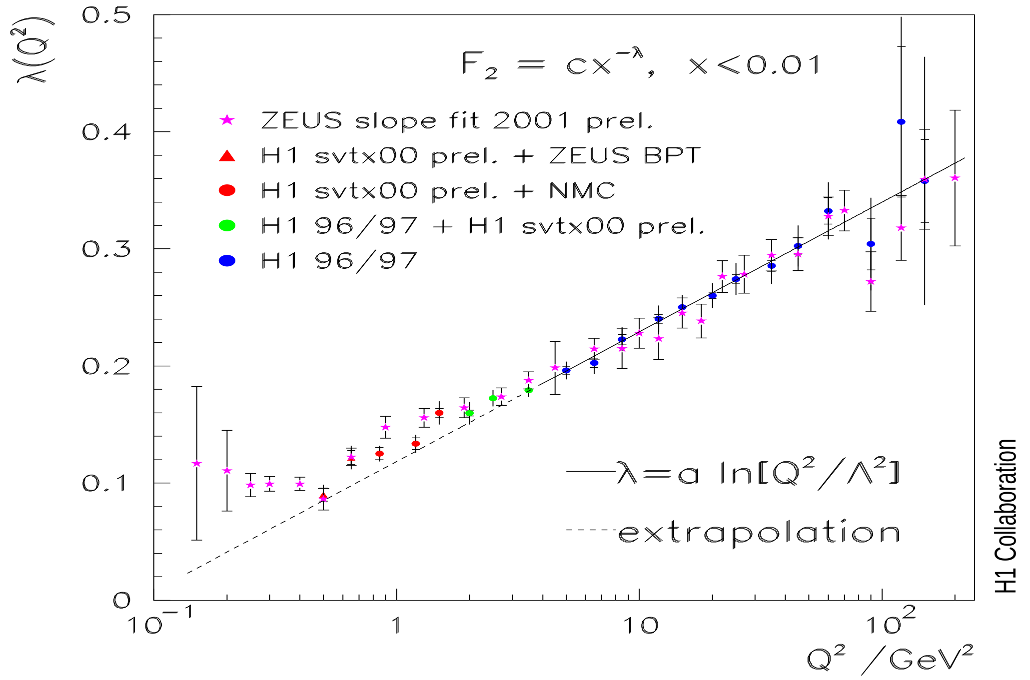

Figure 1.3: Results for λ from H1 and ZEUS obtained in fits of the form $F_2 \sim x^{-\lambda}$ at small x. The dashed line corresponds to a logarithmic behavior of $\lambda(Q^2)$. Taken from [29].

tering, other nuclei like the deuteron have been studied by various fixed-target experiments. World data on the structure functions F_2^p and F_2^d are shown in Figures 1.4 and 1.5.

Beyond the data presented in these figures, the HERMES experiment has collected an outstanding amount of charged-lepton nucleon scattering data on a variety of light and heavy targets. The sizes of proton and deuteron data sets, for instance, are larger than the ones obtained in a similar kinematic region by other experiments: e.g. NMC collected 6 million DIS events (3 million DIS events) on a hydrogen (deuterium) target, while HERMES has a data set of 30 million (28 DIS million) DIS events on a hydrogen (deuterium) target taken between 1996 and 2005. In general, the HERMES experiment has the world largest data set on the deuteron.

The measurement of DIS cross sections on hydrogen and deuterium targets offers the possibility not only to study the structure functions for proton and deuteron, but also to combine both and to extract information about the flavor decomposition in the nucleon. Based on the isospin symmetry, the value of 1/3 as predicted by the Gottfried sum rule is expected if the sea is flavor symmetric. In practice, this can be studied in deuteron-to-proton cross section ratios as discussed in the following section.

1.6 Cross Section Ratios

The cross sections σ^p and σ^d measured on proton and deuteron can be combined as a ratio in order to study the individual effects contributing to the proton-deuteron differences. The advantage of the the ratio is that some systematic uncertainties in σ^p and σ^d such as the overall normalization or certain efficiencies may be minimized or even cancel out.

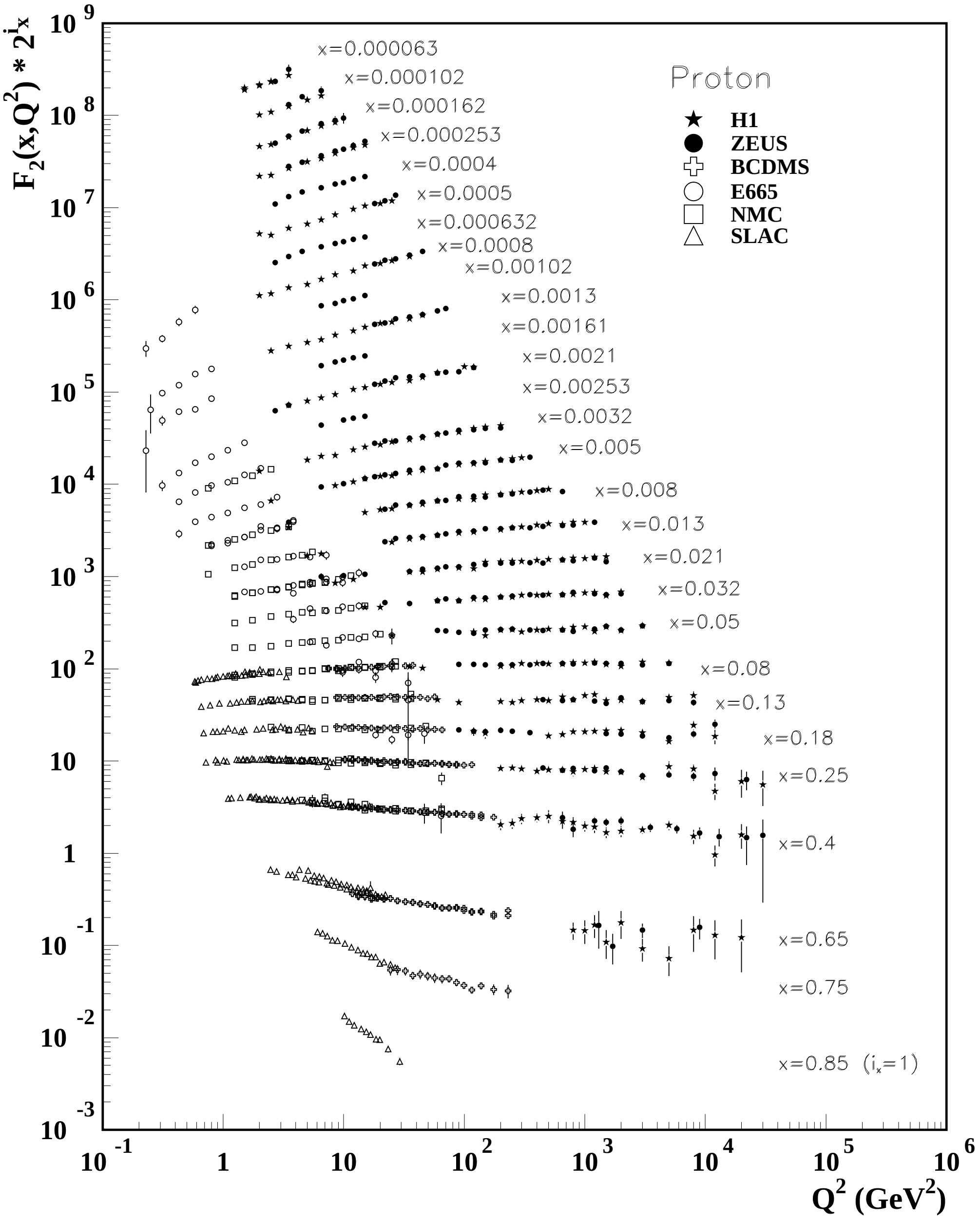

Figure 1.4: An overview of the proton structure function F_2^p [35] measured in lepton-proton scattering with positrons by the collider experiments (H1 [36] and ZEUS [37]) in the kinematic domain of HERA for $x > 0.00006$ and by fixed-target experiments with electrons (SLAC [38]) and muons (BCDMS [39], NMC [40] and E665 [41]). The Q^2 dependence of the structure function F_2^p is shown in bins of x. For clarity of presentation the data have been scaled successively by a factor of 2 for the different x bins.

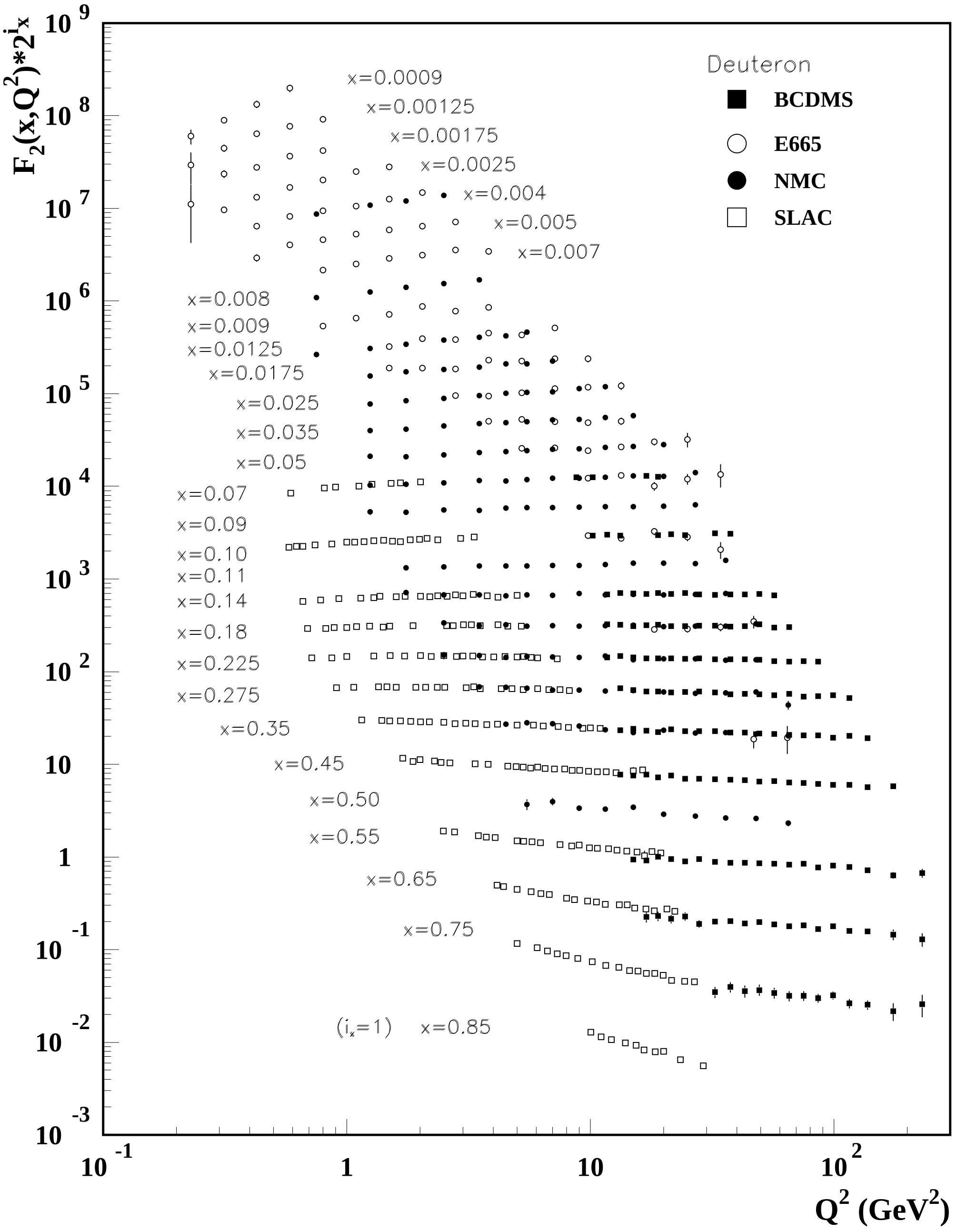

Figure 1.5: An overview of the deuteron structure function F_2^d [35] measured in lepton-deuteron scattering by fixed-target experiments with electrons (SLAC [38, 42]) and muons (BCDMS [43], NMC [44] and E665 [45]). The Q^2 dependence of the structure function F_2^d is shown in bins of x. For clarity of presentation the data have been scaled successively by a factor of 2 for the different x bins.

1.6.1 Higher-Twist Effects

The structure function ratio F_2^d/F_2^p may reveal differences of the contributions to the structure functions from higher-twist effects. Higher-twist effects in the measured F_2 can be accounted for by separating a leading-twist term from the higher-twist expansion according to Equation (1.45). The structure function ratio then takes the form

$$\frac{F_2^d}{F_2^p} \simeq \frac{F_2^{d,LT}}{F_2^{p,LT}}(x,Q^2)\left(1+\frac{C^d(x)-C^p(x)}{Q^2}\right) \tag{1.46}$$

with the higher-twist coefficient functions C^p and C^d for proton and deuteron, respectively.

1.6.2 Evolution

Perturbative QCD calculations predict different scaling behaviors for the structure functions F_2^p and F_2^d, given that the valence quark compositions of proton and deuteron differ. The Q^2 dependence of the leading-twist structure function ratio $F_2^{d,LT}/F_2^{p,LT}$ can be parameterized with only two parameters:

$$\frac{F_2^{d,LT}}{F_2^{p,LT}}(x,Q^2) \simeq b_1(x)+b_2(x)\ln Q^2. \tag{1.47}$$

where $b_1(x)$ corresponds to the structure function ratio at $Q^2 = 1\,\mathrm{GeV}$ and $b_2(x)$ mimics the Q^2 evolution with the logarithmic behavior along Q^2.

1.6.3 Dependence on R

In the same framework of QCD, a possible difference in the ratios of longitudinal and transverse virtual photon absorption cross sections, $R^d - R^p$, is predicted to be sensitive to any difference in the gluon distributions between proton and deuteron [47].

The deuteron-to-proton cross section ratio σ^d/σ^p is related to the structure function ratio F_2^d/F_2^p through the following expression:

$$\frac{\sigma^d}{\sigma^p}(x,Q^2,\varepsilon) = \frac{F_2^d}{F_2^p}(x,Q^2)\frac{1+R^p(x,Q^2)}{1+R^d(x,Q^2)}\frac{1+\varepsilon R^d(x,Q^2)}{1+\varepsilon R^p(x,Q^2)} \tag{1.48}$$

where R^p and R^d are the ratios of longitudinal to transverse virtual-photon absorption cross section for proton and deuteron respectively. From Equation (1.48) it is clear that when $\varepsilon = 1$ the terms in R^p and R^d cancel and the structure function ratio is equivalent to the cross section ratio. In general this is not true, and since ε depends on the kinematics of the experiment, such a dependence can be exploited to isolate any differences on R^p and R^d. Equation (1.48) can be expanded:

$$\frac{\sigma^d}{\sigma^p} \simeq \frac{F_2^d}{F_2^p}\left(1-\frac{1-\varepsilon}{(1+\bar{R})(1+\varepsilon\bar{R})}\Delta R\right) \tag{1.49}$$

where $\bar{R}$ (ΔR) is the average of (difference between) R^p and R^d.

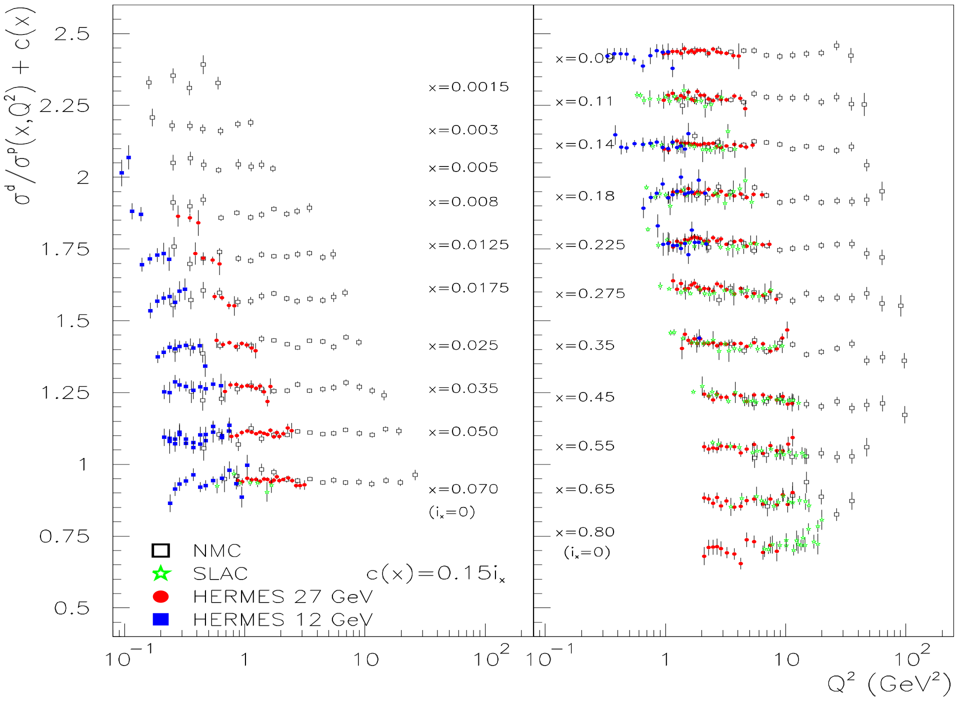

Figure 1.6: The cross section ratio σ^d/σ^p measured by NMC, SLAC and HERMES. The HERMES data points come from an unpublished analysis [48] and are meant for illustrative purposes only.

1.6.4 Fit to world data of σ^d/σ^p

Figures 1.6 and 1.7 show the Q^2 and ε coverage of HERMES data and the data from other experiments. The up to now unexplored regions at low ϵ which are reached by HERMES, as seen from Figure 1.7, can be used to improve the knowledge on ΔR according to Equation 1.49.

Based on the available world data it is possible to perform fits of the form

$$\frac{\sigma^d}{\sigma^p} = \left(b_1 + b_2 \ln Q^2\right)\left(1 + \frac{C^d - C^p}{Q^2}\right)\left(1 - \frac{1-\varepsilon}{(1+\bar{R})(1+\varepsilon\bar{R})}\Delta R\right) \tag{1.50}$$

and obtain the unknown parameters b_1, b_2, $C^d - C^p$ and ΔR. Without implying assumptions on the x-dependences of the parameters, independent fits can be performed for each value of x. This procedure will be applied in Chapter 6.2.

1.7 Nuclear effects

Despite of the fact that energy scales for deep-inelastic scattering are much higher than the nuclear energy scales (i.e. binding energy or the Fermi motion), the nuclear environment influences the observed structure of nucleons. This effect was found in 1982 by the EMC collaboration, therefore referred to as the *EMC effect.* The results of the early measurements of the iron-to-deuterium structure function ratio F_2^{Fe}/F_2^D are shown in Figure 1.7. After that discovery, the EMC effect has been studied in detail for a large number of nuclei from Helium to Lead. From these measurements, different regions in x can be identified:

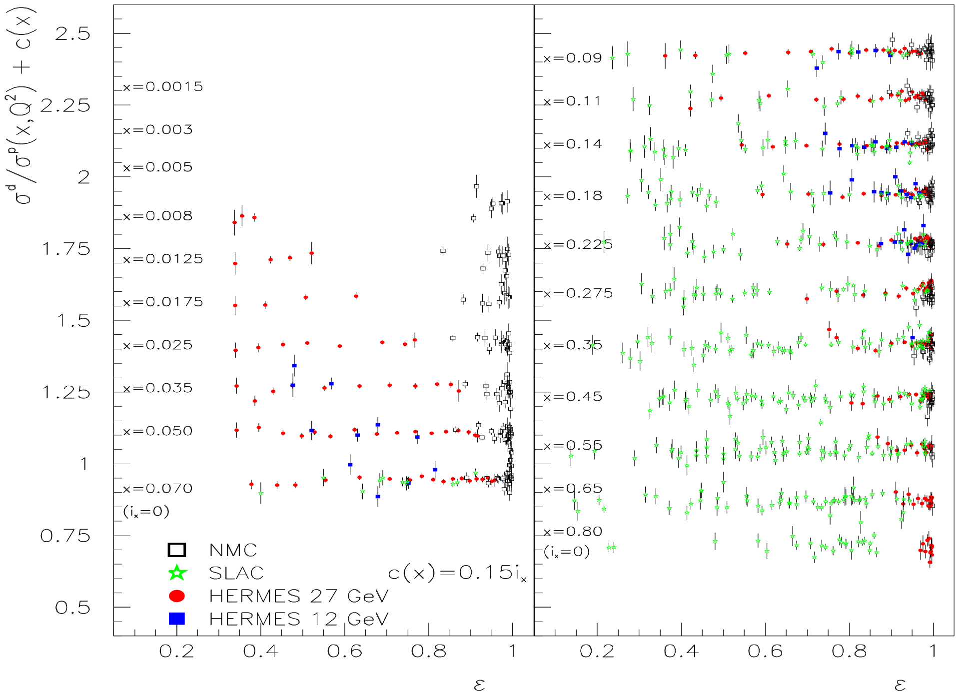

Figure 1.7: Same as Figure 1.6 but coverage in ε.

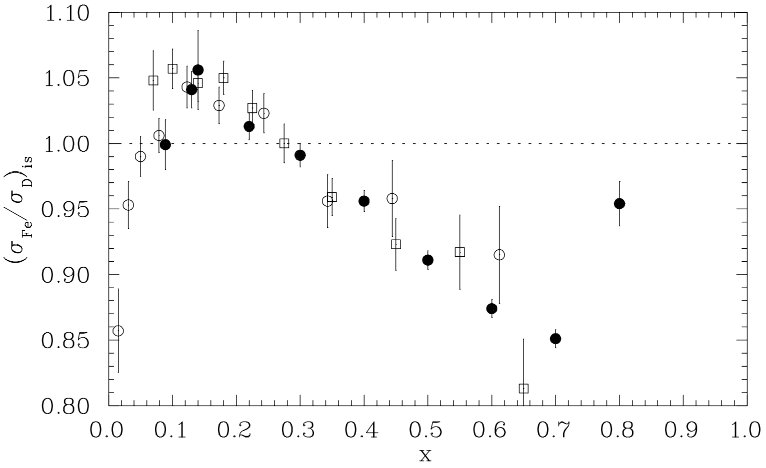

Figure 1.8: σ^{Fe}/σ^{D} ratios as a function of x measured by EMC [25] (open circles), SLAC [49] (closed circles), BCDMS [50] (squares). The data has been averaged over Q^2 and was corrected for the neutron excess in iron.

- *Nuclear shadowing*: In the region $x \lesssim 0.1$, the ratio F_2^A/F_2^d is below unity.
- *Anti-Shadowing*: In the region $0.1 \lesssim x \lesssim 0.3$, the ratio is above unity.
- *EMC effect* (in a narrower sense): In the region $0.3 \lesssim x \lesssim 0.8$, the ratio is below unity.
- *Fermi motion region*: In the region $x \gtrsim 0.8$ the ratio is above unity.

For all regions in x, the effect increases with increasing atomic number A. No or a very small Q^2 dependence is observed over the entire x range. Several models have been proposed to explain the nuclear effects. For instance, models based on convolutions of the free-nucleon structure functions with multi-nucleon effects such as the enhancement of the pion field in the nucleus due to the nucleon-nucleon interactions [51], or rescaling models like the one based on a decreased effective nucleon mass [52] in the nuclear environment. Another category of models modifies the nucleon structure itself for instance by postulating the existence of multi-quark clusters [53] or by assuming an increased confinement radius [54].

The nuclear shadowing effect is usually calculated by Glauber's theory or the VMD model [55]. The total cross section of a photon hitting a heavy nucleus is smaller than the sum of cross sections for the individual nucleons, as if the nuclear matter would cast a shadow on the remainder so that nucleons in the inner part of the nucleus are not exposed to the full photon flux. The parton fusion model [56] reflects both nuclear shadowing and anti-shadowing: in the region of small momentum fractions of the partons, the uncertainty principle leads to localization uncertainties being larger than the nucleon radius. Nucleons overlap so that partons interact with each other and fuse, resulting in a redistribution of the parton densities from lower (shadowing) to higher (anti-shadowing) values of x.

The effect of the Fermi momentum [57] of nucleons is calculated by a convolution of the nucleon structure function with the Fermi momentum distribution. This causes a characteristic rise of the measured structure function ratio at high x because the initial structure function has a flat tail at high x where it gains the most.

Because none of these approaches alone is able to explain all observations at the same time, combinations of different models for the individual regions are therefore used.

1.8 The Gottfried Integral

The Gottfried integral can be recast in terms of the deuteron-to-proton cross section ratio,

$$\begin{aligned} I_G(x_{min}, x_{max}) &= \int_{x_{min}}^{x_{max}} \left(F_2^p(x) - F_2^n(x)\right) \frac{dx}{x} \\ &= \int_{x_{min}}^{x_{max}} 2\left(F_2^p - F_2^d\right) \frac{dx}{x} \\ &= \int_{x_{min}}^{x_{max}} 2F_2^p \left(1 - \frac{F_2^d}{F_2^p}\right) \frac{dx}{x}, \end{aligned} \tag{1.51}$$

using the approximation of $F_2^d = (F_2^p + F_2^n)/2$. This assumption neglects all nuclear effects in deuterium but seems justified because of the $1/x$ term in the Gottfried integral which strongly suppresses the contribution from high values of x. Nuclear shadowing in the deuterium which could affect the low x region of the structure function F_2^d is predicted [58] to be not more than 2% at the lowest x and Q^2 values of the combined data set.

Based on isospin invariance for proton and neutron and flavor symmetry in the sea ($\bar{u} = \bar{d}$), the Gottfried integral over the full x range will take the simple value of

$$\int_0^1 (F_2^p - F_2^n)\,\frac{dx}{x} = \frac{1}{3}. \tag{1.52}$$

The $1/x$ term leads to large contributions to the integral from the low x region which makes an experimental determination of the Gottfried integral in the full x-region difficult.

In an early measurement at SLAC [59] in 1975, the Gottfried Integral was determined to be $I_G = 0.200 \pm 0.040$ indicating already a violation of the Gottfried sum rule. Unfortunately, a serious discussion of the result was not possible since the smallest accessible x value was 0.02 still leaving room for a significant contribution at lower x.

Further experimental information was obtained from Drell-Yan data. The first measurement of this kind was done in 1981 by E288 [65] at Fermilab suggesting a sea flavor asymmetry of $\bar{u} = \bar{d}(1-x)^{3.48}$.

Measurements were also performed using muon scattering by EMC in 1983 and 1987 [66]. The latter one results in a Gottfried integral of $0.197 \pm 0.011(stat.) \pm 0.083(syst.)$ in the region $0.02 \leq x \leq 0.8$ and an extrapolated value of $0.235^{+0.110}_{-0.099}$. In 1990, the other muon collaboration at CERN, BCDMS, measured a value of $0.197 \pm 0.006(stat.) \pm 0.036(syst.)$ in $0.06 \leq x \leq 0.8$ at $Q^2 = 20\,\mathrm{GeV}^2$ [67]. The estimated contribution of the missing low x region is estimated to be between 0.07 and 0.22, thus the result remains consistent with 1/3.

The first breakthrough came in 1991 from the NMC collaboration with a kinematic reach down to x values as small as 0.004 [68]. From a fit to data and an extrapolation to the lower x region, the Gottfried integral over the full range was found to be 0.240 ± 0.016, showing a clear inconsistency with the Gottfried sum rule. Measurements from E665 [69] and HERMES [70] agree with the NMC result. Also the results from semi-inclusive DIS at HERMES [71] support the findings of NMC.

Apart from E288, Drell-Yan data was later analyzed by E772 which found no significant flavor asymmetry in the 800 GeV proton induced Drell-Yan experiment using deuteron, carbon, and tungsten targets. The conclusion from this measurement is questionable due to the contributions of nuclear effects in heavy nuclei. Proton induced Drell-Yan measurements on p and d were also performed by the NA51 collaboration at CERN [72], with a flavor asymmetry of $\bar{u}/\bar{d} = 0.51 \pm 0.04 \pm 0.05$ at $x = 0.18$. Furthermore, E866 [73] measured an integrated sea asymmetry of $\bar{d} - \bar{u} = 0.118 \pm 0.012$ in the range $0.015 \leq x \leq 0.35$. The Drell-Yan results from E866 are consistent with the results from NA51 and the semi-inclusive DIS results from HERMES, as shown in Figure 1.9.

The naïve postulation of a flavor symmetric sea is based on the assumption that the sea quarks are produced perturbatively by gluons that split into quark pairs. With negligible u and d quark masses, the sea is hence expected to be flavor symmetric: $\bar{u} = \bar{d}$. However, the measurements of the sea quark asymmetry in Drell-Yan and DIS are consistent with an excess of $\bar{d}$ quarks over $\bar{u}$ quarks, a fact which motivated the development of new models. It should be noted that higher-order corrections to the parton model prediction of 1/3 for the Gottfried integral are tiny compared with the discrepancies to experimental results. At

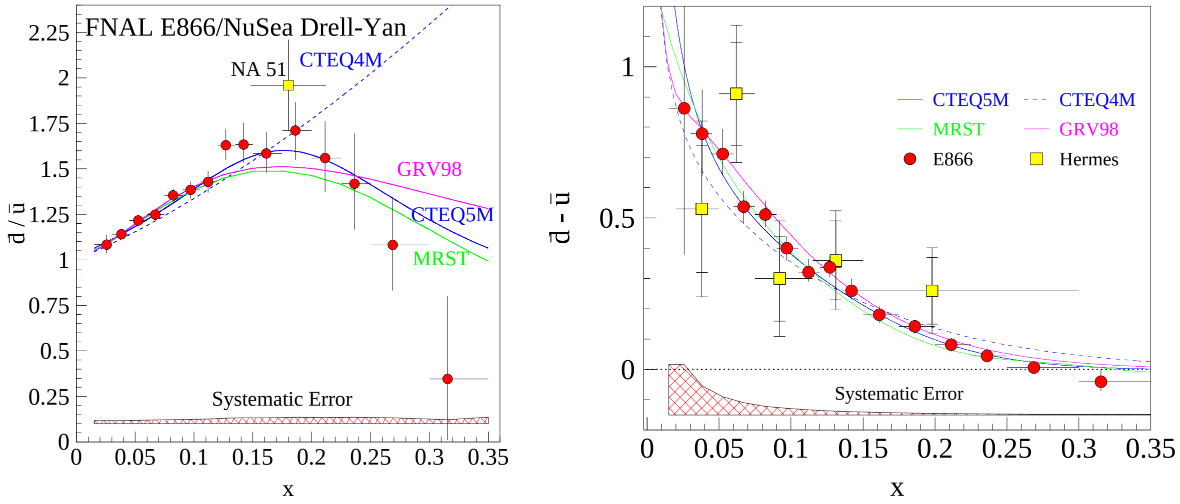

Figure 1.9: Drell-Yan results from E866 [73] on $\bar{d}/\bar{u}$ (left) and $\bar{d}-\bar{u}$ (right) compared to results from NA51 [72] and the semi-inclusive DIS results from HERMES [71].

$Q^2 = 4\,\mathrm{GeV}^2$ for example, the higher-order corrections are only 0.3% in next-to-leading order and 0.4% in next-to-next-to-leading order. The first models which were proposed right after the finding at SLAC, a Pauli-blocking mechanism and diquark models, turned out to be not able to explain the large size of the discrepancy found.

It was pointed out [60] later that the virtual-pion cloud in the field of the proton leads to an enhancement of $\bar{d}$ quarks relative to $\bar{u}$ quarks. In the corresponding models, the physical proton $|P\rangle$ is commonly described by a superposition of a bare proton $|P_0\rangle$ and meson-baryon pairs $|MP\rangle$:

$$|P\rangle = |P_0\rangle + \alpha|MB\rangle. \tag{1.53}$$

Another approach is the chiral model [61, 62] which predicts the production of mesons in the conversion processes of valence quarks $u \to d\pi^+$ and $d \to u\pi^-$ (pion cloud of constituent quarks), giving rise to a flavor asymmetry of the sea. The excess of $\bar{d}$ quarks over $\bar{u}$ quarks in this model results from the additional u valence quark in the proton.

These models describe the non-perturbative contributions to the flavor asymmetry, whereas the perturbative processes naturally reduce the predicted flavor asymmetry. Theoretical considerations [63] predict that perturbative effects alone cannot generate a significant u and d quark asymmetry in the sea exceeding 1%. Furthermore, as a flavor non-singlet quantity, $\bar{u}-\bar{d}$ has the property that its integral is expected to be independent of Q^2 [64]. Hence the experimental evidence of both a possible violation and Q^2 dependence of the Gottfried integral are a direct measure of possible non-perturbative effects.

After the determination of inclusive proton and deuteron DIS cross sections from HERMES data described in the following sections, global analyses of inclusive DIS cross sections will be discussed in Chapter 6. Using the parameterization for F_2^p derived in Section 6.1, and the fit to the cross section ratio σ^d/σ^p performed in Section 6.2, the Gottfried integral will be evaluated in Section 6.2.1. Furthermore, the ratio of valence quark distributions d_v/u_v will be evaluated in Section 6.2.2.

Chapter 2

Hera and Hermes

2.1 The Accelerator and Storage Ring HERA

The accelerator and storage ring complex HERA (Hadron-Elektron-Ring-Anlage) was the largest particle accelerator at the DESY research center (Deutsches Elektronen-Synchrotron) in Hamburg with a circumference of 6336 m. In opposite directions, positrons (or electrons) were accelerated to an energy of 27.5 GeV and protons to energies of 820 GeV (or 920 GeV)[1], in two separate beam tubes. Most of the time, the lepton ring was operated with positrons, while electrons were used only in 1998 and from 2005 until June 2006. The term electron will be used for electrons or positrons within this thesis unless otherwise noted. HERA started running on November 8, 1990 and was shut down on June 30, 2007.

Two experiments, H1 and ZEUS, were located at opposite positions (north and south) on the ring where the electron beam intersected the proton beam. The HERA-B experiment (west) used the proton beam together with a wire target, while the Hermes experiment (east) employed the electron beam in conjunction with a stationary gas target internal to the beam pipe. A sketch of the Hera rings and the positions of the experiments is shown in Figure 2.1.

HERA was operated as follows: First, the beams were filled and ramped up to their operational energies. Initial electron beam currents of up to 50 mA have been achieved. Then, during operation, the electron beam current decreased exponentially. The lifetime of the beam was limited to about 12 hours by losses due to synchrotron radiation or due to the influence of the experiments. At currents of ~ 10 mA the beam was dumped in order to use the time of operation efficiently. Since 2000, the low beam currents at the end of the fill were used at Hermes to inject unpolarized gas at high densities into the target. This offered the dual benefits of quickly concluding the fill and collecting a burst of data at high rate.

Right after the beam energy reached its nominal value, the Sokolov-Ternov-effect [74] caused the beam to build up a transverse polarization. An asymmetric spin-flip amplitude in the synchrotron radiation process favors a parallel (anti-parallel) orientation of the positrons (electrons) with respect to the magnetic bending fields. After a rise time of about 20 minutes typical polarizations of 50%-60% have been reached through 2000. The transverse polarization, parallel (or anti-parallel) to the magnetic bending fields was transformed into longitudinal polarization in front of the Hermes experiment with a set of magnets acting as

---

[1] Protons were accelerated to 820 GeV during the time of operation until 1998, after which the beam energy was increased to 920 GeV.

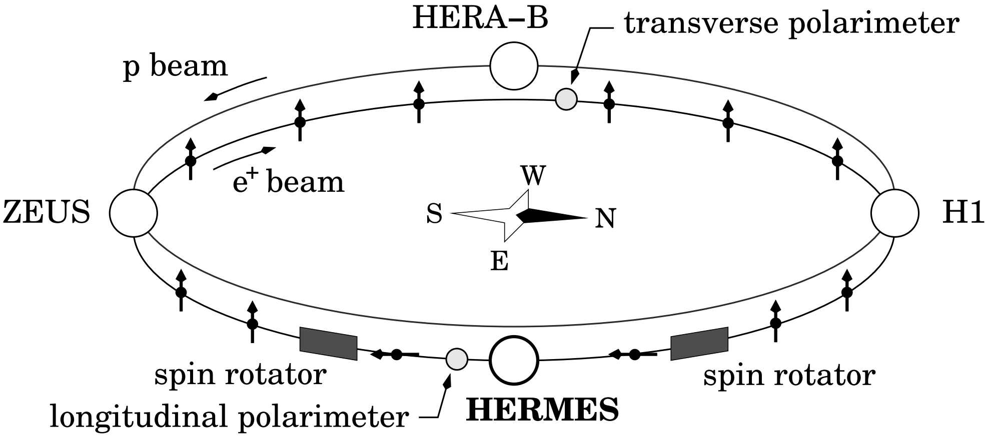

Figure 2.1: Sketch of the HERA facility at DESY.

a spin rotator. Another spin rotator behind the HERMES experimental region returned the beam polarization to the transverse direction.

2.2 The HERMES Target

The HERMES experiment used a gas target internal to the lepton beam pipe. In unpolarized mode, the target gases H_2, D_2, He, N_2, Ne, Kr, Xe were used.

Apart from unpolarized gas targets, HERMES offered the possibility to run also with polarized hydrogen, deuterium and helium-3 gas targets. The data from polarized hydrogen and deuterium targets analyzed within this thesis were provided by the Stern-Gerlach atomic beam source (ABS) which generated the polarized atoms in high rates of about $6.2 \cdot 10^{16}$ atoms per second. The ABS dissociated gas molecules with RF fields and selected and populated hyperfine states with sextupole magnets and RF transmitters. Details about the method are described in [75].

Target polarizations of 97% (92%) have been reached for the hydrogen (deuterium) target at a degree of dissociation of 92% (95%). The atoms had a nuclear polarization the axis of which was defined by an external magnetic holding field. The holding field was longitudinal between 1995 and 2000 and was changed to a transverse one in spring 2002 being in use until November 2005. A schematic view of the target is depicted in Figure 2.2. Two turbomolecular vacuum pumps with a combined power of 4400 l/s evacuated the target chamber to pressures of about $1.5 \cdot 10^{-7}$ mbar.

The advantage of a gas target compared to a solid-state target is the small dilution of the target by undesired material, and the high polarizations which can be reversed within a few seconds. Without consideration of the dilution effects, typical densities of solid targets are in the order of 10^{25} atoms/cm^2 whereas polarized gas jets usually have densities of 2×10^{11} atoms/cm^2. In order to achieve higher areal densities, the gas jet was injected into a target storage cell which was aligned collinear to the beamline. For polarized Deuterium densities of $2.1 \cdot 10^{14}$ atoms/cm^2 [76] were achieved. Two tubes were installed at the center of the target cell: The target gas entered the target cell through the first tube and partly diffused

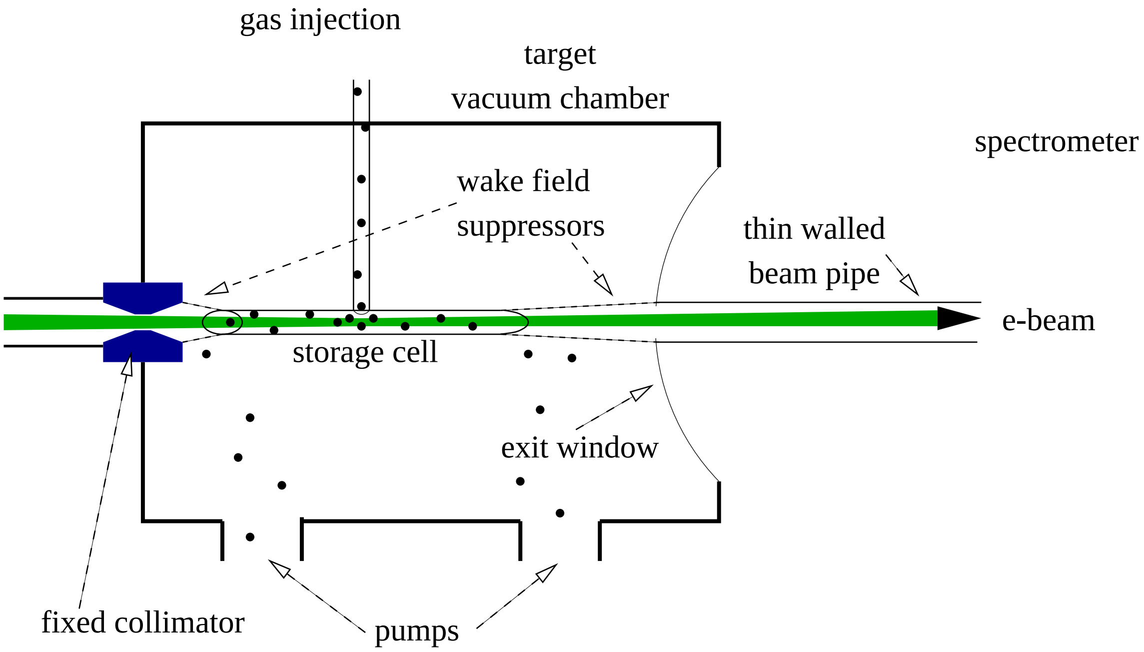

Figure 2.2: Sketch of the HERMES target. The beam enters the target region from the left side. A thin foil used as exit window on the other side of the target aimed at the minimization of undesirable particle interactions.

into a second tube where the atomic polarization was measured by a Breit-Rabi polarimeter (BRP) while the target gas analyzer (TGA) determined the fraction of dissociated atoms. Both quantities are needed for the calculation of the target polarization.

The target cell was 40 cm long. The large-size cell with a height of 9.8 mm and a width of 29.0 mm was exchanged in 2000 by a medium size cell with a height of 9.0 mm and a width of 21.0 mm. However, the longitudinal position of the target cell did not change for the data considered within this thesis.

2.3 The Transverse Target Magnet

In the case of the longitudinally polarized target, the external magnetic field in the target was aligned to the beam so that the magnetic field had no impact on the beam direction and only a tiny effect on scattered charged particles within the acceptance of the HERMES spectrometer. In contrast, the external magnetic field used to generate transverse target polarization after 2001 had a non-negligible impact on the trajectories of the particles emerging from the target, thus the kinematic variables of the tracks have to be corrected for the effect of the transverse magnetic field [77] in order to obtain the unaffected track information of the physics process.

Two methods are used to correct the polar and azimuthal scattering angles as well as the vertex position for the transverse magnetic field:

- Method 1 (TMC1) uses MIT-RAY-TRACE [78] to track particles in Monte-Carlo (MC) simulations through the measured field map of the transverse magnetic field. Taylor series expansions are calculated to convert the initial into the final particle coordinates.

By inversion of this relation, the track coordinates at the tracking chambers can be converted to the initial angles and vertex positions.

- Method 2 (TMC2) uses the zgoubi [79] program to track particles through the measured field map of the transverse target magnet. Relations are recorded between the initial and final coordinates. The recorded information is searched for the trajectory with the smallest distance to the tracked coordinates, thereby it reconstructs scattering angles and vertices before the influence of the transverse magnet.

For technical reasons only TMC2 is valid for 2002 and only TMC1 is available for 2003. Studies have shown that there is no significant difference between the two correction methods.

2.4 The HERMES Spectrometer

Although the HERMES experiment was operated from 1995 until the end of HERA operation, this thesis focuses on HERMES data taken between 1996 and 2005. Typical for fixed-target experiments, the HERMES experiment was based on a forward spectrometer with the capacity to detect, identify and track particles emerging from the scattering process. The detector components were arranged above and below the beam pipe including the vertical dipole magnet. A horizontal iron plate - also referred to as the septum plate - protected both beamlines[2] from the magnetic field of the spectrometer magnet but at the same time restricted the acceptance of the HERMES spectrometer at small scattering angles in vertical directions. This situation favors a mirror symmetric spectrometer with identical design in each half of the spectrometer. Consequently, every detector part consists of identical top and bottom detectors, of which only one half will be described in the following sections. The openings in the field clamps at the front and rear sides of the magnet set the outer horizontal and vertical limits to the acceptance. Altogether, the spectrometer had a horizontal acceptance of ±170 mrad and a vertical acceptance of ±40 mrad to ±140 mrad with respect to the center of the target. The design of the HERMES spectrometer is illustrated in Figure 2.3. The following sections will focus on the detectors for tracking, particle identification, and the luminosity which are relevant for this thesis. More details can be found in [80].

2.4.1 The Tracking System

The spectrometer magnet was used as part of the tracking system for the measurement of momenta through the curvature of reconstructed tracks. It was a vertical dipole magnet with a field integral of $\int B dl = 1.3\,\mathrm{Tm}$. The magnet separated the tracking system into front and back tracking detectors. The front tracking was performed by two modules of front drift chambers (FC1/2). The back tracking was accomplished by four modules of back drift chambers (BC1/2, BC3/4). Additionally, three modules of proportional chambers in the rear half of the magnet gap were used for the detection of low momentum particles which curled up in the magnetic field and did not reach the rear part of the spectrometer.

All tracking detectors consisted of submodules with three wire orientations (X, U, V). The wires of the X plane were oriented vertically, while the U and V planes were tilted towards the X plane by ±30°. A gas mixture of Ar-CO_2-CF_4 was used with the proportions

---

[2] The proton beamline is arranged at a horizontal distance of 70 cm to the electron beamline off-center of the HERMES experiment.

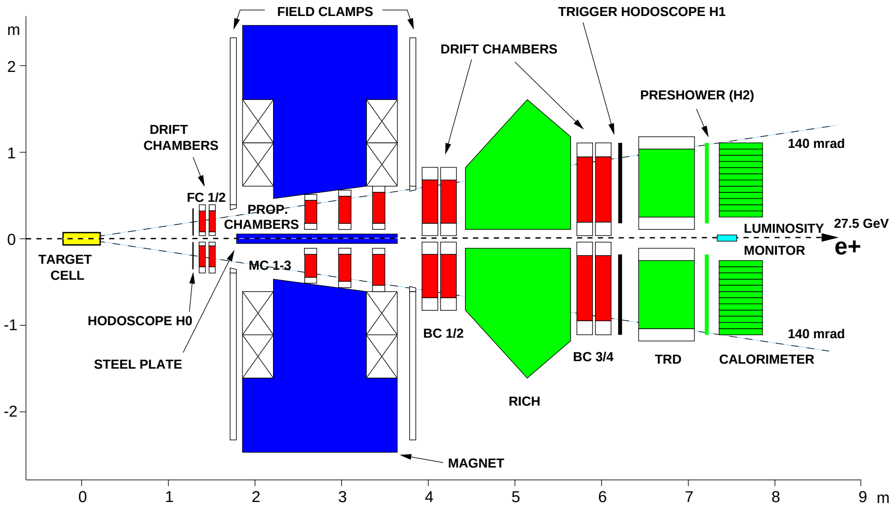

Figure 2.3: Schematic side view of the HERMES experiment as of 2000. A description of the various components is given in the text.

90% – 5% – 5% in the drift chambers, and 85% – 30% – 5% in the magnet chambers.

The Drift Chambers: The tracking chambers FC1/2, BC1/2, BC3/4 were conventional drift chambers. Each drift cell layer had alternating anode and cathode wires between a pair of cathode foils. The cell size was 7 mm for the front drift chambers and 15 mm for the back drift chambers. Each wire orientation was used twice in adjacent layers with an offset of half a drift cell size: (UU', XX', VV') for the front drift chambers and the back drift chambers. The radiation length per module was 0.20% for front drift chambers and 0.26% for the back drift chambers. The spatial resolution for per plane was $\sigma = 250\,\mu m$, $\sigma = 275\,\mu m$ and $\sigma = 300\,\mu m$ for FC1/2, BC1/2 and BC3/4, respectively.

The Proportional Chambers: Multi-wire proportional chambers inside the magnet gap allowed the detection of low-momentum particles or *short tracks*, e.g. from Λ decay, which did not reach the back chambers due to the strong deflection in the magnetic field. The layer scheme for each of the three magnet chambers was (U, X, V) at a cell width of only 2 mm. One chamber had a radiation length of 0.29%.

2.4.2 The Particle Identification System

The Transition Radiation Detector

The transition radiation detector (TRD) was a powerful detector for electron identification. It was based on the principle that relativistic charged particles traversing the boundary between two media with different dielectric properties encounter a sudden change of electric fields and thereby produce photons in the X-ray spectrum. Transition radiation is emitted basically collinear with an opening angle $\phi \propto \frac{1}{\gamma}$ at an average energy proportional to the Lorentz factor γ. In the HERMES kinematic region electrons have large Lorentz factors, $\gamma > 2000$, and can hence be clearly separated from hadrons with $\gamma < 100$ by measuring the transition radiation.

Each of the six identical TRD modules contained an array of polyethylene fibers with a diameter of $20\,\mu$m used as radiator material. The radiated photons were measured in a consecutive multi-wire proportional chamber with the $90:10$ gas mixture of Xe and CH_4.

A background contribution to the energy deposition of transition radiation photons in the multi-wire proportional chambers comes from the direct interaction of the charged particle with the chamber gas by energy loss dE/dx due to ionization. However, together with the transition radiation, the energy deposited by electrons is still more than twice as large as the energy deposited by hadrons.

The Calorimeter

The electromagnetic calorimeter consisted of an array of 42 × 10 radiation-resistant lead-glass blocks in each detector half, where each block had a surface of $9 \times 9\,\mathrm{cm}^2$ and a depth of 50 cm. The rear of each block was connected to a photomultiplier in order to measure the energy deposited in the lead-glass block from electromagnetic showers produced by the incident particles.

The calorimeter allowed a measurement of photon energies. It also provided a signal for scattered electrons which was included in the first-level trigger.

Furthermore, the calorimeter was an important detector for particle identification. Almost the entire energy of electrons was deposited in the calorimeter due to electromagnetic showers, resulting in a peak at $E/p \approx 1$, of the ratio of the energy deposition E to the particle momentum p as inferred from the magnet bending . In contrast, hadrons interacted in the calorimeter by ionization and thus lost only a fraction of their kinematic energy within the depth of the calorimeter. Energy depositions of typically $E/p \approx 0.4$ to 0.5 are therefore associated to hadrons.

The Pre-Shower Detector

The pre-shower detector was located in front of the calorimeter in order to improve electron-hadron separation. It consisted of a passive radiator made of an 11 mm thick lead sheet sandwiched in two 1.3 mm thick stainless steel sheets. The electromagnetic showers initiated in the radiator material were detected by a hodoscope arranged behind the radiator. The hodoscope was composed of 42 plastic scintillator paddles, with a size of $9.3 \times 91 \times 1\,\mathrm{cm}^3$, each of them covering geometrically one vertical row of calorimeter lead glass blocks. Photomultipliers were installed at the outer edges of the scintillator paddles (far away from the beam) in order to detect the scintillation light.

Due to the different longitudinal shapes of the interactions initiated by electrons (electromagnetic showers) and hadrons (ionization), a comparison of signals in pre-shower and calorimeter serves as additional tool for electron-hadron separation. The hodoscope, referred to as H2, provided a fast first-level trigger signal in addition to the calorimeter.

The Čerenkov threshold detector and the RICH detector

Between the two groups of back drift chambers BC1/2 and BC3/4, a threshold Čerenkov detector was used until 1997. The radiator gas was a mixture of nitrogen and perfluorobutane (C_4F_{10}) in the proportion 70 : 30. For this gas mixture, Čerenkov radiation is emitted for pions, kaons and protons beyond the thresholds of 3.8, 13.6 and 25.8 GeV, respectively. Therefore, the Čerenkov detector provides good pion identification for energies up to 13.6 GeV.

This Čerenkov detector was replaced in 1998 by the dual-radiator ring-imaging Čerenkov detector (RICH). The Čerenkov photons produced by charged particles traversing the two radiator materials were focused by a spherical mirror onto a large array of photo-multipliers. The first radiator in the front of the RICH detector was an array of 17 × 5 aerogel tiles followed by the second radiator, a 4000 l volume of C_4F_{10} gas. The combination of two different radiators with refractive indices of $n = 1.03$ (aerogel) and $n = 1.0014$ (C_4F_{10}), in combination with the capacity of the RICH detector to allow the reconstruction of opening angles of the Čerenkov radiation cones, provides a reliable identification of all stable charged hadrons in the energy region 2 GeV<E< 15 GeV.

2.4.3 The Luminosity Detector

The luminosity $\mathcal{L}$ can be determined by comparing measured event rates R_{ref} with known cross sections σ_{ref} of elastic reference processes

$$\mathcal{L} = \frac{R_{ref}}{\sigma_{ref}}. \tag{2.1}$$

A suitable process in the case of an electron or positron beam impinging on a gas target is the interaction of the beam with the shell electrons of the target gas. *Møller* scattering

$$e^- e^- \rightarrow e^- e^- \tag{2.2}$$

is used as reference process in the case of an electron beam, while in the case of a positron beam *Bhabha* scattering

$$e^+ e^- \rightarrow e^+ e^- \tag{2.3}$$

and the annihilation process

$$e^+ e^- \rightarrow \gamma\gamma \tag{2.4}$$

are used.

The counting rate for such events is limited by the geometric acceptance and the detection efficiency of the luminosity detector. In order to determine the reference cross section in the acceptance both factors are taken into account using

$$\sigma_{ref} = \int\limits_{\Omega_{acc}} \varepsilon \frac{d\sigma_{ref}}{d\Omega} d\Omega, \tag{2.5}$$

where $\frac{d\sigma_{ref}}{d\Omega}$ is the differential reference cross section in the solid angle $d\Omega$, ε is the detection efficiency of the luminosity detector, Ω_{acc} is the geometric acceptance of the luminosity detector and σ_{ref} the total cross section measured by the luminosity detector. The calculation (2.5) implies an integration over the distribution of the target density.

The inverse of the coincidence cross section measured by the luminosity detector is referred to as the luminosity constant $C_{Lumi} = \sigma_{ref}^{-1}$. The primary difficulty of the approach is the determination of the acceptance as described in Chapter 4.8

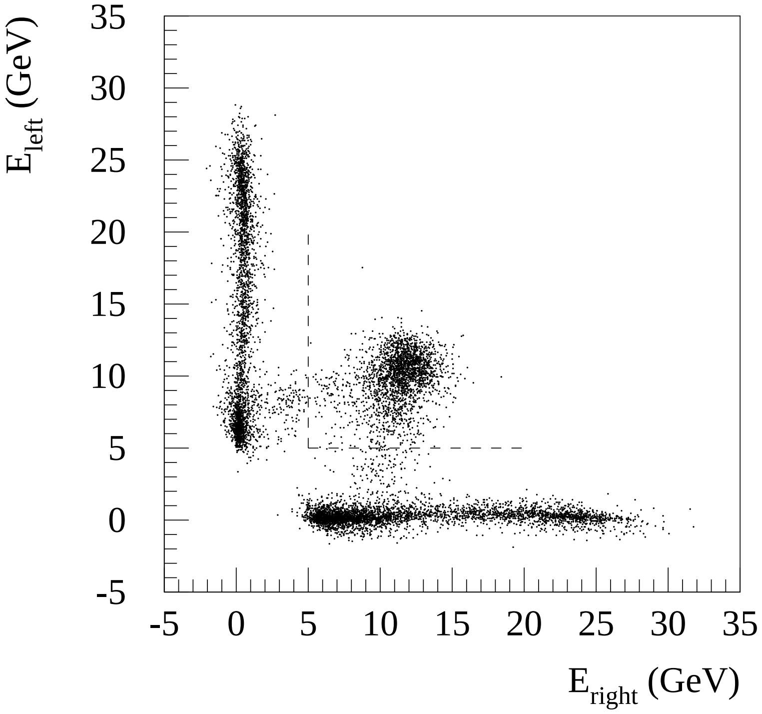

Figure 2.4: Energy deposition [80] in the left and right calorimeter of the luminosity detector.

The Design of the Luminosity Detector

The luminosity detector consists of two identical calorimeters, with readout devices, and a positioning system. Each calorimeter was built from 12 Čerenkov crystals ($NaBi(WO_4)_2$) with the dimensions of $2.2 \times 2.2 \times 20\,\mathrm{cm}^3$ arranged in a 3×4 matrix. In order to avoid optical cross-talk between the crystals, i.e. to obtain undiffused signals, all sides of the crystals except the rear side were covered by a 25μm thin Mylar-foil vacuum-metalized with Aluminum. Each crystal was read out with a photo-multiplier attached to the rear side.

The cross sections of Møller scattering, Bhabha scattering and the annihilation process in the laboratory system are peaked at low scattering angles. Therefore, both calorimeters were directly attached to the beam pipe, as illustrated in Figure 2.5. They were located 7.21 m behind the interaction point on the left and the right hand sides of the beam pipe. In the region of the calorimeters, the beam pipe diameter was reduced to the smallest size possible to ensure undisturbed circulation of the beam. The calorimeter crystals on the left and right hand sides have a distance of 65.5 mm to each other and cover a horizontal acceptance of 4.6 mrad to 8.5 mrad.[3]

The correlation of energy depositions in left and right calorimeter luminosity detector is shown in Figure 2.4. The reference rate $R_{ref.}$ in Equation (2.1) is obtained from events with coincident energy depositions above 4.5 GeV in each of the calorimeters within a time resolution interval of 80 ns.

Due to the event kinematics of the desired processes, energy depositions below 4.5 GeV correspond to large scattering angles that are beyond the acceptance of the luminosity de-

---

[3] The scattering angles are given for events originating from the center of the target.

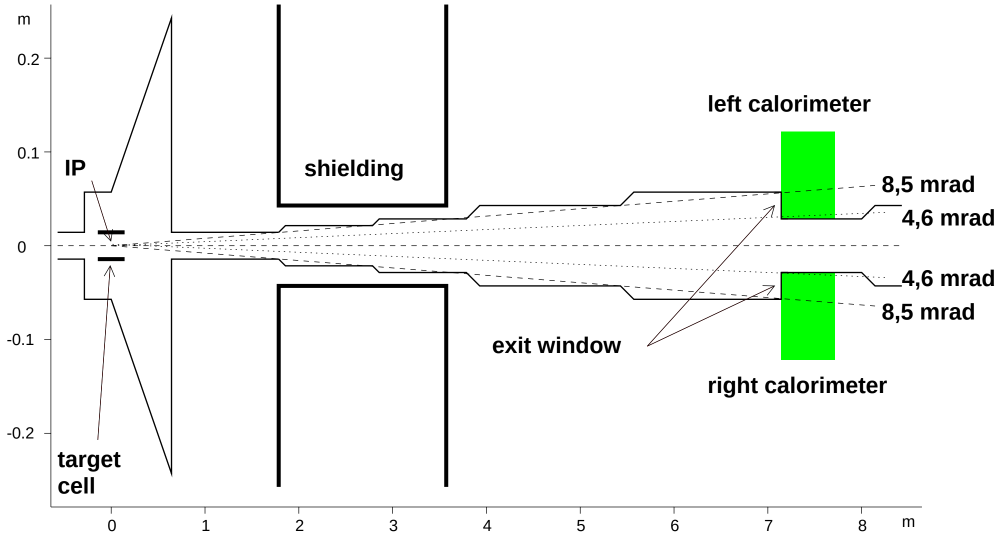

Figure 2.5: Horizontal cut through the HERMES experiment at the position of the electron beam pipe. The illustration is stretched in the direction transverse to the beam axis. Based on [81].

tector. Photons or charged particles which did not origin from the desired processes may still deposit larger energies but are mostly not measured in coincidence in both luminosity detectors. If the energy depositions in the two detectors originate from one of the desired processes but correspond to two different events, the measured luminosity rate is effected by a contribution of *accidental coincidence*. The calculation of the luminosity as it was done in this analysis is described in Section 4.8.

2.5 The Trigger System

Triggers were defined in order to distinguish events of specific interest from background with high efficiency and to initiate digitization and readout of the detector signals. Signals from several detectors were used by the trigger system in different combinations. These logical combinations as defined within programmable logic units (PLU) were evaluated separately in both detector halves and then combined in order to form the final trigger. The final trigger was counted by scaler units. Pre-scalers were used in order to ensure that the data acquisition system (DAQ) did not receive more trigger signals than it could handle. The maximum trigger rate the DAQ could handle was close to 500 Hz at a dead-time of less than 10%. The pre-scale factors as well as the definitions of logical combinations of signals forming a trigger signal were programmable in the PLU.

The trigger mostly used in data analysis, trigger 21, identified events involving a DIS lepton by requiring hits in the hodoscopes $H0$, $H1$, $H2$ and an energy deposition in the calorimeter above a certain threshold in coincidence with the HERA lepton beam bunches. The hodoscope $H1$ was located behind the back drift chambers and had a design identical to that of the hodoscope $H2$ described earlier, but without the pre-shower foil in front of it. The hodoscope upstream of the front drift chambers ($H0$) consisted of a single sheet of 3.2 mm thick (0.7% radiation length) plastic scintillator with photo-multipliers detecting the scintillation light at the edges far from the beam. It was installed in 1996 in order to reduce the backwards-going particle background from the proton beam. This background was identified by the time-of-flight measurement between the signal in $H0$ and the signals in $H1$ and $H2$. Neutral particle background from beam interactions in the collimators and from neutral particles from the photoproduction regime was suppressed within the DIS trigger 21 by requiring hits in both $H0$ and $H1$.

Further triggers, defined by similar combinations of signals as the trigger 21 but with one of the signal requirements missing, were used to extract trigger efficiencies. After 1997, triggers 24 and 25 were defined as the top and the bottom separated contribution to trigger 21.

Another trigger was dedicated to quasi-real photoproduction. It detected decaying charged particles from K,ρ,J/Ψ and Λ which are mostly produced at low values of Q^2 where lepton scattering angles are usually too small to be detected. The trigger required signals in both detector halves from all three hodoscopes and the first back drift chamber in coincidence with the HERA lepton beam bunch.

2.6 Data Acquisition

Events associated with a trigger signal were read out and entered the data acquisition (DAQ) as single event records. The second type of records contained *slow control* information, i.e. information which changed on a slow time scale. Slow control information such as the luminosity rate, the beam current, polarization, or the hardware conditions was read out only approximately every 10 s. The time interval between two of such scaler events defines a *burst*. Data quality is monitored on burst level. 'Official' burst lists are provided by the HERMES Data Quality Group which contain comprehensive information for each individual burst about its usability for the analysis.

The data stream from the DAQ was written in EPIO (Experimental Physics Input Output) file format into files referred to as *runs* which are defined for technical reasons by their size of up to 450 Mbytes. A run finished automatically when either the maximum size was reached or when it was stopped by the shift crew. The files were saved on staging discs during a fill of the HERA storage ring and were copied over to tape robots on the DESY main site in between the fills. For redundancy, the data was additionally stored on local DLT drives.

2.7 Data Production

The recorded data are processed in the data production chain separately in the main production, the slow control production, and the production of micro data summary tapes (μDST). The main production takes the following steps:

- HDC (HERMES DeCoder): This program uses the raw readout information from ADC (Analogue to Digital Converter) and TDC (Time-to-Digital Converter) modules and applies a mapping of wires, includes the geometry information and performs the calibration of signals.
- HRC (HERMES Reconstruction program): This program reconstructs tracks from the hits in the tracking chambers and associates them with the detector responses in the PID detectors.

- ACE calculates permutated plane efficiencies (PPE) in the tracking chambers.

The HRC output is synchronized with the slow control information and written into comprehensive run-wise ADAMO files (μDST files) by the μDST-maker. The μDST files contain all important physics quantities that are needed for the data analysis.

The first main production, called the *a production*, uses calibration information from previous running. New calibration constants and detector efficiencies are determined from the *a* production and are used as input to a reproduction of μDST files in the *b production*. Iteratively, the quality of calibrations is improved with subsequent productions. The analysis presented in this thesis is based on the latest available *c* and *d* productions.

2.8 Track reconstruction by HRC

In order to reconstruct a track, a one dimensional 2^n bit pattern is defined from the hits of each tracking plane with n chosen such that the resolution of the pattern is four to five times larger than the detector resolution. *Tree-lines* are constructed as straight lines from the patterns separately in the U, X and V planes and are combined to 3-dimensional partial tracks.

The method used by HRC to find tracks is called tree-search-algorithm. It is based on pattern recognition using a pattern data bank with all possible track patterns for various resolutions. The bit pattern obtained in data is compared to patterns provided by the data bank. For each *parent pattern* at an arbitrary resolution, the number of *child patterns* at higher resolution which fit into the parent pattern is limited. Iteratively, the resolution is increased by a factor of two whenever a matching pattern is found until certain depths are reached. The final depths correspond to resolutions [82] of 1.4 mm and 0.6 mm in the front chambers and the back chambers, respectively, the *road widths*.

If a single plane does not fire, the whole track could not be reconstructed with the algorithm described above. To account for limited efficiencies in the tracking planes, a tolerant pattern matching algorithm is applied which requires 3 out of 4 matching bits so that tracks are found with this tree search even if there are a few missing hits.

Chapter 3

Data Selection

The presented measurement of F_2 is based on the data taken with hydrogen and deuterium targets using the latest data productions for the years 1996 (96d0), 1997 (97d1), 2000 (00d2), 2002 (02c0), 2003 (03c0) 2004 (04c1) and 2005 (05c1). The data taken in 1998 and 1999 have been excluded from the present analysis due to the overwhelming statistics of the 2000 and 2005 data.

For consistency reasons, the same tracking method NOVC is applied for all data. The so-called STD tracking method is not used since it includes information from vertex chambers which were not available in 1996 and after 1998. This avoids varying efficiencies and resolutions and hence allows a consistent extraction of F_2 from the data taken in all years.

3.1 Data Quality

A preselection of data is based on the official data quality list on burst level. Data are discarded in periods in which one of the PID detectors or one of the tracking detectors was not fully operational (e.g. in case of high voltage trips). Also, periods with problems in the data acquisition were eliminated as well as data with unphysical values or values which have never been reached (e.g. for burst length, beam current and luminosity).

Apart from the data quality provided by the burst lists, additional data quality cuts are applied in the analysis code. A minimum cut on the permutated plane efficiency is used at 99% for each of the four quadrants of the tracking system, see Section 4.4.1. Also, data are discarded for which the μDST entry for the target gas type used disagrees with the run level information recorded in a log file during data taking.

The inspection of data quality is done separately for the top and bottom detector halves, leading to several ranges of bursts or runs in which only the top or only the bottom detector half are used. Top and bottom detector halves are treated as two completely independent detectors. Correspondingly, the integration of luminosity is performed separately for the ranges in which the top or the bottom detector half is considered to be usable for data analysis.

The raw luminosity coincidence rate for data taken with a polarized target shows high statistical fluctuations from one burst to another and was fitted to obtain a smooth behavior. In each burst the luminosity was corrected for the trigger dead-time and for accidental coincidences between the left and the right calorimeters of the luminosity detector as described in Section 2.4.3.

Year	Prod.	Target	DIS, in million		$L = \int \mathcal{L}\, dt$, pb^{-1}	
			top	bot	top	bot
proton						
1996	d0	polarized	0.326	0.346	10.11	10.09
1996	d0	unpolarized	0.783	0.832	24.01	24.07
1997	d1	polarized	1.251	1.322	41.32	41.27
1997	d1	unpolarized	0.976	1.015	31.05	30.95
2000	d2	unpolarized	4.833	4.715	148.71	136.14
2002	c0	polarized	0.493	0.500	15.61	15.29
2002	c0	unpolarized	0.379	0.373	11.73	11.18
2003	c0	polarized	0.283	0.288	8.16	8.61
2004	c1	polarized	1.833	1.627	54.62	48.72
2004	c1	unpolarized	0.089	0.089	2.87	2.87
2005	c1	polarized	3.477	3.447	107.79	108.73
2005	c1	unpolarized	0.344	0.343	9.83	9.88
deuteron						
1996	d0	unpolarized	1.341	1.419	46.80	46.56
1997	d1	unpolarized	1.515	1.592	56.06	55.94
2000	d2	polarized	4.990	5.393	170.44	172.16
2000	d2	unpolarized	1.068	1.146	37.14	37.30
2002	c0	unpolarized	0.323	0.334	11.48	11.64
2005	c1	unpolarized	4.250	4.192	141.58	142.46

Table 3.1: Number of DIS events and luminosities per nucleon on proton and deuteron targets used in the analysis. Numbers are separated into the top and the bottom halves of the spectrometer for each year. The number of DIS events was obtained by applying the cuts in Table 3.2, while the luminosity per nucleon was calculated using Equation (4.40).

The numbers of DIS events together with the luminosities used in the analysis are given in Table 3.1. In total, 30.0 million DIS events are used from the hydrogen target, and 27.6 million DIS events from the deuterium target.

3.2 Event Selection

$0.1 < y < 0.85$	Charge = Beam Charge
$0.1\,\mathrm{GeV}^2 < Q^2$	$\lvert z_{vertex} \rvert < 18.0\,\mathrm{cm}$
$5.0\,\mathrm{GeV}^2 < W^2$	$\lvert d_{vertex} \rvert < 0.75\,\mathrm{cm}$
PID > 0	Fiducial Volume Cuts

Table 3.2: Cuts imposed on track level to identify DIS events.

The cuts imposed to identify DIS events are listed in Table 3.2. If more than one track passes all DIS cuts, the event is discarded. The fraction of events with more than one potential DIS lepton reaches a maximum of less than 0.4% in the region $y > 0.8$.

The lower cut on y is chosen according to the detector performance. The constraint $y > 0.1$ excludes the region of high momentum in which the momentum resolution starts to degrade [80].

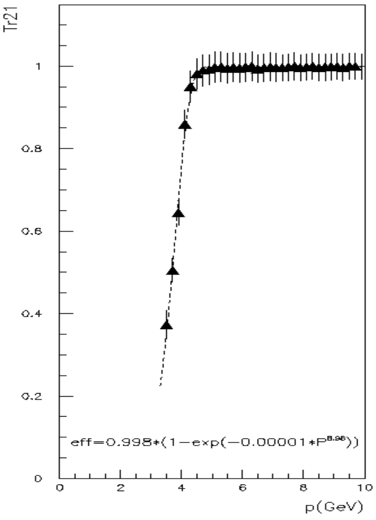

Figure 3.1: Trigger 21 efficiency involving a calorimeter threshold of 3.5 GeV.

The upper cut on y is related to the calorimeter trigger efficiency. The trigger signal comes with two settings for cuts on the particle energies, as mentioned in Section 2.4.2. Energies of at least 1.4 GeV and 3.5 GeV for the maximum deposited energy were required by the calorimeter trigger, which only in principle corresponds to values of $y = 0.95$ and $y = 0.87$ for the DIS lepton: To save computing time, the energies calculated on trigger level were not the full cluster energy, but the maximum sum of energies in two adjacent vertical columns of blocks. Such an algorithm is fast but imposes an inaccurate cut on the lowest momentum. If two tracks at a small distance hit the calorimeter, the maximum track energy can be overestimated. If the cluster is larger than the size of two columns, the energy is underestimated.

By variation of the y-cuts and comparison of the trigger efficiencies, corresponding cuts at $y < 0.91$ and $y < 0.85$ were found to be safe towards the effects of the calorimeter threshold.

For the final analysis, a common cut of $y < 0.85$ was applied to data taken at either calorimeter thresholds. This is in particular required for combining or dividing the contents of bins adjacent to the upper y cut for data sets taken at different calorimeter thresholds. Apart from the calorimeter threshold, the upper y cut sets boundaries to particle misidentification and the charge symmetric background to DIS events, since both contributions have maxima at low particle momenta, see Sections 4.1 and 4.2.

In order to exclude events from the resonance region, a cut of $W^2 > 5$ GeV^2 is chosen in a conservative manner, since the region coincides with the region of large detector smearing.

To extend the kinematic range to low values of x, a low cut is used for Q^2 at 0.1 GeV^2. At the same time the binning is chosen such that the traditional DIS region $Q^2 > 1$ GeV can easily be separated from the region 0.1 GeV$^2 < Q^2 < 1$ GeV^2, as discussed in Section 3.4.

Furthermore, cuts are applied to ensure that only events are accepted which have their vertex positions inside the target cell as illustrated in Figure 3.2. The location of the target cell was constantly between -20 cm$< z_{vertex} < 20$ cm in the present analysis. A cut of $|z_{vertex}| < 18$ cm efficiently selects events originating from the target cell, and at the same time eliminates background tracks e.g. from electromagnetic showers and scattering in the collimator, see Section 4.2. A less restrictive cut on the radial distance is applied at $d_{vertex} <$ 0.75 cm.

The geometric acceptance of the HERMES spectrometer covers a polar region between 0.04 rad $< \theta <$ 0.22 rad for events originating in the center of the target. Since the geometric acceptance depends on the longitudinal vertex position z_{vertex} and the magnet bend of a particular track, no general cuts are imposed on the angular acceptance of the detector. The *fiducial volume cuts* are more accurately applied to the individual front and back partial tracks in order to exclude tracks going through the magnet chamber frames or hitting the field clamps in front of or behind the spectrometer magnet. Furthermore, a vertical inner cut

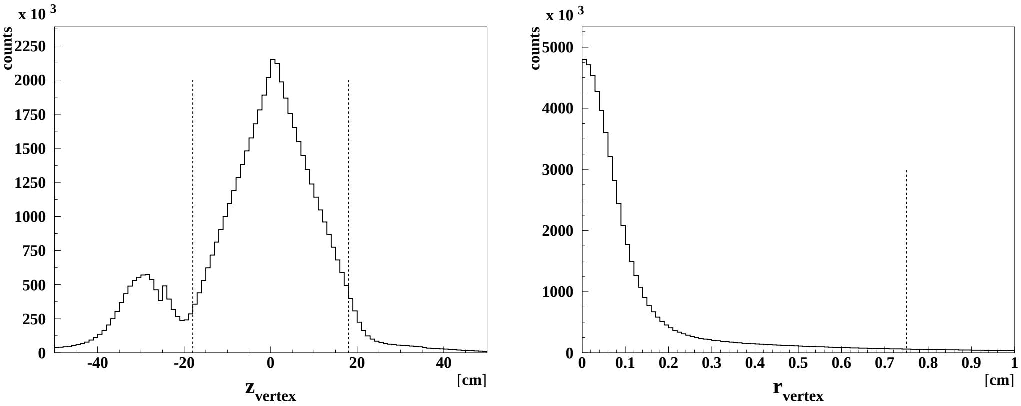

Figure 3.2: Axial and radial distribution of the vertex positions for events passing DIS cuts others than vertex cuts. Vertex cuts will be applied at $|z_{vertex}| < 18\,\text{cm}$ and $d_{vertex} < 0.75\,\text{cm}$, as depicted by the vertical lines.

is applied to exclude the volume of the septum plate.

Another set of fiducial volume cuts is related to the calorimeter. If particles hit the outer region of the array of lead glass blocks and produce electromagnetic showers, it can be expected that parts of the showers are not included in the calorimeter, thus a cluster energy is calculated which does not correspond to the energy of the particle. In order to ensure that particles considered in the analysis have optimal lepton-hadron separation, the acceptance is restricted by cuts on the outer regions of the calorimeter. Cuts of 6 cm are applied in vertical directions, corresponding to 2/3 of a block size, and more restrictive cuts of 14 cm are applied in horizontal directions, due to a higher probability of showers leaking in the side surfaces at larger horizontal entering angles.

3.3 Yields

After applying general data quality cuts and identifying the DIS events in the data sets, further data quality studies are performed to ensure the stability of DIS yields as a function of time, where yields are defined as the luminosity-normalized raw numbers of DIS events. For the determination of the luminosity from the luminosity coincidence rate, please refer to Section 4.8.

Yields are calculated for each year and for the hydrogen and deuterium targets separately. A further separation into polarized and unpolarized targets is in particular required by the different luminosity constants applied during the operation of the transverse target magnet, see Section 4.8. Various run ranges were identified with yields strongly deviating from the average yields. The observed effects were compared to corresponding observations during data taking and to other information in the μDST tables in order to introduce additional data quality cuts or to legitimate the explicit exclusion of the particular run ranges. An example is the time dependence of the 2002 hydrogen yields, shown in Figure 3.3. In the first 808 runs of 2002 the RICH was running with Nitrogen instead of C_4H_{10}. The lower refractive index of Nitrogen ($n = 0.0003$), compared to C_4H_{10} ($n = 0.0014$), is associated with a smaller Čerenkov angle θ_C and leads to a distortion of particle identification. These runs have been rejected. Furthermore, a certain run range in 2000 was found to have a high

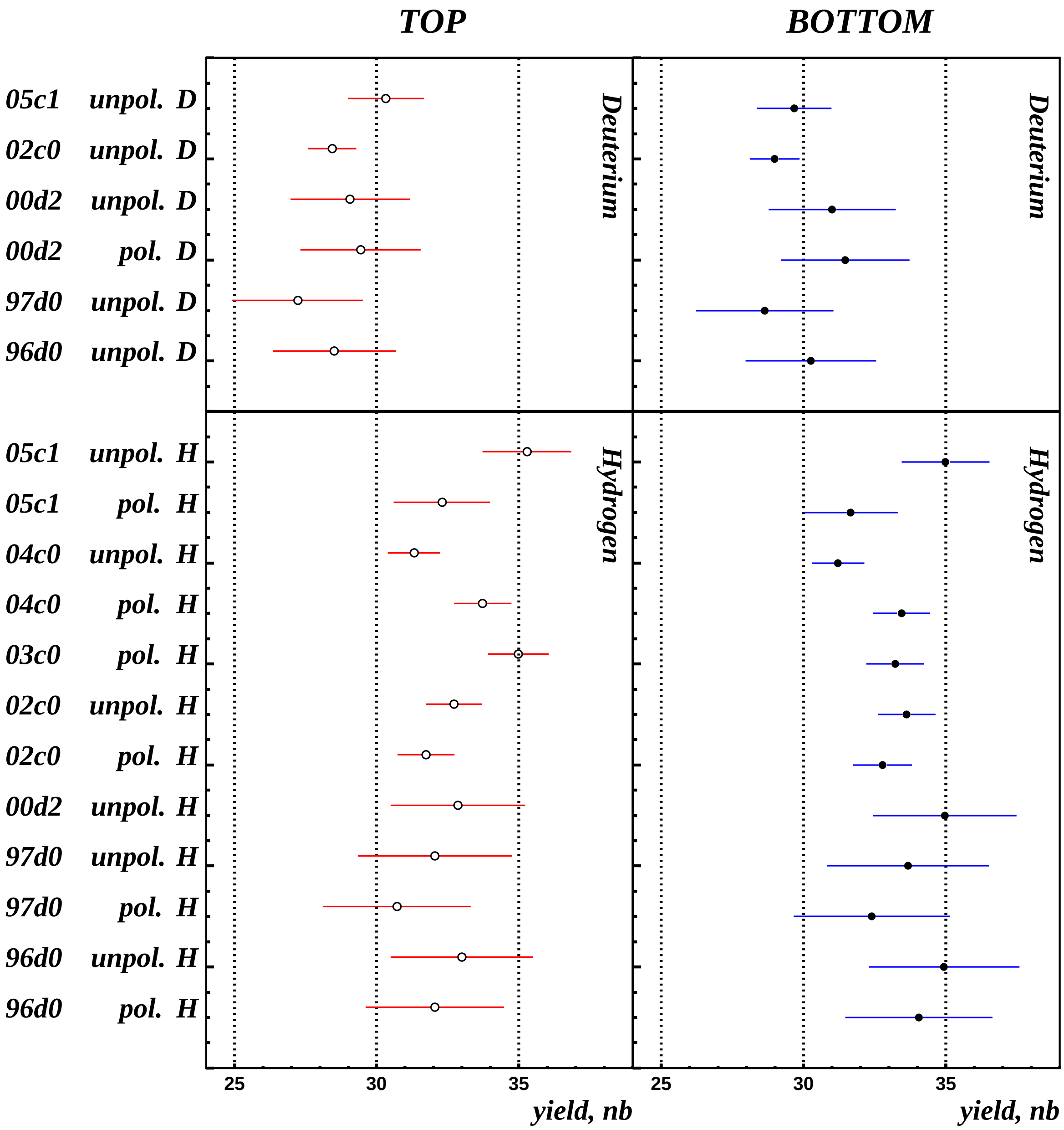

Figure 3.3: Yields obtained in different data sets. The normalization uncertainties originating from the uncertainties of the luminosity constants are represented by the horizontal error bars. Note that the luminosity constants are the same for the top and bottom detector halves. Statistical uncertainties are negligible.

calorimeter threshold of 5.95 GeV which would cause a lack of tracks in the low-momentum region. An explicit requirement is therefore imposed to allow only for the two calorimeter threshold settings of 1.4 GeV and 3.5 GeV. Chamber thresholds[1] were changed several times, but a correlation with the behavior of the yields is not observed.

---

[1] Chamber thresholds are defined by the minimum electric signal collected at the wires and required in order to recognize signals as hits.

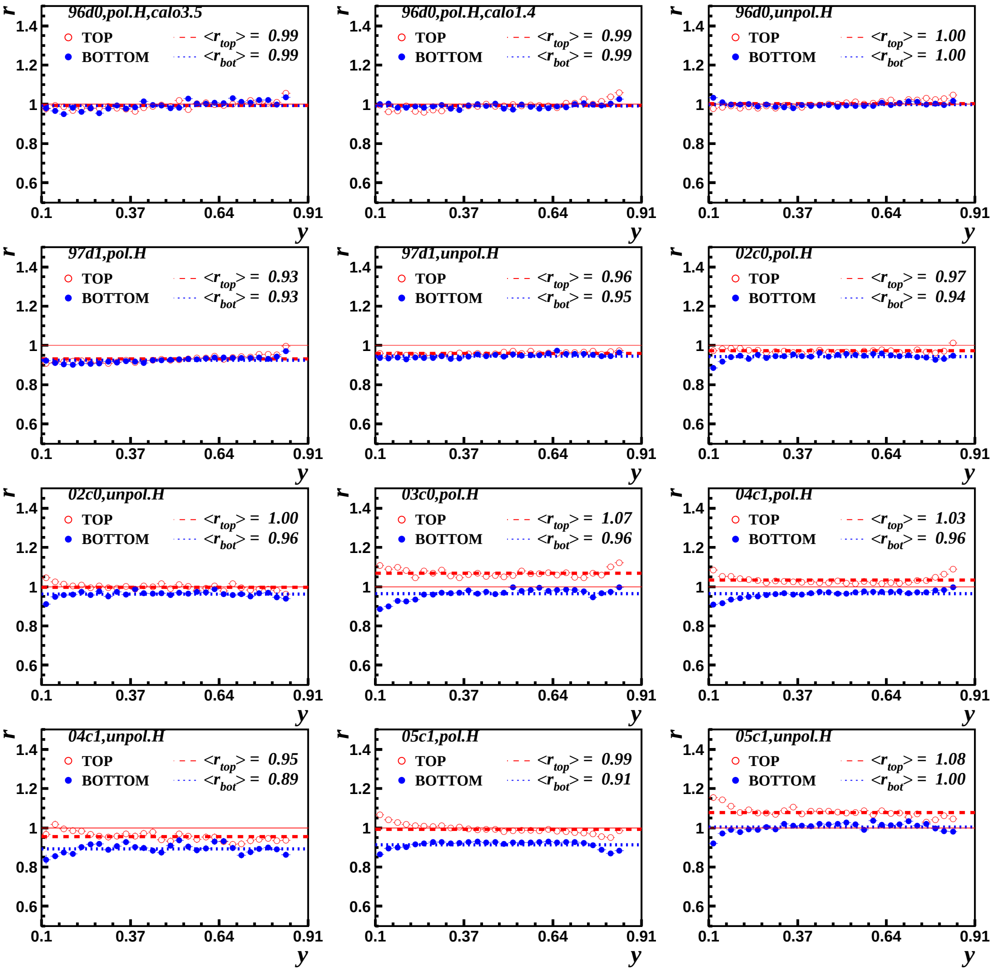

Figure 3.4: Ratios of yields measured in each year with the hydrogen target to the hydrogen yield measured in 2000 as a function of the variable y.

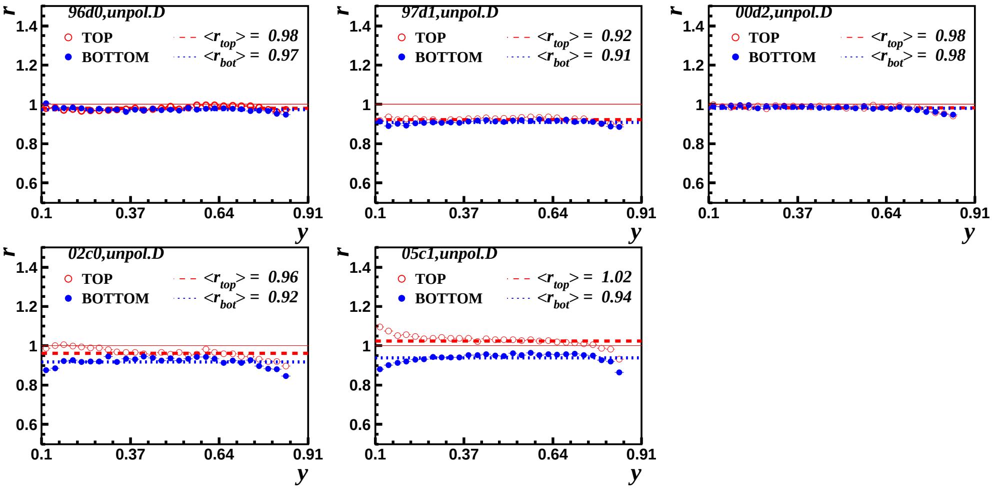

Figure 3.5: Ratios of yields measured in each year with the deuterium target to the deuterium yield measured in 2000 as a function of the variable y.

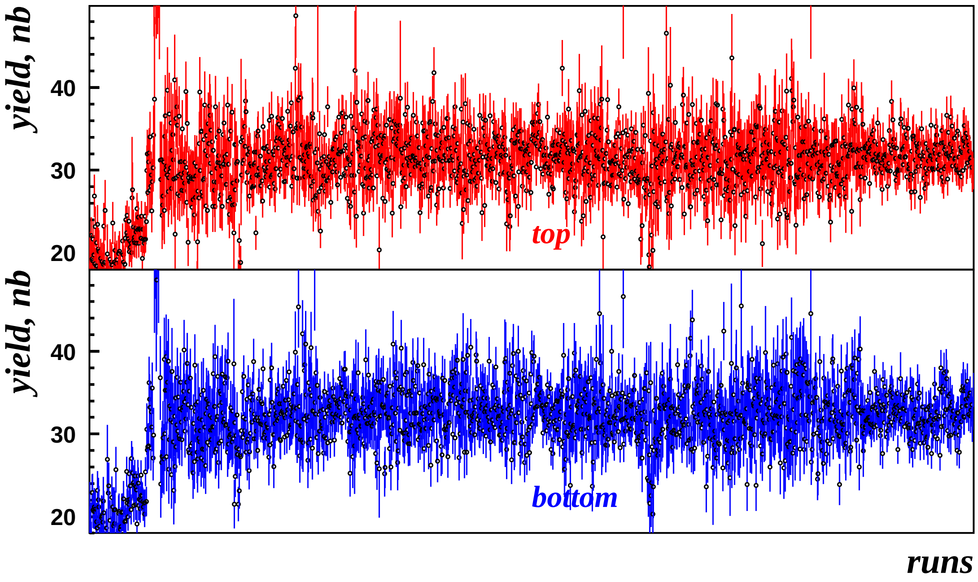

Figure 3.6: An example of rejected data: In the first 808 runs in 2002, the RICH detector was operated with nitrogen instead of C_4H_{10}, thus affecting the particle identification and consequently the yields.

After all, the time dependence of yields, integrated over all kinematic variables has shown a stable behavior, see Figures A.1-A.18. The horizontal lines represent the average yields over all runs measured in the top and bottom detector halves. Figure 3.3 summarizes the results of average yields for all data sets. The error bars illustrate the uncertainties due to the luminosity measurement. The average yields for each data set as used in the analysis can be calculated from Table 3.1. The resulting yields are slightly smaller than the run-averaged yields (Figures A.1-A.18, 3.3) due to the additional cuts imposed by the binning[2].

Figures 3.4 and 3.5 show the yield of each data set as a ratio to the yield in 2000 for the same target gas, this time integrated over all accepted data but resolved in the kinematic variable y. The flat shapes of the ratios indicate that the differences of the yields in different data sets are to some extent due to the normalization. Yields in the top and bottom halves of the detector are normalized using identical luminosity constants. Hence the differences between the yields of the top and bottom detector halves within the same data set are attributed to the top-bottom-misalignment, see Section 4.7, and to some extent to trigger efficiencies, see Section 4.3.

3.4 F_2 Binning

The x-Q^2 binning used for this analysis was determined in studies aiming at a flat distribution of statistical uncertainties with simultaneous consideration of detector resolution effects and radiative corrections.

In a first step the x-binning was selected to match increasing detector smearing and smaller statistics at higher x with gradually increased x-bin sizes towards higher x. The x-bin sizes

---

[2] A small fraction of events, i.e. the 'corner' at $x > 0.054$ and $Q^2 < 1\,\mathrm{GeV}^2$, is purposely omitted by the binning because of low statistics.

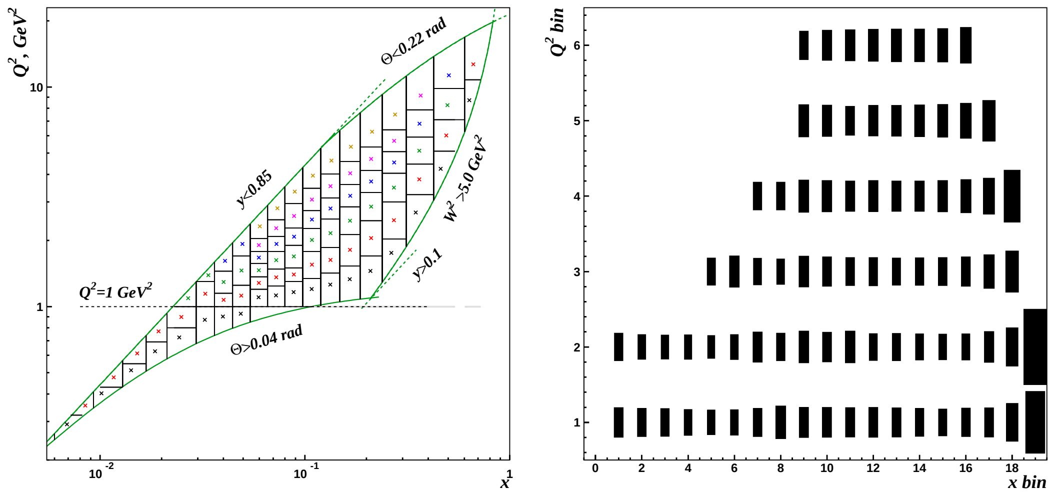

Figure 3.7: Left: Binning in the $x - Q^2$ kinematic plane. The covered phase space is limited by the cuts on y, W^2 and the geometric acceptance in θ. A well-adjusted subdivision of x-bins into two to six Q^2-bins is chosen. In each bin, the center of kinematics is marked with a cross.
Right: Population of events in the binning. The area covered by the boxes is proportional to the fractional statistical uncertainty. In this illustration for the unpolarized Hydrogen data in 2000, the maximum statistical uncertainty of 2.8% is obtained in bin $(x, Q^2) = (19, 2)$.

were chosen to be at maximum 0.3 at the expense of larger statistical uncertainties in the highest x bins. In the other limit, $x < 0.05$, the x bin sizes were increased - having a desired subdivision into at least two Q^2 bins in mind - in order to gain statistics: In this region, large radiative corrections will be responsible for large (inflated) statistical uncertainties on BORN level. Radiative corrections decrease with increasing Q^2, which suggests a progressively finer subdivision from two Q^2 bins at low x (and low Q^2) to six Q^2 bins at $x \approx 0.3$ (and larger $Q^2 > 1.5\,\mathrm{GeV}^2$). Due to decreasing statistics at high x, the subdivision is again gradually reduced down to two Q^2 bins in the very highest x bin. Even though the subdivision into Q^2 bins is chosen to be different for each x bin, a common bin limit at $Q^2 = 1\,\mathrm{GeV}^2$ is defined in order to allow a separation of the traditional DIS region, $Q^2 > 1\,\mathrm{GeV}^2$, from the region with $Q^2 < 1\,\mathrm{GeV}^2$.

The final binning used in the analysis is depicted in Figure 3.7. The kinematic plane covered by the HERMES experiment is limited by the geometric acceptance and the restrictions imposed on y and W^2.

Chapter 4

Data Analysis

4.1 Particle Identification

The analysis of deep-inelastic scattering requires a reliable identification of the scattered lepton. In order to achieve high efficiencies, the HERMES experiment employs four independent detectors which are dedicated to particle identification (PID) and were briefly described in Chapter 2.4.2: The pre-shower detector, the calorimeter, the TRD and a threshold gas Čerenkov detector that was replaced by a dual radiator ring imaging Čerenkov detector (RICH) in 1998.

4.1.1 Formalism

The probability for the hypothesis $H_{l(h)}$ that a particular track is a lepton (hadron), can be formed from the particle fluxes $P(H_{l(h)}|p,\theta)$ and parent distributions $P(E|H_{l(h)},p)$ using Bayes' theorem:

$$P(H_{l(h)}|E,p,\theta) = \frac{P(H_{l(h)}|p,\theta)P(E|H_{l(h)},p)}{\Sigma_{i=l,h}P(H_i|p,\theta)P(E|H_i,p)} \tag{4.1}$$

The particle's momentum p and its polar angle θ are provided by the tracking system. When traversing the PID detectors the particle leaves a signature of its identity through the detector response E. The expected detector response E for a particle is expressed by the parent distribution, while the fluxes are probability distributions for a certain particle type to be found at given values of the kinematic variables p and θ.

In order to achieve lepton-hadron discrimination a PID value is calculated for each track from the corresponding probabilities:

$$PID = log_{10}\frac{P(H_l|E,p,\theta)}{P(H_h|E,p,\theta)} \tag{4.2}$$

Using equation (4.1) this can be written in terms of parent distributions and fluxes:

$$PID = log_{10}\frac{P(E|H_l,p)P(H_l|p,\theta)}{P(E|H_h,p)P(H_h|p,\theta)} = PID_{det} - log_{10}\Phi, \tag{4.3}$$

where

$$PID_{det} = log_{10}\frac{P(E|H_l,p)}{P(E|H_h,p)} \tag{4.4}$$

and

$$\Phi = P(H_h|p,\theta)/P(H_l|p,\theta). \tag{4.5}$$

Each of the individual PID detectors, the Čerenkov detector or two RICH radiators, the Pre-shower detector, the Calorimeter, and the six TRD modules contribute with probabilities $P(E|H_l,p)$ and $P(E|H_h,p)$. Combining the probabilities from all detectors in Equation 4.4 results in a sum of PID values

$$PID_{det} = PID_{Cer(RICH)} + PID_{pre} + PID_{calo} + PID_{TRD}, \tag{4.6}$$

where $PID_{RICH} = \Sigma_{i=1}^{2} PID_{RICH,i}$ and $PID_{TRD} = \Sigma_{i=1}^{6}, PID_{TRD,i}$. The following PID values are commonly used in the Hermes analysis:

$$\begin{aligned} PID_2 &= PID_{calo} + PID_{pre} \\ PID_3 &= PID_{calo} + PID_{pre} + PID_{cer(RICH)} \\ PID_5 &= PID_{TRD}. \end{aligned} \tag{4.7}$$

In an old scheme the logarithmic likelihoods from Pre-Shower, Calorimeter and Čerenkov were combined with the truncated mean energy of the TRD by a linear combination. This became obsolete with the quantity PID_5 using the result of a TRD probability analysis.

The full PID potential of the Hermes detector is hence exploited using

$$PID = PID_3 + PID_5 - log_{10(\Phi)}. \tag{4.8}$$

4.1.2 Parent Distributions

Parent distributions reflect the performance of the PID detectors and are independent on the physics processes. In principle, they can be measured in test-beam facilities with appropriate beams of leptons and hadrons. Alternatively, parent distributions can be extracted from measured data. This has the advantage that aging effects are taken into account. The extraction of parent distribution for a particular PID detector requires a high purity of particle identities. This is accomplished by applying restrictive cuts on the other PID detectors, e.g. the parent distributions for the Calorimeter are extracted from data by applying PID cuts on the detector response of the pre-shower, TRD, and Čerenkov (RICH). This procedure assumes independence on the detector response of all PID detectors. The large correlations between the Pre-shower and the Calorimeter were studied [83] and are accounted for by applying only a loose cut on the Pre-shower detector response when extracting parent distributions for the Calorimeter. In order to prevent effects from small correlations between the two radiators of the RICH as well as between the 6 TRD modules, no cuts are applied among these units. Another case of correlated detector responses, even though rare, is given for events in which particles interact upstream of most TRD modules and simultaneously influence the responses in all PID detectors.

The algorithm for the calculation of parent distributions is implemented in the program `xparent`. The library PIDlib is used for the calculation of the PID ratios. Details can be found in [84].

4.1.3 Fluxes

Fluxes for leptons and hadrons are in principle a result of the particle identification and are not known at the point of calculation of PID values. Using equation (4.8) without the flux term $log_{10(\Phi)}$ means to assume equal count rates for leptons and hadrons. Particle fluxes are determined by an iterative method starting with the assumption of equal fluxes in the first step:

$$\Phi_0(p,\theta)_0 = 1. \tag{4.9}$$

BBy integration of the PID distributions the PID fluxes for the next iteration are obtained, respectively:

$$\Phi_1(p,\theta) = \frac{N_{PID<0}(p,\theta)}{N_{PID>0}(p,\theta)}. \tag{4.10}$$

Convergence is typically reached after less than five iteration steps.

4.1.4 Efficiencies and Contaminations

A cut on the PID value is always connected to efficiency losses and contaminations. The efficiency of lepton identification is defined by the fraction of true leptons which pass the cut on the PID value whereas the contamination is the fractional contribution of hadrons to the sample identified by the same cut. A low cut value ensures that the true leptons are contained in the identified lepton sample with a large fraction, but the contamination by hadrons becomes high at the same time. The higher the cut value, the lower the contamination of hadrons in the lepton sample at the expense of a lower efficiency for leptons. By a high cut value a high purity of the lepton sample can be obtained but the measurement of DIS cross sections requires not only a clean sample but also correct count rates. In this analysis the cut on the PID value is chosen at $PID_l = 0$ to keep hadron contamination low and lepton efficiency high at the same time.

The calculation of efficiencies $\mathcal{E}$ and contaminations $\mathcal{C}$ requires integrations over the lepton distribution N_l and the hadron distribution N_h:

$$\mathcal{C}(PID_l) = \frac{\int_{PID_l} dPID\, N_h}{\int_{PID_l} dPID(N_l+N_h)} \tag{4.11}$$

$$\mathcal{E}(PID_l) = \frac{\int_{PID_l} dPID\, N_l}{\int dPID\, N_l}. \tag{4.12}$$

According to Equation 4.2, the PID value is connected to the ratio of probabilities for a particle being a lepton and being a hadron, and thus to the fractional contributions of leptons

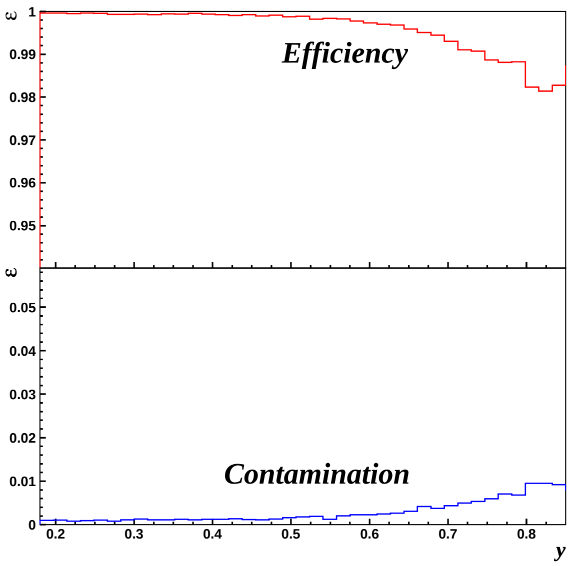

Figure 4.1: Lepton efficiency and hadron contamination of the DIS sample calculated using Equations (4.11) and (4.12)

and hadrons. Using this Equation in combination with the unity condition

$$P(H_l|E,p,\theta) + P(H_h|E,p,\theta) = 1, \tag{4.13}$$

the distributions N_l and N_h required by Equations (4.11) and (4.12) can be derived:

$$N_l = P(H_l|E,p,\theta) = \frac{10^{PID}}{1+10^{PID}} \quad \text{and} \tag{4.14}$$

$$N_h = P(H_h|E,p,\theta) = \frac{1}{1+10^{PID}}. \tag{4.15}$$

Figure 4.2 shows the distributions of the PID value and the contributions of leptons and hadrons according to Equations 4.14 and 4.15.

The number of identified leptons $N(PID > PID_l)$ is corrected for efficiencies and contaminations:

$$N_l^{cor.} = N(PID > PID_l) \cdot \frac{1 - \mathcal{C}(PID_l)}{\mathcal{E}(PID_l)}. \tag{4.16}$$

The size of this correction is mostly far below 1% and reaches ~3% for a few bins in the low momentum region. However, correlations between PID detectors as described in Section (4.1.2) cannot be completely avoided. They may bias the calculation of parent distributions and thus the correction for particle identification. These effects are covered by the assignment of a conservative PID uncertainty of the full size of the correction applied in Equation (4.16).

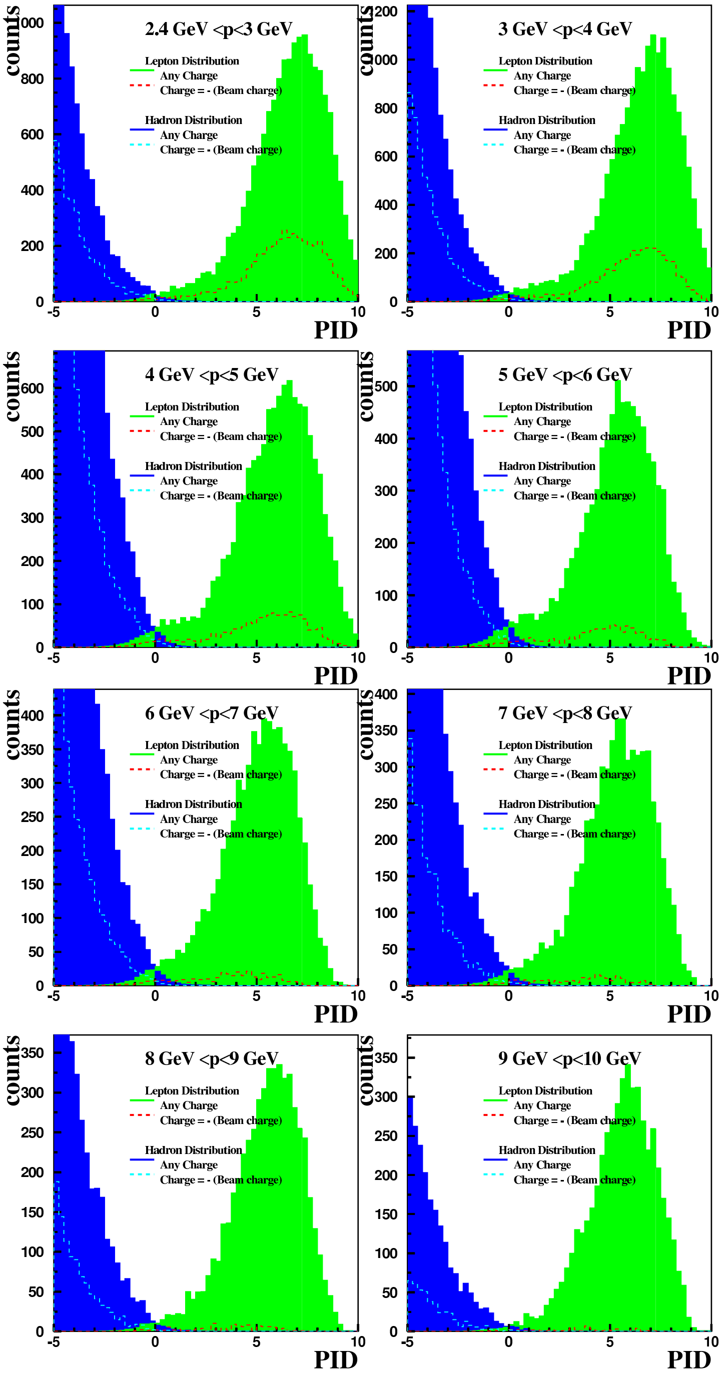

Figure 4.2: Distributions of leptons N_l (green) and hadrons N_h (blue) according to Equations (4.14) and (4.15) in momentum bins $2.4\,\mathrm{GeV} < p < 10\,\mathrm{GeV}$. The dashed curves illustrate the contribution from the opposite beam charge. In case of the lepton sample this contribution is attributed to charge symmetric background, see Section 4.2.

4.2 Charge Symmetric Background

A certain amount of leptons can be observed which pass all kinematic and geometric cuts listed in Table 3.2 but have the opposite electric charge of the beam leptons. They can by no means be distinguished from the desired DIS leptons except by their charge. The opposite-charged leptons are attributed to charge symmetric processes such as the Dalitz decay $\pi^0 \rightarrow e^+e^-\gamma$ or photon conversion $\gamma \rightarrow e^+e^-$. Due to the charge symmetry of these background processes, the sample of DIS leptons passing the charge condition is contaminated by the same amount of leptons which do not pass the charge condition. A correction for charge symmetric background processes can be performed by counting particles with a charge opposite to the beam charge by a negative weight.

Charge symmetric background is significant only in the high y region as shown in Figure 4.3. The contribution of charge symmetric background to the sample of DIS events exceeds 10% in this region of low energies. It is attributed to the following sources:

- Beam leptons producing electromagnetic showers in the collimators,
- photons, e.g. from bremsstrahlung, which convert into e^+e^- pairs in the detector material, and
- decays such as the Dalitz decay $\pi^0 \rightarrow e^+e^-\gamma$, or dilepton decays such as $\rho^0 \rightarrow e^+e^-$ or $J/\Psi \rightarrow e^+e^-$.

In the vertex distribution of leptons along the z-axis, a peak at $z_{vertex} < -18\,cm$ indicates interactions in the collimator C2. The leptons with such a low z vertex position and a charge opposite to the beam charge are attributed to electromagnetic showers in the collimator material induced by the lepton beam. In large parts, theses contributions are eliminated with

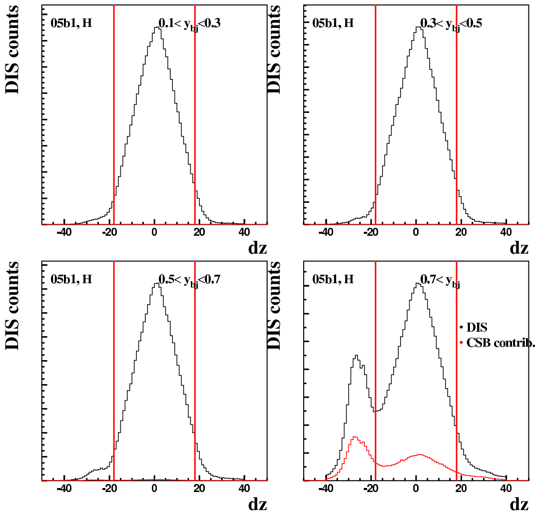

Figure 4.3: The vertex distribution along the z-axis for events passing the DIS cuts without charge and vertex conditions in the regions $0.1 < y < 0.3$, $0.3 < y < 0.5$, $0.5 < y < 0.7$, $0.7 < y$ (black) together with the corresponding contribution from leptons with the opposite charge of the beam (red).

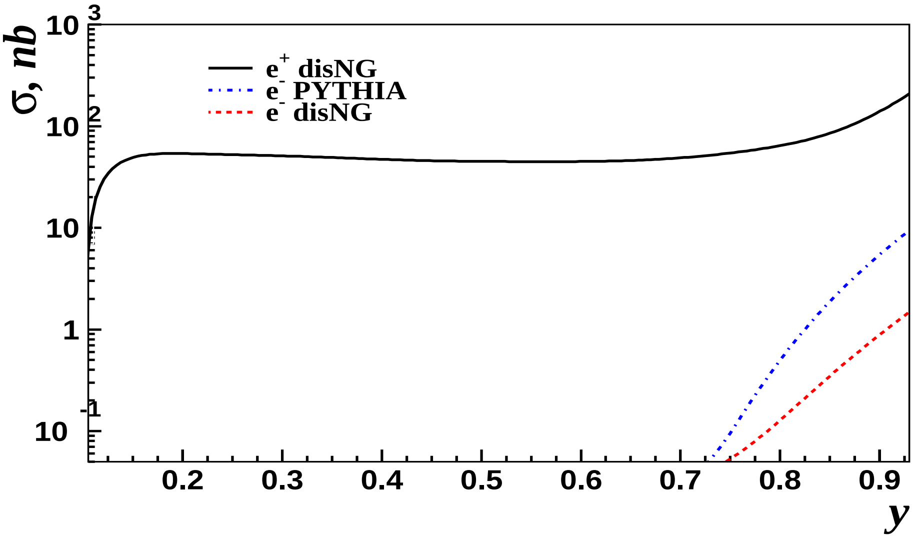

Figure 4.4: A comparison of the charge symmetric background simulated by Pythia (dashed-dotted) and `gmc_disNG` MC (dashed).

a cut $|z_{vertex}| < 18\,cm$. Other contributions to the charge symmetric background are either originating from radiative photons or from electromagnetic decays of hadrons. Synchrotron radiation is not regarded as a source of charge symmetric background since the respective energy scale is in the keV region, in which charged particles curl up in the magnetic field and do not reach the PID detectors in the rear part of the spectrometer.

The predictions of two Monte Carlo simulations are compared to each other. The `gmc_disNG` MC production that will be described in Section 4.5.2 simulates lepton-nucleon scattering down to $Q^2 = 0.1\,\mathrm{GeV}^2$ and includes the effects of radiative photons. The Pythia MC simulation used does not include photon radiation but has a lower cut of $Q^2 \approx m_e^2$. Due to the increase of cross sections at low Q^2 which is attributed to the hadronic structure of the exchanged photon, a large contribution to the cross section originating from the low Q^2 region is not simulated by `gmc_disNG`. Hadronic decays in this region can strongly contribute to contaminations in the measured kinematic region by produced leptons which are mistaken as the scattered lepton. Even though the identification of DIS events includes a cut $Q^2 > 0.1\,\mathrm{GeV}^2$, leptons from electromagnetic decays produced below this threshold can be reconstructed with apparent values of $Q^2 > 0.1\,\mathrm{GeV}^2$. They are predominantly produced at small energies corresponding to high values of y. The comparison of the charge symmetric background cross section predicted by Pythia and `gmc_disNG` is shown in Figure 4.4.

In the context of the data analysis, it is irrelevant which of the well-known charge symmetric processes is responsible for a particular opposite charged lepton. Regardless the source, a correction is applied by counting such a lepton with negative weight.

4.3 Trigger Efficiencies

A good knowledge of the efficiencies in the apparatus is a prerequisite for the measurement of absolute cross sections. In this section the correction for trigger efficiencies is discussed.

Each trigger requires a certain combination of fast signals, e. g. trigger 21 requires signals from the hodoscopes $H0$, $H1$ and $H2$ and a sufficiently high energy deposition in the calorimeter (CA). This makes the trigger 21 efficiency sensitive to the individual efficiencies in $H0$, $H1$, $H2$ and the calorimeter. Apart from trigger 21, other triggers are defined by various other combinations of signals. If no particular trigger is required in the analysis, the trigger with the highest efficiency dominates. For instance, the low efficiency of the hodoscope $H0$ shown later has no effect on the data analysis, if also triggers 18 or 26 are equally used which do not rely on H0 and have negligible trigger inefficiencies.

4.3.1 Definitions

The efficiencies of $H0$, $H1$, $H2$, CA have been extracted which allows the calculation of the the Trigger 21 efficiency [85] . In the following, the symbol + will be used as a logical OR, & as a logical AND and $\not\&$ needed later as a logical AND NOT. The triggers which are relevant in this context are:

$$
\begin{aligned}
\mathrm{Tr18} &= (H1 \;\&\; H2 \;\&\; CA)_{\mathrm{top}} \\
\mathrm{Tr26} &= (H1 \;\&\; H2 \;\&\; CA)_{\mathrm{bot}} \\
\mathrm{Tr19} &= (H0 \;\&\; H2 \;\&\; CA)_{\mathrm{top}} + ()_{\mathrm{bot}} \\
\mathrm{Tr20} &= (H0 \;\&\; H1 \;\&\; CA)_{\mathrm{top}} + ()_{\mathrm{bot}} \\
\mathrm{Tr28} &= (H0 \;\&\; H1 \;\&\; H2 \;\&\; BC)_{\mathrm{top}} \;\&\; ()_{\mathrm{bot}} \\
\mathrm{Tr21} &= (H0 \;\&\; H1 \;\&\; H2 \;\&\; CA)_{\mathrm{top}} + ()_{\mathrm{bot}} = \mathrm{Tr24} + \mathrm{Tr25} \\
\mathrm{Tr24} &= (H0 \;\&\; H1 \;\&\; H2 \;\&\; CA)_{\mathrm{top}} \\
\mathrm{Tr25} &= (H0 \;\&\; H1 \;\&\; H2 \;\&\; CA)_{\mathrm{bot}}
\end{aligned}
\tag{4.17}
$$

Triggers 24 and 25 separate trigger 21 into the top and the bottom detector, respectively, and allow a separate correction for trigger efficiencies in each detector half. The efficiencies of $H0$, $H1$, $H2$ are derived from the triggers listed above by comparing trigger 24 or 25 to the corresponding trigger without the particular hodoscope. This is done separately for top and bottom by excluding cases in which the corresponding trigger in the other half fired. Trigger 25 was explicitely excluded for the calculation of efficiencies in the top detector and trigger 24 was excluded for the calculation of efficiencies in the bottom detector.

$$
\varepsilon(H0)_{\mathrm{top}} = \frac{N_{18\ \&\ 24\ \not\&\ 25}}{N_{18\ \not\&\ 25}} \qquad \varepsilon(H0)_{\mathrm{bot}} = \frac{N_{26\ \&\ 25\ \not\&\ 24}}{N_{26\ \not\&\ 24}} \tag{4.18}
$$

$$
\varepsilon(H1)_{\mathrm{top}} = \frac{N_{19\ \&\ 24\ \not\&\ 25}}{N_{19\ \not\&\ 25}} \qquad \varepsilon(H1)_{\mathrm{bot}} = \frac{N_{19\ \&\ 25\ \not\&\ 24}}{N_{19\ \not\&\ 24}} \tag{4.19}
$$

$$
\varepsilon(H2)_{\mathrm{top}} = \frac{N_{20\ \&\ 24\ \not\&\ 25}}{N_{20\ \not\&\ 25}} \qquad \varepsilon(H2)_{\mathrm{bot}} = \frac{N_{20\ \&\ 25\ \not\&\ 24}}{N_{20\ \not\&\ 24}} \tag{4.20}
$$

In the case of the Calorimeter, Trigger 28 was used to imitate trigger 21 without Calorimeter because it is the best available approximation. The presence of a logical AND instead of a logical OR in the definition of trigger 28, see Equation 4.17, requires that events with at least 2 tracks have to be selected, of which one has to be in the top and one in the bottom half of the detector.

The efficiencies were calculated according to:

$$\varepsilon(CA)_{\text{top}} = \frac{N_{28\&24}}{N_{28}} \qquad \varepsilon(CA)_{\text{bot}} = \frac{N_{28\&25}}{N_{28}}. \tag{4.21}$$

$$\tag{4.22}$$

The efficiencies of Triggers 24 and 25 are then derived from the product of efficiencies:

$$\varepsilon(\text{Tr}24) = \varepsilon(H0)_{\text{top}} \cdot \varepsilon(H1)_{\text{top}} \cdot \varepsilon(H2)_{\text{top}} \cdot \varepsilon(CA)_{\text{top}} \tag{4.23}$$

$$\varepsilon(\text{Tr}25) = \varepsilon(H0)_{\text{bot}} \cdot \varepsilon(H1)_{\text{bot}} \cdot \varepsilon(H2)_{\text{bot}} \cdot \varepsilon(CA)_{\text{bot}}. \tag{4.24}$$

An example for the trigger efficiencies is given in Figure 4.3.1 for data taken in 2000. Apparently, the efficiencies of trigger 21 are dominated by the low efficiencies of the hodoscope $H0$. The disagreement of trigger efficiencies in the top and bottom halves is partly responsible for the top-bottom asymmetry of DIS yields as pointed out in Chapter 3.3.

4.3.2 Correction

Due to restrictions of the data traffic during data taking, certain triggers were pre-scaled by high factors of e.g. 10 which means that only one out of 10 events that generated a trigger signal was accepted by the data acquisition. The pre-scaling was relevant for high density unpolarized data, where due to data traffic reasons pre-scaling factors were used for triggers other than the trigger 21, leading to the dominance of this trigger, the low efficiencies of which require a correction. Since other triggers still contribute to unpolarized data, an explicit requirement of trigger 21 is made in the analysis in order to precisely correct for the inefficiency of this particular trigger. If the DIS lepton is measured in the top (bottom) detector half, trigger 24 (trigger 25) is required.

A correction of the corresponding trigger efficiency is applied track-by-track separately for each year and fill, depending on the polar angle θ and the momentum p of the DIS lepton. The DIS lepton is counted with a weight w given by the inverse of the trigger efficiency ϵ.

$$w = \frac{1}{\epsilon} \tag{4.25}$$

The statistical uncertainties of the trigger efficiencies were found to be negligible.

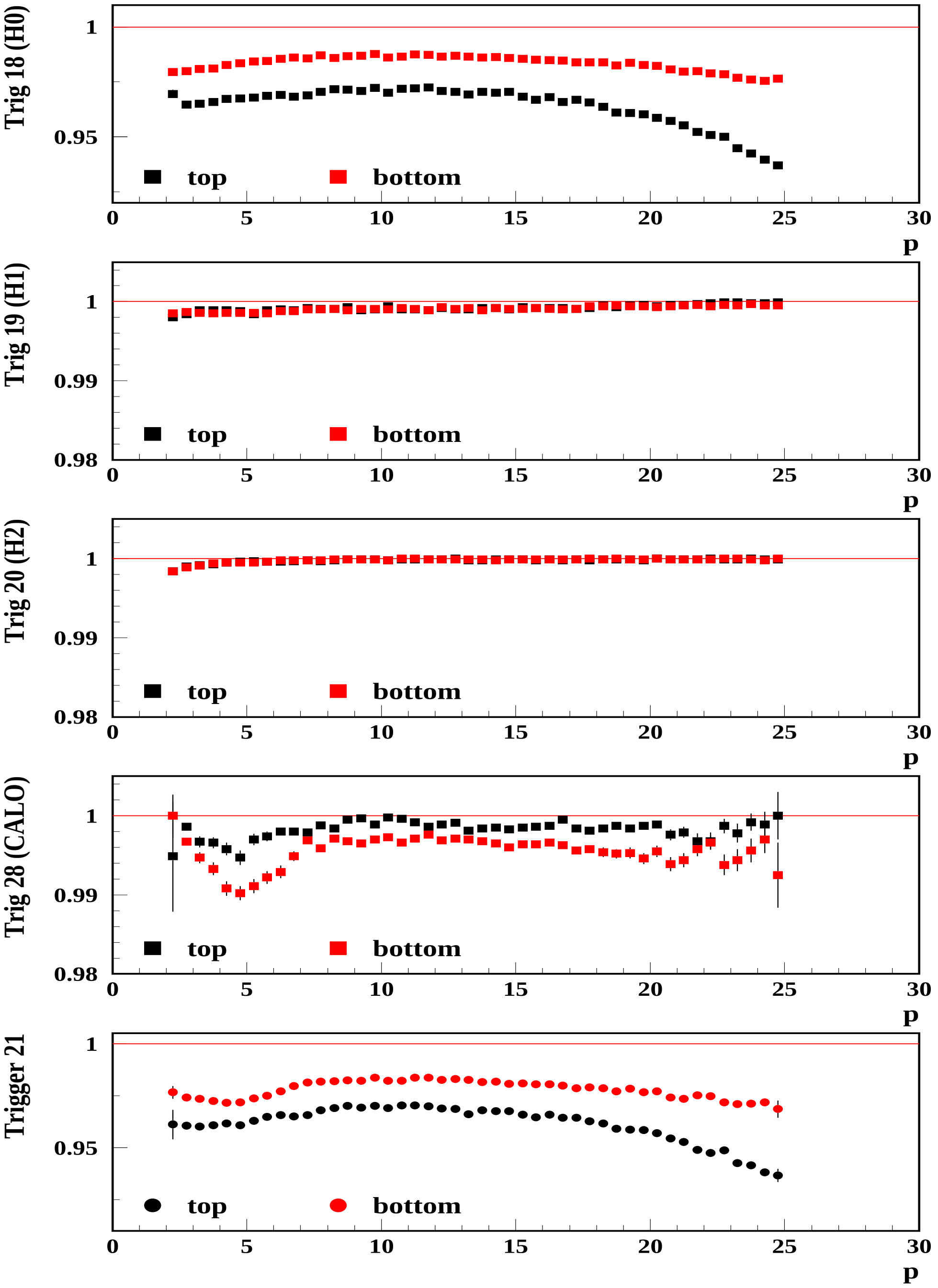

Figure 4.5: Momentum dependence of trigger efficiencies for 2000, [85].

4.4 Tracking

If the hit pattern obtained from the tracking detectors is not sufficient for a track reconstruction, those hits are not considered in the data analysis. The main sources for these inefficiencies are if either too few wires along a track fire (plane efficiencies) or if too many wires in a single event fire (`maxmul` cut).

4.4.1 Permutated Plane Efficiencies

A small number of hits in the tracking chambers may imply that HRC is unable to reconstruct a track from the hits. Even though it is impossible to calculate directly the fraction of reconstructed tracks from all tracks which should have been reconstructed, it is possible to determine efficiencies for single tracking planes, and then to combine them to the efficiency by which HRC finds a track.

The plane efficiency ε_i for tracking plane i is calculated as the ratio of the number N_i^{hit} of tracks with a hit in plane i to the number $N_i^{sel.}$ of tracks selected for plane i:

$$\varepsilon_i = \frac{N_i^{hit}}{N_i^{sel.}}. \tag{4.26}$$

Tracks being suitable for the calculation of plane efficiencies have to be chosen carefully to avoid any bias from requirements made by HRC on the following tracking parameters:

- The minimum number of hits within the road width of a partial track
- The minimum number of hits within the road width of a tree-line
- At least one plane per module has a hit for each tree-line

A bias due to these requirements is prevented by selecting only tracks which fulfill the requirements already without the plane under study.

ACE [86] is a program which calculates the plane efficiencies in the various tracking detectors from the tracks previously reconstructed by HRC. Global plane efficiencies are calculated separately for the front upper half, the front lower half, back upper half, and the back lower half of the spectrometer. The procedure to combine plane efficiencies has to take

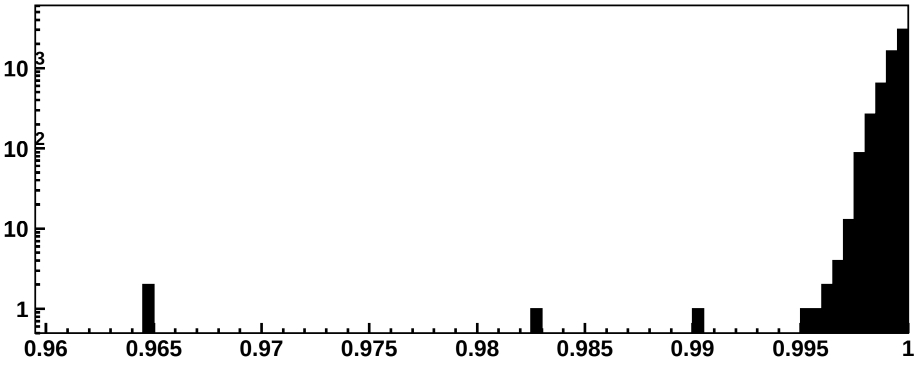

Figure 4.6: An example for the distribution of permutated plane efficiencies, obtained in the front bottom half in 1996.

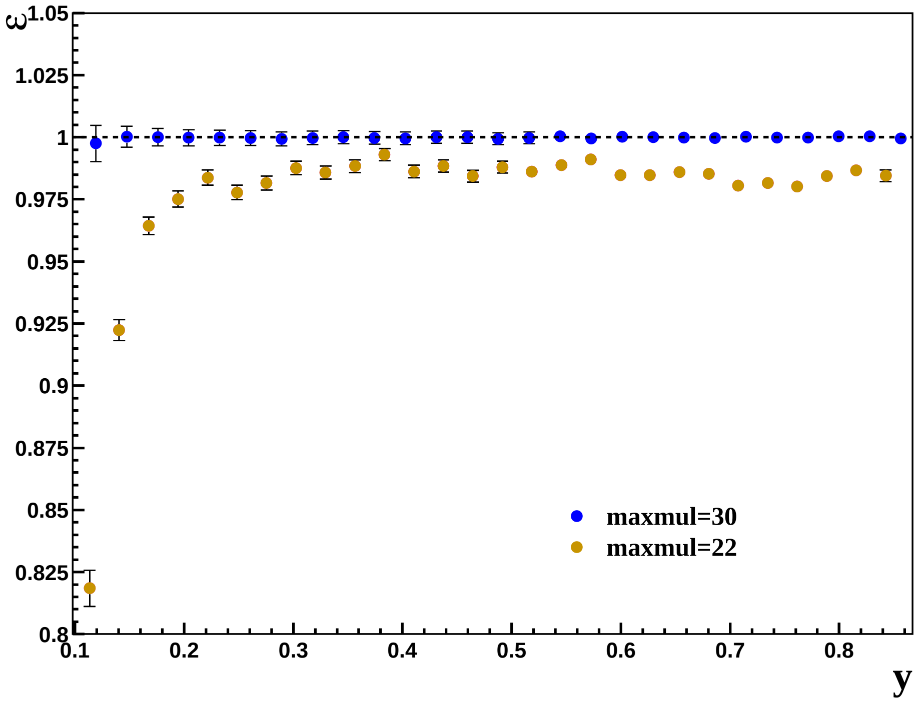

Figure 4.7: The track reconstruction efficiency of DIS events due to the `maxmul` cut applied by the track reconstruction code as a function of the kinematic variable y.

into account all requirements of HRC made for finding a track. This is performed by ACE by summing up the probabilities for all permutations of firing and not firing planes which would allow a reconstruction by HRC.

The distribution of global tracking efficiencies in data is peaked above 99%, see Figure 4.6. A cut is applied as a data quality cut in a way that bursts in which the average global tracking efficiency in at least one of the four regions was below the limit of 99%, are not used in the analysis.

4.4.2 The `maxmul` Cut

For events with high multiplicities, not only the CPU time for reconstruction increases drastically, but also the probability increases to find hits in a straight line which do not correspond to a real particle. The track reconstruction code HRC assumes that events for which the maximum number of hits per tracking plane (`maxmul`) exceeds 22 are mainly caused by showers of particles in the tracking detectors and should not be reconstructed. The `maxmul` cut applied by HRC introduces a kinematic-dependent bias[1] to the analysis of absolute cross sections, as seen in a cut variation study: DIS events from MC were reconstructed using different settings for the variable `maxmul`: 22, 30 and 40. Normalizing the yields obtained with cuts at 22 and 30 to the yield obtained with the cut at 40 shows that no significant difference can

---

[1] Besides the kinematic dependence, the impact of the `maxmul` cut is also process dependent: Higher hit multiplicities than for DIS events are observed for nuclear elastic scattering events due to the extended showers, initiated by high-energy radiative photons. This issue is relevant for the correction described in Section 4.6.5.

be observed for a cut at 30 and above. The efficiency of the standard `maxmul` cut at 22 is approximately 98.5% for a large kinematic region, as shown in Figure 4.14. In the region of higher energies, $y < 0.22$, the efficiency decreases to approximately 80%.

Due to the process and kinematic dependence, the `maxmul` cut cannot be taken into account by a data quality cut hence a correction for this cut is applied. This was practically accomplished in the course of the unfolding procedure described in Section 4.6.

4.5 Monte Carlo Simulations

4.5.1 Framework

In order to study different processes like inclusive deep inelastic scattering and deeply virtual Compton scattering or to study transversity, various generators were developed or adapted and built into the general FORTRAN-based MC framework GMC. In a second step after event generation, the produced particles are tracked through the detector. A HERMES Monte Carlo simulation (HMC) based on the GEANT3 package [87] simulates the variety of interactions of the previously generated particles inside the HERMES detector including the measured detector response.

The output of HMC is in the same format (ADAMO) as real data, so it can be fed into the same track reconstruction code HRC. Compared to real data, the production of μDST files is expanded by the additional information on the true values of the kinematic variables and on the true particle identities, whereas no tables containing slow control information exist.

4.5.2 `gmc_disNG`

The `gmc_disNG` simulation code was used for the main MC studies performed in the course of this analysis. It is based on LEPTO [88] for the generation of deep inelastic scattering events, uses RADGEN [89] for the calculation of radiative corrections due to elastic, quasielastic and inelastic scattering, and JETSET [90] for the simulation of fragmentation processes. This MC is suitable for an inclusive analysis, in which only the detection of the scattered lepton is required, and where both inelastic and elastic processes contribute. The consideration of elastic processes will become particularly important for the unfolding procedure, see Chapter 4.6.

The `gmc_disNG` MC is a weighted MC: Events are generated flat in a ν - $log\, Q^2$ -box and assigned a weight w^i to account for the actual cross section of the event i. This has the advantage that the inclusive cross section can be simulated with evenly distributed MC statistics even for tails of small cross sections. The number of MC events in a bin is calculated in the analysis by summing up the MC weights of all events generated in this bin,

$$N = \sum_{i=1}^{N_{gen}} w^i \,, \tag{4.27}$$

with the 1-σ MC uncertainty given by

$$\sigma = \sqrt{\sum_{i=1}^{N_{gen}} (w^i)^2} \,. \tag{4.28}$$

The practical procedure applied in `gmc_disNG` for the production of a tracked MC is to generate observed event kinematics ν_{obs}, Q^2_{obs} and to subsequently recalculate the kinematics on BORN level. The advantage of this reverse-order procedure is the reduction of computing time by populating the selected kinematic region directly instead of generating on 4π-BORN level, i.e. BORN level without cuts on the geometric acceptance, and then making use of only the fraction of events in the acceptance. The weights for the generated events are calculated from the BORN cross section σ_{BORN} , the size of the box in which the observed kinematics are generated, $\Delta ln(Q^2)\Delta\nu$, and a radiative correction factor C_{rad} computed by RADGEN:

$$w^i = \sigma_{\text{BORN}}\,(\nu_{obs}, Q^2_{obs}) \cdot \Delta ln(Q^2)\Delta\nu \cdot C_{rad}. \tag{4.29}$$

Appropriate parameterizations of BORN cross sections were used for the simulation of scattering off protons and deuterons, respectively. The proton DIS BORN cross section was calculated from the ALLM97 parameterization of F_2^p[91] and the parameterization R_{1990}[92], whereas the deuteron DIS BORN cross section was derived from the same parameterizations in conjunction with the fit [94] to F_2^d/F_2^p measured by NMC, SLAC and BCDMS. The electric and magnetic form factors of the proton and neutron from which the elastic cross sections are derived are taken from the fits in [95] and [96]. The radiative correction factor C_{rad} is the ratio of BORN and observed cross sections at the generated observed kinematics:

$$C_{rad} = \frac{\sigma_{obs}(\nu_{obs}, Q^2_{obs})}{\sigma_{\text{BORN}}\,(\nu_{obs}, Q^2_{obs})}. \tag{4.30}$$

RADGEN simulates the radiative corrections to the BORN cross section which will be discussed in Section 4.6.3.

The resulting weights w^i are used to calculate the measured cross sections in a bin by normalizing the sum of weights for the events generated in this bin by the total unweighted number N^{tot}_{gen} of all events generated in the box:

$$\sigma_{DIS} = \frac{1}{N^{tot}_{gen}} \cdot \sum_{i=1}^{N_{gen}} w^i \tag{4.31}$$

A second `gmc_disNG` MC production was generated in the full 4π acceptance on BORN level. It will be used for the calculation of the 4π-BORN cross section in MC needed for the unfolding of data to BORN level, as described in Chapter 4.6.

4.6 Unfolding and Treatment of the HERMES Effect

The distributions of measured cross sections involve effects from higher-order QED corrections and detector smearing. Figure 4.8 illustrates how the population of events originating from an arbitrarily chosen bin is smeared out due to both effects. A significant amount of events is measured in bins different from the one to which they belong according to their kinematics on BORN level. In the following, a stochastic method will be described that is used for the correction of event migration due to both effects. The properties of QED radiative effects and detector smearing will be discussed later in Sections (4.6.3) and (4.6.4).

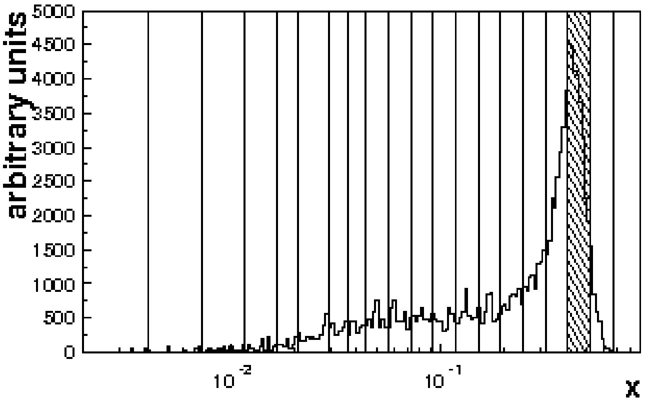

Figure 4.8: The distribution [76] of events originating from the arbitrarily selected x-bin shown as a shaded area, from a simulation of QED radiative effects and detector smearing, using a proton target. The vertical lines indicate the x-bin boundaries. The normalization is arbitrary.

4.6.1 The Unfolding Procedure

Both effects, radiative corrections as well as detector smearing, modify the Born kinematics resulting in altered reconstructed kinematic variables - an effect which can be well described by probability distributions. The basic idea of the unfolding method is to extract migration probabilities for the relevant kinematic variables with high accuracy from MC and use them to correct the measured distributions. Furthermore, acceptance and efficiency corrections can be included.

A MC-based unfolding method [97, 98, 83] was originally developed for the correction of asymmetries to obtain the Born asymmetries, but the principle can be applied to cross sections in a similar manner. For this purpose a new unfolding code was developed.

A migration matrix $n(i,j)$ for a certain binning is defined representing the number of events originating from bin j on Born level and measured in bin i. The migration matrix in a one-dimensional binning in x is illustrated in Figure 4.9. The migration matrix has an additional column $j=0$ which is reserved for events which cannot be assigned to a regular bin number $j>0$. For instance, the events corresponding to the matrix elements $n(i,0)$ with $i>0$ are reconstructed in one of the well-defined bins but they cannot be assigned to a bin on Born level. The particular matrix elements are composed of inelastic events, migrating into the acceptance from outside[2], and of elastic events which may have - due to photon radiation - the same apparent kinematics (e.g. $x<1$) as inelastic events. Section 4.6.5 will be devoted to the special properties of elastic events and their treatment in the analysis.

In the case of a binning in x and Q^2, the two-dimensional binning is projected onto one dimension in such a way that the bin numbers are arranged in loops over all x and Q^2 bins. This appears in Figure 4.10 as a repetition of shapes similar to the matrix shown in Figure 4.9. However, only one single Born bin 0 is defined.

---

[2] The term acceptance is used in this context from the point of view of the analysis and is defined generally by the possibility to assign a regular bin. Geometric acceptance cuts however are not necessarily applied on Born level. If no acceptance cuts are applied on Born level, the unfolding method implies an acceptance correction in addition to the correction for bin migration, otherwise no acceptance correction is included.

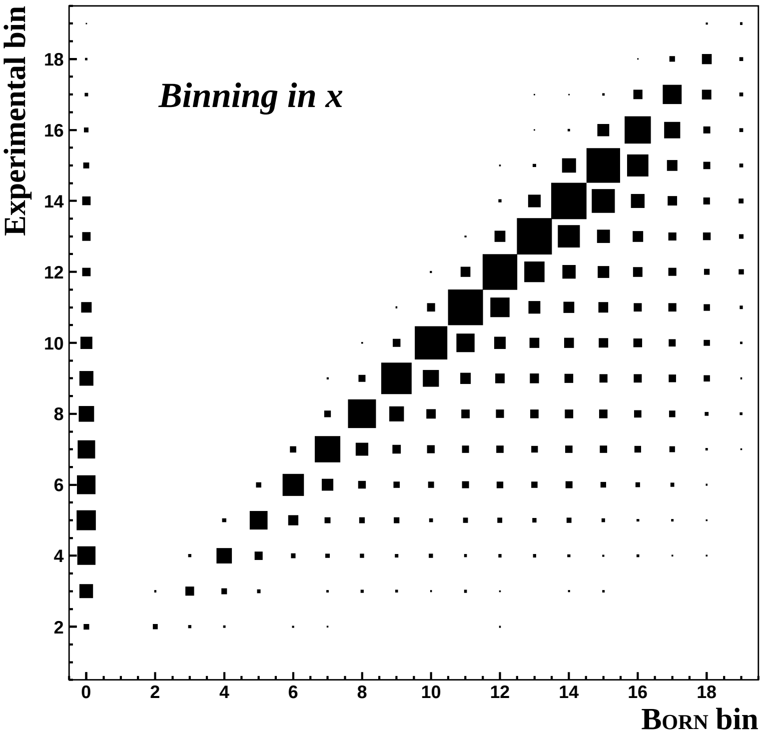

Figure 4.9: The migration matrix $n(i,j)$ is shown for a one-dimensional binning only in x. The box sizes represent the number of events originating from a given bin (j) on BORN level which migrate into a particular experimental bin (i). The diagonal elements correspond to events with the same bin number on the experimental level as on BORN level. The matrix elements for the BORN bin number 0 contain events which cannot be assigned to a bin on BORN level.

For a certain binning, a smearing matrix

$$S(i,j) = \frac{\partial\sigma^{\mathrm{Exp}}(i)}{\partial\sigma^{\mathrm{Born}}(j)} = \frac{n(i,j)}{n^{\mathrm{Born}}(j)} \qquad i,j = 0..n_{bins} \tag{4.32}$$

is determined from the migration matrix $n(i,j)$ and the vector $n^{\mathrm{Born}}(j)$ of event numbers on BORN level. As indicated in the previous Chapter, two different MC simulations are relevant. The tracked MC is used to extract the migration matrix $n(i,j)$. It is generated for the observed kinematics and includes all the relevant effects of event migration. Track reconstruction in this MC imposes a `maxmul` cut of 22. The second MC is generated for the kinematic variables on BORN level and includes the BORN cross section offering the basis to extract the BORN vector $n^{\mathrm{Born}}(j)$.

The smearing matrix comprises the probabilistic information of how events migrate from bin j on BORN level to experimental bin i. It relates the BORN distribution $\sigma^{\mathrm{Born}}(j)$ to the experimental distribution $\sigma^{\mathrm{Exp}}(j)$ in the following way:

$$\sigma^{\mathrm{Exp}}(i) \;=\; \sum_{j=0}^{n_{bins}} S(i,j)\sigma^{\mathrm{Born}}(j)$$

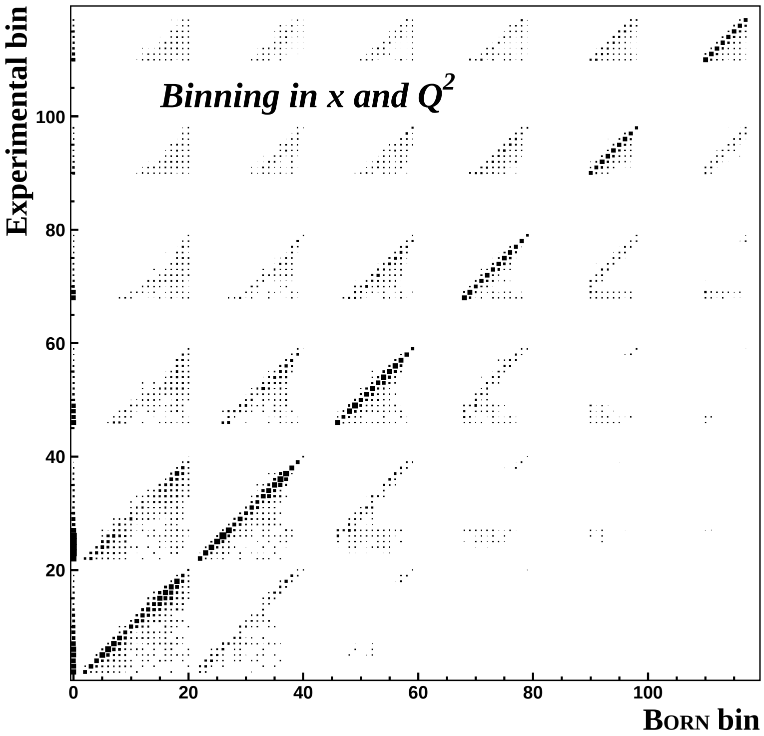

Figure 4.10: The representation of the migration matrix $n(i,j)$ for a two-dimensional $x-Q^2$-binning.

$$= \sum_{j=1}^{n_{bins}} S(i,j)\sigma^{\textsc{Born}}(j) + S(i,0)\sigma^{\textsc{Born}}(0). \tag{4.33}$$

The background term $S(i,0)\,\sigma^{\textsc{Born}}(0)$ is split off the sum in order to isolate the desired BORN cross section in the acceptance:

$$\sum_{j=1}^{n_{bins}} S(i,j)\sigma^{\textsc{Born}}(j) \quad = \quad \sigma^{\text{Exp}}(i) - S(i,0)\sigma^{\textsc{Born}}(0). \tag{4.34}$$

The distribution $\sigma^{\text{Exp}}(i)$ is observable only for $i > 0$ hence a squared submatrix is defined to enable the matrix inversion. Let $S'(i,j)$ be defined as the squared submatrix with $i,j = 1...n_{bins}$, then the inverted matrix S'^{-1} converts the experimental distribution $\sigma^{\text{Exp}}(i)$ to the BORN distribution $\sigma^{\textsc{Born}}(j)$ after substraction of the background term $S(i,0)\,\sigma^{\textsc{Born}}(0)$:

$$\sigma^{\textsc{Born}}(j) = S'^{-1}(j,i)\times \quad [\sigma^{\text{Exp}}(i) \quad -S(i,0)\sigma^{\textsc{Born}}(0)] \tag{4.35}$$

The procedure is sensitive to the impact of radiative effects as calculated by RADGEN, see Chapter 4.5, as well as to detector smearing effects, the simulation of which is based on the detailed model of the detector material. It should be emphasized that the procedure is independent from the generated cross section distributions in the acceptance because they cancel in the definition of the smearing matrix according to Equation (4.32). A dependence on MC distributions enters only through the background term $S(i,0)\,\sigma^{\textsc{Born}}(0)$.

The unfolding technique was used in this analysis to calculate cross sections on Born level for both hydrogen and deuterium targets and was applied separately to the top and the bottom detector halves. Special requirements for different years of data taking had to be taken into account by producing separate MC samples: Since detector smearing depends on the materials traversed by the particles, different MC productions were used for the spectrometer operating with the threshold Čerenkov counter and for the ring-imaging Čerenkov detector, respectively.

The *sanity check* in Figure 4.11 shows that the code is able to reproduce the Born cross sections after the unfolding of reconstructed MC distributions.

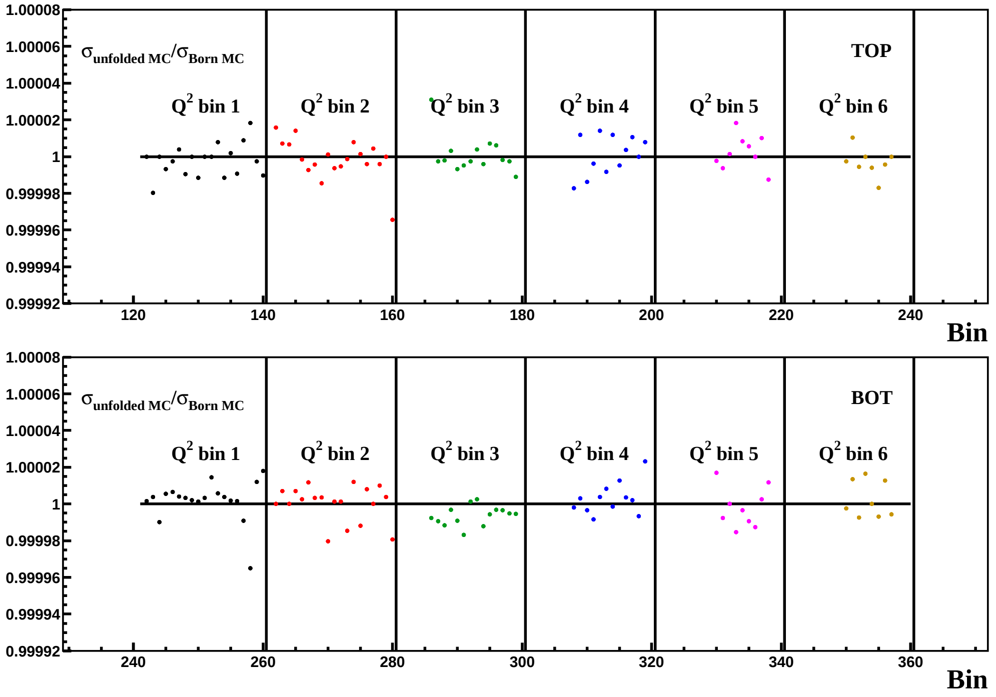

Figure 4.11: Sanity check of the unfolding procedure: Ratio of the unfolded MC distribution to the Born MC distribution. Both distributions are expected to be equal. The small differences in the order of $2 \cdot 10^{-5}$ are attributed to numerical inaccuracies. The sanity check shown here is based on the binning of the final analysis, see Appendix C. It is illustrated separately for the top and the bottom detector halves in loops over the x bins for each of the Q^2 bin numbers.

4.6.2 Calculation of Inflated Errors

The variance $V_{j,k}^{Born}$ of the cross section on Born level is related to its variance $V_{j,k}^{Exp.}$ on experimental level according to:

$$V_{j,k}^{Born} = \sum_{i=1}^{n_{bins}} S^{-1}(j,i) S^{-1}(k,i) V_i^{Exp.}. \tag{4.36}$$

Since the content of each bin gains contributions from several experimental bins by unfolding, the uncertainty increases - the resulting uncertainty is therefore referred to as *inflated error*.

Fluctuations were observed in the unfolded distribution which are inconsistent with the error calculated from Equation (4.36). It was found that the fluctuations can be attributed to insufficient MC statistics of both, the migration matrix $n(i,j)$ and the Born vector $n^{\mathrm{Born}}(j)$ in Equation 4.32. A *complete inflated error* was therefore calculated by taking MC statistics into account. Since the analytic solution for the propagation of errors through the inversion of a matrix is complicated, a Monte-Carlo technique was employed. All elements in the migration matrix and in the Born vector were varied independently by Gaussian distributions with a width of the respective uncertainties of the elements. A large number N_S of such matrices was calculated and inverted to $S^{-1}_{k=1\ldots N_S}(j,i)$. The variance of each element $S^{-1}(j,i)$ was estimated from the distribution of the matrices $S^{-1}_k(j,i)$ in terms of the expectation value

$$V[S_k^{-1}(j,i)] = \sum_{k=1}^{N_S} \frac{(S_k^{-1}(j,i) - \langle S^{-1}(j,i)\rangle)^2}{N_S}, \tag{4.37}$$

where $\langle S^{-1}(j,i)\rangle$ is the mean of the distribution.

Before unfolding, the data points are correlated because they are composed of the contributions of other bins. After unfolding the data points are uncorrelated, while their statistical uncertainties are correlated. This requires statistical uncertainties of a corrected distribution to be expressed by a correlation matrix rather than treating uncertainties to be independent.

4.6.3 QED Radiative Corrections

The four QED processes that contribute to the radiative corrections are illustrated in Figure 4.12: Initial and final state radiation as well as vacuum polarization and vertex correction.

Initial and Final State Radiation

The photon radiation of the incoming (initial state radiation) or outgoing (final state radiation) leptons results in a difference between the apparent kinematic variables reconstructed from the incoming and outgoing leptons and those at the virtual-photon lepton vertex. In the case of final state radiation, the outgoing lepton radiates a photon with the four-momentum ξ so that the four-momentum of the lepton afterwards is $k'_{\mathrm{Exp}} = k'_{Born} - \xi$ while it is k'_{Born} on Born level. Due to the emission of photons the apparent values of x_{Exp}, Q^2_{Exp} differ from the values x_{Born}, Q^2_{Born} on Born level such that not only inelastic events are included in the measured sample of inelastic scattering events but also elastic or quasi-elastic events, as defined and discussed in Section 4.6.5. These *elastic and quasi-elastic tails* enter the acceptance from outside and thus increase the total measured DIS cross sections. They are included in the background term $S(i,0)\,\sigma^{\mathrm{Born}}(0)$ and hence accounted for in the unfolding procedure.

Vacuum Polarization and Vertex Correction

Vacuum polarization describes a process in which the DIS virtual-photon propagator is interrupted by loops of virtual lepton-antilepton pairs reducing the total cross section of the deep inelastic scattering process. The vertex correction involves a virtual-photon loop between the incoming and outgoing lepton propagator. Both effects contribute to the inelastic part of the cross section and are included in the MC simulation of QED radiative processes.

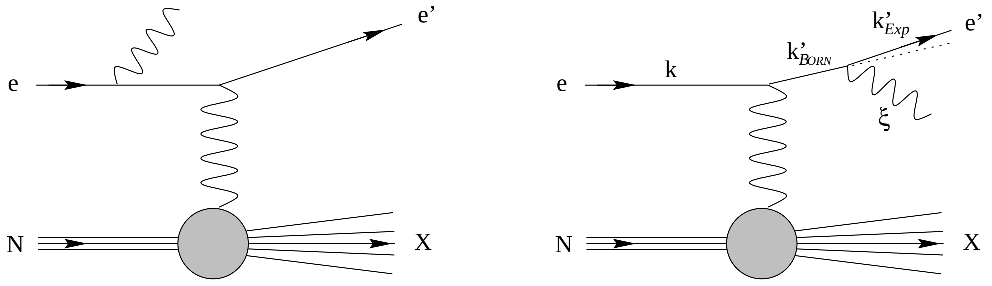

initial state bremsstrahlung

final state bremsstrahlung

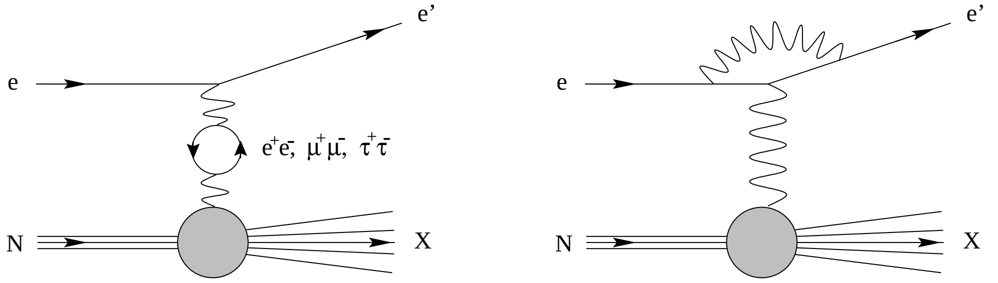

vacuum polarization

vertex correction

Figure 4.12: Feynman diagrams contributing to radiative corrections. The processes are included in the MC used for the unfolding.

4.6.4 Detector Smearing

Due to multiple scattering of the particles emerging from the DIS process, the kinematic variables of the event may be reconstructed in adjacent bins at higher or lower apparent values of x and Q^2 with respect to the true values. Particle interactions in the detector put a physical lower limit to detector resolution. The detector resolution was simulated by a detailed Monte Carlo model involving all relevant detector materials. The size of a bin should obviously not be smaller than the actual detector resolution, otherwise the large fraction of migrating events would cause artificially large inflated uncertainties.

4.6.5 Bethe-Heitler efficiencies

The Bethe-Heitler cross section equation [100] describes the radiation of real photons associated with the interaction of a charged particle with the electromagnetic nuclear fields. The upper two Feynman diagrams shown in Figure 4.12 for the radiation of real photons ($ep \rightarrow e\gamma X$) in the initial and final states have corresponding amplitudes [101] $\propto \left[(q_l^2 - m_e^2) \cdot q^2\right]^{-1}$ with q_l being the 4-vector of the virtual lepton between the two photon vertices. The dominating contribution is consequently obtained for q_l^2 and q^2 being close to zero, a kinematic domain in which the scattering angles are small. Two configurations can be distinguished in the angular acceptance of the HERMES experiment:

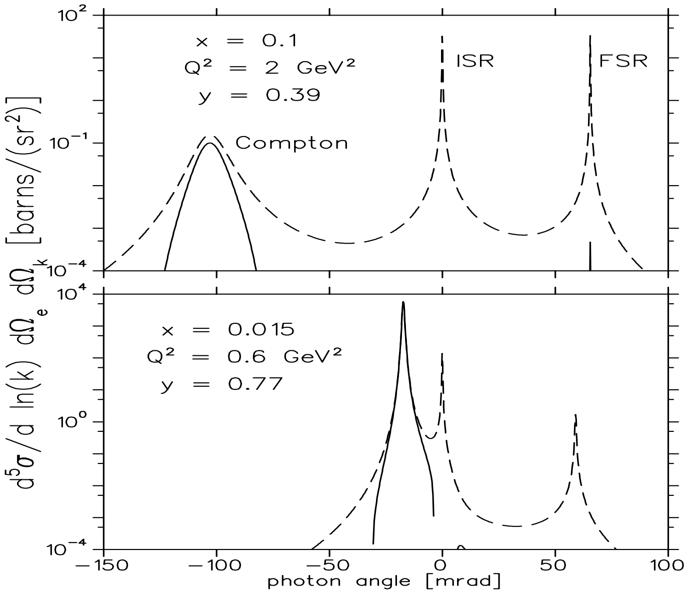

Figure 4.13: The nuclear-elastic Bethe-Heitler cross section on ${}^{14}N$ in two different kinematic conditions labeled with the apparent DIS kinematic variables. The solid curves represent the cross-section after taking the nuclear form factor into account. Taken from [99].

- $q_l^2 \simeq 0$ and q^2 finite: The lepton scatters at a finite angle and photons are radiated along the incoming (ISR) or scattered lepton (FSR). The FSR photons have a chance to be observed by the detector since they are radiated basically collinear to the scattered leptons. The ISR photons are usually not detected because they remain in the beam pipe.
- $q^2 \simeq 0$ and q_l^2 finite: The lepton interacts with the target by exchange of a quasi-real photon in association with the radiation of a real photon at finite angles. This process is called QED Compton scattering.

The angular distribution of radiated photons in the Bethe-Heitler cross-section on ${}^{14}N$ is shown in Figure 4.13 for two kinematic situations. The peaks corresponding to ISR, FSR and Compton scattering can be clearly identified. ISR is peaked around the incoming lepton beam, whereas the photons from FSR are peaked around the scattered-lepton direction, which is well-defined in each kinematic situation. Compton scattering involves photon radiation with a transverse momentum that compensates the transverse momentum of the scattered lepton, thus the angles of photon and lepton have opposite signs. For deuteron and heavier nuclei, the Compton peak has two contributions: In addition to the *elastic scattering* off the entire nucleus, the *quasi-elastic* scattering refers to the scattering off a single nucleon in the nucleus.

A peculiar instrumental effect in the HERMES detector, which is known to be the origin of the so-called HERMES effect [99], interferes with the measurement of QED Compton events at small values of apparent x and Q^2. Inefficiencies for the detection of these processes are significant, consequently the size of the correction for radiative (quasi-) elastic events has to be decreased according to the individual efficiencies. If the efficiencies were not taken into account, the contribution of (quasi-) elastic events included in the background term $S(i,0)\,\sigma^{\mathrm{BORN}}(0)$ in Equation (4.35) would be overestimated.

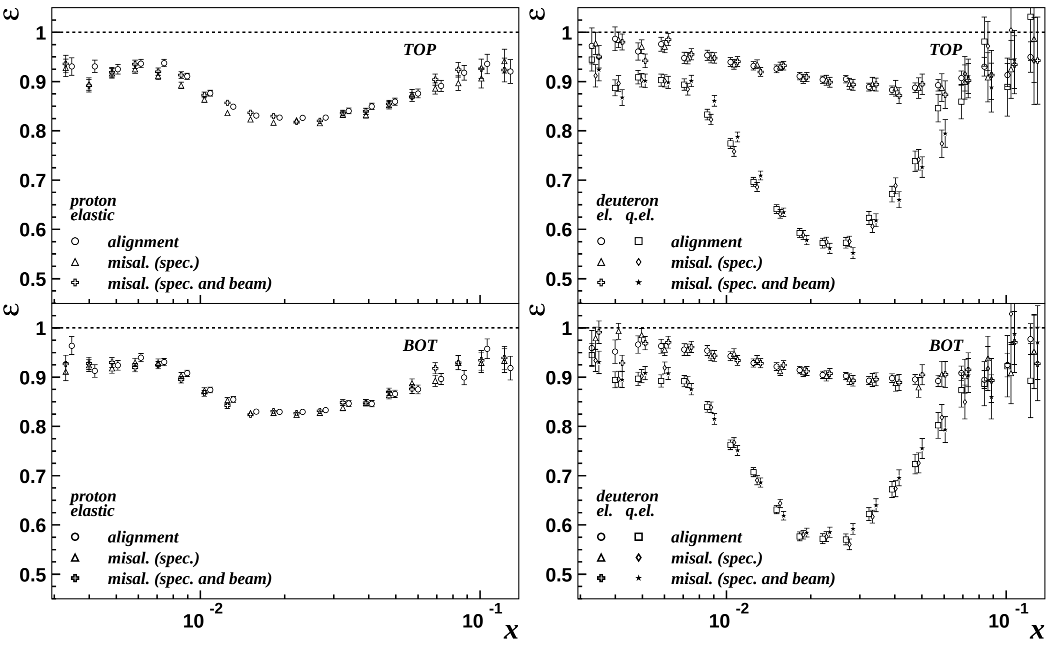

Figure 4.14: Efficiencies for the detection of Bethe-Heitler nuclear elastic (el.) and quasi-elastic (q.el.) events in the Hermes spectrometer are represented by the data points for scattering on both deuteron and proton. The efficiencies are shown for perfect alignment, for the misaligned spectrometer, and for the misaligned spectrometer and beam. Left: proton, right: deuteron.

In the region of small apparent values of x and Q^2, corresponding to large values of y, the radiated photon carries most of the energy of the incoming lepton. The angle θ_γ of the radiated photon is correspondingly smaller than the scattering angle $\theta_{e'}$ of the lepton but not negligible:

$$(1-y)\, sin\theta_{e'} = y\, sin\theta_\gamma. \tag{4.38}$$

This can have serious consequences concerning the mirror symmetric open geometry of the Hermes detector. The radiated photons have a high probability of hitting the detector frames close to the beamline in front of the dipole magnet. Extended electromagnetic showers originating from these interactions can cause large hit multiplicities in the tracking detectors. For many of these events track reconstruction becomes impossible, because a cut (`maxmul`) had to be imposed on the maximum number of hits per tracking plane in the track reconstruction code (HRC). The understanding of interactions in the detector frames is crucial for an accurate systematic treatment of elastic Bethe-Heitler events[3].

A complete description of materials close to the beam pipe is available in the GEANT-based Monte Carlo offering the possibility to extract efficiencies for the detection of elastic Bethe-Heitler events. The results for Bethe-Heitler efficiencies are shown in the left (right) panel of Figure 4.14 for a proton (deuteron) target, separately for the top and the bottom halves of the detector. In a perfectly symmetric detector, the Bethe-Heitler efficiencies in both

---

[3] The effect of the `maxmul` cut on DIS events is discussed in Section 4.4.2.

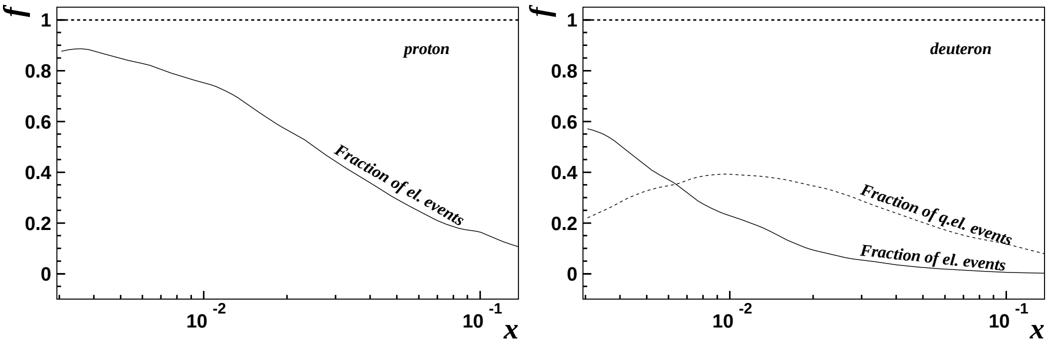

Figure 4.15: The curves illustrate the simulated fractions of elastic $f_{el.}$ and quasi-elastic $f_{q.el.}$ events with respect to all events migrating into the acceptance from outside.

detector halves are in agreement with each other. The misalignment of the spectrometer and the beam will be discussed in Section 4.7, while a possible correlation between misalignment and Bethe-Heitler efficiencies is addressed already here. The sizes of showers produced by the radiated hard photons depend on the locations at which the photons initially interact with the detector frames. Misalignment can have an impact on these positions and hence on the Bethe-Heitler efficiencies. As illustrated in Figure 4.14, the effects of misalignment on the Bethe-Heitler efficiencies are on the few-percent level. The differences of unfolded cross-sections using Bethe-Heitler efficiencies respectively extracted from Monte-Carlo simulations with and without the misalignment of detector and beam will enter the results of this analysis as an uncertainty δ_{rad} of radiative corrections.

The unfolding procedure is modified by applying the individual efficiencies to elastic and quasi-elastic processes. The correction for Bethe-Heitler efficiencies is performed in the following way: Since the background term $S(i,0)\,\sigma^{\mathrm{BORN}}(0)$ is composed of contributions from inelastic events and (quasi-) elastic events, the efficiencies of elastic $\epsilon_{el.}$ and quasi-elastic $\epsilon_{q.el.}$ events are weighted with the fractional contributions $f_{el.}$ and $f_{q.el.}$ of these processes, shown in Figure 4.15, to correct the distribution $n(i,0)_{MC}$

$$n(i,0)_{cor.} = n(i,0)_{MC} \cdot (f_{el.}\epsilon_{el.} + f_{q.el.}\epsilon_{q.el.} + f_{inel.}), \tag{4.39}$$

where $f_{inel.} = 1 - f_{el.} - f_{q.el.}$ is the unaffected fraction of radiative inelastic events migrating into the acceptance from outside.

4.7 Misalignment

The ideal spectrometer position is a perfect alignment with respect to the nominal beam position in the HERA coordinate system: no shifts, no tilts. In practice there are two different types of misalignment: *i*) the top and bottom parts of the spectrometer can be displaced from their ideal positions, *ii*) the actual beam position in HERA during a data taking period is usually never the nominal one. The positions of the top and bottom detector

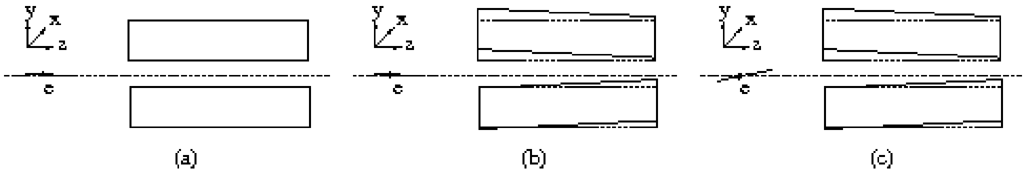

Figure 4.16: Possible scenarios for the misalignment of the spectrometer and the beam. a) The spectrometer is perfectly aligned. b) The spectrometer is misaligned. c) The beam and the spectrometer are both misaligned.

halves have an impact on the reconstruction of tracks. Furthermore, the determination of track parameters is based on the assumption that the primary event vertex is on the z-axis in the center of the beam pipe. This can cause a bias when the beam is shifted away from the z-axis. Apart from track reconstruction, the calculation of event kinematics relies on the assumption that the beam has no angle with respect to the z-axis. Actual deviations of true positions of spectrometer and beam from their ideal positions, as illustrated in Figure 4.16, are referred to as misalignment.

Indirect methods like the analysis of tracks in the top and bottom detector halves are used in order to determine the relative beam positions as seen from each detector half and thus to obtain indicative information about the relative positions of the top and bottom detector halves. Studies [102] with a so-called *beam finder* code showed that misalignment between the top and the bottom halves is considerable.

4.7.1 Input to Misalignment Studies

Misalignment of the spectrometer was studied [103] for the years 1996 to 2003, see tables 4.1 and 4.2. The measurement [104] of beam position and slopes by the beam position monitors (BPMs) in 1998 (e^-) and 2000 (e^+) is summarized in Table (4.3).

	top	bot
x-slope (mrad)	0.44	0.24
y-slope (mrad)	-1.20	0.02
x-offset (cm)	-0.09	-0.11
y-offset (cm)	-0.01	0.11

Table 4.1: Misalignment of the spectrometer in 1996-2000 [103] . The reference point is (0,0,0).

Monte Carlo studies were performed based on the misalignment information about beam and spectrometer for data taken in 2000.

Misalignment was simulated in MC by using ‘non-misaligned’ alignment files for the reconstruction of tracks (HRC) but ‘misaligned’ geometry files only in the Hermes MC Code (HMC) whereas MC without misalignment was consequently produced by using misaligned

	top	bot
x-slope (mrad)	-0.18	-0.42
y-slope (mrad)	-0.62	0.49
x-offset (cm)	0.30	0.29
y-offset (cm)	-0.08	0.11

Table 4.2: Misalignment of the spectrometer in 2002-2003 [103]. The reference point is (0,0,0).

	e^-	e^+
x-slope (mrad)	-0.014	0.035
y-slope (mrad)	0.120	-0.420
x-offset (cm)	0.015	0.017
y-offset (cm)	-0.090	0.160

Table 4.3: Misalignment of the beam in 1998 and 2000 [104] extracted from the hydrogen data sample. The reference point is (0,0,0).

alignment files also for reconstruction of tracks (HRC). In the following, the MC productions will be referred to as *aligned MC* and *misaligned MC* for simplicity.

4.7.2 Impact of Misalignment

The measurement of absolute cross sections is directly influenced by misalignment effects. Note that misalignment is not a stochastic effect and cannot be corrected by unfolding. In principle, a track-by-track correction could be applied by using appropriate offsets to the track parameters, or alternatively even a correction on the level of track reconstruction (HRC) could be performed. Until now, such corrections do not exist hence the effects of misalignment are accounted for by a systematic uncertainty in the context of this analysis.

The cross section ratio of experimental cross sections in a misaligned MC and an aligned MC, simply referred to as the *misalignment ratio*, serves as an estimate of the systematic uncertainty due to misalignment.

In order to be able to apply a systematic uncertainty for misalignment to unfolded data, the misalignment ratio has to be evaluated on Born level. It is unfolded not as a whole but separately for the misaligned MC in the numerator and the aligned MC in the denominator. As mentioned above, the misaligned MC cannot be unfolded to reproduce the true Born distributions, due to the non-stochastic nature of misalignment. In order to understand the effect of misalignment on unfolded data, the migration matrix used for unfolding the misaligned MC in the numerator has to be chosen to be the same one as the one applied to data regardless of misalignment. Trivially, the application of this migration matrix to the aligned MC in the denominator results in the Born distribution. The misalignment ratios are shown in Figures 4.17 (tracked), 4.18 (unfolded in acceptance), and 4.19 (unfolded to born level).

Figure 4.17 shows the misalignment ratio on the experimental level, the ratios in Figures 4.18 and 4.19 were unfolded to Born level within the acceptance and to 4π, respectively.

There is an apparent agreement between the unfolded misalignment in the acceptance and on 4π Born level. The explanation for this is that the ratio between the unfolded cross sections in the acceptance and on 4π Born level is simply the acceptance function,

Figure 4.22. Bin correlations do not play a role here and the acceptance function cancels out in the misalignment ratio when moving from the acceptance to 4π. This agreement can be taken as another consistency check of the unfolding procedure.

Ratios of data and aligned MC, either both on experimental level or both unfolded to Born level are shown in Figures 4.20 and 4.21. The function in the bottom of each panel illustrates the misalignment ratio, representing the signed misalignment uncertainty. A clear correspondence can be recognized comparing the shapes of the data-to-MC ratio and the misalignment ratio.

4.8 Determination of the Luminosity

The luminosity is calculated from the coincidence rate R_{LR} in the left and right luminosity detectors and the luminosity constant C_{Lumi}, a year dependent conversion factor. The luminosity constant is related to the acceptance of the luminosity detector via Equation (2.5).

Various factors have an impact on the acceptance of the luminosity detector. The position of the luminosity detector relative to the beam pipe in the septum plate defines the area on the luminosity detector which can be covered by Møller and Bhabha scattering particles. The beam position within the beam pipe has an impact on the acceptance through its horizontal and vertical positions in the target and its slopes, as well as through its profile. In addition, the angular acceptance of the luminosity detector varies with the longitudinal positions of interactions within the target cell for geometric reasons, thus the target gas distribution has to be taken into account. The deflection of charged particles by the transverse magnetic holding field of the polarized targets used between 2002 and 2005 is another relevant factor.

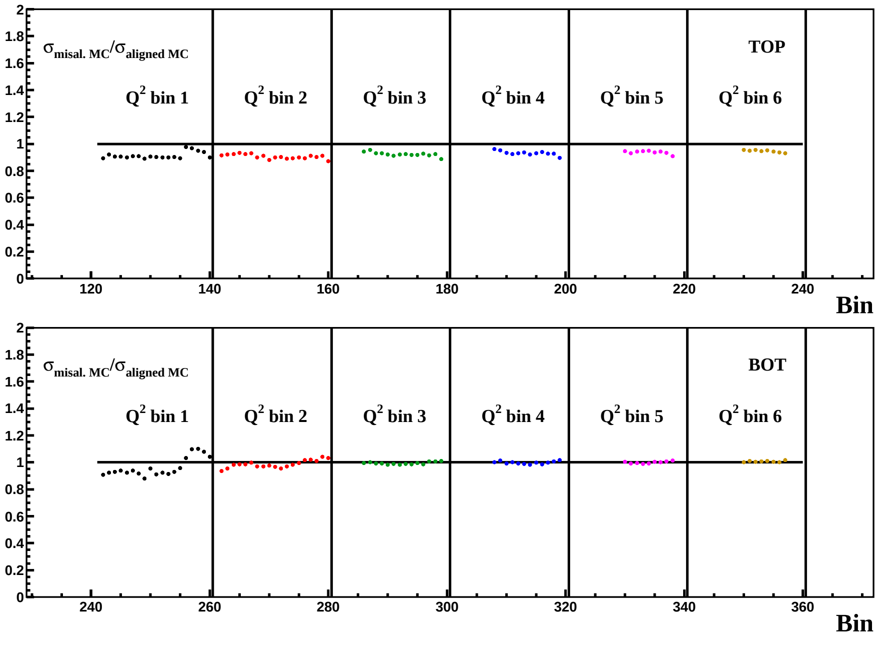

Figure 4.17: Ratio of the cross section obtained from a misaligned MC to that obtained from an aligned MC.

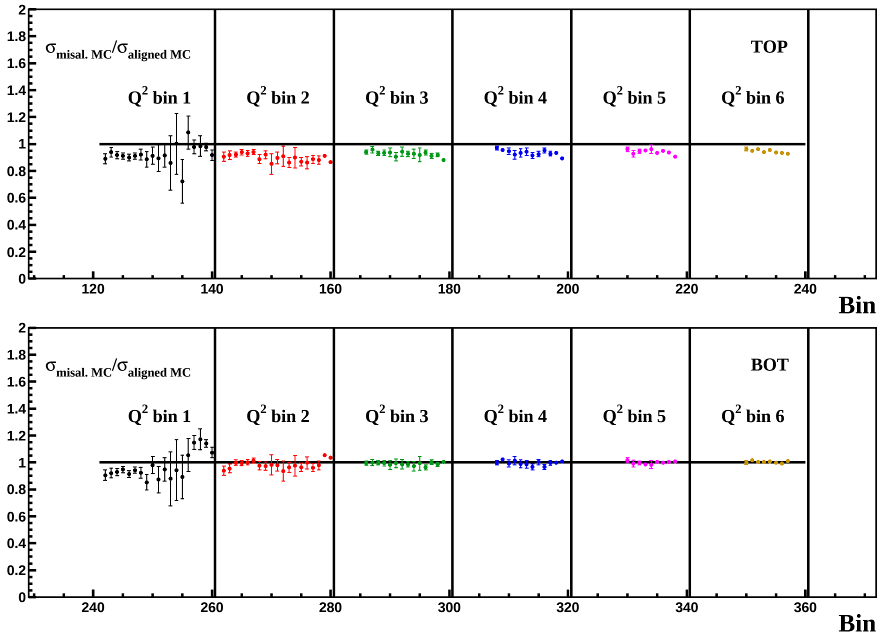

Figure 4.18: Misalignment ratio from Figure 4.17 unfolded in the acceptance.

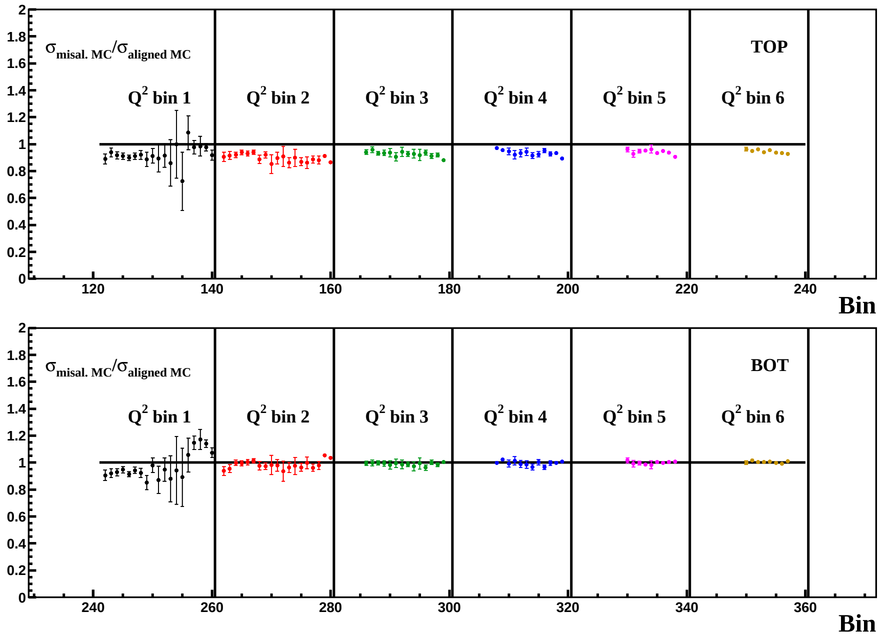

Figure 4.19: Misalignment ratio from Figure 4.17 unfolded to 4π Born level.

Experimental access to the acceptance of the luminosity detector is only gained indirectly.

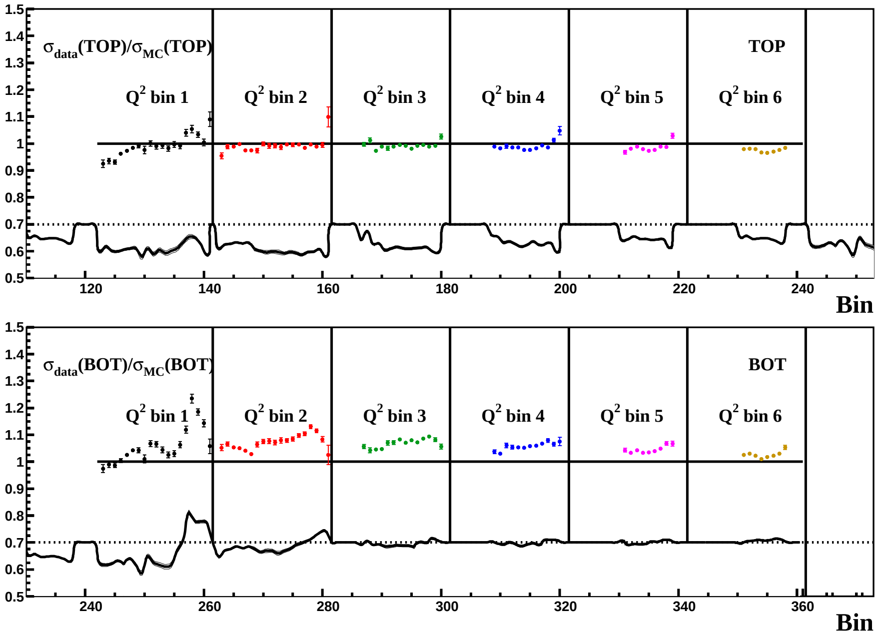

Figure 4.20: Data on the experimental level normalized with the corresponding aligned MC. The function in the bottom of each panel is the misalignment ratio with the dotted line being at unity.

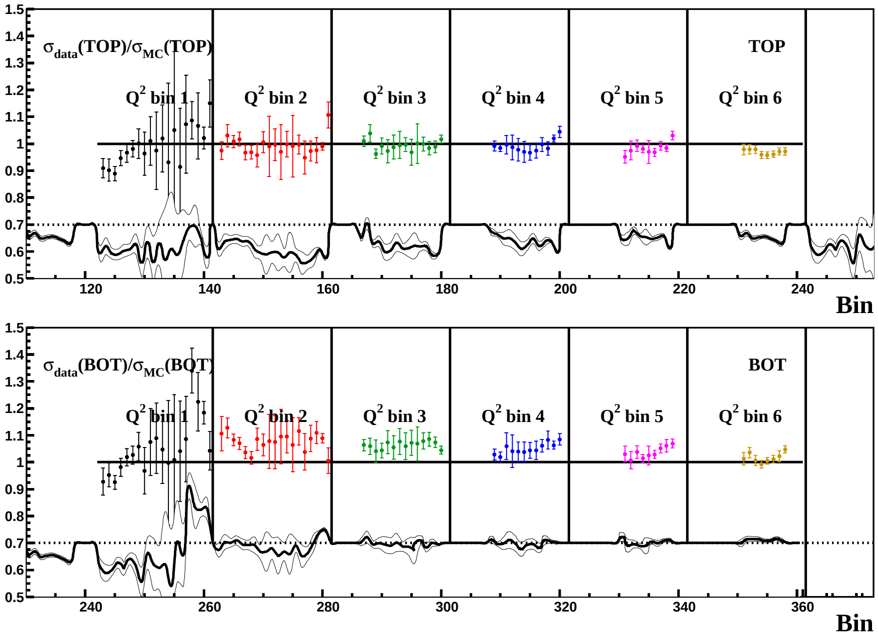

Figure 4.21: Data on Born level normalized with Born MC. The function in the bottom of each panel is the misalignment ratio with the dotted line being at unity. After unfolding, errors are inflated for the data-MC-ratio but also for the misalignment ratio.

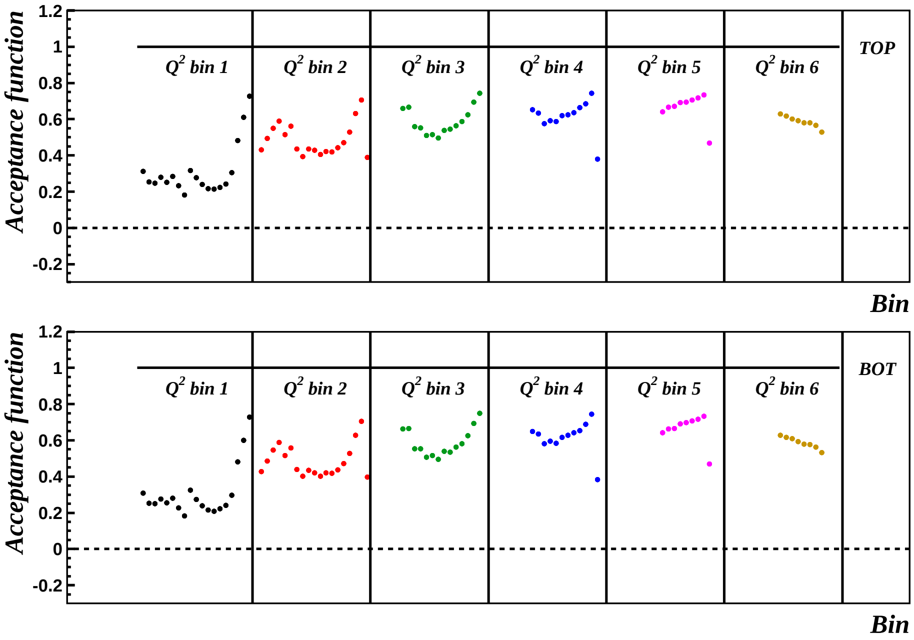

Figure 4.22: The acceptance function shown here is defined by the fraction of DIS events which are within the geometric acceptance. A MC was used for this study by applying acceptance cuts on BORN distributions. Thereby, the acceptance function was derived independently from radiative effects and detector smearing.

The measurement of coincidence rates normalized to the beam currents at different beam positions and slopes was performed in the *luminosity scans*, which were subject of studies in MC. MC simulations [105] were performed based on all relevant aspects of the detector and the beam in order to reproduce the results of luminosity scans and to determine the acceptance of the luminosity detector. The luminosity constants obtained for the various years are listed in Table 4.4.

In this analysis, the integrated luminosity L was calculated from the luminosity count rates according to

$$L = \int \mathcal{L}\, dt = (R_{LR} - \Delta t \cdot R_L \cdot R_R) \cdot C_{Lumi} \cdot \frac{A}{Z} \cdot l \cdot \Delta b, \tag{4.40}$$

where R_L and R_R are the count rates in the left and and right luminosity detector, respectively, R_{LR} is the coincidence rate measured within a time window of $\Delta t = 80\,ns$, A/Z is the ratio of nucleons (A) and shell electrons (Z) of the target gas, l is the trigger lifetime contribution, and Δb is the time interval in which the luminosity rates were obtained. Coincidences of signals in the left and the right calorimeter of the luminosity detector are ideally related to the same events. The term $\Delta t \cdot R_L \cdot R_R$ in Equation 4.40 corrects for accidental coincidences according to the statistical expectation.

Since the number of elastic scattering events off the shell electrons is proportional to the shell electron density, a correction factor A/Z has to be applied when calculating luminosities per nucleon. This factor is redundant in the case of a hydrogen target, and it is 2 in the case of a deuterium target.

The trigger lifetime contribution l is defined as the fraction of events which were accepted

Year	Target magnet	C_{Lumi}, mb^{-1}
1996	on/off	422 ± 32
1997	on/off	426 ± 36
2000	on/off	417 ± 30
2002	on	1046 ± 33
2002	off	532 ± 16
2003	on	949 ± 29
2003	off	543 ± 16
2004	on	969 ± 29
2004	off	508 ± 15
2005	on	267 ± 14
2005	off	317 ± 14

Table 4.4: Table of luminosity constants C_{Lumi} [106] used to convert the coincidence rates in the left and the right luminosity detector to luminosities.

by the data acquisition system out of all events generating a trigger signal. This quantity is limited by the readout time of the data acquisition. Events are lost if triggers cannot be accepted by the readout system. It is typically above 90%. The luminosity rate is not affected by this physics trigger life time, but it requires a correction in order to be compatible to the physics event rates. For the analysis of events firing a certain trigger, its particular lifetime has to be applied, thus a global trigger lifetime is used when all accepted events are analyzed without the requirement that a particular trigger fired.

4.9 Normalization Uncertainty of σ^d/σ^p

Combining the cross sections measured in different years separately for hydrogen and deuterium targets and then calculating the ratio would involve large uncertainties due to the luminosity constants. In order to benefit from the cancellation of uncertainties, cross section ratios are calculated year-by-year and then combined. This requires that data is used within a year with the same luminosity constant. In the years between 2002 and 2005, only data taken with unpolarized hydrogen and deuterium targets were used because of the effect of the transverse target magnet on the acceptance of the luminosity detector. With this selection of data, the normalization uncertainty of the cross section ratio σ^d/σ^p becomes disconnected from the large uncertainty of the luminosity constant. Since the beam conditions that influence the measurement of the luminosity can change within a year, small remaining normalization differences can occur between subsets on proton and deuteron targets. These are studied from relative deviations of the cross section ratios in different years. The ratios of the results in 1996, 1997, 2002 and 2005 to the result obtained in 2000 were found to be consistent in top and bottom within the uncertainties. Consequently, top and bottom results were combined and the ratios to 2000 were determined for 1996, 1997, 2002 and 2005 to be 0.9978 ± 0.0043, 0.9749 ± 0.0041, 0.9774 ± 0.0057 and 0.9602 ± 0.0047, respectively. This yields an average normalization of $\langle n \rangle = 0.9821 \pm 0.0021$. Using the estimate for the variance

$$V[n] = \frac{\sum_{i=1,5}(n_i - \langle n \rangle)^2}{5} \tag{4.41}$$

with the relative normalizations n_i in the various years, the overall normalization uncertainty is determined to be $\delta_{norm.} = 1.1\%$

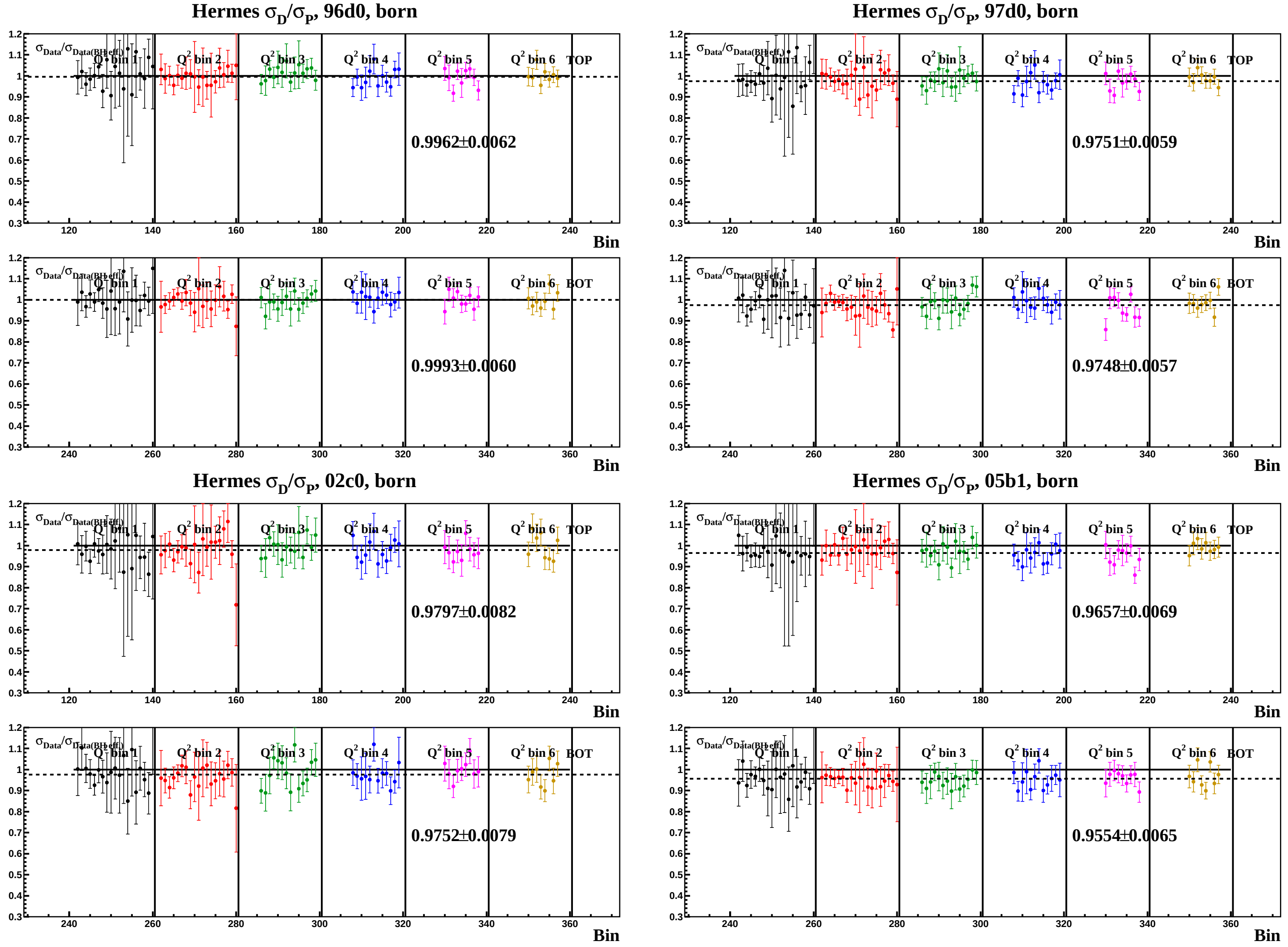

Figure 4.23: σ^d/σ^p in various years divided by the ratio found in 2000.

Chapter 5

Results

5.1 Results on the Structure Function F_2

The determination of F_2 is accomplished in consecutive steps: Corrected yields are first obtained by applying all corrections described in the previous chapter to the numbers of DIS events and by normalizing the numbers according to Equation (4.40). Secondly, the obtained distributions are unfolded to 4π-BORN level as discussed in Chapter 4.6. Hereafter, the differential cross sections are calculated by normalization of the cross sections with the bin sizes (phase space normalization). Finally, F_2 is derived using equation (1.23) and the parameterization R_{1998}.

Combination of Data Sets

Results on the DIS BORN cross sections are determined for proton and deuteron targets separately and for each year of data taking. Within a year, a further separation into polarized and unpolarized targets is required due to different luminosity constants. Additionally, the top-bottom-separation is necessary because of the differences in systematics.

As a last step of the analysis, the data sets $i = 1, .., n$ are combined by calculating bin-by-bin averages $\bar{s}$ of the values s_i, which represent the values of either F_2 or $\frac{d^2\sigma}{dx\,dQ^2}$ in each data set, weighted with the total inverse variances $1/\sigma_i^2$:

$$\bar{s} = \frac{\sum_{i=1}^{n}(s_i/\sigma_i^2)}{\sum_{i=1}^{n}(1/\sigma_i^2)}. \tag{5.1}$$

Ideally, the uncertainties σ_i comprise only those which are independent like statistical and uncorrelated systematic uncertainties. In practice, the uncertainties of the luminosity constants are included through

$$\sigma_i^2 = \sigma_{stat.,i}^2 + \sigma_{Lumi,i}^2 \tag{5.2}$$

in order to account for different precisions of the data sets regarding normalizations, despite of the partial correlation discussed below. The estimate of the average in Equation 5.1 has a variance with a contribution V_{stat} from the statistical uncertainties:

$$V_{stat}[\bar{s}] = \frac{1}{\sum_{i=1}^{n}(1/\sigma_{i,\,stat}^2)}. \tag{5.3}$$

Systematic deviations are usually strongly correlated for data sets from the same experiment and do not scale with the number of data sets merged. Such systematic uncertainties are estimated from the particular contributions $\sigma^2_{i,\,syst}$ in the various data sets weighted with the respective integrated luminosities L_i, that indicate the size of the data sets:

$$V_{syst}[\bar{s}] = \frac{\sum_{i=1}^{n}(\sigma^2_{i,\,syst} \cdot L_i)}{\sum_{i=1}^{n} L_i}. \tag{5.4}$$

The requirements for using Equation (5.4) are fulfilled for the various systematic uncertainties: The luminosity constants from different data sets are partially correlated, for instance due to the luminosity detector position and calibrations. Equation (5.4) is chosen in order to prevent an underestimation of the normalization uncertainty. The overall normalization uncertainty of the combined data sets due to the uncertainties of the luminosity constants is thereby determined to be 6.4% for data on the proton target, and 6.6% for data on the deuteron target. The numbers are derived directly from Tables 3.1 and 4.4. Efficiencies and contaminations from particle identification are defined by fractions of events hence Equation (5.4) is appropriate in order to obtain the efficiencies and contaminations of the combined sample. A special case of Equation (5.4) is given for identical uncertainties assigned for all data: Misalignment contributes with an uncertainty which is assumed to be conservatively valid for all data, thus it is applied to the result after merging data. The uncertainties of Bethe-Heitler radiative corrections due to misalignment are simulated in MC independently from the year of data taking, so they are also applied to the combined result.

The results on the structure functions F_2^p and F_2^d are listed in Tables E.1 and E.2, respectively. The (x, Q^2) dependence of the results on $F_2^{p,d}$ is shown in Figures 5.1 (5.2) for proton (deuteron), using a compact coordinate scale. A more detailed view is presented in Figures D.1-D.3 (D.4-D.6).

5.2 Results on the Cross Section Ratio σ^d/σ^p

The results for the cross section ratio σ^d/σ^p as obtained from the proton and deuteron cross sections measured in the years years 1996, 1997, 2002 and 2005 are combined using again Equation (5.1) by weighting with the statistical uncertainty:

$$\sigma_i^2 = \sigma^2_{stat,i} \tag{5.5}$$

As the ratio was calculated year-by-year for data with the same luminosity constants, the cancellation of systematic uncertainties applies to luminosity constants, PID efficiencies, and the effects from misalignment. These contributions are considered to be independent from the target type. The uncertainty of Bethe-Heitler efficiencies δ_{rad} as well as the normalization uncertainty δ_{norm} are both applicable directly to the combined result and are therefore not included in the weighting. The statistical uncertainty is correspondingly calculated using Equation (5.3).

The combined results on the cross section ratio σ^d/σ^p are listed in Table E.3. Figures 5.3 and 5.4 illustrate the Q^2 and ε dependence of the result on σ^d/σ^p, respectively, in bins of x.

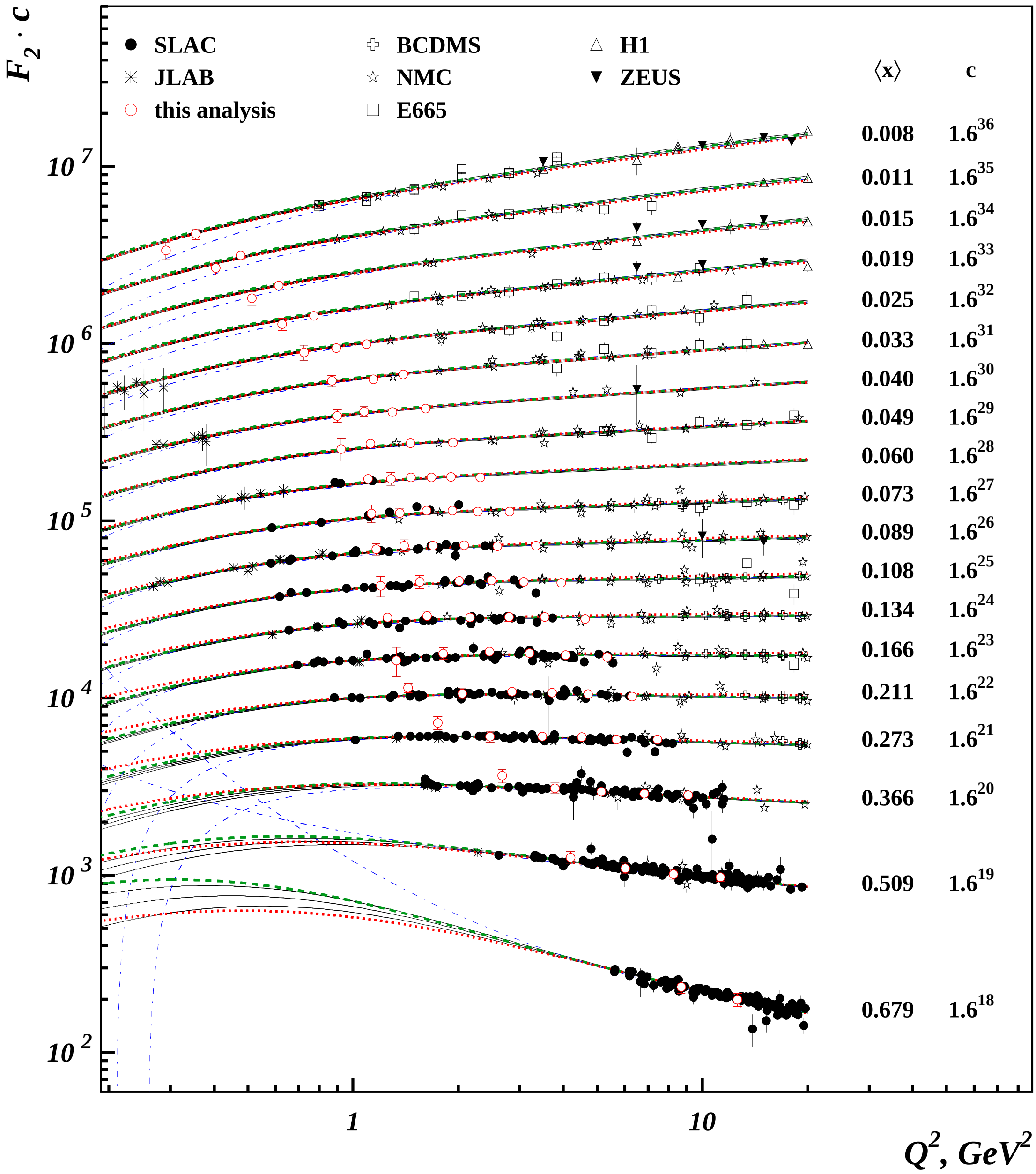

Figure 5.1: The world data of F_2^p is compared to phenomenological parameterizations. The Q^2 dependence of F_2^p is shown in the x binning of this analysis as listed in Table C.1. A bin-center-correction was performed to data in order to match the central values of the x bins. The values of F_2^p were scaled by powers of 1.6. All data points have been corrected using the normalization parameters obtained from the GD08 fit as described in Chapter 6.1. The GD08 fit (solid curve) is shown with error band, while only central values are shown for the GD07 fit [107] (dashed curve), the ALLM97 fit [91] (dotted curve) and the SMC fit [108] (dashed-dotted curve). The entire kinematic region covered by the HERMES experiment is shown in this figure. Larger scales are shown in Figs. D.1, D.2, and D.3.

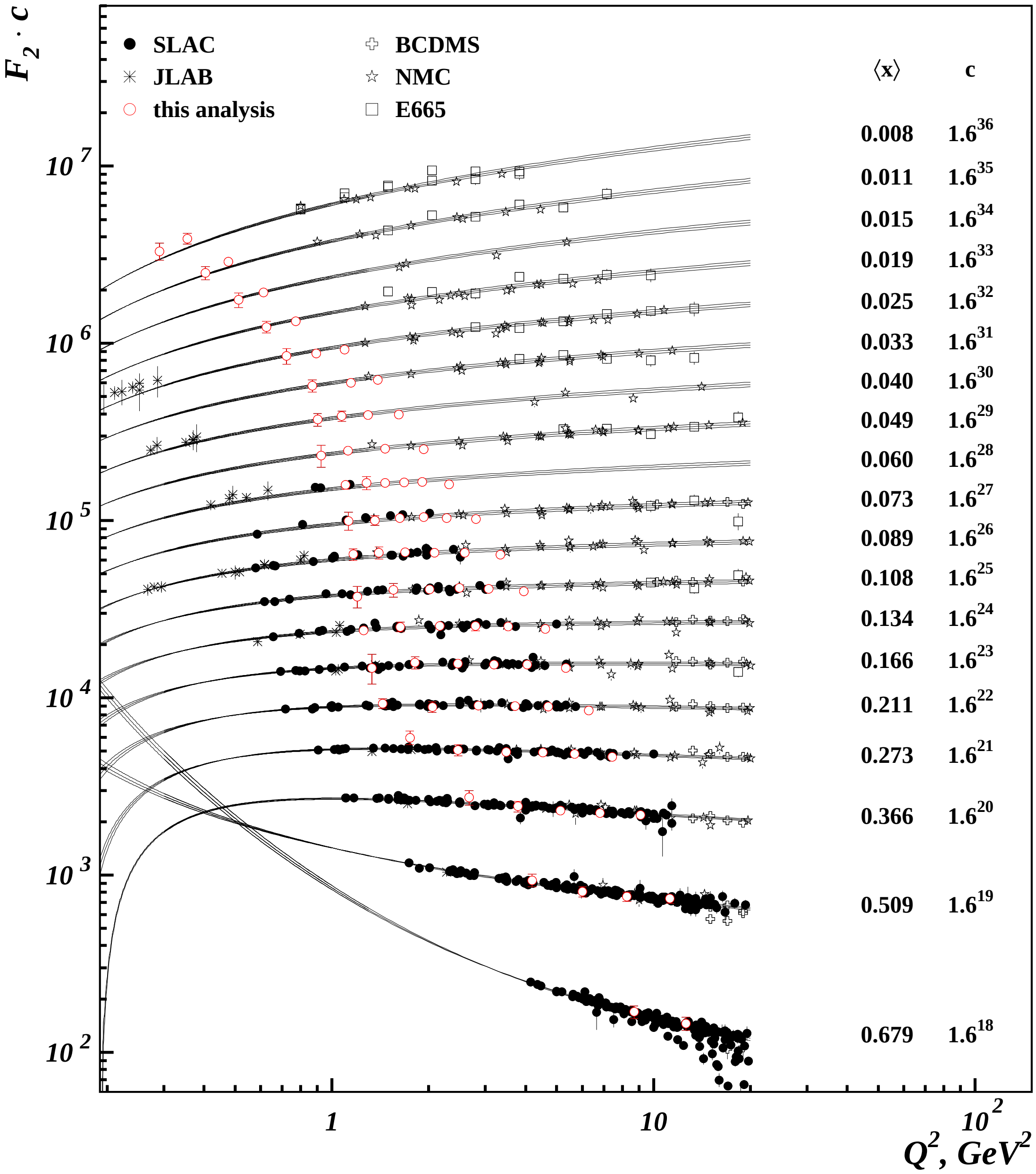

Figure 5.2: World data of F_2^d is compared to the SMC phenomenological parameterization [108]. The Q^2 dependence of F_2^d is shown in the x binning of this analysis as listed in Table C.1. A bin-center-correction was performed to data in order to match the central values of the x bins. The values of F_2^d were scaled by powers of 1.6. The entire kinematic region covered by the HERMES experiment is shown in this figure. Larger scales are shown in Figs. D.4, D.5, and D.6.

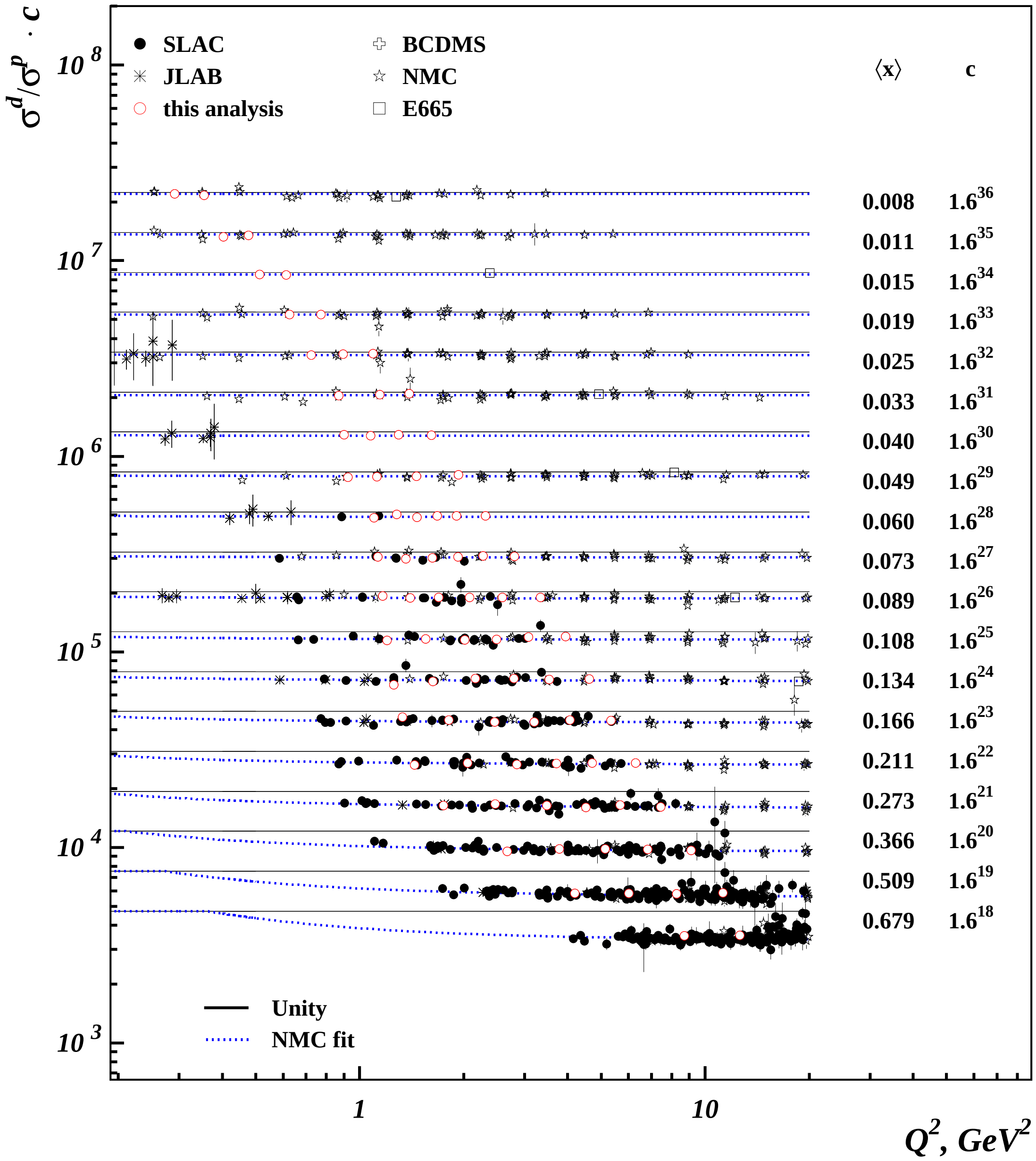

Figure 5.3: The cross section ratio σ^d/σ^p versus Q^2 in bins of x. The values of σ^d/σ^p are scaled by powers of 1.6. The horizontal solid lines indicate the correspondingly scaled unity in each x bin. The dotted curves represent the NMC fit [94] to the data from NMC, SLAC and BCDMS. Larger scales are shown in Figs. D.7-D.12.

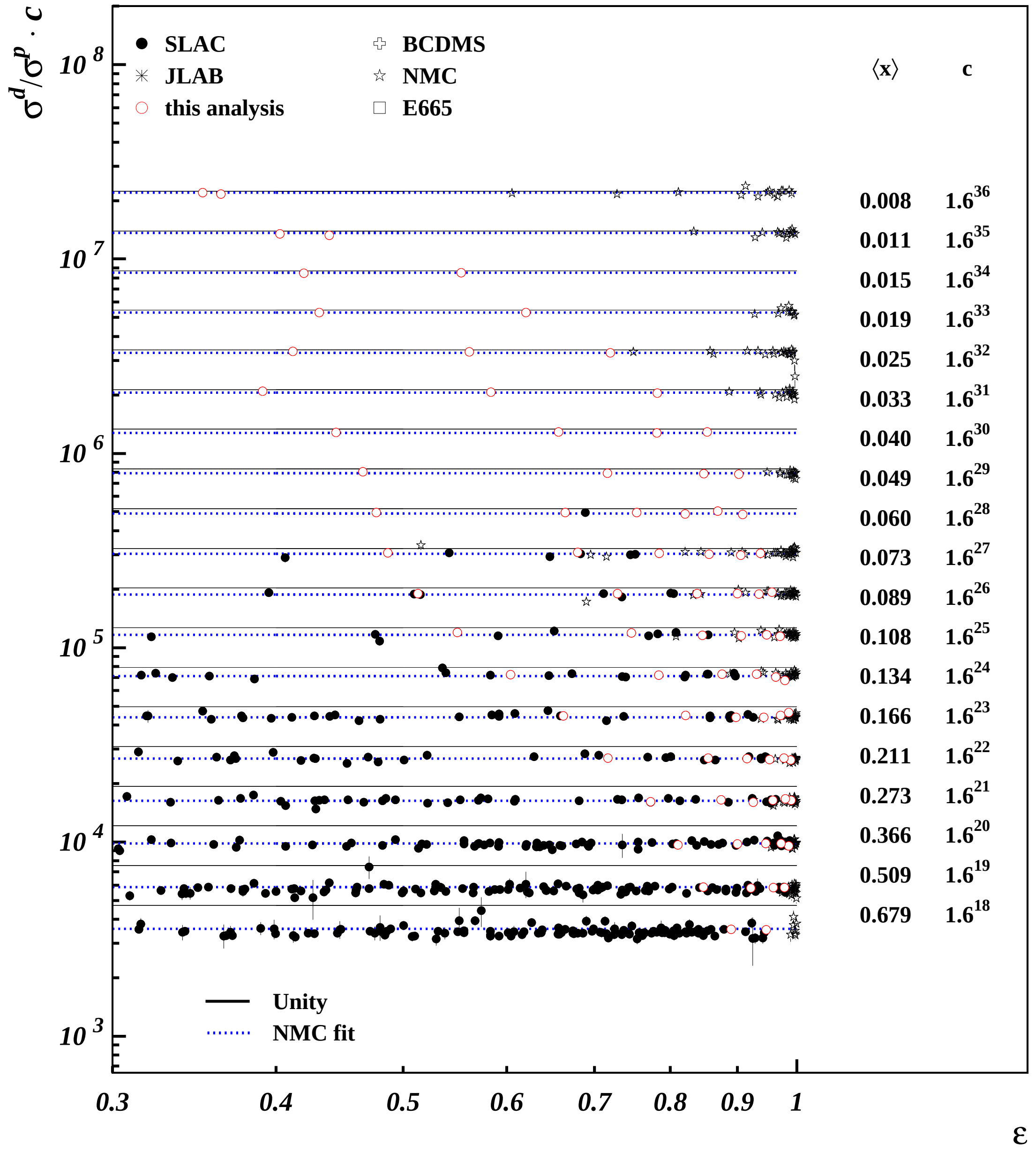

Figure 5.4: The cross section ratio σ^d/σ^p, similar to Figure 5.3 but versus ε in bins of x. Only data with Q^2 values similar to those of the HERMES data are shown. The dotted curves represent the NMC fit [94] to the data from NMC, SLAC and BCDMS at the arbitrary value of $Q^2 = 2.5\,\mathrm{GeV}^2$.

Chapter 6

Fits to World Data

6.1 Fit of the Proton DIS Cross Section

6.1.1 Introduction

Deep-inelastic scattering on protons has been studied with high precision in the last decades at various energies, covering a large kinematic region provided by collider and fixed-target experiments, thus providing us with our modern understanding of the proton structure.

As we have seen in Chapter 1.1, the inclusive DIS cross section in the one-photon-exchange approximation is related to the unpolarized structure function $F_2(x, Q^2)$ and the ratio $R(x, Q^2)$ of longitudinal and transverse photo-absorption cross sections by Equation (1.23). Consequently, a single measurement of the cross section is not sufficient to extract both, F_2 and R, instead the variation of the beam energy E at fixed values of x and Q^2 can give access to both quantities. Alternatively, F_2 can be extracted using parameterizations of world data on R: Two common examples are R_{1990} [92] and R_{1998} [93], the differences of which reflect the status of world knowledge at the time they were obtained, see Figure 6.1. The sensitivity of the cross section to R increases with y as can be seen in Equation (1.23). The discrepancy in the extracted values of F_2 using the two parameterizations of R can exceed 4% in the region of maximum y.

The structure function F_2 is related to the full photon-proton cross section σ_{L+T} by Equation (1.18) and can be written in the form

$$\sigma_{L+T} \equiv \sigma_L + \sigma_T = \frac{4\pi^2\alpha_{em}}{Q^4}\frac{Q^2 + 4M^2x^2}{1-x}F_2 \ . \tag{6.1}$$

For virtual photons this relation employs the Hand convention for the virtual photon flux which is used to establish consistency between real and virtual-photon processes.

6.1.2 Data and the Functional Form

A new fit [107] of the photon-proton cross section σ_{L+T} was performed in the context of this thesis which reflects the recent world knowledge on the cross section and is *self-consistent* with respect to the use of R.

In several earlier phenomenological fits to world data, inconsistencies in data due to the use of different extraction methods or assumptions concerning R were ignored. The present fit takes this issue into account. Using all available information published on the particular

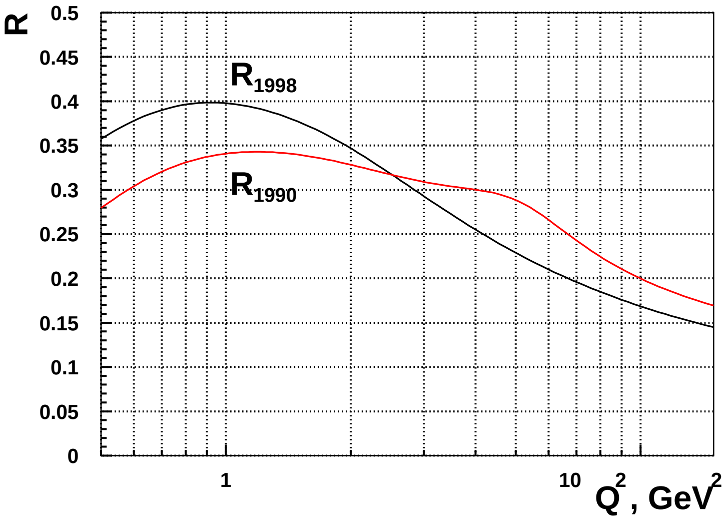

Figure 6.1: Comparison of the two common parameterizations of R: R_{1990}(red) and R_{1998}(*black*). Shown is the Q^2 dependence at x=0.01.

F_2 extractions, a self-consistent collection of data sets was prepared. In those cases when measured cross sections were published, they were used directly, in all other cases the cross sections were reconstructed using the value of R that had been used to extract the published values of F_2.

The fit includes 2821 data points: 574 from the SLAC experiments E49a, E49b, E61, E87, E89a, E89b [38]; 81 points from this analysis of HERMES data; 292 from NMC [40]; 229 from BCDMS [39]; 91 from E665 [41]; 787 from H1 [36]; 570 from ZEUS [37]; Real photon data comprise 196 points from Ref. [109] and 1 from ZEUS [110]. The kinematic plane covered by the available data is displayed in Figure 6.2. The available JLAB data [111] do not allow a reconstruction of the measured cross section, so they are not included in the fit.

The functional form selected for the fit was first described in [113] and [91] and used in fits referred to as the ALLM parameterizations. The ALLM functional form is a 23-parameter model of σ_{L+T} where F_2 is described by Reggeon and Pomeron exchange, valid for $W^2 > 4\,\mathrm{GeV}^2$, i.e., above the resonance region, and any Q^2 including the real photon process. Here, W^2 is the invariant squared mass of the photon-proton system. The ALLM parameterizations are fits of σ_{L+T} with the functional form

$$\sigma_{L+T} = \frac{4\pi^2\alpha_{em}}{Q^2+m_0^2}\frac{1+\gamma^2}{1-x}\left[F_2^{\mathcal{P}}+F_2^{\mathcal{R}}\right] , \tag{6.2}$$

where m_0 is the effective photon mass accounting for the hadronic structure of the photon at low Q^2, and the functions

$$\begin{aligned} F_2^{\mathcal{P}} &= c_{\mathcal{P}}(t)x_{\mathcal{P}}^{\alpha_{\mathcal{P}}(t)}(1-x)^{b_{\mathcal{P}}(t)}, \\ F_2^{\mathcal{R}} &= c_{\mathcal{R}}(t)x_{\mathcal{R}}^{\alpha_{\mathcal{R}}(t)}(1-x)^{b_{\mathcal{R}}(t)} \end{aligned} \tag{6.3}$$

correspond to the contributions of the Pomeron and Reggeon exchanges to F_2, respectively.

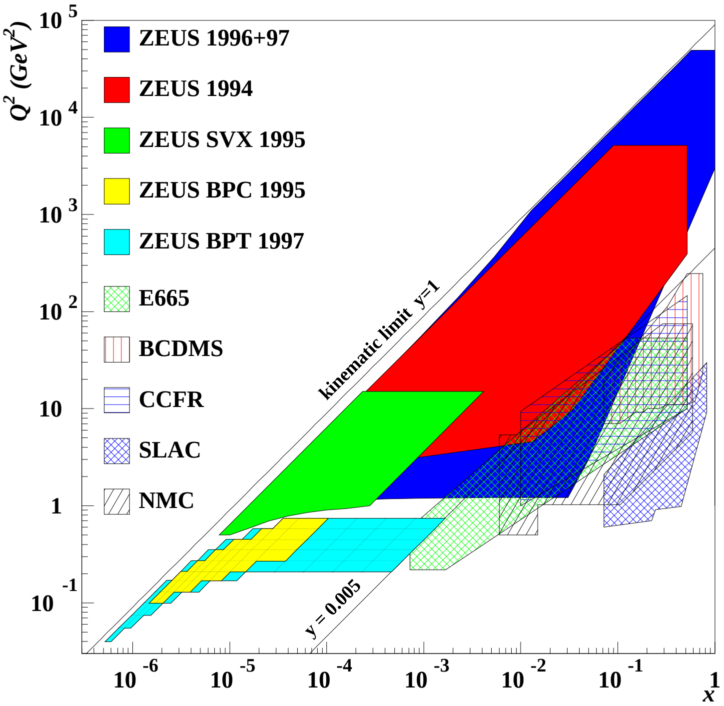

Figure 6.2: World data covering the $x - Q^2$ plane [?].

The slowly varying function t is defined as

$$t = \ln \left(\frac{\ln \frac{Q^2+Q_0^2}{\Lambda^2}}{\ln \frac{Q_0^2}{\Lambda^2}} \right), \tag{6.4}$$

where Λ is the QCD scale and Q_0^2 is a parameter. The two scaled variables $x_{\mathcal{P}}$ and $x_{\mathcal{R}}$ are modified Bjørken-x variables which include mass parameters $m_{\mathcal{P}}$ and $m_{\mathcal{R}}$, interpreted as effective Pomeron and Reggeon masses:

$$\begin{aligned} x_{\mathcal{P}} &= \left(1 + \frac{W^2 - M^2}{Q^2 + m_{\mathcal{P}}^2}\right)^{-1} \\ x_{\mathcal{R}} &= \left(1 + \frac{W^2 - M^2}{Q^2 + m_{\mathcal{R}}^2}\right)^{-1}. \end{aligned} \tag{6.5}$$

The functions $c_{\mathcal{R}}$, $a_{\mathcal{R}}$, $b_{\mathcal{R}}$ and $b_{\mathcal{P}}$ increase with Q^2 as

$$f(t) = f_1 + f_2\, t^{f_3} \tag{6.6}$$

while $c_{\mathcal{P}}$ and $a_{\mathcal{P}}$ decrease with Q^2 like

$$g(t) = g_1 + (g_1 - g_2) \left[\frac{1}{1 + t_3^g} - 1 \right]. \tag{6.7}$$

The explicit functional form of the parameterization is given in appendix B.1.

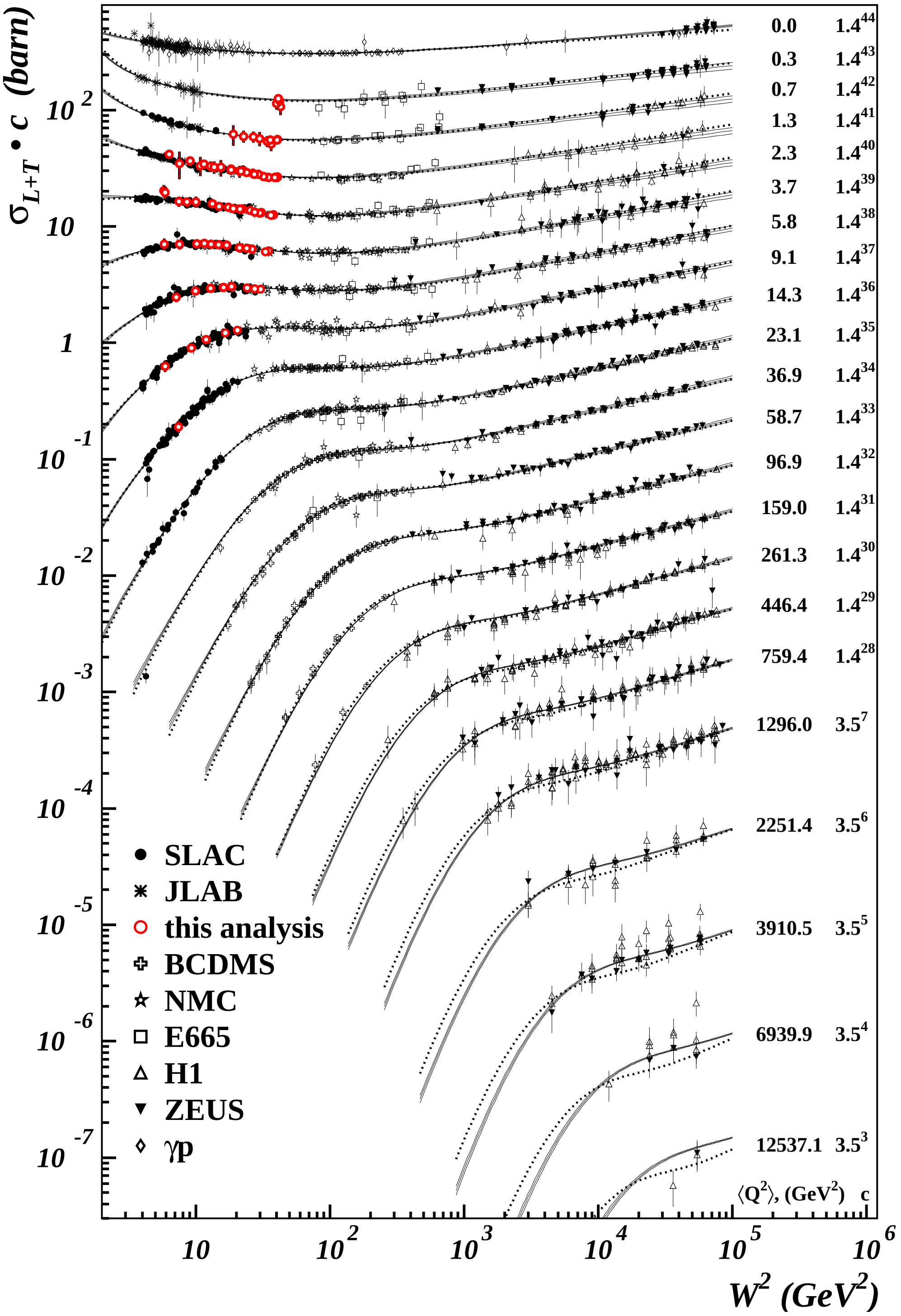

Figure 6.3: World data on the full cross-section σ_{L+T} as a function of W^2 in bins of x, together with the results from the ALLM97 fit (dotted curves) and this fit including uncertainties (solid curves).

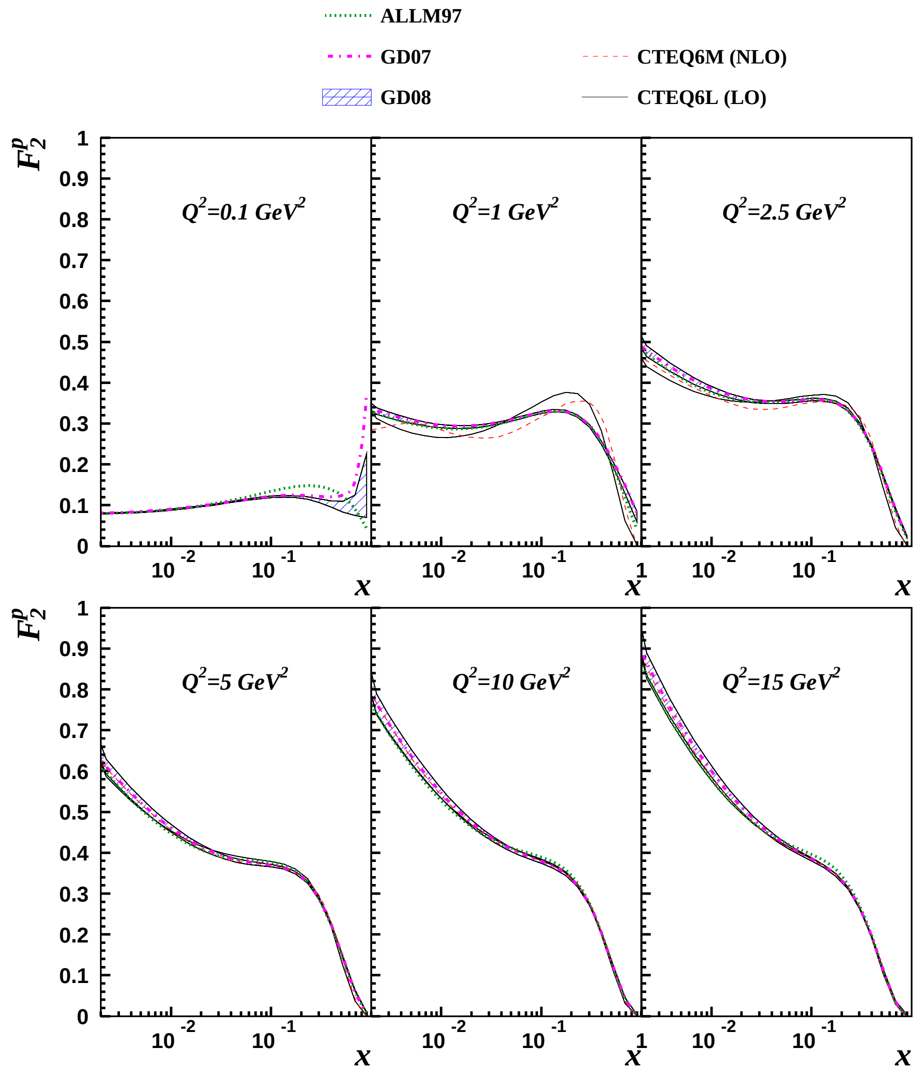

Figure 6.4: A comparison of the fit results on F_2^p from this fit (GD08) with error band, the previous fit (GD07) and the ALLM97 fit to the predictions from CTEQ6 in LO and NLO. CTEQ6 predictions are omitted for $Q^2 < 1\,\mathrm{GeV}$.

A commonly used cut $Q^2 > 1\,\mathrm{GeV}^2$, as required for QCD fits, eliminates any predictive power below this region. The striking advantage of the ALLM functional form compared to other functions is that it is able to describe data in all measured regions above the resonance region, thus no lower cut on Q^2 is required.

6.1.3 The Fitting Procedure

The new fit was performed by minimizing the value of χ^2 defined as

$$\chi^2(\mathbf{p},\boldsymbol{\nu}) = \sum_{i,k} \frac{[D_{i,k}(W^2,Q^2)\cdot(1+\delta_k\nu_k) - T(\mathbf{p},W^2,Q^2)]^2}{(\sigma_{i,k}^{stat^2} + \sigma_{i,k}^{syst^2})\cdot(1+\delta_k\nu_k)^2} + \sum_k \nu_k^2$$

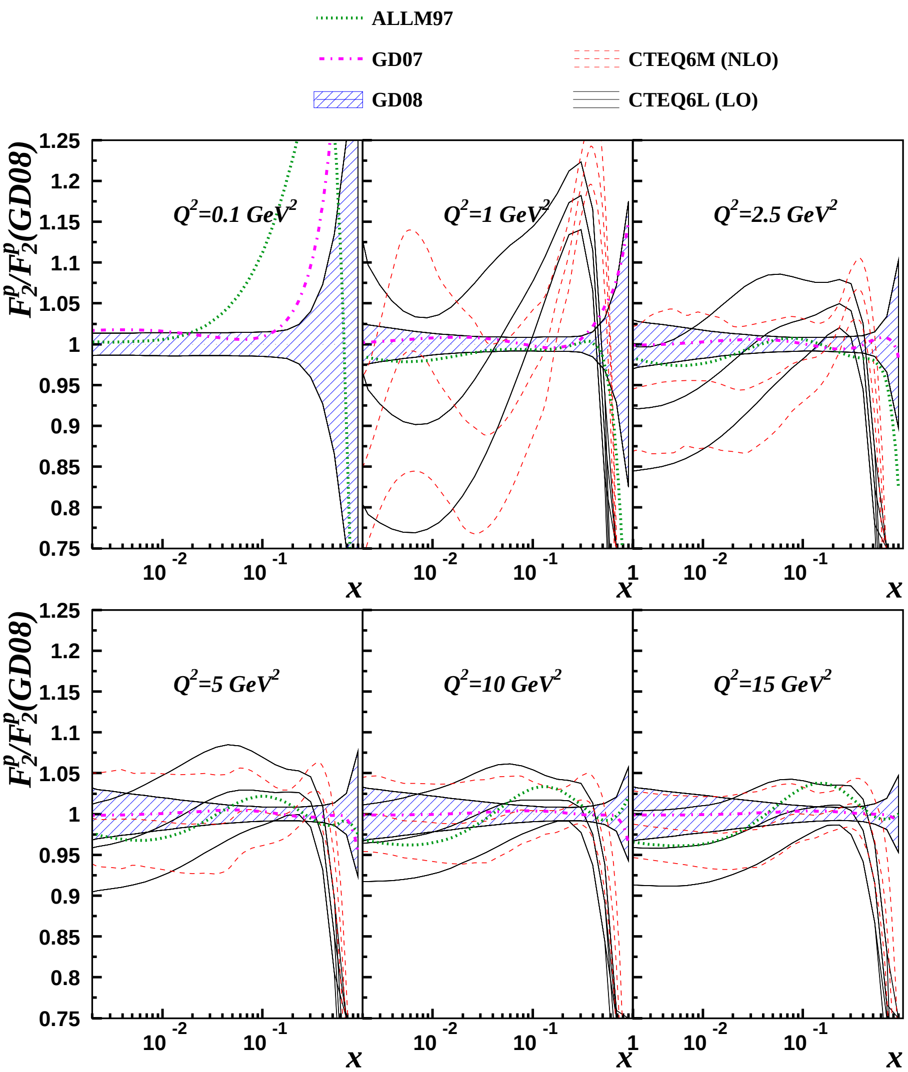

Figure 6.5: A comparison similar to Figure 6.4. All fits have been *divided* by the central values of the GD08 fit. Error bands are shown for GD08 and for CTEQ6 in LO and NLO.

$$\approx \sum_{i,k} \frac{[D_{i,k}(W^2,Q^2) - T(\mathbf{p},W^2,Q^2)\cdot(1-\delta_k\nu_k)]^2}{{\sigma_{i,k}^{stat}}^2 + {\sigma_{i,k}^{syst}}^2} + \sum_k \nu_k^2 \ , \tag{6.8}$$

where $D_{i,k} \pm \sigma_{i,k}^{stat} \pm \sigma_{i,k}^{syst}$ are the values of σ_{L+T} for data point i within the data set k, δ_k is the normalization uncertainty in data set k quoted by the experiment, ν_k is a parameter for the normalization of each data set in units of the normalization uncertainty, $T(\mathbf{p},W^2,Q^2)$ is the 23-parameter ALLM functional form. The definition of χ^2 takes into account point-by-point statistical and systematic uncertainties and overall normalization uncertainties. For each data set one normalization parameter is defined which applies a normalization to all data points within the data set. Absolute values for the uncertainties are normalized accordingly to conserve the fractional values. Since the normalization parameters are preferably supposed to normalize data within the known normalization uncertainties, they are scaled with these uncertainties and considered by a penalty term $\sum_k \nu_k^2$ to control their variation in $\pm 1\sigma$ limits.

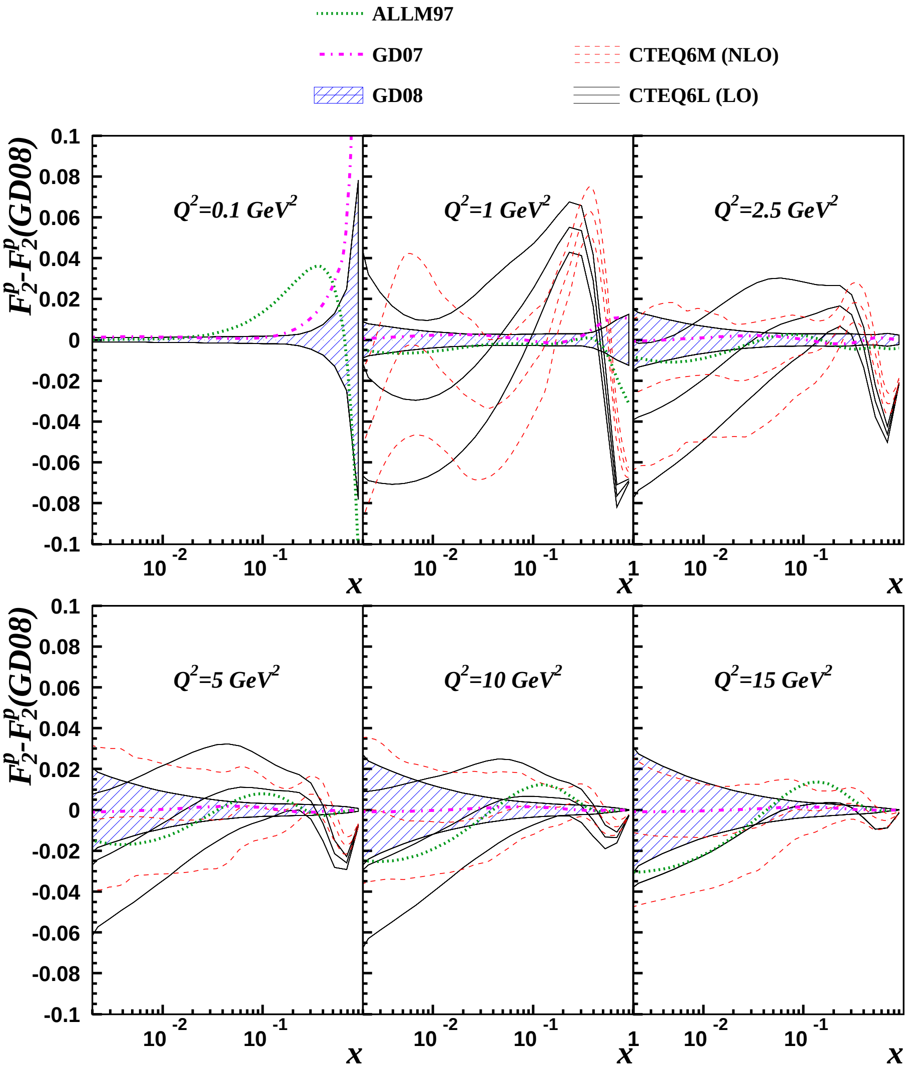

Figure 6.6: A comparison similar to Figure 6.4. All fits have been *shifted* by the central values of the GD08 fit. Error bands are shown for GD08 and for CTEQ6 in LO and NLO.

The fit was performed using MINUIT [114] by calls to MIGRAD for the minimization of the χ^2-function and by calls to HESSE for the calculation of the covariance matrix. The total number of parameters for $\mathbf{p}$ and $\boldsymbol{\nu}$ is above the limit of 50 parameters which MINUIT can handle as free parameters at the same time. This problem could in principle be solved by iteratively fixing and releasing various parameters, so that only 50 parameters are free at the same time. A more convenient and precise solution is chosen within this work: For a fixed set of functional parameters, the normalization parameters being necessary to reach the minimum of the χ^2-function, are analytically determined. It can be shown by differentiation of the χ^2-function with respect to the normalization parameters, that the minimum is defined by Equation (6.9):

$$\nu_k = \frac{\sum_i \delta_k T_{i,k}(T_{i,k} - D_{i,k})/\sigma_{i,k}^2}{\sum_i T_{i,k}^2 \delta_k^2/\sigma_{i,k}^2 + 1}, \tag{6.9}$$

This equation was obtained by requiring $\partial\chi^2/\partial\nu_k = 0$ in the context of the approximation for χ^2 in the second line of Equation (6.8); here $\sigma_{i,k}^2 = \sigma_{i,k}^{stat\,2} + \sigma_{i,k}^{syst\,2}$.

This separate extraction of all normalization parameters is only possible since the normalization parameters are not correlated among each other and depend only on the involved data points and the functional parameters. The analytical equation (6.9) for ν_k was substituted into the χ^2-function, Equation (6.8), and thus the final fit was obtained by minimizing χ^2 only with respect to the functional parameters. Similar methods were used by others in order to save computing time [115] [116].

6.1.4 Fit Results

The resulting fit has a χ^2/ndf equal to 0.94 where ndf is the number of degrees of freedom of the χ^2 distribution.

The contributions from each data set together with the normalization parameters are listed in Table 6.1. Table 6.2 shows the final parameters from this fit with the corresponding uncertainties and, for comparison, the parameters from the ALLM97 fit. Since the ALLM97 fit is a good first approximation for the current fit, its parameters were used as starting parameters for the minimization. Figure 6.3 shows the new fit in comparison with world data and with the ALLM97 fit.

The covariance matrix of the parameter space at the minimum of the χ^2-function is obtained for an accurate error calculation. Only for convenience, the parameter uncertainties listed in table 6.2 are the uncertainties corresponding to the diagonal elements of the full covariance matrix [117] which *must* be used to calculate uncertainties in F_2 or cross sections.

The uncertainties of the fit results on F_2 and σ_{L+T} at each value of Q^2 and W^2 are calculated from the derivatives of the functional form of the fit with respect to the parameters, the parameter values, and their uncertainties. The derivatives are given in appendix B.2.

The uncertainties of the parameters are, as it is usually done, the one standard deviation (hereafter called "1σ"). This error defintion corresponds to the default MINUIT internal parameter setting UP$= 1$ for which the error limits of a single parameter surround the region corresponding to a 1σ probability, while the other parameters are fixed at their central values.

A different error definition corresponding to an inclusion of a 1σ probability by a simultaneous variation of all parameters within the multi-dimensional hyper-contour is used by several QCD fits but is not used here. By simple scaling, both error calculations can be converted into each other.

A full comparison between ALLM97 and the current fit (GN08) is not possible as in the ALLM97 fit parameter uncertainties were not provided. Presumably, these uncertainties are larger than those of the new fit, since the size of the current data set is more than twice as large. The uncertainties in the cross sections calculated from the fit as represented by the error bands in the figure are much smaller than individual error bars on the original data points because of the smoothness constraint inherent in the fitted model. The fit evaluated at any kinematic point is effectively an average of a number of data points.

In conclusion, a new fit of world data on σ_{L+T} and F_2 is presented. In contrast to ALLM, this fit is consistent in the choice of the R parameterization R_{1998}. Also, for the first time, parameter and fit uncertainties are calculated. A subroutine that allows the calculation of σ_{L+T} and F_2 with their fit uncertainties is available [117].

The fit will be used as input to the analysis of the cross section ratio σ^d/σ^p in the following section.

Nr.	data set	n	χ^2/n	δ_k^{nor}	ν_k
1.	SLAC-E49a	98	0.51	2.1	0.06
2.	SLAC-E49b	187	1.15	2.1	-0.28
3.	SLAC-E61	25	0.24	2.1	0.01
4.	SLAC-E87	94	0.68	2.1	0.07
5.	SLAC-E89a	72	1.06	2.1	1.31
6.	SLAC-E89b	98	1.01	2.1	0.17
7.	NMC 90 GeV	73	0.77	2.0	-0.37
8.	NMC 120 GeV	65	1.54	2.0	0.14
9.	NMC 200 GeV	75	1.13	2.0	-0.09
10.	NMC 280 GeV	79	0.94	2.0	-0.24
11.	E665	91	1.04	1.8	0.67
12.	BCDMS 100 GeV	58	1.13	3.0	-1.20
13.	BCDMS 120 GeV	62	0.73	3.0	0.03
14.	BCDMS 200 GeV	57	1.32	3.0	-1.09
15.	BCDMS 280 GeV	52	1.12	3.0	-1.03
16.	H1 94 a	37	0.35	3.9	0.05
17.	H1 94 b	156	0.63	1.5	1.13
18.	H1 SVX	44	0.49	3.0	-3.02
19.	ZEUS 94	188	1.15	2.0	1.66
20.	ZEUS BPC	34	0.40	2.4	-1.28
21.	ZEUS SVX	36	0.76	3.0	-1.00
24.	ZEUS 9697	1	0.75	2.0	0.09
25.	ZEUS 97	196	0.97	2.0	-2.23
26.	H1 99 00	242	1.01	1.5	-1.08
27.	H1 98 99	70	1.37	1.8	-1.38
28.	H1 94 97	147	0.79	1.5	-1.46
29.	H1 96 97 a	126	1.05	1.7	1.77
30.	H1 96 97 b	130	0.82	1.7	2.02
31.	**this analysis**	**81**	**0.40**	**6.4**	**0.67**

Table 6.1: The data sets which enter the fit are listed together with the corresponding numbers of data points n, the χ^2-contributions, as well as normalization uncertainties δ_k^{nor}, and normalization parameters ν_k. In total the fit covers 2821 data points and has a reduced χ^2 of 0.93

Parameter	ALLM97	GD07	GD08 (this fit)	uncertainty
m_0^2(GeV^2)	0.31985	0.454	0.4576	0.0256
$m_{\mathcal{P}}^2$(GeV^2)	49.457	30.7	31.4550	2.9193
$m_{\mathcal{R}}^2$(GeV^2)	0.15052	0.118	0.0565	0.0232
Q_0^2(GeV^2)	0.52544	1.13	1.1005	0.3059
Λ_0^2(GeV^2)	0.06527	0.06527	0.0653	-
$a_{\mathcal{P}1}$	-0.0808	-0.105	-0.1045	0.0046
$a_{\mathcal{P}2}$	0.44812	-0.496	-0.4921	0.0282
$a_{\mathcal{P}3}$	1.1709	1.31	1.3346	0.2254
$b_{\mathcal{P}4}$	0.36292	-1.43	-0.6442	0.4323
$b_{\mathcal{P}5}$	1.8917	4.50	3.7881	0.4997
$b_{\mathcal{P}6}$	1.8439	0.554	0.7664	0.1788
$c_{\mathcal{P}7}$	0.28067	0.339	0.3441	0.0179
$c_{\mathcal{P}8}$	0.22291	0.128	0.1247	0.0207
$c_{\mathcal{P}9}$	2.1979	1.17	1.2075	0.2421
$a_{\mathcal{R}1}$	0.584	0.373	0.3789	0.0303
$a_{\mathcal{R}2}$	0.37888	0.994	0.9433	0.0828
$a_{\mathcal{R}3}$	2.6063	0.781	0.6253	0.0899
$b_{\mathcal{R}4}$	0.01147	2.70	3.1864	0.2900
$b_{\mathcal{R}5}$	3.7582	1.83	1.2231	0.4327
$b_{\mathcal{R}6}$	0.49338	1.26	1.6522	0.4363
$c_{\mathcal{R}7}$	0.80107	0.837	1.1112	0.1566
$c_{\mathcal{R}8}$	0.97307	2.34	1.8408	0.4708
$c_{\mathcal{R}9}$	3.4942	1.79	1.8016	0.2256

Table 6.2: Parameters of the functional form used in the ALLM parameterization [113]. Results of the ALLM97 fit [91] in comparison to the previous fit GD07[107] before including HERMES data and the results of the fit discussed in this chapter (GD08) which are given with uncertainties. These uncertainties correspond to only the diagonal elements of the full covariance matrix [117] which *must* be used to calculate uncertainties in F_2 or cross sections. The parameter Λ_0^2 has no uncertainty as it was fixed in the fit.

6.2 Fit of the Cross Section Ratio σ^d/σ^p

Additionally to the determination of structure functions, results on DIS cross sections on proton and deuteron targets are used to evaluate the deuteron-to-proton cross-section-ratio. The ratio of the structure functions F_2^d and F_2^p is of particular interest as it is directly linked to the ratio of neutron and proton structure functions and thus to the ratio of down and up valence quark distributions. Widely different predictions exist for the structure function ratio F_2^d/F_2^p in the limit $x \to 1$, depending on the assumed behavior of the valence quarks. In the limit $x \to 0$ the structure function ratio is known to be close to unity because of the similarity of sea quark distributions in the proton and deuteron.

Perturbative QCD calculations predict slightly different scaling behaviors for the structure functions F_2^p and F_2^d, given that the valence quark compositions of proton and deuteron differ. In the same framework, a possible difference in the ratios of longitudinal and transverse virtual-photon absorption cross sections, $R^d - R^p$, is predicted to be sensitive to any deviation

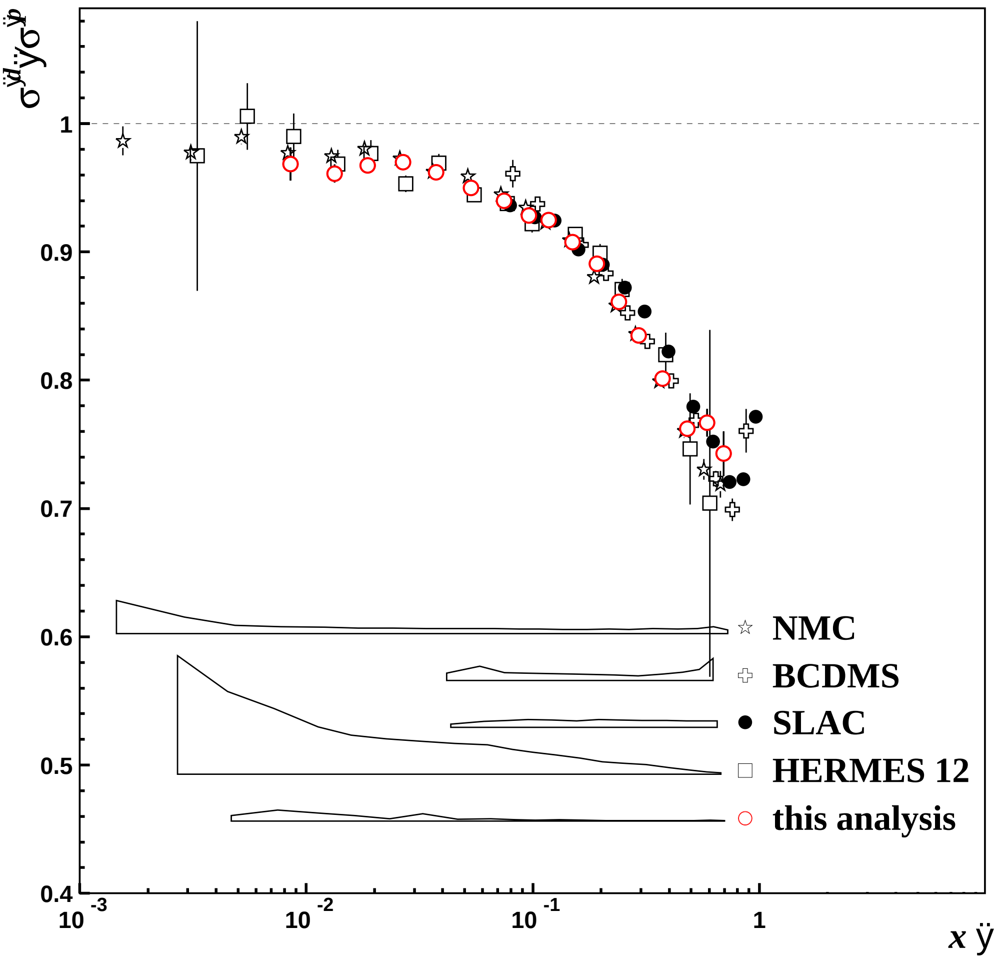

Figure 6.7: The x dependence of σ^d/σ^p is shown for data from SLAC (full circles), an old analysis of HERMES data taken at a 12 GeV beam energy (squares), the new results from HERMES as presented in this thesis taken at a beam energy of 27.6 GeV (open circles), NMC (stars), and BCDMS (crosses) integrated over the acceptance of the experiments. The error bars on the data points cover only the statistical uncertainties. The systematic errors are represented by the error bands in the bottom part of the figure.

of the gluon distributions between the two nuclei. Moreover, the structure function ratio F_2^d/F_2^p may reveal differences in possible contributions to the structure functions from quark-gluon correlations known as higher-twist effects. The impact of such effects is usually assumed to grow at small Q^2.

Each of these effects is expected to be small, consequently high precision data is needed over a large kinematic region in x, Q^2 and ε to identify the individual contributions. A simultaneous consideration of all effects is accomplished by a comprehensive analysis based on a fit to the new HERMES results of data taken at a beam energy of 27.6 GeV, results from an old unpublished HERMES analysis of the 12.0 GeV data taken in a short period in 2000, and the results published by SLAC, NMC and BCDMS. The data on σ^d/σ^p is depicted in Figure 6.7.

The structure function ratio F_2^d/F_2^p will appear as one of the results of the fit. High precision data of F_2^d/F_2^p covering the x-Q^2 plane can be used to study the flavor symmetry breaking of the sea quarks, i.e. $\bar{u} \neq \bar{d}$, by evaluating the Gottfried integral [13], see Section 1.8. The only existing evaluation of the Gottfried integral on the full x-range by NMC [68] is not consistent to the naïve expectation of 1/3, as a significant flavor asymmetry of the sea quarks was measured at $Q^2 = 4\,\mathrm{GeV}^2$: $(\bar{d} - \bar{u}) = 0.140 \pm 0.024$. After performing the fit of σ^d/σ^p to world data in this work, the Gottfried integral is evaluated for three values of Q^2: $1\,\mathrm{GeV}^2$, $4\,\mathrm{GeV}^2$, $10\,\mathrm{GeV}^2$ in order to investigate a possible Q^2 dependence of the Gottfried integral.

Before performing the actual fit, the normalizations of the data sets with respect to each other were studied. The normalization uncertainty of the NMC data is negligible whereas other data sets have typical normalization uncertainties of 2%. For this reason the relative normalizations of data sets towards NMC data were determined. The average normalization ratios of a given data set with respect to NMC were found to be 0.984(8) for BCDMS, 0.998(5) for SLAC, 1.006(9) for HERMES 27 GeV and 0.99851 for HERMES 12 GeV. The value of χ^2 is close to unity for the ratios being constant over x.

The fit of σ^d/σ^p was performed using the functional form

$$\frac{\sigma^d}{\sigma^p} = \left(\frac{F_2^d}{F_2^p} + b \ln Q^2\right)\left(1 + \frac{C^d - C^p}{Q^2}\right)\left(1 - \frac{1-\varepsilon}{(1+\bar{R})(1+\varepsilon\bar{R})}\Delta R\right). \tag{6.10}$$

where the structure function ratio F_2^d/F_2^p, the slope parameter b, the difference of the higher-twist coefficients $C^d - C^p$ and the difference of the ratio R in deuteron and proton $R^d - R^p$ are parameters of the fit. For the average of the ratios R^d and R^p the approximation $\bar{R} = R_{1998}$ was used.

The fit results are shown in Figure 6.8. The result of the structure function ratio F_2^d/F_2^p at $Q^2 = 1\,\mathrm{GeV}$ is illustrated in the top left panel. The expression for the cross section ratio σ^d/σ^p, Equation 6.10, takes higher-twist effects and a possible impact of differences in the ratio R into account. However, the difference of R^d and R^p turns out to be consistent with zero as shown in the bottom right panel indicating equal gluon distributions in the deuteron and the proton. As illustrated in the bottom left panel, the higher-twist coefficients of deuteron and proton differ by significantly positive values, for $x > 0.2$. Only in the region $x < 0.2$ the differences are clearly consistent with 0 implying that higher-twist effects can be neglected. The slope parameter b is shown in the top right panel. It displays a very small logarithmic Q^2 dependence and shows a tendency to decrease with x, with slightly negative slopes at higher x. The slope parameter is predominantly driven by NMC and BCDMS data which cover higher values of Q^2.

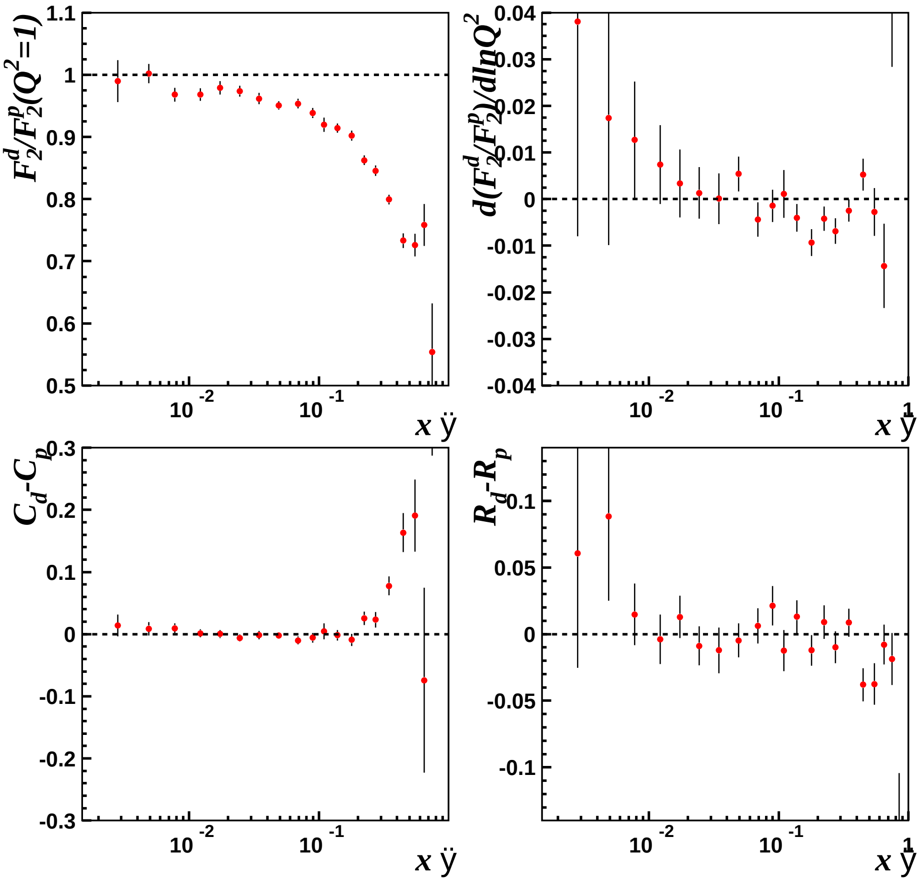

Figure 6.8: The 4 parameters obtained in the fit of σ^d/σ^p to world data are presented as functions of x: The structure function ratio F_2^d/F_2^p is shown in the top left panel, the logarithmic slope parameter $dF_2/d\,ln(Q^2)$ in the top right panel, the difference of higher-twist coefficients $C^d - C^p$ in the bottom left panel and the difference between the ratios of longitudinal and transverse virtual photon absorption cross section $R^d - R^p$ in the bottom right panel.

6.2.1 Evaluation of the Gottfried Integral

The fit results obtained on the cross section ratio σ^d/σ^p together with a parameterization of F_2^p enter the evaluation of the Gottfried integral according to Equation (1.51). The choice of the parameterization is made as follows: For the study of F_2^d/F_2^p including the higher-twist contribution term, the parameterization GD08 from the previous Section was used. In case of a leading-twist approximation, the predictions of CTEQ6M (NLO) served as parameterization of F_2^p. This ensures a consistent calculation of the Gottfried integral for the leading-twist and for the measured structure function ratio:

$$I_G^{LT}(x_{min}, x_{max}) = \int_{x_{min}}^{x_{max}} 2F_2^{p,CTEQ} \left(1 - \frac{F_2^d}{F_2^p}^{LT}\right) \frac{dx}{x} \tag{6.11}$$

$$I_G^{meas.}(x_{min}, x_{max}) = \int_{x_{min}}^{x_{max}} 2F_2^{p,GD08} \left(1 - \frac{F_2^d}{F_2^p}^{meas.}\right) \frac{dx}{x}, \tag{6.12}$$

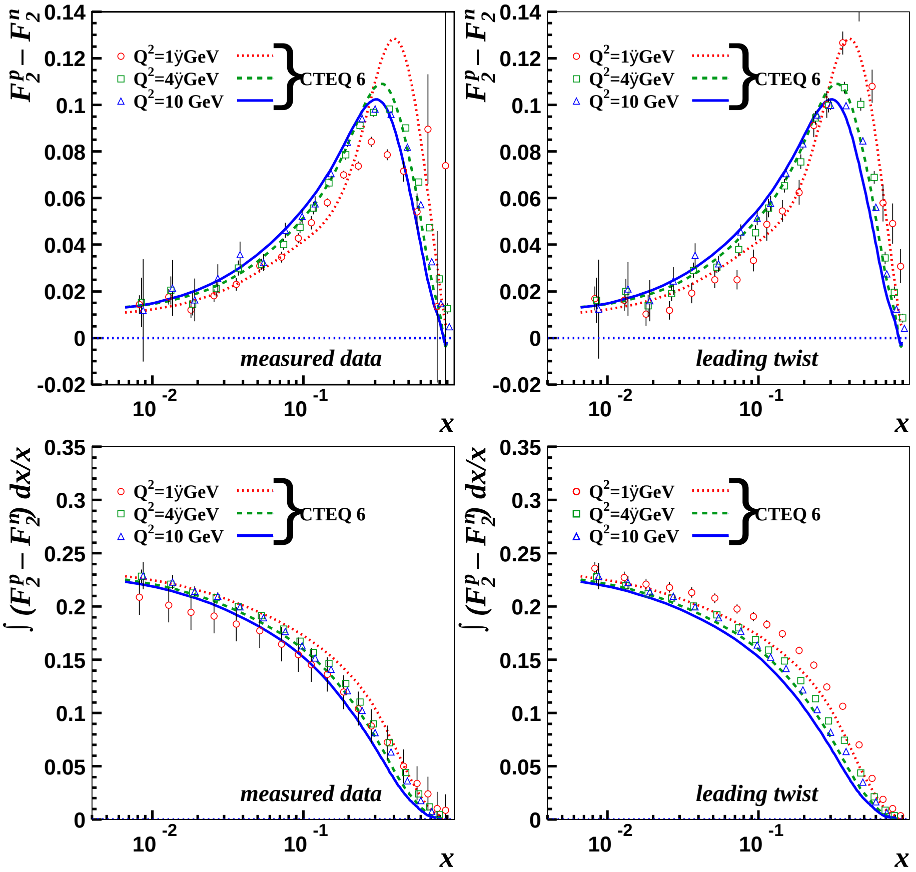

Figure 6.9: This figure illustrates the calculation of the Gottfried integral. The upper two panels show the differences of the structure functions $F_2^p - F_2^n$, while the bottom two panels show the running Gottfried integral $\int_x^{x_{max}}(F_2^p - F_2^n)/x\,dx$ with $x_{max} = 0.9$. CTEQ6M (NLO) predictions are drawn as functions for $Q^2 = 1\,\mathrm{GeV}^2$ (dotted curve), $Q^2 = 4\,\mathrm{GeV}^2$ (dashed curve), and $Q^2 = 10\,\mathrm{GeV}^2$ (solid curve). The data points represent the result obtained in this work from the fit of σ^d/σ^p to world data.

Q^2	x-range	$I_G^{meas.}$	I_G^{LT}
$1\,\mathrm{GeV}^2$	0.006-0.9	0.208 ± 0.016	0.236 ± 0.006
$4\,\mathrm{GeV}^2$	0.006-0.9	0.228 ± 0.006	0.228 ± 0.006
$10\,\mathrm{GeV}^2$	0.006-0.9	0.228 ± 0.013	0.228 ± 0.012

Table 6.3: Results on the Gottfried integral obtained in the 4-parameter fit of the cross section ratio σ^d/σ^p to data from SLAC, HERMES, NCM and BCDMS. The Gottfried integral was evaluated for three different values of Q^2: $1\,\mathrm{GeV}^2$, $4\,\mathrm{GeV}^2$, and $10\,\mathrm{GeV}^2$ in the range $0.006 < x < 0.9$. The fourth column (labeled with I_G^{LT}) was calculated from the leading-twist contribution of the ratio F_2^d/F_2^p while the third column ($I_G^{meas.}$) shows the results for the measured cross section ratios together with the phenomenological parameterization GD08 described in Section 6.1.

where

$$\frac{F_2^d}{F_2^p}^{LT} = \left(\frac{F_2^d}{F_2^p} + b\ln Q^2\right) \tag{6.13}$$

and

$$\frac{F_2^d}{F_2^p}^{meas.} = \frac{F_2^d}{F_2^p}^{LT}\left(1 + \frac{C^d - C^p}{Q^2}\right). \tag{6.14}$$

The determination of the Gottfried integral is illustrated in Figure 6.9. The results for the Gottfried integral in the region $0.006 < x < 0.9$ at $Q^2 = 1\,\mathrm{GeV}^2$, $Q^2 = 4\,\mathrm{GeV}^2$, and $Q^2 = 10\,\mathrm{GeV}^2$ are summarized in Table 6.3 for the leading-twist (LT) and measured (meas) structure function ratio F_2^d/F_2^p. No indication is found for a Q^2 dependence of the Gottfried integral. The result of the Gottfried integral at $Q^2 = 4\,\mathrm{GeV}^2$ is in agreement with the Gottfried integral of 0.236 ± 0.008 found by NMC in the similar range $0.004 < x < 0.8$.

6.2.2 Evaluation of the ratio d_v/u_v

The deuteron-to-proton structure function ratio F_2^d/F_2^p is related to the valence quark ratio d_v/u_v in leading-order by the following equation:

$$\frac{F_2^d}{F_2^p} = \frac{1}{2}\left(1 + \frac{F_2^n}{F_2^p}\right) \simeq \frac{1}{2}\left(1 + \frac{4\frac{d_v}{u_v} + 1 + S_1}{4 + \frac{d_v}{u_v} + S_2}\right) \approx \frac{5}{2} \cdot \frac{1 + \frac{d_v}{u_v}}{4 + \frac{d_v}{u_v}}, \tag{6.15}$$

where $S_1 = \frac{2}{u_v}(u_s + 4d_s + s_s)$ and $S_2 = \frac{2}{u_v}(4u_s + d_s + s_s)$ are the fractional sea quark contributions. The last approximation in Equation (6.15) is valid in the limit of large x where the sea quark distributions q_s are negligible and hence $S_1, S_2 \approx 0$. The valence quark distribution ratio d_v/u_v is extracted from the leading twist result of the structure function ratio F_2^d/F_2^p as obtained from the previous fit to σ^d/σ^p. Figure 6.10 shows the results for $Q^2 = 1\,\mathrm{GeV}^2$, $Q^2 = 4\,\mathrm{GeV}^2$, and $Q^2 = 10\,\mathrm{GeV}^2$, obtained for the values of $S_{1,2}$ predicted by CTEQ and for $S_{1,2} = 0$, respectively. The comparison shows that towards small x the sea quark contribution dominates the result whereas at $x > 0.35$ it has an effect the size of which is smaller than the total uncertainty originating from the fit to σ^d/σ^p.

The comparison in Figure 6.10 reveals a compatibility of the results on d_v/u_v obtained from the world fit on σ^d/σ^p shown in Section 6.2 with the predictions of CTEQ6L and MRST04.

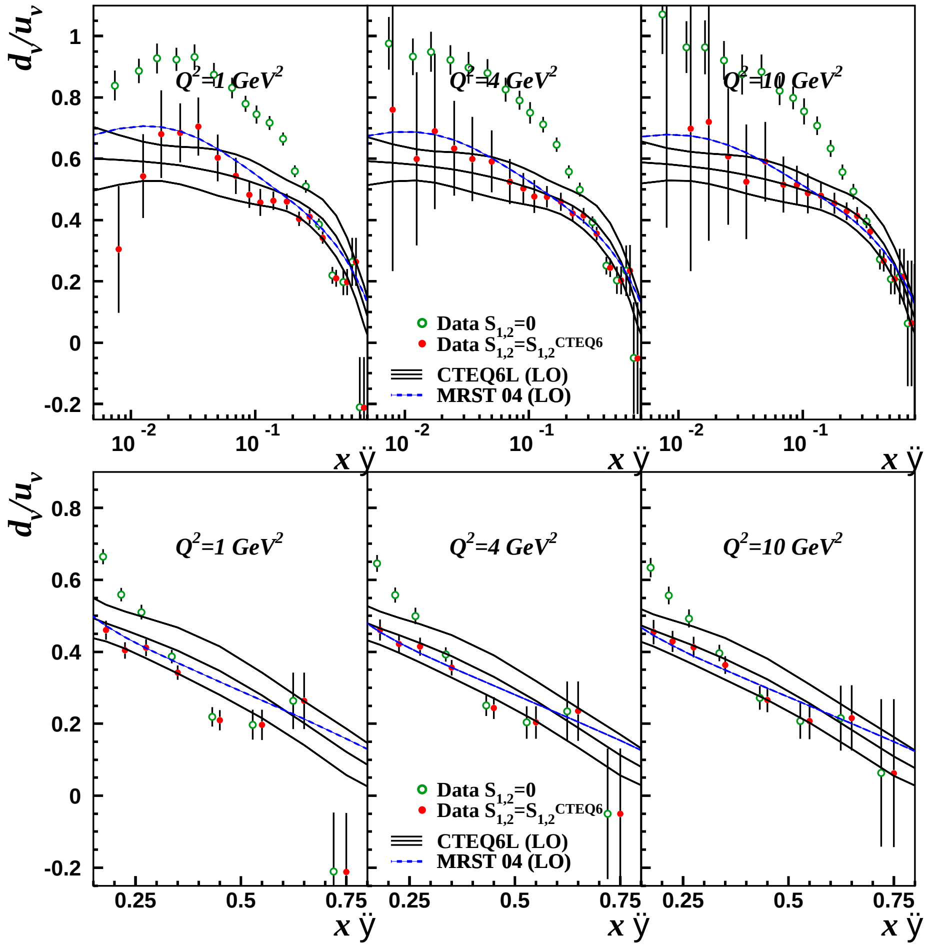

Figure 6.10: Results on d_v/u_v obtained from the previously performed fit to data on the cross section ratio σ^d/σ^p using the sea quark contributions $S_{1,2}$ as predicted by CTEQ6L (closed points) and using $S_{1,2} = 0$ (open points). A comparison of the result to CTEQ6L (LO) and MRST04 (LO) is shown for three values of Q^2. The top panel shows the full x range being studied (0.006< x <0.9). The bottom panel focuses on the region $x > 0.15$. For clarity of presentation the open points are shifted to lower values of x.

Chapter 7

Summary

The first measurement of inclusive DIS cross sections on proton and deuteron at the HERMES experiment was presented in this thesis. The stability of yields over time was studied in detail and yield-sensitive systematic effects like trigger efficiencies, PID efficiencies and tracking-related effects were taken into account. Systematic corrections were performed for radiative effects, detector smearing and the acceptance by a MC-based unfolding procedure which was adapted to the requirements of a cross-section measurement. The effects of elastic Bethe-Heitler events in the HERMES detector were taken into account by a Bethe-Heitler efficiency correction in the framework of this unfolding procedure. The effects of misalignment of spectrometer and beam on the measured cross sections were estimated in a conservative manner and found to contribute with a dominant systematic uncertainty exceeding 10% in the limit of small scattering angles, whereas the statistical uncertainty is typically on the one-percent level. The uncertainty due to particle identification exceeds one percent only in the limit of large y. A possible influence of misalignment on Bethe-Heitler efficiencies was studied and the size of the effect was found to be mainly below one percent. The data from different years was combined and compared to world data. The results for both F_2^p and F_2^d are in excellent agreement with world data in overlapping kinematic regions and cover in addition previously unexplored kinematic regions at small x and Q^2.

In the second part of this work, global fits to world data were performed including the new results from HERMES presented in this thesis. A new phenomenological fit of the structure function F_2^p was presented using the functional form first suggested by ALLM, updated with the current world data set of inclusive proton DIS cross sections. The size of the world data set is increased by a factor of two compared to the latest ALLM fit. In contrast to the previous applications of this functional form, the new fit is accurately based on a consistent treatment of the ratio R for all data. Moreover, it involves a determination of fit uncertainties and provides a correlation matrix for the first time.

Furthermore, a fit of the cross section ratio σ^d/σ^p was performed in order to study leading-twist and higher-twist contributions, the Q^2 dependence, the possible difference of R for the proton and deuteron, and to extract the Gottfried integral and the valence quark ratio d_v/u_v. The fit benefits from the reach of the HERMES data towards small values of ϵ and can thereby confirm the agreement of R^p and R^d. The Gottfried integral in the region $0.006 < x < 0.9$ is determined to be 0.228 ± 0.006 at $Q^2 = 4\,\mathrm{GeV}^2$ and agrees with previous measurements by NMC in a similar range of $0.004 < x < 0.8$. This result implies a violation of the Gottfried sum rule and can be interpreted as an excess of $\bar{d}$ quarks over $\bar{u}$ quarks in the nucleon.

Various non-perturbative models such as virtual pion models and the chiral model have been suggested to explain the sea flavor asymmetry. Furthermore, no indication is found for a Q^2 dependence of the Gottfried integral in the range $1\,\mathrm{GeV}^2 < Q^2 < 10\,\mathrm{GeV}^2$.

Appendix A

Yields

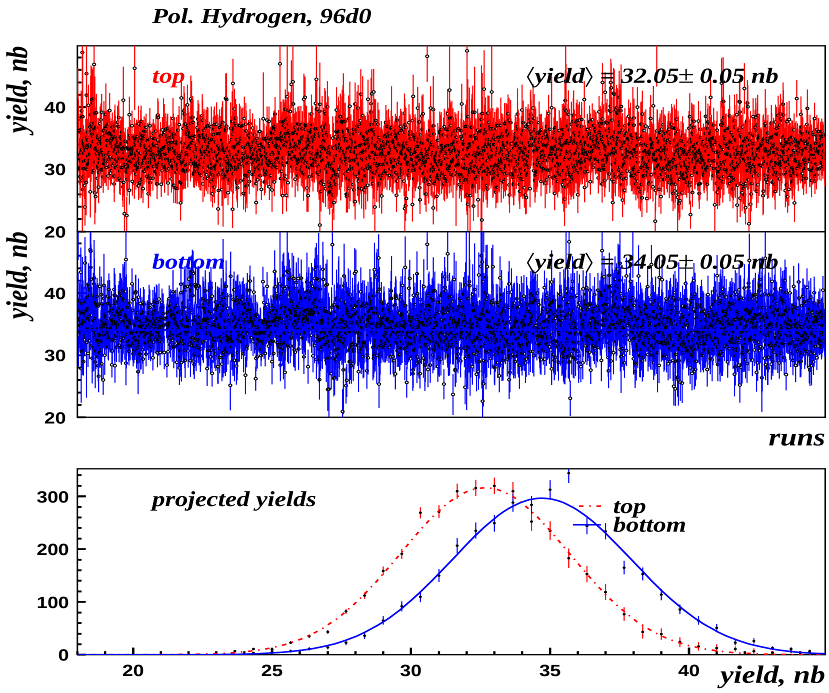

Figure A.1: Yields of DIS events for the runs of the 96d0 production measured on a polarized hydrogen target in the top and the bottom detector. The bottom panel shows the projected distribution of yields.

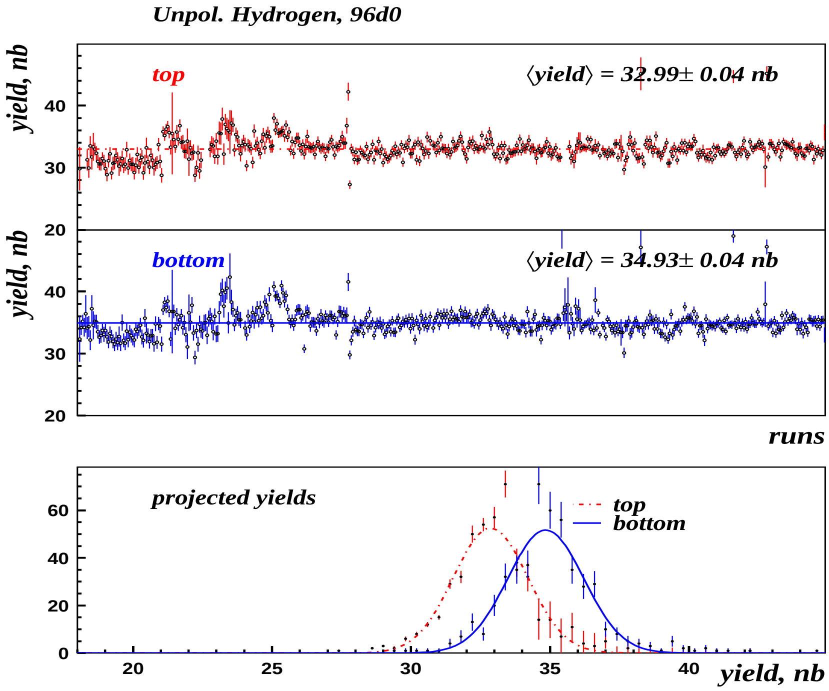

Figure A.2: Yields of DIS events for the runs of the 96d0 production measured on an unpolarized hydrogen target in the top and the bottom detector. The bottom panel shows the projected distribution of yields.

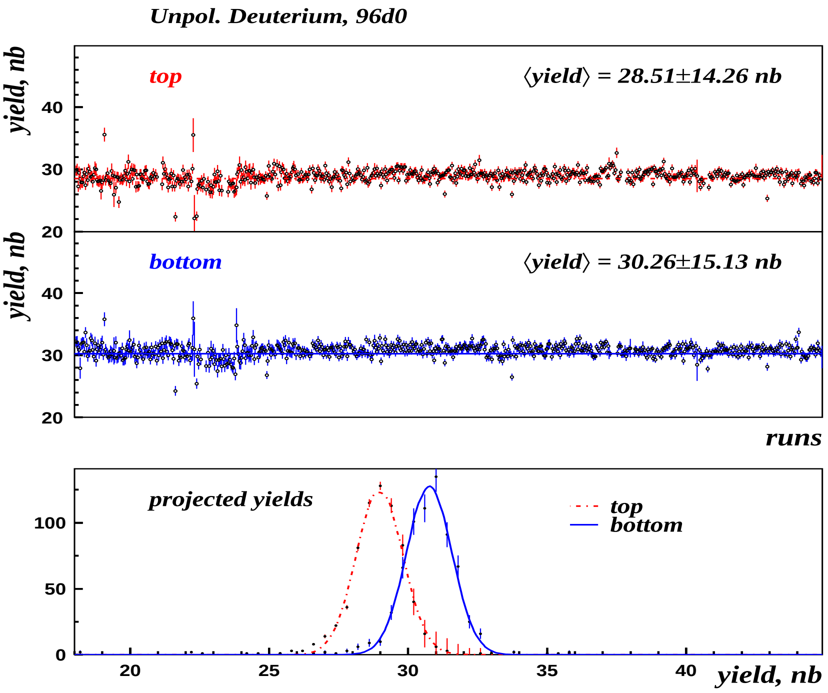

Figure A.3: Yields of DIS events for the runs of the 96d0 production measured on an unpolarized deuterium target in the top and the bottom detector. The bottom panel shows the projected distribution of yields.

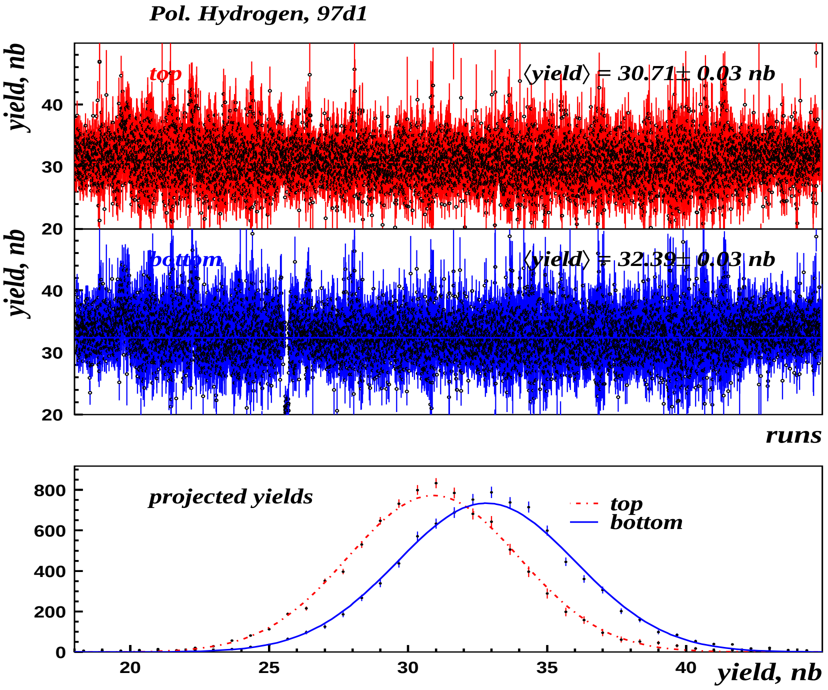

Figure A.4: Yields of DIS events for the runs of the 97d1 production measured on a polarized hydrogen target in the top and the bottom detector. The bottom panel shows the projected distribution of yields.

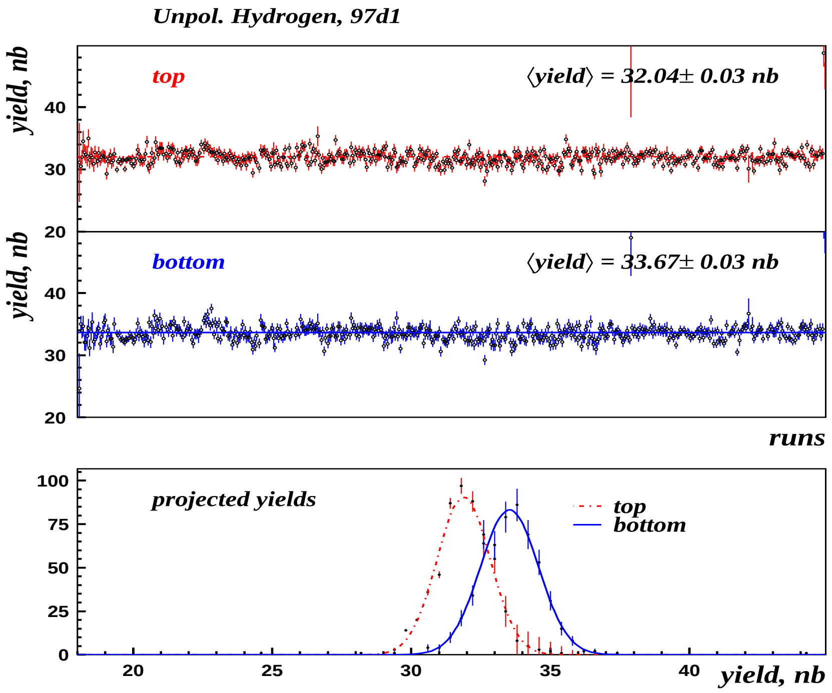

Figure A.5: Yields of DIS events for the runs of the 97d1 production measured on an unpolarized hydrogen target in the top and the bottom detector. The bottom panel shows the projected distribution of yields.

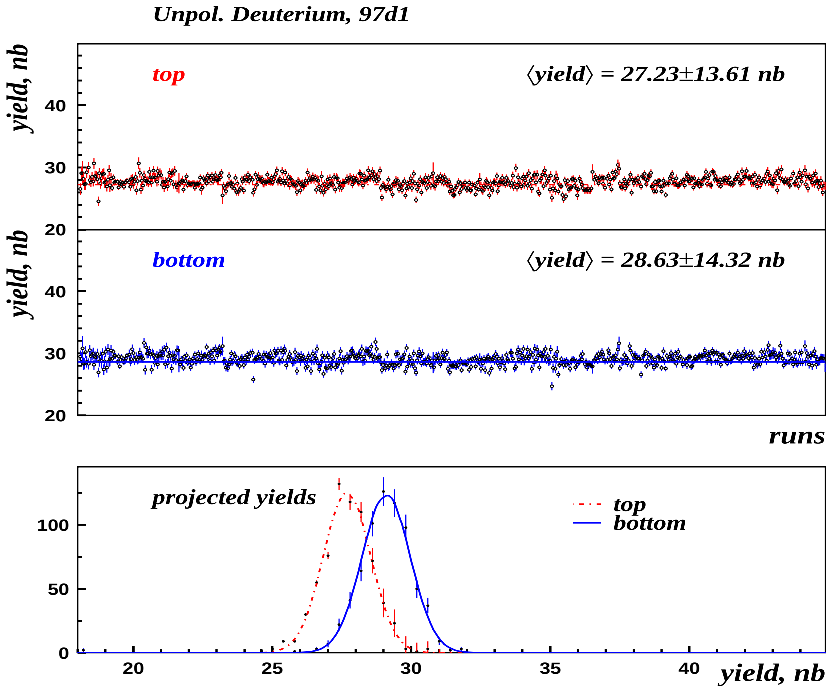

Figure A.6: Yields of DIS events for the runs of the 97d1 production measured on a unpolarized deuterium target in the top and the bottom detector. The bottom panel shows the projected distribution of yields.

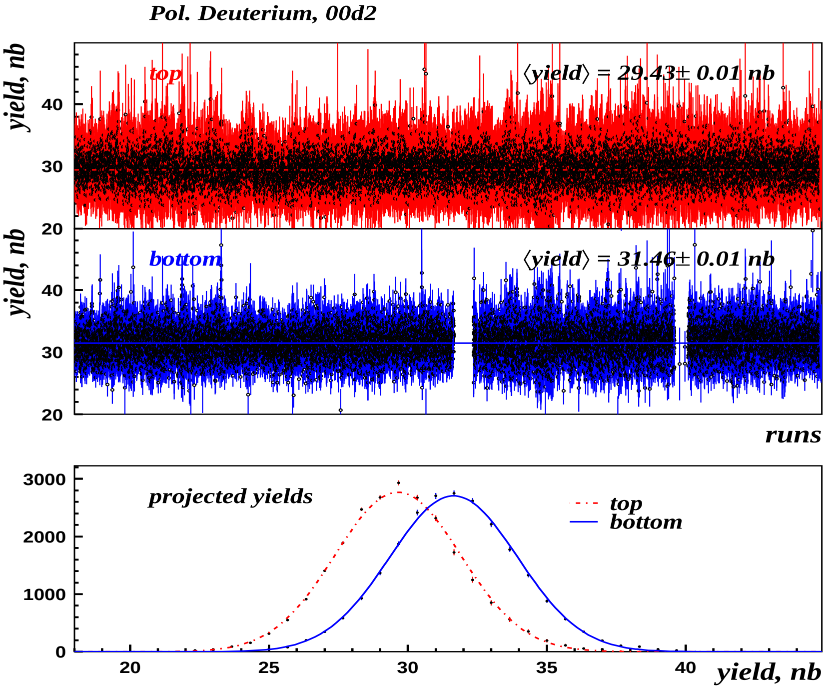

Figure A.7: Yields of DIS events for the runs of the 00d2 production measured on a polarized deuterium target in the top and the bottom detector. The bottom panel shows the projected distribution of yields.

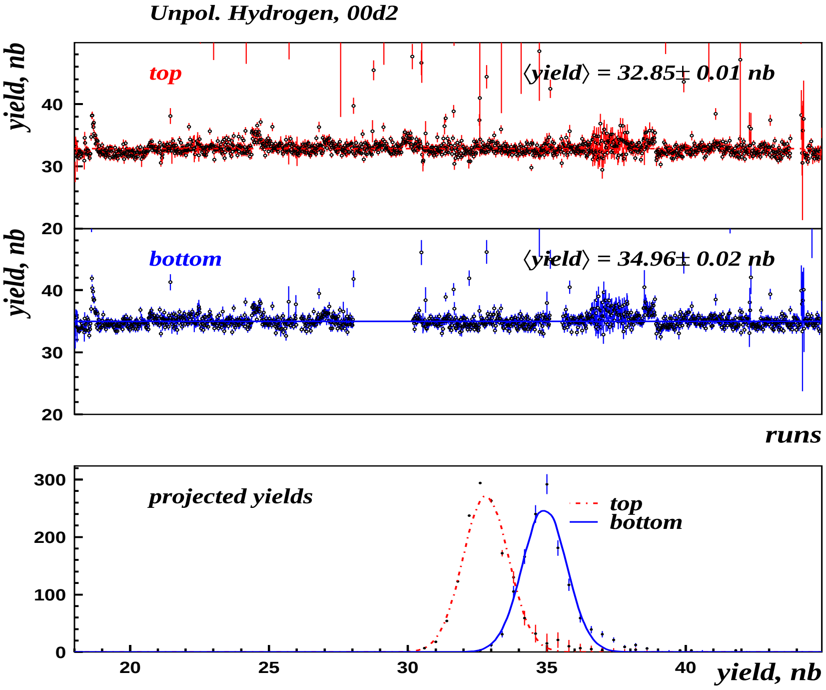

Figure A.8: Yields of DIS events for the runs of the 00d2 production measured on an unpolarized hydrogen target in the top and the bottom detector. The bottom panel shows the projected distribution of yields.

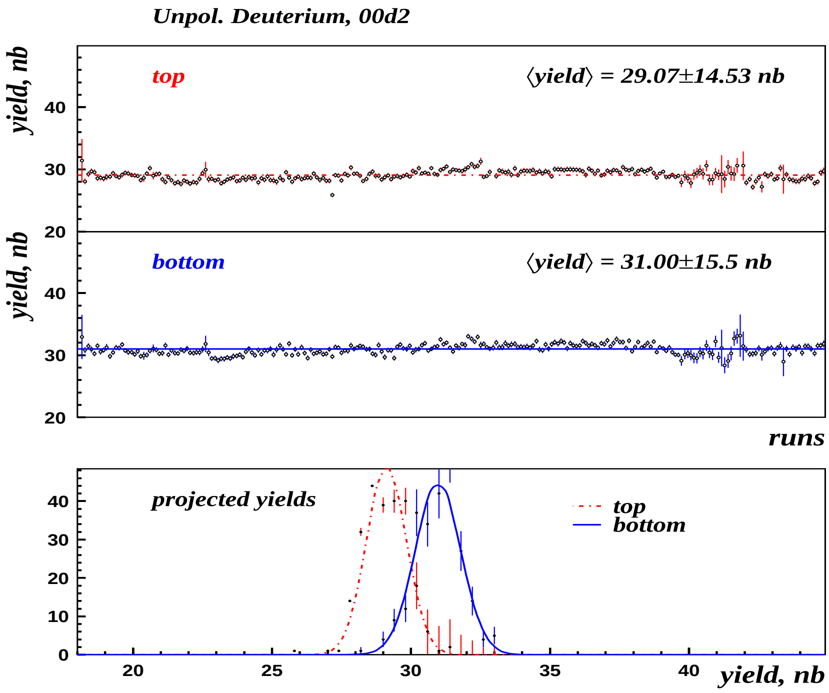

Figure A.9: Yields of DIS events for the runs of the 00d2 production measured on a unpolarized deuterium target in the top and the bottom detector. The bottom panel shows the projected distribution of yields.

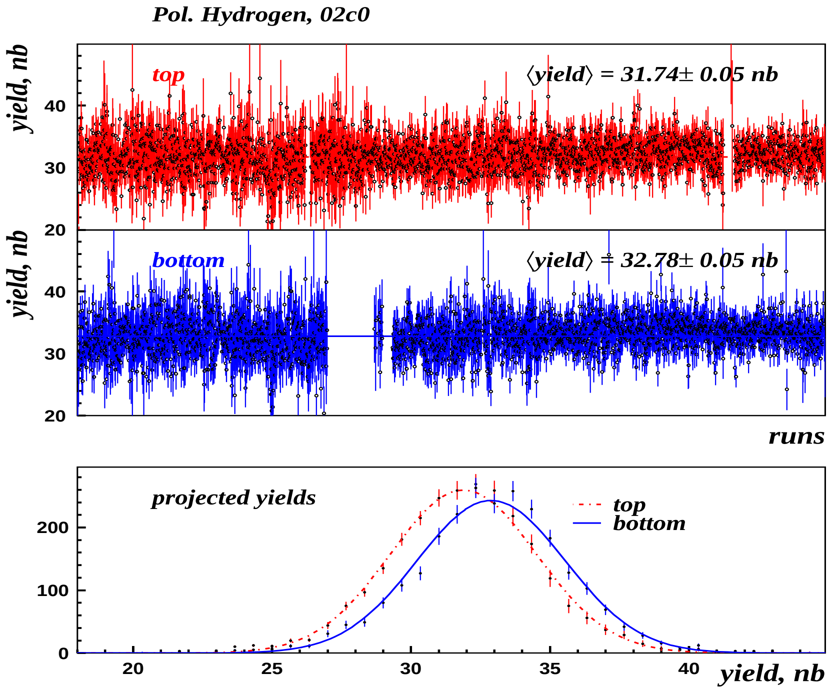

Figure A.10: Yields of DIS events for the runs of the 02c0 production measured on a polarized hydrogen target in the top and the bottom detector. The bottom panel shows the projected distribution of yields.

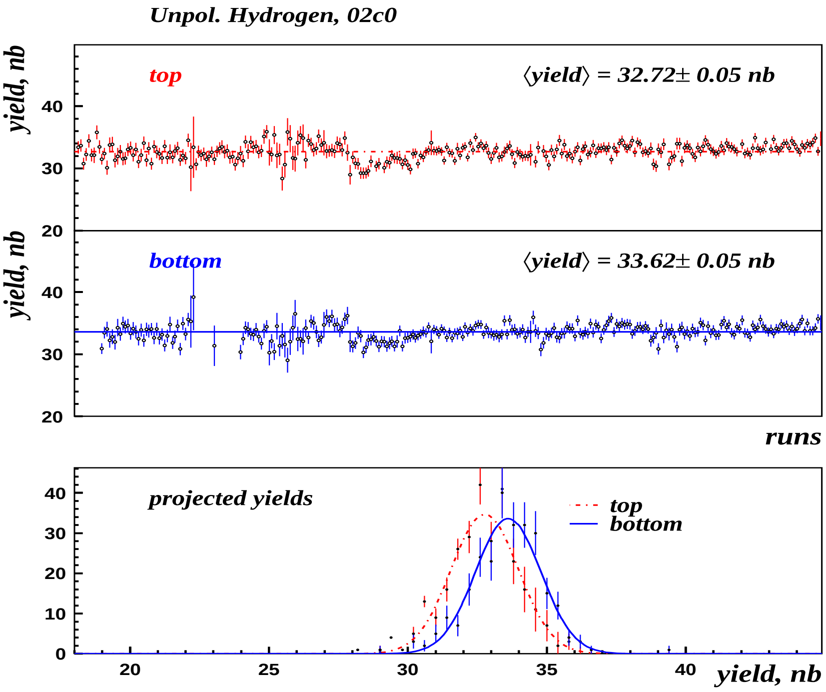

Figure A.11: Yields of DIS events for the runs of the 02c0 production measured on an unpolarized hydrogen target in the top and the bottom detector. The bottom panel shows the projected distribution of yields.

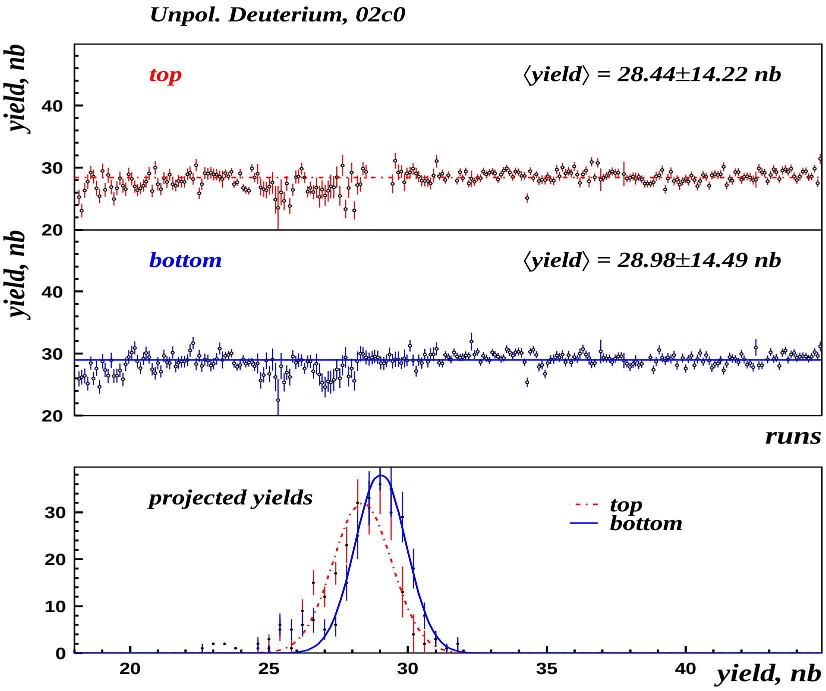

Figure A.12: Yields of DIS events for the runs of the 02c0 production measured on an unpolarized deuterium target in the top and the bottom detector. The bottom panel shows the projected distribution of yields.

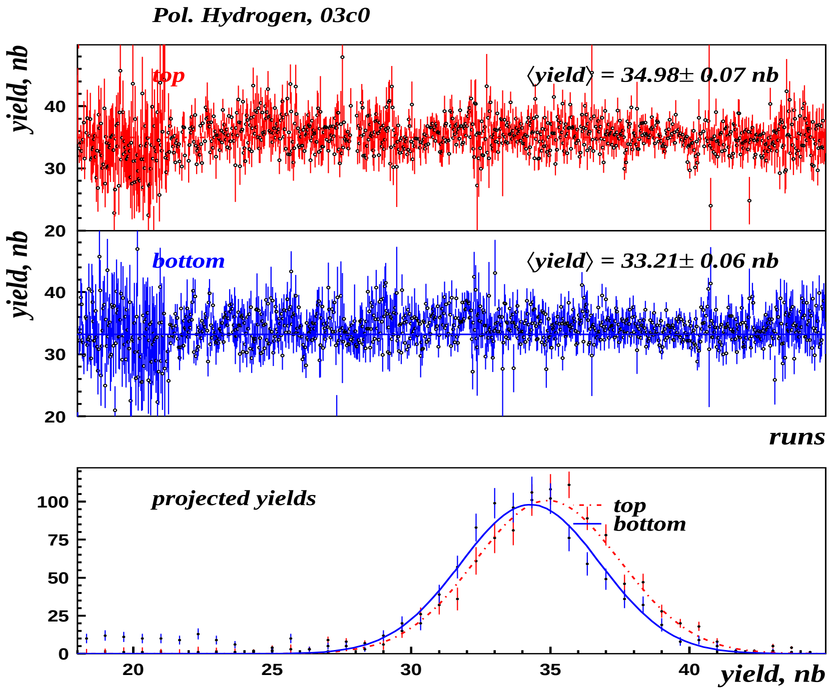

Figure A.13: Yields of DIS events for the runs of the 03c0 production measured on a polarized hydrogen target in the top and the bottom detector. The bottom panel shows the projected distribution of yields.

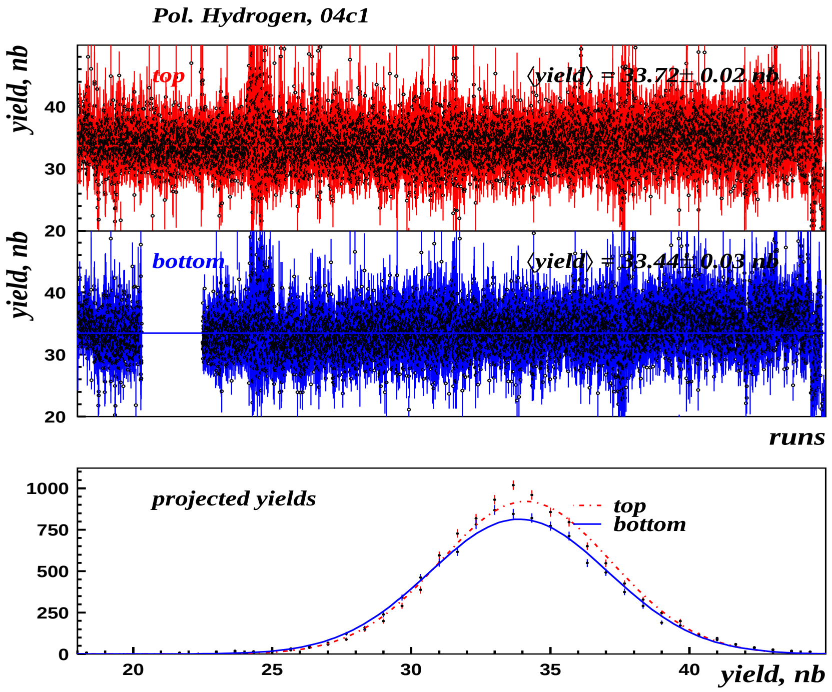

Figure A.14: Yields of DIS events for the runs of the 04c1 production measured on a polarized hydrogen target in the top and the bottom detector. The bottom panel shows the projected distribution of yields.

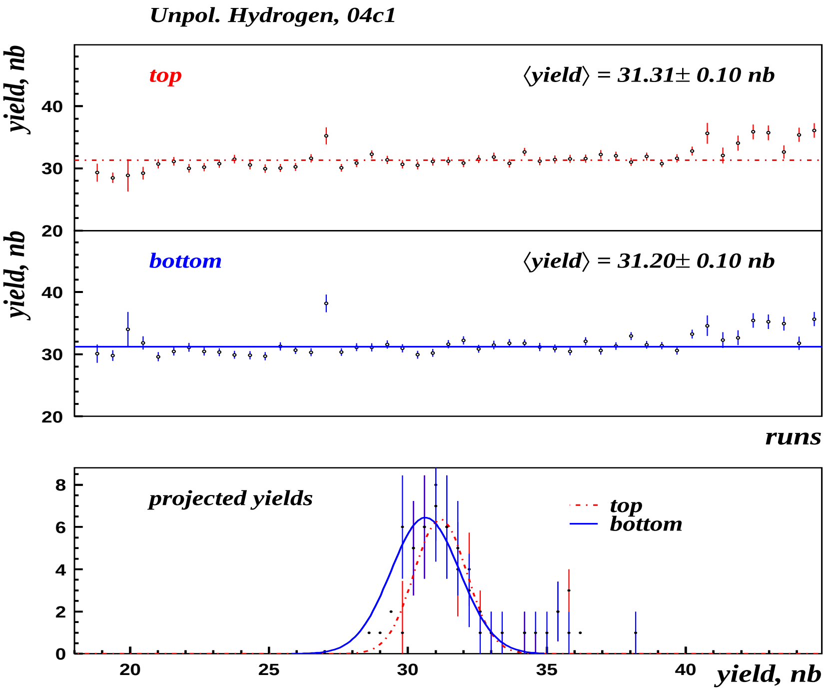

Figure A.15: Yields of DIS events for the runs of the 04c1 production measured on an unpolarized hydrogen target in the top and the bottom detector. The bottom panel shows the projected distribution of yields.

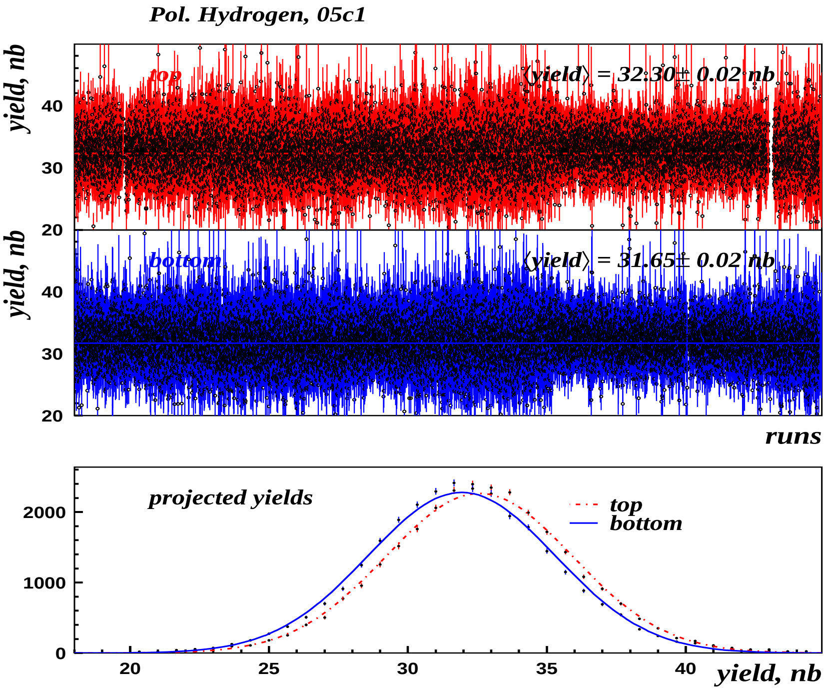

Figure A.16: Yields of DIS events for the runs of the 05c1 production measured on a polarized hydrogen target in the top and the bottom detector. The bottom panel shows the projected distribution of yields.

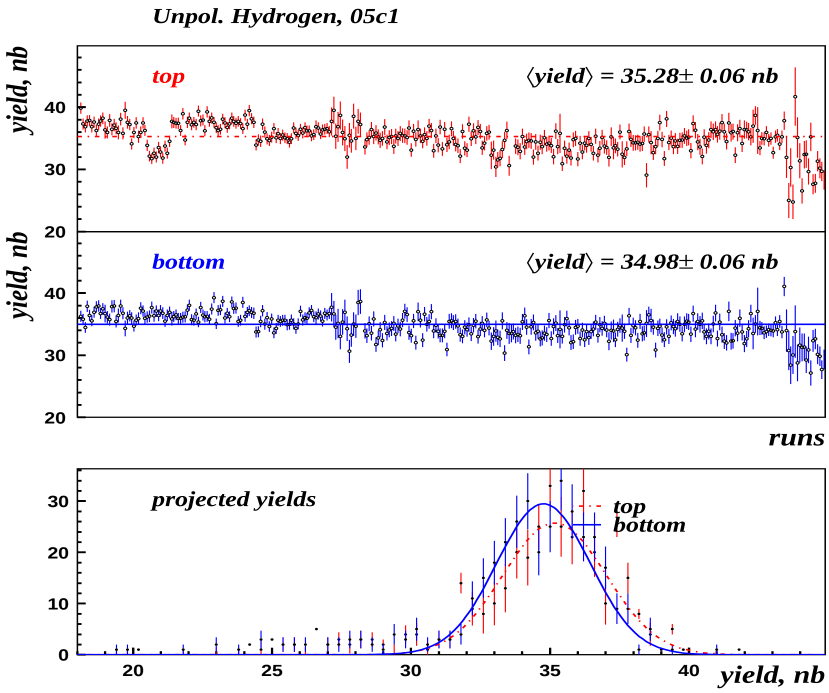

Figure A.17: Yields of DIS events for the runs of the 05c1 production measured on an unpolarized hydrogen target in the top and the bottom detector. The bottom panel shows the projected distribution of yields.

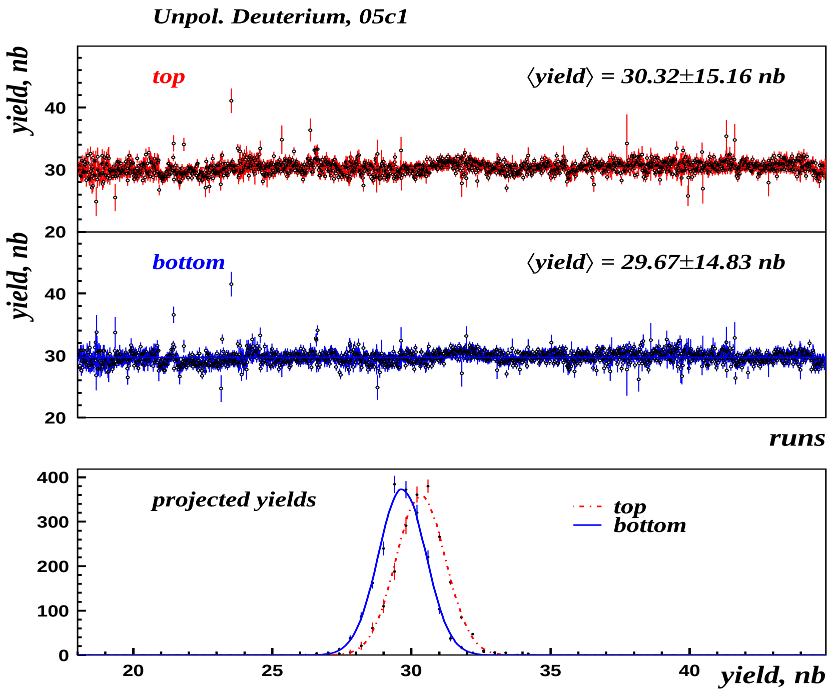

Figure A.18: Yields of DIS events for the runs of the 05c1 production measured on an unpolarized deuterium target in the top and the bottom detector. The bottom panel shows the projected distribution of yields.

Appendix B

The ALLM Parameterization

B.1 Functional Form

$$
\begin{aligned}
F_2(x, Q^2) \quad = \quad & \frac{Q^2}{Q^2 + p_1} \{ \\
& c_P(p_{12}, p_{13}, p_{14}, p_4, p_5) x_P(p_2)^{a_P(p_4,p_5,p_6,p_7,p_8)} (1-x)^{b_P(p_4,p_5,p_9,p_{10},p_{11})} + \\
& c_R(p_{21}, p_{22}, p_{23}, p_4, p_5) x_R(p_3)^{a_R(p_4,p_5,p_{15},p_{16},p_{17})} (1-x)^{b_R(p_4,p_5,p_{18},p_{19},p_{20})} \\
& \}
\end{aligned}
$$

$$
\begin{aligned}
t &= \ln\left[\frac{\ln\left(\frac{Q^2+p_4}{p_5}\right)}{\ln\left(\frac{p_4}{p_5}\right)}\right] \\
x_P &= \left[1 + \frac{W^2 - M^2}{Q^2 + p_2}\right]^{-1} \\
x_R &= \left[1 + \frac{W^2 - M^2}{Q^2 + p_3}\right]^{-1} \\
c_P &= p_{12} + (p_{12} - p_{13})\left(\frac{1}{1 + t^{p_{14}}} - 1\right) \\
a_P &= p_6 + (p_6 - p_7)\left(\frac{1}{1 + t^{p_8}} - 1\right) \\
b_P &= p_9 - p_{10} t^{p_{11}} \\
c_R &= p_{21} - p_{22} t^{p_{23}} \\
a_R &= p_{15} - p_{16} t^{p_{17}} \\
b_R &= p_{18} - p_{19} t^{p_{20}}
\end{aligned}
$$

B.2 Uncertainties

$$\sigma^2(F_2) = \sum_{i,j} \frac{\partial F_2}{\partial p_i}\frac{\partial F_2}{\partial p_j}\sigma(p_i)\sigma(p_j)\cdot corr(p_i,p_j)$$

$$\begin{aligned}
\frac{\partial F_2}{\partial p_1} &= -\frac{1}{Q^2+p_1}\cdot F_2 \\
\frac{\partial F_2}{\partial p_2} &= \frac{Q^2}{Q^2+p_1}\ c_P\ (1-x)^{b_P}\ a_P\ x_P^{a_P+1}\ \frac{W^2-M^2}{(Q^2+p_2)^2} \\
\frac{\partial F_2}{\partial p_3} &= \frac{Q^2}{Q^2+p_1}\ c_R\ (1-x)^{b_R}\ a_R\ x_R^{a_R+1}\ \frac{W^2-M^2}{(Q^2+p_3)^2} \\
\frac{\partial F_2}{\partial p_4} &= -\frac{Q^2}{Q^2+p_1}\left\{ x_P^{a_P}\ (1-x)^{b_P}\ (p_{12}-p_{13})\frac{p_{14}t^{(p_{14}-1)}}{(1+t^{p_{14}})^2}\right. \\
&+\ c_P\ x_P^{a_P}\ (1-x)^{b_P}\ \ln x_P\ (p_6-p_7)\ p_8\ \frac{t^{(p_8-1)}}{(1+t^{p_8})^2} \\
&+\ c_P\ x_P^{a_P}\ (1-x)^{b_P}\ \ln(1-x)\ p_{10}\ p_{11}\ t^{(p_{11}-1)} \\
&+\ x_R^{a_R}\ (1-x)^{b_R}\ p_{22}\ p_{23}\ t^{(p_{23}-1)} \\
&+\ c_R\ x_R^{a_R}\ (1-x)^{b_R}\ \ln x_R\ p_{16}\ p_{17}\ t^{(p_{17}-1)} \\
&+\ \left. c_R\ x_R^{a_R}\ (1-x)^{b_R}\ \ln(1-x)\ p_{19}\ p_{20}\ t^{(p_{20}-1)}\ \right\} \left(\frac{1}{Q^2+p_4}\frac{1}{\ln\left(\frac{Q^2+p_4}{p_5}\right)} - \frac{1}{p_4}\frac{1}{\ln\left(\frac{p_4}{p_5}\right)}\right) \\
\frac{\partial F_2}{\partial p_5} &= -\frac{Q^2}{Q^2+p_1}\left\{ x_P^{a_P}\ (1-x)^{b_P}\ (p_{12}-p_{13})\frac{p_{14}t^{(p_{14}-1)}}{(1+t^{p_{14}})^2}\right. \\
&+\ c_P\ x_P^{a_P}\ (1-x)^{b_P}\ \ln x_P\ (p_6-p_7)\ p_8\ \frac{t^{(p_8-1)}}{(1+t^{p_8})^2} \\
&+\ c_P\ x_P^{a_P}\ (1-x)^{b_P}\ \ln(1-x)\ p_{10}\ p_{11}\ t^{(p_{11}-1)} \\
&+\ x_R^{a_R}\ (1-x)^{b_R}\ p_{22}\ p_{23}\ t^{(p_{23}-1)} \\
&+\ c_R\ x_R^{a_R}\ (1-x)^{b_R}\ \ln x_R\ p_{16}\ p_{17}\ t^{(p_{17}-1)} \\
&+\ \left. c_R\ x_R^{a_R}\ (1-x)^{b_R}\ \ln(1-x)\ p_{19}\ p_{20}\ t^{(p_{20}-1)}\ \right\} \frac{1}{p_5}\left(\frac{1}{\ln\left(\frac{p_4}{p_5}\right)} - \frac{1}{\ln\left(\frac{Q^2+p_4}{p_5}\right)}\right) \\
\frac{\partial F_2}{\partial p_6} &= \frac{Q^2}{Q^2+p_1}\ c_P\ (1-x)^{b_P}\ x_P^{a_P}\ \frac{1}{1+t^{p_8}}\ \ln x_P \\
\frac{\partial F_2}{\partial p_7} &= \frac{Q^2}{Q^2+p_1}\ c_P\ (1-x)^{b_P}\ x_P^{a_P}\ \left(1-\frac{1}{1+t^{p_8}}\right)\ \ln x_P \\
\frac{\partial F_2}{\partial p_8} &= -\frac{Q^2}{Q^2+p_1}\ c_P\ (1-x)^{b_P}\ x_P^{a_P}\ \frac{(p_6-p_7)}{(1+t^{p_8})^2}\ t^{p_8}\ \ln t\ \ln x_P \\
\frac{\partial F_2}{\partial p_9} &= \frac{Q^2}{Q^2+p_1}\ c_P\ x_P^{a_P}\ (1-x)^{b_P}\ \ln(1-x)
\end{aligned}$$

$$
\begin{aligned}
\frac{\partial F_2}{\partial p_{10}} &= -\frac{Q^2}{Q^2+p_1}\ c_P\ x_P^{a_P}\ (1-x)^{b_P}\ t^{p_{11}}\ \ln(1-x) \\
\frac{\partial F_2}{\partial p_{11}} &= -\frac{Q^2}{Q^2+p_1}\ c_P\ x_P^{a_P}\ (1-x)^{b_P}\ \ln(1-x)\ p_{10}\ t^{p_{11}}\ \ln t \\
\frac{\partial F_2}{\partial p_{12}} &= \frac{Q^2}{Q^2+p_1}\ x_P^{a_P}\ (1-x)^{b_P}\ \frac{1}{1+t^{p_{14}}} \\
\frac{\partial F_2}{\partial p13} &= \frac{Q^2}{Q^2+p_1}\ x_P^{a_P}\ (1-x)^{b_P}\ \left(1-\frac{1}{1+t^{p_{14}}}\right) \\
\frac{\partial F_2}{\partial p_{14}} &= -\frac{Q^2}{Q^2+p_1}\ x_P^{a_P}\ (1-x)^{b_P}\ \frac{(p_{12}-p_{13})}{(1+t^{p_{14}})^2}\ t^{p_{14}}\ \ln t \\
\frac{\partial F_2}{\partial p_{15}} &= \frac{Q^2}{Q^2+p_1}\ c_R\ (1-x)^{b_R}\ x_R^{a_R}\ \ln x_R \\
\frac{\partial F_2}{\partial p_{16}} &= -\frac{Q^2}{Q^2+p_1}\ c_R\ (1-x)^{b_R}\ x_R^{a_R}\ \ln x_R\ t^{p_{17}} \\
\frac{\partial F_2}{\partial p_{17}} &= -\frac{Q^2}{Q^2+p_1}\ c_R\ (1-x)^{b_R}\ x_R^{a_R}\ \ln x_R\ p_{16}\ t^{p_{17}}\ \ln t \\
\frac{\partial F_2}{\partial p_{18}} &= \frac{Q^2}{Q^2+p_1}\ c_R\ x_R^{a_R}\ (1-x)^{b_R}\ \ln(1-x) \\
\frac{\partial F_2}{\partial p_{19}} &= -\frac{Q^2}{Q^2+p_1}\ c_R\ x_R^{a_R}\ (1-x)^{b_R}\ \ln(1-x)\ t^{p_{20}} \\
\frac{\partial F_2}{\partial p_{20}} &= -\frac{Q^2}{Q^2+p_1}\ c_R\ x_R^{a_R}\ (1-x)^{b_R}\ \ln(1-x)\ p_{19}\ t^{p_{20}}\ \ln t \\
\frac{\partial F_2}{\partial p_{21}} &= \frac{Q^2}{Q^2+p_1}\ x_R^{a_R}\ (1-x)^{b_R} \\
\frac{\partial F_2}{\partial p_{22}} &= -\frac{Q^2}{Q^2+p_1}\ x_R^{a_R}\ (1-x)^{b_R}\ t^{p_{23}} \\
\frac{\partial F_2}{\partial p_{23}} &= -\frac{Q^2}{Q^2+p_1}\ x_R^{a_R}\ (1-x)^{b_R}\ p_{22}\ t^{p_{23}}\ \ln t
\end{aligned}
$$

Appendix C

The F_2-Binning

x bin	x region	Q^2 bin 1	Q^2 bin 2	Q^2 bin 3	Q^2 bin 4	Q^2 bin 5	Q^2 bin 6
1	0.0060 - 0.0093	0.1 - 0.32	0.32 - 22.0	-	-	-	-
2	0.0093 - 0.0129	0.1 - 0.43	0.43 - 22.0	-	-	-	-
3	0.0129 - 0.0168	0.1 - 0.55	0.55 - 22.0	-	-	-	-
4	0.0168 - 0.0212	0.1 - 0.69	0.69 - 22.0	-	-	-	-
5	0.0212 - 0.0295	0.1 - 0.80	0.80 - 1.0	1.0 - 22.0	-	-	-
6	0.0295 - 0.0362	0.1 - 1.00	1.00 - 1.3	1.3 - 22.0	-	-	-
7	0.0362 - 0.0444	0.1 - 1.00	1.00 - 1.0	1.15 - 1.45	1.45 - 22.0	-	-
8	0.0444 - 0.0540	0.1 - 1.00	1.00 - 1.25	1.25 - 1.70	1.70 - 22.0	-	-
9	0.0540 - 0.0657	1.0 - 1.20	1.20 - 1.37	1.37 - 1.57	1.57 - 1.78	1.78 - 2.04	2.04 - 22.0
10	0.0657 - 0.0800	1.0 - 1.24	1.24 - 1.48	1.48 - 1.78	1.78 - 2.09	2.09 - 2.49	2.49 - 22.0
11	0.0800 - 0.0976	1.0 - 1.30	1.30 - 1.50	1.50 - 1.90	1.90 - 2.28	2.28 - 2.95	2.95 - 22.0
12	0.0976 - 0.1198	1.0 - 1.34	1.34 - 1.78	1.78 - 2.27	2.27 - 2.76	2.76 - 3.46	3.46 - 22.0
13	0.1198 - 0.1483	1.0 - 1.42	1.42 - 1.86	1.86 - 2.50	2.50 - 3.13	3.13 - 4.02	4.02 - 22.0
14	0.1483 - 0.1861	1.0 - 1.53	1.53 - 2.13	2.13 - 2.84	2.84 - 3.60	3.60 - 4.58	4.58 - 22.0
15	0.1861 - 0.2382	1.0 - 1.70	1.70 - 2.46	2.46 - 3.31	3.31 - 4.17	4.17 - 5.33	5.33 - 22.0
16	0.2382 - 0.3128	1.0 - 2.03	2.03 - 3.00	3.00 - 4.05	4.05 - 5.08	5.08 - 6.39	6.39 - 22.0
17	0.3128 - 0.4251	1.0 - 3.24	3.24 - 4.46	4.46 - 5.92	5.92 - 7.87	7.87 - 22.0	-
18	0.4251 - 0.6027	1.0 - 5.10	5.10 - 7.10	7.10 - 9.85	9.85 - 22.0	-	-
19	0.6027 - 0.9000	1.0 - 10.8	10.8 - 22.0	-	-	-	-

Table C.1: Binning used in this analysis. Q^2 bin limits are in GeV^2. Note that the subdivision into Q^2-bins is different in each x-bin in terms of bin limits and the number of bins. The total number of bins is 81.

Appendix D

Results

D.1 F_2^p

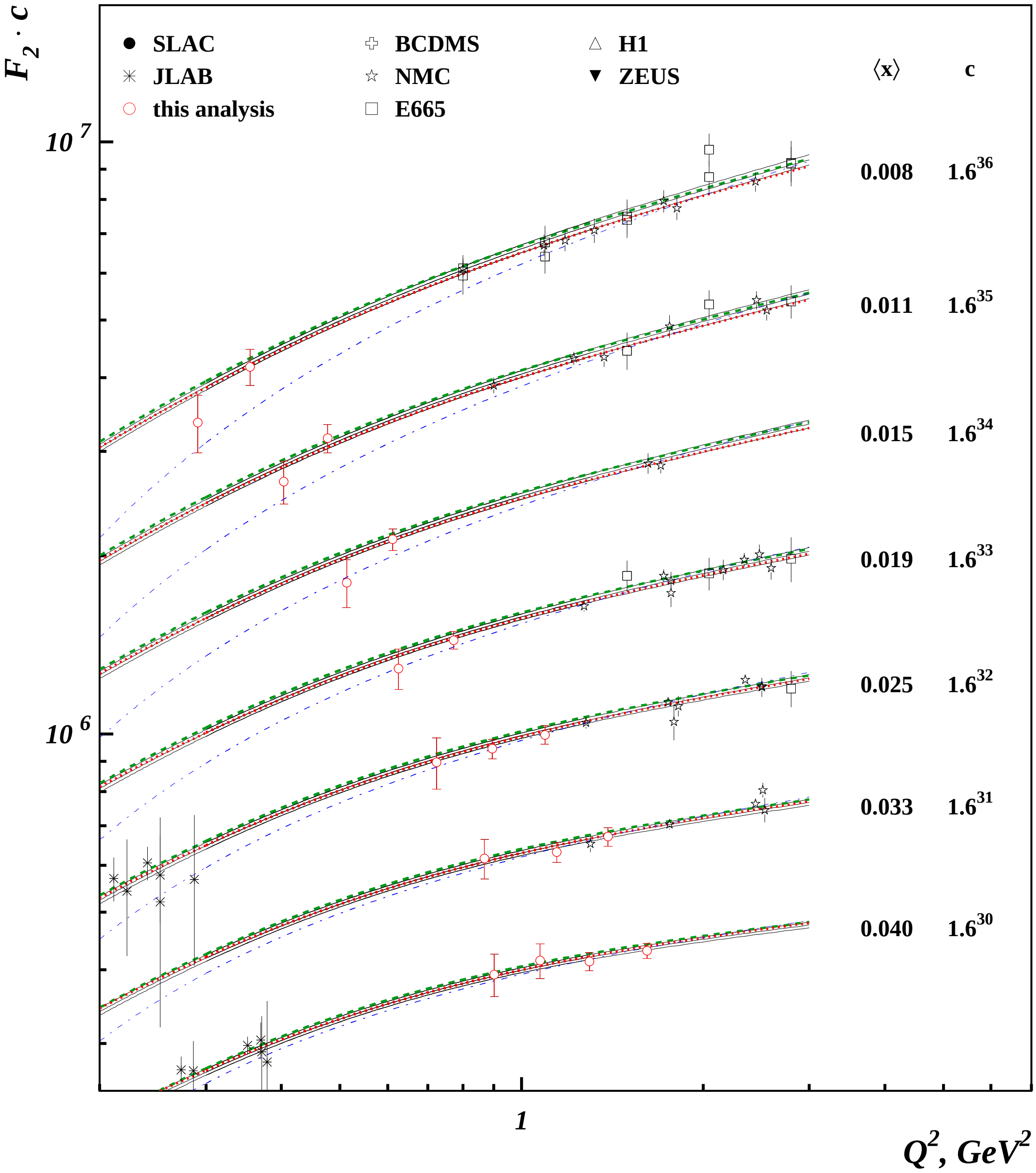

Figure D.1: See the caption of Figure 5.1 for details.

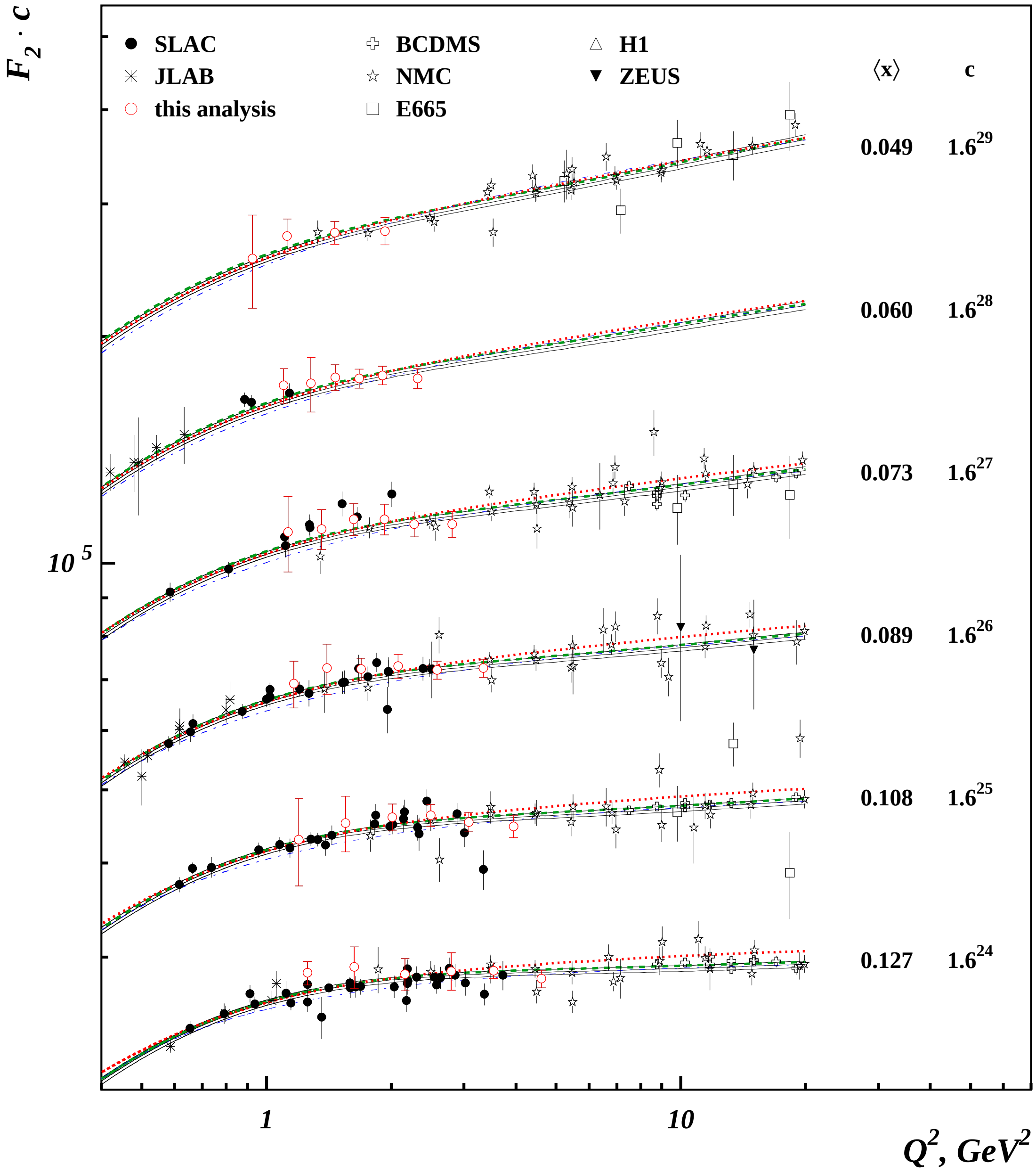

Figure D.2: See the caption of Figure 5.1 for details.

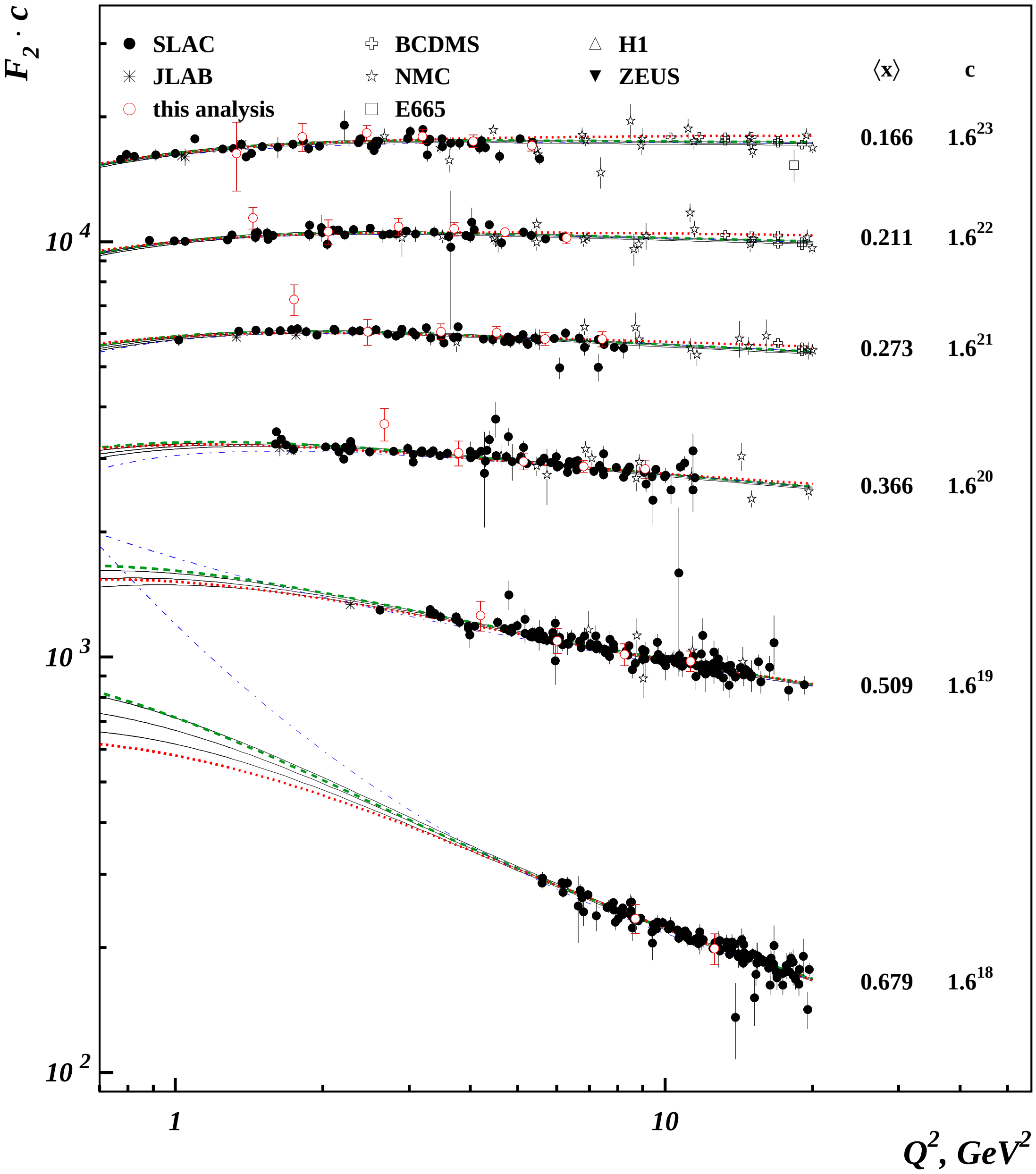

Figure D.3: See the caption of Figure 5.1 for details.

D.2 F_2^d

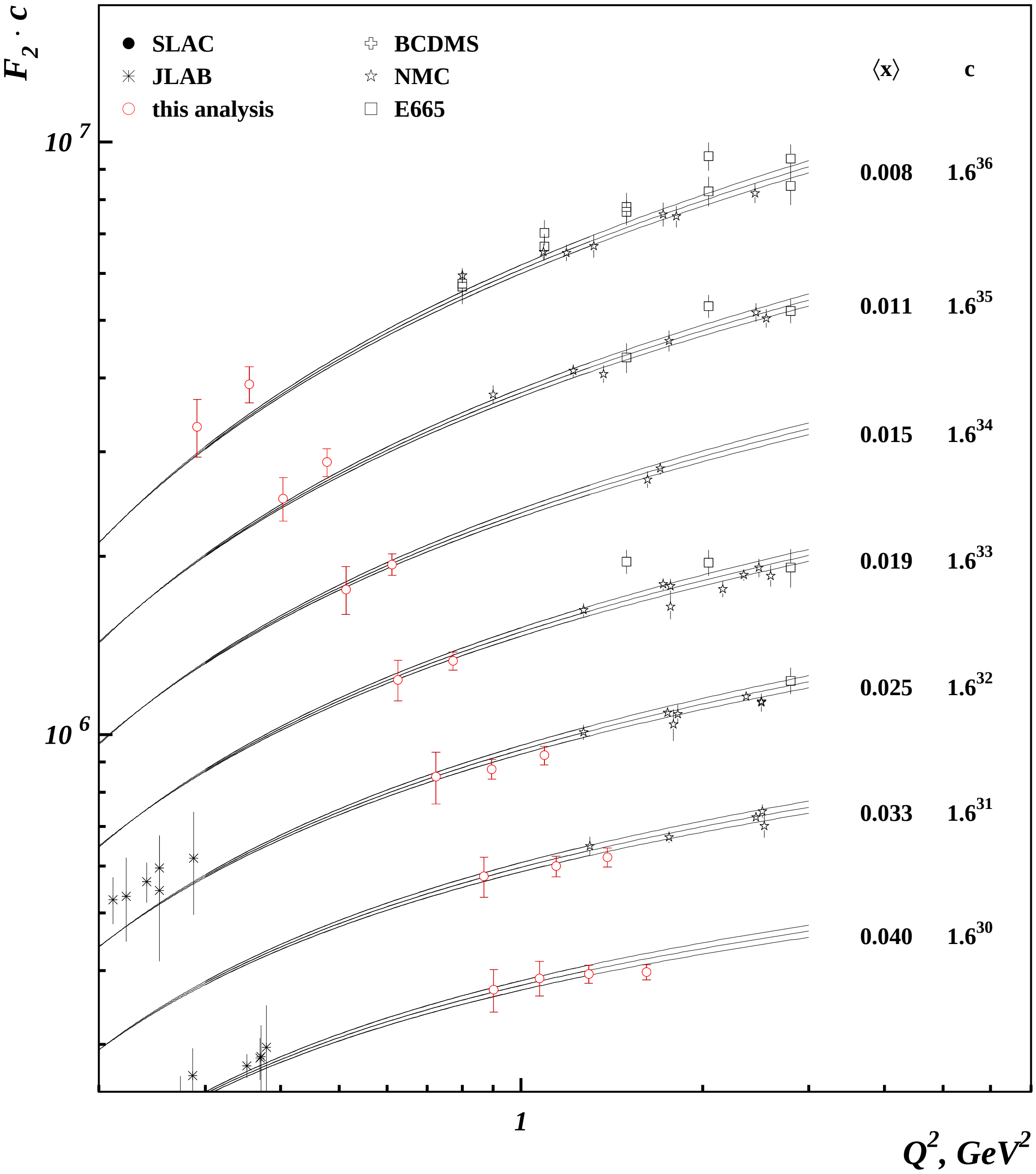

Figure D.4: See the caption of Figure 5.2 for details.

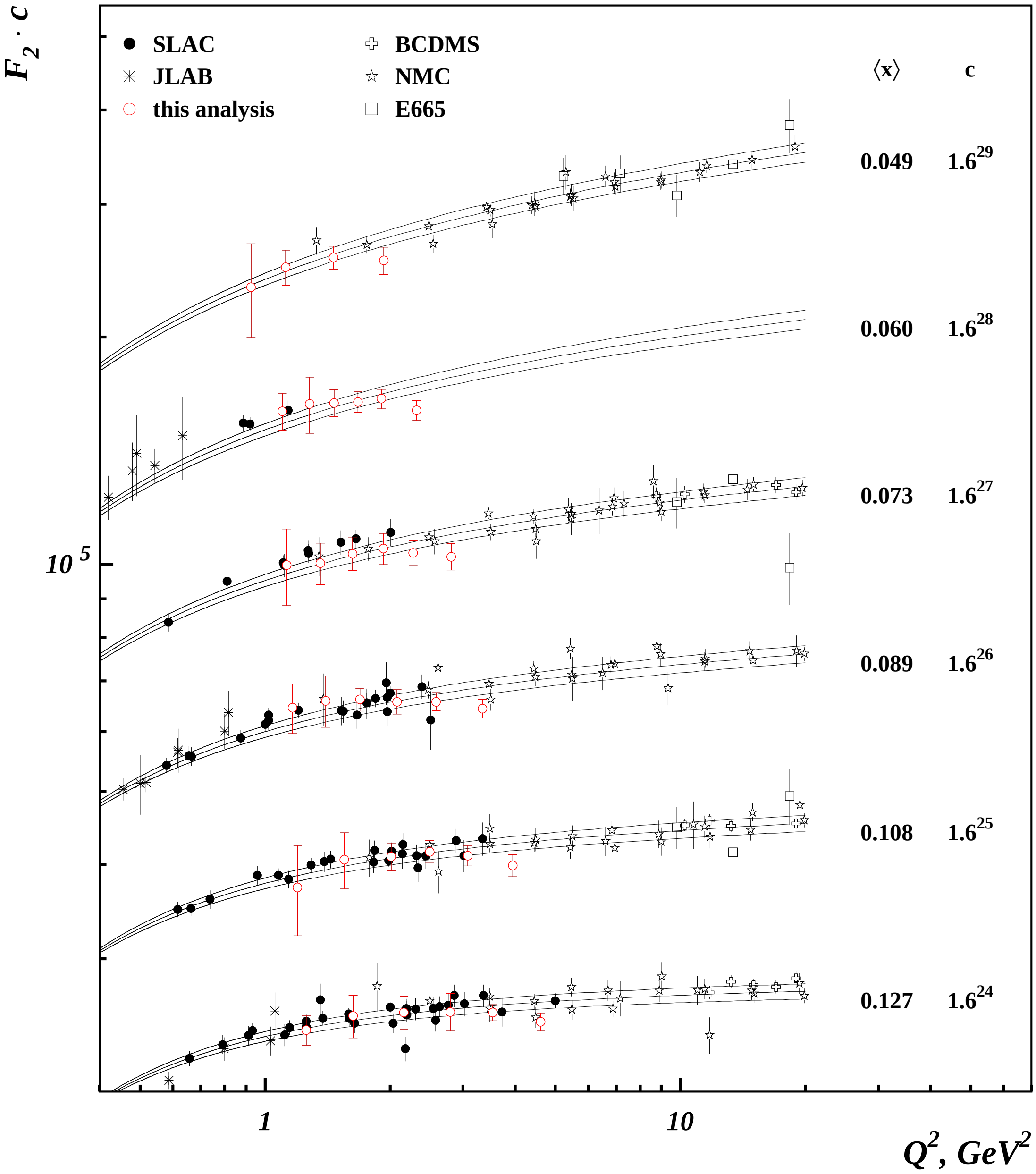

Figure D.5: See the caption of Figure 5.2 for details.

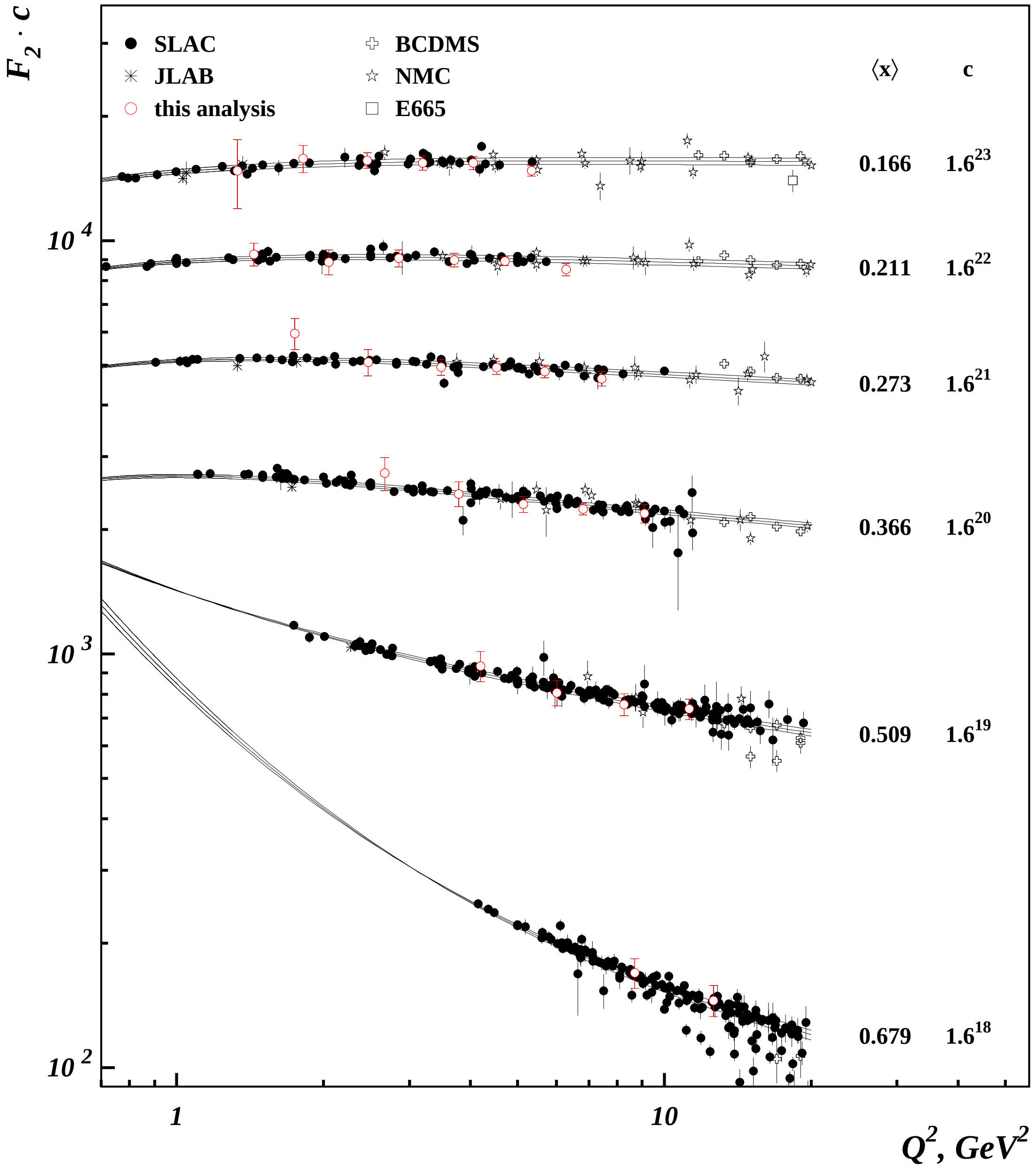

Figure D.6: See the caption of Figure 5.2 for details.

D.3 σ^d/σ^p

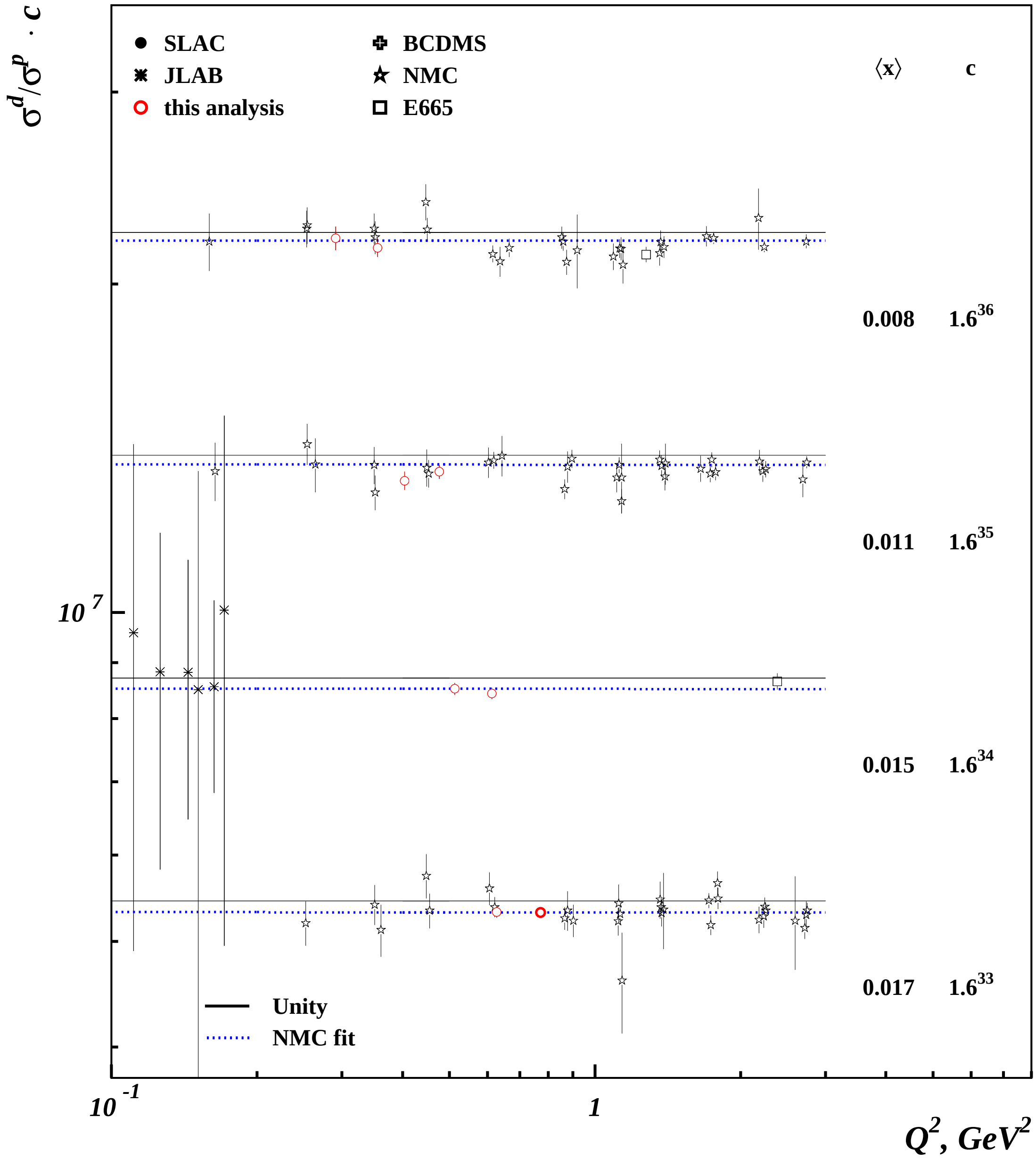

Figure D.7: See the caption of Figure 5.3 for details.

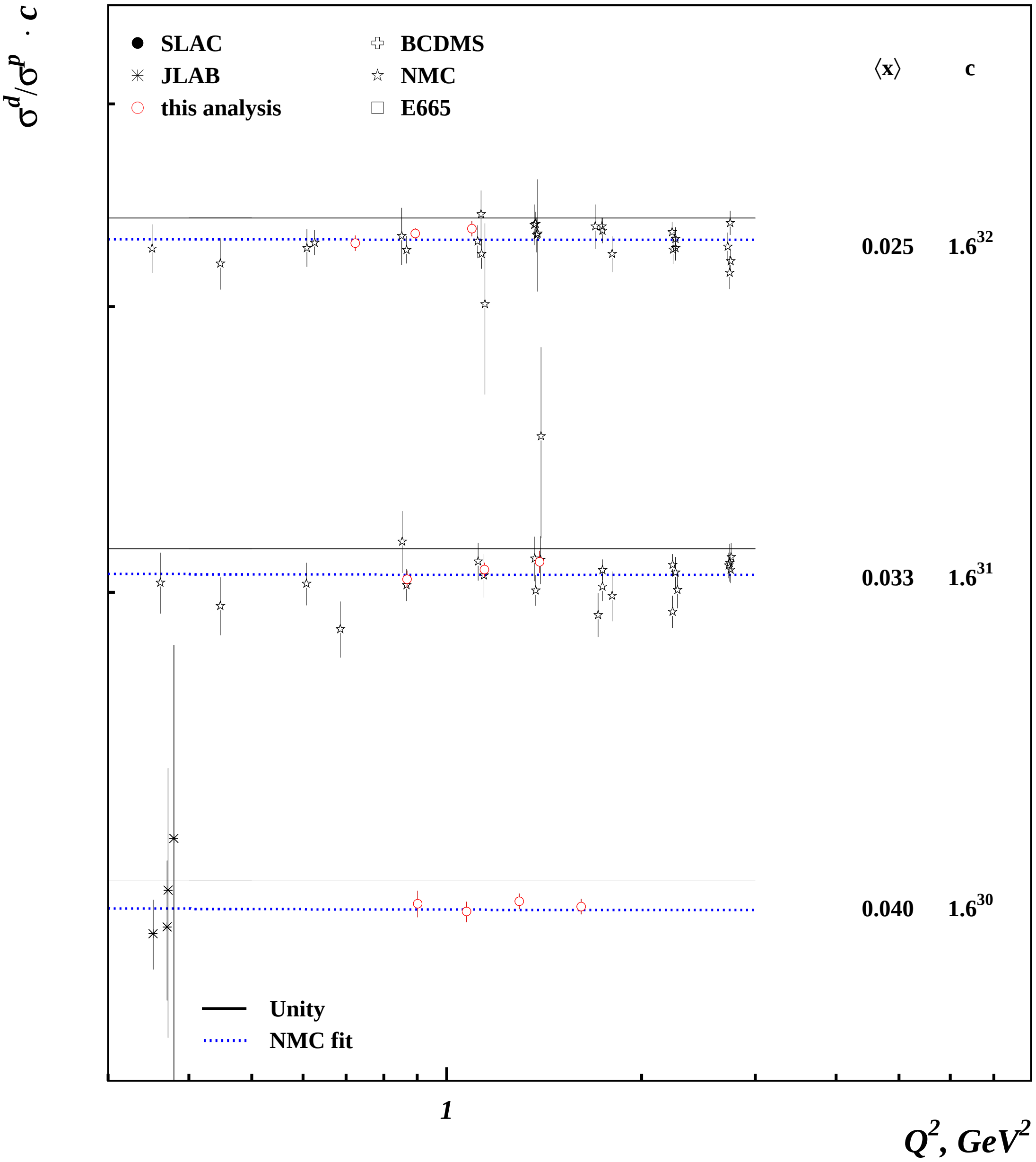

Figure D.8: See the caption of Figure 5.3 for details.

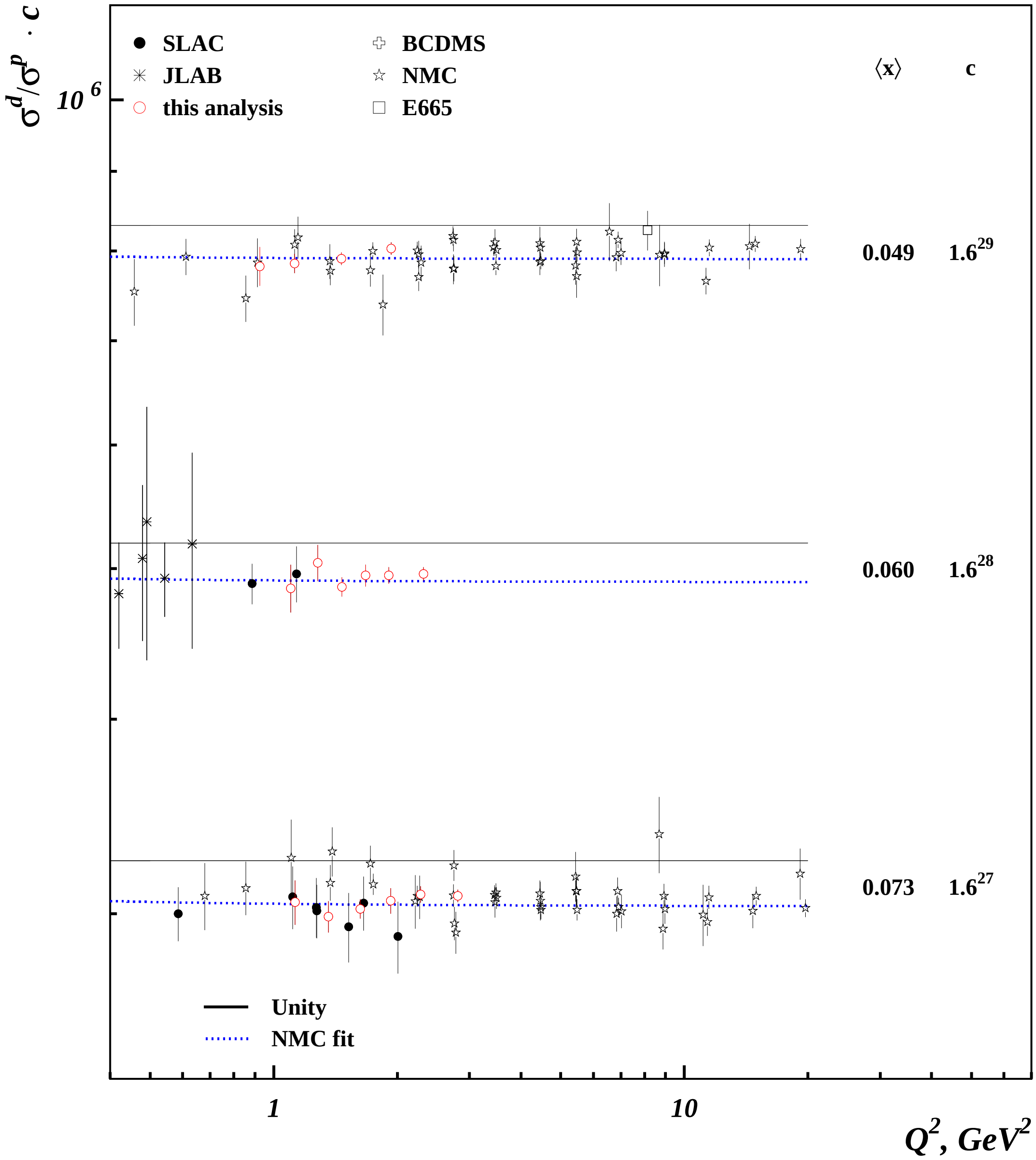

Figure D.9: See the caption of Figure 5.3 for details.

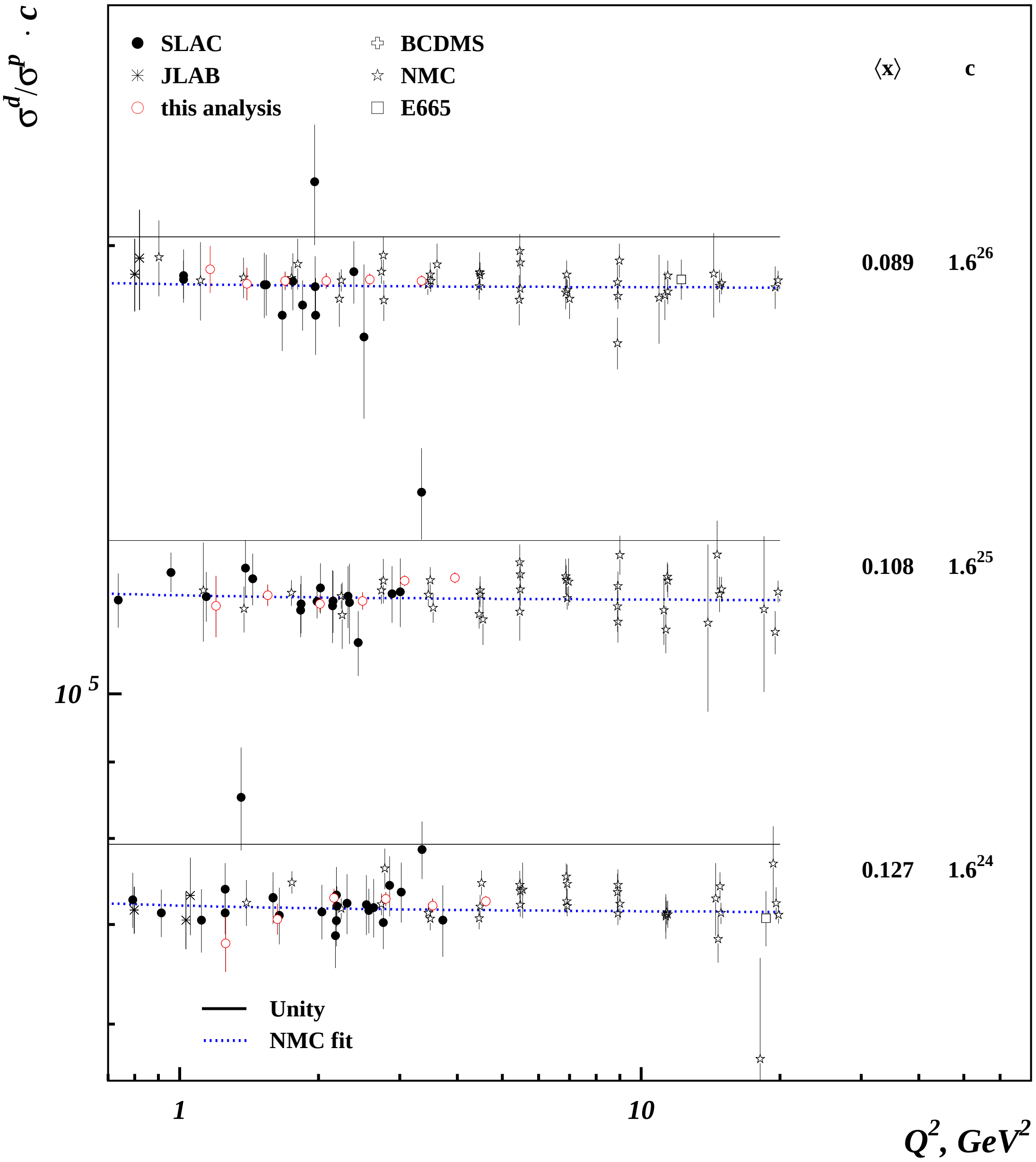

Figure D.10: See the caption of Figure 5.3 for details.

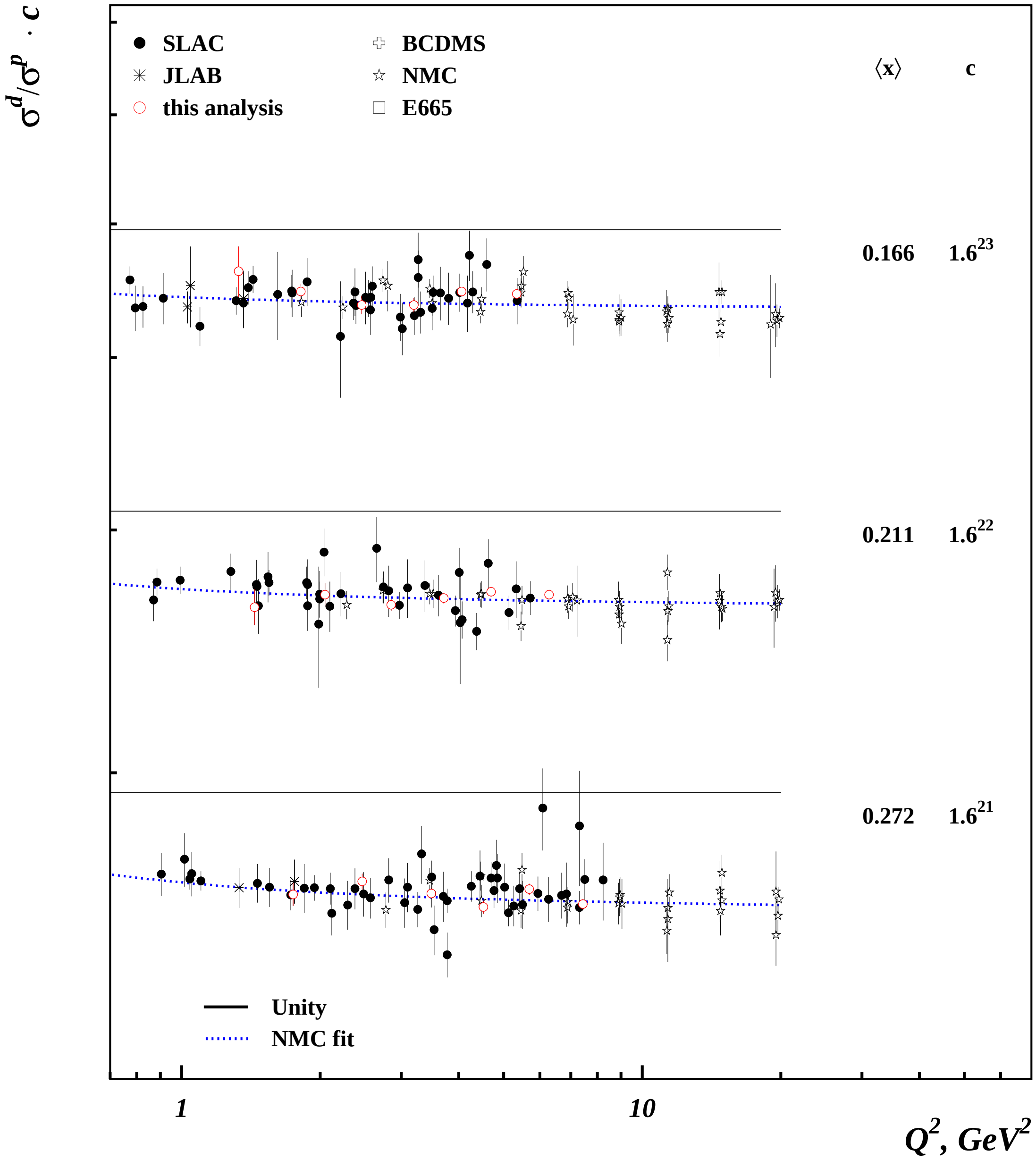

Figure D.11: See the caption of Figure 5.3 for details.

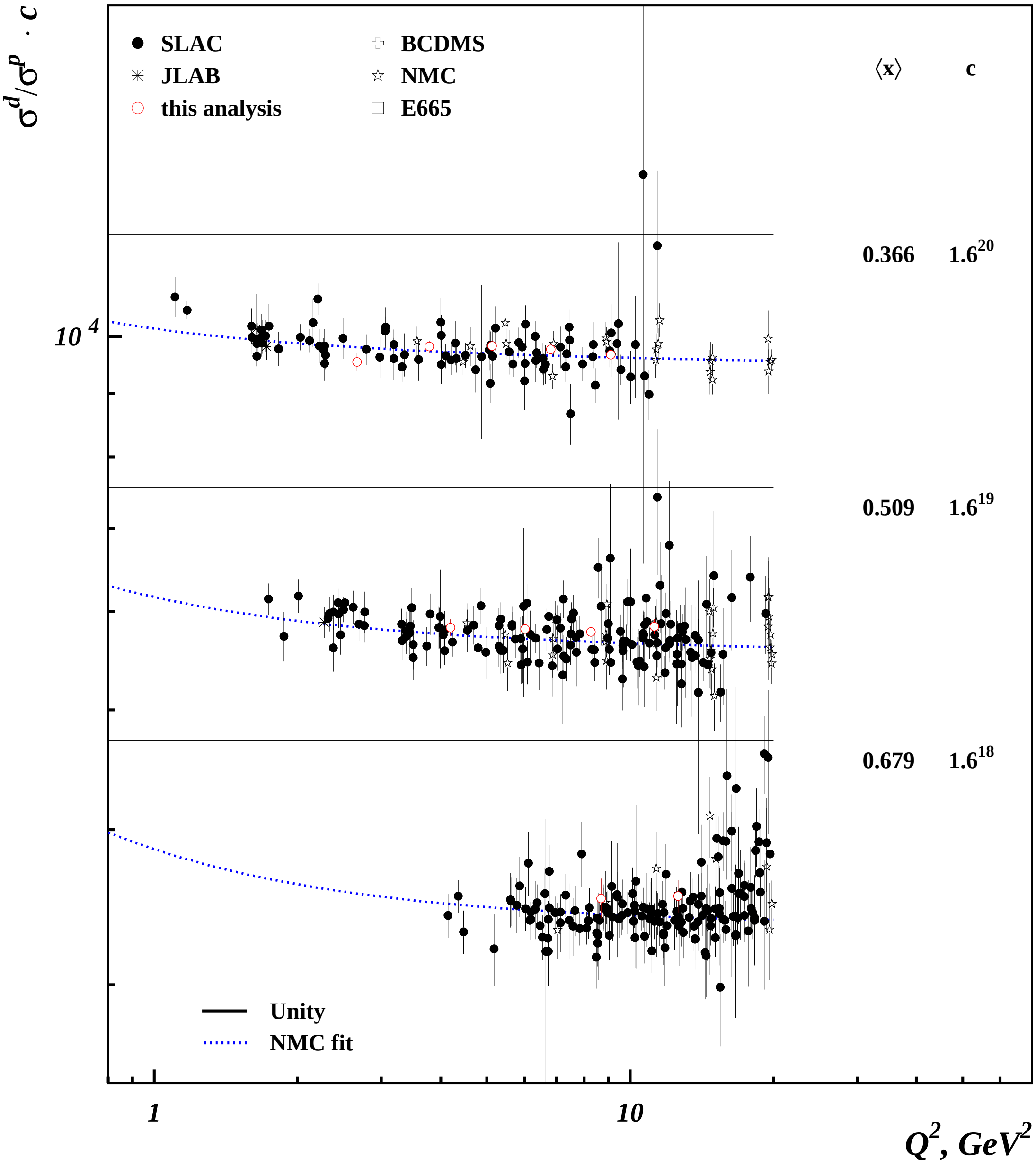

Figure D.12: See the caption of Figure 5.3 for details.

Appendix E

Tables

x bin	Q^2 bin	$\bar{x}$	$\bar{Q^2}$	$\frac{d^2\sigma^p}{dx\,dQ^2}$	F_2^p	$\delta_{stat.}$	$\delta_{mis.}$	$\delta_{rad.}$	δ_{PID}
1	1	0.0069	0.291	$2.86\cdot10^4$	0.144	1.15	11.05	1.75	0.69
2	1	0.0102	0.404	$1.30\cdot10^4$	0.183	0.99	8.32	0.48	0.87
3	1	0.0142	0.513	$6.69\cdot10^3$	0.198	0.68	9.19	0.08	0.61
4	1	0.0186	0.626	$4.14\cdot10^3$	0.227	0.70	7.80	0.10	0.36
5	1	0.0244	0.723	$2.82\cdot10^3$	0.252	0.59	9.98	0.24	0.10
6	1	0.0325	0.869	$1.72\cdot10^3$	0.278	0.62	7.71	0.39	0.01
7	1	0.0398	0.902	$1.44\cdot10^3$	0.283	0.92	8.17	0.71	0.05
8	1	0.0486	0.925	$1.24\cdot10^3$	0.293	1.49	14.08	0.27	0.07
9	1	0.0595	1.102	$7.97\cdot10^2$	0.318	1.72	5.21	0.60	0.05
10	1	0.0723	1.127	$6.70\cdot10^2$	0.325	1.70	11.44	0.71	0.06
11	1	0.0882	1.164	$5.46\cdot10^2$	0.327	1.75	7.13	0.67	0.07
12	1	0.1078	1.198	$4.35\cdot10^2$	0.325	2.44	13.28	0.54	0.07
13	1	0.1330	1.257	$3.54\cdot10^2$	0.346	2.11	3.48	0.83	0.07
14	1	0.1660	1.331	$2.35\cdot10^2$	0.316	1.96	18.88	1.27	0.06
15	1	0.2091	1.439	$1.81\cdot10^2$	0.354	1.50	5.97	0.62	0.06
16	1	0.2635	1.747	$1.02\cdot10^2$	0.365	0.90	8.58	0.55	0.05
17	1	0.3480	2.669	$2.61\cdot10^1$	0.301	0.94	9.12	0.15	0.05
18	1	0.4606	4.196	$5.05\cdot10^0$	0.190	0.84	8.27	0.08	0.04
19	1	0.6348	8.693	$2.73\cdot10^{-1}$	0.064	1.99	7.91	0.06	0.08
1	2	0.0085	0.355	$1.99\cdot10^4$	0.180	1.04	6.81	1.35	0.93
2	2	0.0117	0.477	$9.30\cdot10^3$	0.218	0.63	5.15	1.44	1.22
3	2	0.0152	0.612	$4.80\cdot10^3$	0.235	0.51	3.87	0.76	1.50
4	2	0.0193	0.772	$2.57\cdot10^3$	0.254	0.52	2.87	0.51	1.80
5	2	0.0250	0.895	$1.65\cdot10^3$	0.266	0.42	3.57	0.41	1.07
6	2	0.0327	1.144	$8.49\cdot10^2$	0.285	0.52	3.80	0.15	0.92
7	2	0.0401	1.074	$9.80\cdot10^2$	0.299	0.79	6.66	0.15	0.01
8	2	0.0490	1.123	$8.37\cdot10^2$	0.314	0.76	5.31	0.23	0.03
9	2	0.0596	1.282	$5.49\cdot10^2$	0.320	1.45	8.34	0.56	0.06
10	2	0.0725	1.359	$4.49\cdot10^2$	0.328	1.28	6.10	0.40	0.06
11	2	0.0884	1.400	$3.71\cdot10^2$	0.343	1.39	7.66	0.14	0.06
12	2	0.1080	1.552	$2.57\cdot10^2$	0.342	0.89	8.52	0.15	0.06
13	2	0.1335	1.630	$2.00\cdot10^2$	0.352	1.26	6.25	0.35	0.06
14	2	0.1662	1.814	$1.35\cdot10^2$	0.346	0.75	7.58	0.14	0.05
15	2	0.2103	2.051	$7.96\cdot10^1$	0.328	1.05	6.78	0.26	0.05
16	2	0.2728	2.467	$3.95\cdot10^1$	0.301	0.75	7.20	0.17	0.05
17	2	0.3628	3.784	$9.91\cdot10^0$	0.248	0.62	6.91	0.06	0.04
18	2	0.4901	6.018	$1.71\cdot10^0$	0.150	0.47	6.89	0.02	0.04
19	2	0.6588	12.612	$7.83\cdot10^{-1}$	0.047	1.64	8.45	0.10	0.05

Table E.1: Results on the differential BORN cross section $\frac{d\sigma^p}{dx\,dQ^2}$ (nbarn) and F_2^p. The statistical uncertainty $\delta_{stat.}$, and the systematic uncertainties $\delta_{mis.}$ (misalignment), $\delta_{rad.}$ (Bethe-Heitler efficiencies), δ_{PID} (particle identification) are given in %. Corresponding x bin numbers and Q^2 bin numbers and the average values $\bar{x}$ and $\bar{Q^2}$ (GeV^2) are listed in the first four columns. The overall normalization uncertainty is 6.4%. The fit to world data described in Chapter 6.1 reveals a correction factor of 1.043 due to normalization which has not been included in this table.

x bin	Q^2 bin	$\bar{x}$	$\bar{Q^2}$	$\frac{d^2\sigma^p}{dx\,dQ^2}$	F_2^p	$\delta_{stat.}$	$\delta_{mis.}$	$\delta_{rad.}$	δ_{PID}
5	3	0.0270	1.093	$1.01\cdot10^{3}$	0.282	0.57	2.59	0.18	2.39
6	3	0.0338	1.391	$5.27\cdot10^{2}$	0.303	0.83	1.99	0.29	2.98
7	3	0.0401	1.295	$6.11\cdot10^{2}$	0.298	0.61	3.43	0.17	0.38
8	3	0.0490	1.462	$4.32\cdot10^{2}$	0.317	0.51	3.49	0.12	0.17
9	3	0.0596	1.465	$4.02\cdot10^{2}$	0.326	0.81	3.92	0.45	0.01
10	3	0.0726	1.626	$2.93\cdot10^{2}$	0.338	0.79	4.86	0.25	0.04
11	3	0.0884	1.691	$2.40\cdot10^{2}$	0.342	0.80	3.34	0.06	0.05
12	3	0.1081	2.014	$1.45\cdot10^{2}$	0.348	0.69	4.10	0.06	0.05
13	3	0.1334	2.162	$1.05\cdot10^{2}$	0.344	0.77	4.92	0.15	0.05
14	3	0.1660	2.460	$6.86\cdot10^{1}$	0.354	0.84	4.16	0.12	0.05
15	3	0.2103	2.851	$3.95\cdot10^{1}$	0.337	0.55	4.65	0.06	0.04
16	3	0.2725	3.481	$1.85\cdot10^{1}$	0.302	0.50	4.41	0.09	0.04
17	3	0.3623	5.135	$4.88\cdot10^{0}$	0.237	0.46	4.48	0.02	0.04
18	3	0.4966	8.265	$7.52\cdot10^{-1}$	0.136	0.51	6.09	0.00	0.05
7	4	0.0409	1.615	$3.44\cdot10^{2}$	0.311	0.55	1.41	0.35	2.58
8	4	0.0497	1.931	$2.10\cdot10^{2}$	0.319	0.50	3.30	0.20	2.49
9	4	0.0596	1.675	$2.91\cdot10^{2}$	0.325	0.90	2.94	0.18	0.04
10	4	0.0726	1.927	$1.94\cdot10^{2}$	0.338	1.02	4.64	0.16	0.01
11	4	0.0885	2.080	$1.46\cdot10^{2}$	0.345	0.67	3.64	0.16	0.03
12	4	0.1084	2.493	$8.54\cdot10^{1}$	0.350	0.73	3.30	0.13	0.04
13	4	0.1336	2.795	$5.71\cdot10^{1}$	0.347	0.61	5.69	0.10	0.04
14	4	0.1662	3.196	$3.68\cdot10^{1}$	0.347	0.65	3.92	0.08	0.04
15	4	0.2103	3.709	$2.14\cdot10^{1}$	0.333	0.51	3.80	0.09	0.05
16	4	0.2728	4.523	$1.03\cdot10^{1}$	0.300	0.62	3.62	0.02	0.05
17	4	0.3623	6.807	$2.50\cdot10^{0}$	0.231	0.43	3.33	0.01	0.04
18	4	0.5037	11.259	$3.33\cdot10^{-1}$	0.127	0.74	5.66	0.01	0.07
9	5	0.0598	1.908	$2.08\cdot10^{2}$	0.328	0.69	2.83	0.17	0.30
10	5	0.0726	2.276	$1.24\cdot10^{2}$	0.333	0.69	3.82	0.16	0.22
11	5	0.0885	2.585	$8.53\cdot10^{1}$	0.341	0.52	2.69	0.03	0.09
12	5	0.1085	3.076	$5.02\cdot10^{1}$	0.343	0.43	3.03	0.01	0.03
13	5	0.1334	3.536	$3.23\cdot10^{1}$	0.347	0.60	2.40	0.01	0.02
14	5	0.1663	4.055	$2.01\cdot10^{1}$	0.338	0.43	3.55	0.04	0.04
15	5	0.2110	4.703	$1.18\cdot10^{1}$	0.327	0.44	2.39	0.05	0.05
16	5	0.2726	5.682	$5.78\cdot10^{0}$	0.290	0.49	3.48	0.03	0.04
17	5	0.3674	9.101	$1.19\cdot10^{0}$	0.224	0.51	5.08	0.01	0.05
9	6	0.0601	2.316	$1.23\cdot10^{2}$	0.325	0.57	1.81	0.13	2.40
10	6	0.0734	2.804	$7.14\cdot10^{1}$	0.333	0.53	3.35	0.15	2.17
11	6	0.0895	3.341	$4.38\cdot10^{1}$	0.343	0.52	2.21	0.11	1.58
12	6	0.1094	3.946	$2.59\cdot10^{1}$	0.338	0.47	3.18	0.08	0.96
13	6	0.1350	4.612	$1.60\cdot10^{1}$	0.338	0.44	2.64	0.03	0.41
14	6	0.1673	5.337	$9.88\cdot10^{0}$	0.330	0.43	2.94	0.04	0.11
15	6	0.2123	6.282	$5.62\cdot10^{0}$	0.316	0.47	3.30	0.02	0.02
16	6	0.2762	7.432	$2.90\cdot10^{0}$	0.287	0.43	4.13	0.01	0.04

x bin	Q^2 bin	$\bar{x}$	$\bar{Q^2}$	$\frac{d^2\sigma^d}{dx\,dQ^2}$	F_2^d	$\delta_{stat.}$	$\delta_{mis.}$	$\delta_{rad.}$	δ_{PID}
1	1	0.0069	0.291	$2.90\cdot10^{4}$	0.147	1.17	11.05	0.36	0.69
2	1	0.0102	0.404	$1.27\cdot10^{4}$	0.178	1.09	8.32	0.47	0.87
3	1	0.0142	0.513	$6.72\cdot10^{3}$	0.201	0.70	9.19	0.40	0.61
4	1	0.0186	0.626	$4.07\cdot10^{3}$	0.227	0.79	7.80	0.30	0.36
5	1	0.0244	0.723	$2.76\cdot10^{3}$	0.249	0.67	9.98	0.27	0.10
6	1	0.0325	0.869	$1.65\cdot10^{3}$	0.271	0.73	7.71	0.22	0.01
7	1	0.0398	0.902	$1.41\cdot10^{3}$	0.279	1.10	8.17	0.10	0.05
8	1	0.0486	0.925	$1.18\cdot10^{3}$	0.280	1.89	14.08	0.29	0.07
9	1	0.0595	1.102	$7.66\cdot10^{2}$	0.307	2.18	5.21	0.70	0.05
10	1	0.0723	1.127	$6.32\cdot10^{2}$	0.307	2.20	11.44	0.45	0.06
11	1	0.0882	1.164	$5.29\cdot10^{2}$	0.318	2.20	7.13	1.18	0.07
12	1	0.1078	1.198	$3.90\cdot10^{2}$	0.294	3.16	13.28	1.18	0.07
13	1	0.1330	1.257	$3.16\cdot10^{2}$	0.304	2.72	3.48	0.94	0.07
14	1	0.1660	1.331	$2.22\cdot10^{2}$	0.298	2.40	18.88	0.90	0.06
15	1	0.2091	1.439	$1.55\cdot10^{2}$	0.300	2.02	5.97	0.52	0.06
16	1	0.2635	1.747	$8.80\cdot10^{1}$	0.314	1.10	8.58	0.56	0.05
17	1	0.3480	2.669	$2.12\cdot10^{1}$	0.238	1.19	9.12	0.21	0.05
18	1	0.4606	4.196	$3.95\cdot10^{0}$	0.150	0.94	8.27	0.11	0.04
19	1	0.6348	8.693	$2.05\cdot10^{-1}$	0.049	2.26	7.91	0.02	0.08
1	2	0.0085	0.355	$1.91\cdot10^{4}$	0.177	1.07	6.81	0.81	0.93
2	2	0.0117	0.477	$8.99\cdot10^{3}$	0.208	0.64	5.15	0.69	1.22
3	2	0.0152	0.612	$4.52\cdot10^{3}$	0.223	0.52	3.87	0.36	1.50
4	2	0.0193	0.772	$2.46\cdot10^{3}$	0.245	0.54	2.87	0.40	1.80
5	2	0.0250	0.895	$1.60\cdot10^{3}$	0.257	0.43	3.57	0.12	1.07
6	2	0.0327	1.144	$8.38\cdot10^{2}$	0.282	0.57	3.80	0.30	0.92
7	2	0.0401	1.074	$9.48\cdot10^{2}$	0.292	0.88	6.66	0.17	0.01
8	2	0.0490	1.123	$7.89\cdot10^{2}$	0.298	0.88	5.31	0.24	0.03
9	2	0.0596	1.282	$5.36\cdot10^{2}$	0.314	1.74	8.34	0.36	0.06
10	2	0.0725	1.359	$4.15\cdot10^{2}$	0.309	1.58	6.10	0.36	0.06
11	2	0.0884	1.400	$3.53\cdot10^{2}$	0.325	1.71	7.66	0.05	0.06
12	2	0.1080	1.552	$2.40\cdot10^{2}$	0.320	1.06	8.52	0.19	0.06
13	2	0.1335	1.630	$1.81\cdot10^{2}$	0.317	1.60	6.25	0.34	0.06
14	2	0.1662	1.814	$1.23\cdot10^{2}$	0.319	0.87	7.58	0.05	0.05
15	2	0.2103	2.051	$6.97\cdot10^{1}$	0.287	1.32	6.78	0.09	0.05
16	2	0.2728	2.467	$3.45\cdot10^{1}$	0.263	0.89	7.20	0.18	0.05
17	2	0.3628	3.784	$8.29\cdot10^{0}$	0.204	0.73	6.91	0.04	0.04
18	2	0.4901	6.018	$1.34\cdot10^{0}$	0.116	0.53	6.89	0.01	0.04
19	2	0.6588	12.612	$5.93\cdot10^{-2}$	0.036	1.85	8.45	0.01	0.05

Table E.2: Results on the differential BORN cross section $\frac{d\sigma^d}{dx\,dQ^2}$ (nbarn) and F_2^d. The statistical uncertainty $\delta_{stat.}$, and the systematic uncertainties $\delta_{mis.}$ (misalignment), $\delta_{rad.}$ (Bethe-Heitler efficiencies), δ_{PID} (particle identification) are given in %. Corresponding x bin numbers and Q^2 bin numbers and the average values $\bar{x}$ and $\bar{Q^2}$ (GeV^2) are listed in the first four columns. The overall normalization uncertainty is 6.6%.

x bin	Q^2 bin	$\bar{x}$	$\bar{Q^2}$	$\frac{d^2\sigma^d}{dx\,dQ^2}$	F_2^d	$\delta_{stat.}$	$\delta_{mis.}$	$\delta_{rad.}$	δ_{PID}
5	3	0.0270	1.093	$9.65 \cdot 10^2$	0.272	0.58	2.59	0.25	2.39
6	3	0.0338	1.391	$5.06 \cdot 10^2$	0.292	0.84	1.99	0.43	2.98
7	3	0.0401	1.295	$5.98 \cdot 10^2$	0.297	0.66	3.43	0.15	0.38
8	3	0.0490	1.462	$4.18 \cdot 10^2$	0.307	0.58	3.49	0.12	0.17
9	3	0.0596	1.465	$3.87 \cdot 10^2$	0.315	0.92	3.92	0.24	0.01
10	3	0.0726	1.626	$2.74 \cdot 10^2$	0.318	0.94	4.86	0.07	0.04
11	3	0.0884	1.691	$2.28 \cdot 10^2$	0.326	0.94	3.34	0.02	0.05
12	3	0.1081	2.014	$1.33 \cdot 10^2$	0.323	0.81	4.10	0.08	0.05
13	3	0.1334	2.162	$9.69 \cdot 10^1$	0.320	0.93	4.92	0.05	0.05
14	3	0.1660	2.460	$6.09 \cdot 10^1$	0.316	1.03	4.16	0.07	0.05
15	3	0.2103	2.851	$3.41 \cdot 10^1$	0.293	0.64	4.65	0.07	0.04
16	3	0.2725	3.481	$1.57 \cdot 10^1$	0.256	0.57	4.41	0.03	0.04
17	3	0.3623	5.135	$4.03 \cdot 10^0$	0.193	0.52	4.48	0.04	0.04
18	3	0.4966	8.265	$5.88 \cdot 10^{-1}$	0.106	0.57	6.09	0.02	0.05
7	4	0.0409	1.615	$3.30 \cdot 10^2$	0.299	0.57	1.41	0.34	2.58
8	4	0.0497	1.931	$1.98 \cdot 10^2$	0.304	0.51	3.30	0.10	2.49
9	4	0.0596	1.675	$2.80 \cdot 10^2$	0.316	1.02	2.94	0.06	0.04
10	4	0.0726	1.927	$1.83 \cdot 10^2$	0.323	1.23	4.64	0.01	0.01
11	4	0.0885	2.080	$1.37 \cdot 10^2$	0.324	0.75	3.64	0.07	0.03
12	4	0.1084	2.493	$8.06 \cdot 10^1$	0.328	0.85	3.30	0.18	0.04
13	4	0.1336	2.795	$5.28 \cdot 10^1$	0.320	0.70	5.69	0.11	0.04
14	4	0.1662	3.196	$3.27 \cdot 10^1$	0.311	0.76	3.92	0.01	0.04
15	4	0.2103	3.709	$1.84 \cdot 10^1$	0.290	0.58	3.80	0.04	0.05
16	4	0.2728	4.523	$8.64 \cdot 10^0$	0.255	0.74	3.62	0.04	0.05
17	4	0.3623	6.807	$2.04 \cdot 10^0$	0.188	0.47	3.33	0.01	0.04
18	4	0.5037	11.25	$2.62 \cdot 10^{-1}$	0.100	0.83	5.66	0.02	0.07
9	5	0.0598	1.908	$2.01 \cdot 10^2$	0.319	0.75	2.83	0.08	0.30
10	5	0.0726	2.276	$1.18 \cdot 10^3$	0.319	0.77	3.82	0.13	0.22
11	5	0.0885	2.585	$7.98 \cdot 10^3$	0.324	0.57	2.69	0.11	0.09
12	5	0.1085	3.076	$4.74 \cdot 10^3$	0.324	0.45	3.03	0.03	0.03
13	5	0.1334	3.536	$2.96 \cdot 10^3$	0.319	0.68	2.40	0.04	0.02
14	5	0.1663	4.055	$1.85 \cdot 10^3$	0.311	0.45	3.55	0.03	0.04
15	5	0.2110	4.703	$1.04 \cdot 10^3$	0.288	0.47	2.39	0.05	0.05
16	5	0.2726	5.682	$4.95 \cdot 10^3$	0.250	0.55	3.48	0.00	0.04
17	5	0.3674	9.101	$9.47 \cdot 10^3$	0.180	0.57	5.08	0.02	0.05
9	6	0.0601	2.316	$1.16 \cdot 10^2$	0.308	0.62	1.81	0.06	2.40
10	6	0.0734	2.804	$6.77 \cdot 10^1$	0.315	0.55	3.35	0.03	2.17
11	6	0.0895	3.341	$4.06 \cdot 10^1$	0.317	0.55	2.21	0.07	1.58
12	6	0.1094	3.946	$2.43 \cdot 10^1$	0.314	0.48	3.18	0.07	0.96
13	6	0.1350	4.612	$1.46 \cdot 10^1$	0.309	0.45	2.64	0.06	0.41
14	6	0.1673	5.337	$8.90 \cdot 10^0$	0.298	0.46	2.94	0.02	0.11
15	6	0.2123	6.282	$4.91 \cdot 10^0$	0.274	0.52	3.30	0.02	0.02
16	6	0.2762	7.432	$2.40 \cdot 10^0$	0.238	0.47	4.13	0.03	0.04

x bin	Q^2 bin	$\bar{x}$	$\bar{Q^2}$	σ^d/σ^p	$\delta_{stat.}$	$\delta_{rad.}$
1	1	0.0069	0.291	0.988	2.0	1.52
2	1	0.0102	0.404	0.948	1.7	0.94
3	1	0.0142	0.513	0.978	1.2	0.43
4	1	0.0186	0.626	0.977	1.2	0.39
5	1	0.0244	0.723	0.965	1.1	0.10
6	1	0.0325	0.869	0.958	1.1	0.57
7	1	0.0398	0.902	0.967	1.7	0.82
8	1	0.0486	0.925	0.941	2.8	0.54
9	1	0.0595	1.102	0.935	3.2	1.49
10	1	0.0723	1.127	0.940	3.2	0.63
11	1	0.0882	1.164	0.951	3.1	1.84
12	1	0.1078	1.198	0.904	4.5	1.51
13	1	0.1330	1.257	0.858	3.8	1.97
14	1	0.1660	1.331	0.933	3.4	2.48
15	1	0.2091	1.439	0.852	2.7	1.24
16	1	0.2635	1.747	0.844	1.6	1.09
17	1	0.3480	2.669	0.789	1.7	0.09
18	1	0.4606	4.196	0.771	1.5	0.19
19	1	0.6348	8.693	0.746	3.7	0.07
1	2	0.0085	0.355	0.968	1.8	0.69
2	2	0.0117	0.477	0.966	1.1	0.99
3	2	0.0152	0.612	0.968	0.9	0.81
4	2	0.0193	0.772	0.976	0.9	0.33
5	2	0.0250	0.895	0.978	0.7	0.27
6	2	0.0327	1.144	0.971	0.9	0.45
7	2	0.0401	1.074	0.956	1.4	0.32
8	2	0.0490	1.123	0.945	1.4	0.07
9	2	0.0596	1.282	0.971	2.6	0.57
10	2	0.0725	1.359	0.920	2.3	0.18
11	2	0.0884	1.400	0.930	2.5	0.14
12	2	0.1080	1.552	0.919	1.6	0.36
13	2	0.1335	1.630	0.891	2.3	0.73
14	2	0.1662	1.814	0.902	1.3	0.17
15	2	0.2103	2.051	0.870	1.9	0.25
16	2	0.2728	2.467	0.862	1.3	0.06
17	2	0.3628	3.784	0.812	1.1	0.09
18	2	0.4901	6.018	0.769	0.9	0.03
19	2	0.6588	12.612	0.749	3.0	0.09

Table E.3: Results on the BORN cross section ratio σ^d/σ^p. The statistical uncertainty $\delta_{stat.}$, and the systematic uncertainty $\delta_{rad.}$ due to radiative corrections are given in %. Corresponding x bin numbers and Q^2 bin numbers and the average values of x and Q^2 (in GeV^2) are listed in the first four columns. The overall normalization uncertainty is 1.1%.

x bin	Q^2 bin	$\bar{x}$	Q^2	σ^d/σ^p	$\delta_{stat.}$	$\delta_{rad.}$
5	3	0.0270	1.093	0.985	1.0	0.43
6	3	0.0338	1.391	0.982	1.4	0.73
7	3	0.0401	1.295	0.970	1.1	0.07
8	3	0.0490	1.462	0.952	0.9	0.19
9	3	0.0596	1.465	0.937	1.4	0.20
10	3	0.0726	1.626	0.931	1.4	0.26
11	3	0.0884	1.691	0.934	1.4	0.08
12	3	0.1081	2.014	0.907	1.3	0.05
13	3	0.1334	2.162	0.921	1.4	0.17
14	3	0.1660	2.460	0.882	1.5	0.10
15	3	0.2103	2.851	0.855	1.0	0.01
16	3	0.2725	3.481	0.845	0.9	0.08
17	3	0.3623	5.135	0.813	0.8	0.03
18	3	0.4966	8.265	0.765	0.9	0.02
7	4	0.0409	1.615	0.963	1.0	0.51
8	4	0.0497	1.931	0.966	0.9	0.24
9	4	0.0596	1.675	0.953	1.6	0.22
10	4	0.0726	1.927	0.942	1.9	0.12
11	4	0.0885	2.080	0.934	1.2	0.10
12	4	0.1084	2.493	0.911	1.3	0.31
13	4	0.1336	2.795	0.919	1.1	0.21
14	4	0.1662	3.196	0.882	1.2	0.10
15	4	0.2103	3.709	0.865	0.9	0.10
16	4	0.2728	4.523	0.826	1.1	0.02
17	4	0.3623	6.807	0.808	0.8	0.02
18	4	0.5037	11.25	0.772	1.4	0.02
9	5	0.0598	1.908	0.953	1.2	0.18
10	5	0.0726	2.276	0.951	1.2	0.20
11	5	0.0885	2.585	0.936	0.9	0.14
12	5	0.1085	3.076	0.940	0.8	0.04
13	5	0.1334	3.536	0.910	1.1	0.04
14	5	0.1663	4.055	0.902	0.7	0.06
15	5	0.2110	4.703	0.874	0.8	0.04
16	5	0.2726	5.682	0.851	0.9	0.04
17	5	0.3674	9.101	0.800	0.9	0.02
9	6	0.0601	2.316	0.955	1.0	0.14
10	6	0.0734	2.804	0.949	0.9	0.15
11	6	0.0895	3.341	0.934	0.9	0.09
12	6	0.1094	3.946	0.944	0.8	0.08
13	6	0.1350	4.612	0.916	0.8	0.05
14	6	0.1673	5.337	0.898	0.8	0.03
15	6	0.2123	6.282	0.870	0.8	0.01
16	6	0.2762	7.432	0.830	0.8	0.04

Bibliography

[1] M. Anselmino, A. Efremov and E. Leader, Phys. Rept. **261** 1-124 (1995), hep-ph/9501369.

[2] F. E. Close, *An Introduction to Quarks and Partons*, Academic Press (1979).

[3] F. Halzen, A. D. Martin, *Quarks and Leptons*, John Wiley & Sons (1984).

[4] Bjørken, J. D., Phys. Rev. **179** 1547-1553 (1969).

[5] L. N. Hand, Phys. Rev. **129** 1834-1846 (1963).

[6] H. Abramowicz and A. Caldwell, Rev. Mod. Phys. **71** 1275-1410 (1999); hep-ex/9903037.

[7] R. P. Feynman, Phys. Rev. Lett. **23** 1415 (1969).

[8] M. Gell-Mann, Phys. Lett. **8** 214 (1964).

[9] G. Zweig, CERN Reports No. 8182/Th.401 and No. 8419/Th.412, 1964 (unpublished).

[10] Jr. Callan, G. Curtis, David J. Gross, Phys. Rev. Lett. **22** 156-159 (1969).

[11] S. L. Adler, Phys. Rev. **143** 1144 (1966).

[12] D. J. Gross and C. H. Llewellyn Smith, Nucl. Phys. **B14** 337 (1969).

[13] K. Gottfried, Phys. Rev. Lett. **18**, 1174 (1967).

[14] J. C. Collins, D. E. Soper, and G. Sterman, Adv. Ser. Direct. High Energy Phys. **5** 1-91 (1988), hep-ph/0409313.

[15] V. N. Gribov, L. N. Lipatov, Sov. J. Nucl. Phys., **B47** 365-368 (1973).

[16] V. N. Gribov, L. N. Lipatov, Sov. J. Nucl. Phys. **15** 675 (1972).

[17] Yu. L. Dokshitzer, Sov. Phys. JETP **46** 641 (1977).

[18] G. Altarelli, G. Parisi: Nucl. Phys. **B 126** 298 (1977).

[19] R. G. Roberts, *The Structure of the Proton. Deep Inelastic Scattering*, Cambridge University Press (1990).

[20] J. J. Sakurai, Phys. Rev. Lett. **22** 981 (1969).

[21] T. H. Bauer *et al.*, Rev Mod. Phys. **50** 261 (1978).

[22] J. M. Conrad, M. H. Shaevitz, T. Bolton, Rev. Mod. Phys. **70** 1341-1392 (1998).

[23] L. Montanet *et al.*, *Review of Particle Properties*, Phys. Rev. **D 50** 1173 (1994).

[24] D. B. MacFarlane *et al.*, Zeit. f. Phys. **C 26** 1 (1984).

[25] J. J. Aubert *et al.*, Phys. Lett. **B 123** (1983) 275.

[26] J. Ashman *et al.*, Phys. Lett. **B 206** 364 (1988); Nucl. Phys. **B 328** 1 (1989).

[27] J. Ellis and R. L. Jaffe, Phys. Rev. **D 9** 1444 (1974); **D 10** (1974) 1669(E).

[28] B. Adeva *et al.*, Phys. Lett. **B 302** 533 (1993); Phys. Lett. **B 320** 400 (1994).

[29] P. Newman, Int. J. Mod. Phys. **A 19** 1061 (2004).

[30] I. Abt *et al.*, Nucl. Phys. **B 408** 515 (1993).

[31] M. Derrick *et al.*, Phys. Lett. **B 316** 412 (1993).

[32] E. A. Kuraev, L. N. Lipativ, V. S. Fadin, Sov. Phys. JETP **44** 443 (1976).

[33] E. A. Kuraev, L. N. Lipativ, V. S. Fadin, Sov. Phys. JETP **45** 199 (1977).

[34] I. I. Balitsky, L. N. Lipatov, Sov. J. Nucl. Phys. **28** 822 (1978).

[35] W.-M. Yao *et al.*, *The Review of Particle Physics*, Journal of Physics, **G 33** 1 (2006).

[36] A. Aid *et al.*, Nucl. Phys. **B 470** 3 (1996); C. Adloff *et al.*, Nucl. Phys. **B 497** 3 (1997); C. Adloff *et al.*, Eur. Phys. J. **C 13** 609 (2000); C. Adloff *et al.*, Eur. Phys. J. **C 19** 269 (2001); C. Adloff *et al.*, Eur. Phys. J. **C 21** 33 (2001); C. Adloff *et al.*, Eur. Phys. J. **C 30** 1 (2003).

[37] M. Derrick *et al.*, Z. Phys. **C 72** 399 (1996); M. Derrick *et al.*, Z. Phys. **C 69** 607 (1996); J. Breitweg *et al.*, Phys. Lett. **B 407** 432 (1997); J. Breitweg *et al.*, Phys. Lett. **B 487** 53 (2000); S. Chekanov *et al.*, Eur. Phys. J. **C 21** 443 (2001).

[38] L. W. Whitlow, Dissertation, Stanford University, SLAC Report 357 (1990); L. W. Whitlow *et al.*, Phys. Lett. **B 282** 475 (1992).

[39] A. C. Benvenuti *et al.*, Phys. Lett. **B 223** 485 (1989).

[40] M. Arneodo *et al.*, Nucl. Phys. **B 83** 3 (1997).

[41] M. R. Adams *et al.*, Phys. Rev. **D 54** 3006 (1996).

[42] S. Dasu *et al.*, Phys. Rev. **D 49** 5641 (1994).

[43] A. C. Benvenuti *et al.*, Phys. Lett. **B 237** 592 (1989).

[44] M. Arneodo *et al.*, Phys. Lett. **B 364** 107 (1995).

[45] M. R. Adams *et al.* Phys. Rev. **D 54** 3006 (1996).

[46] M. Arneodo *et al.*, Nucl. Phys. **B 333** 1 (1989).

[47] T. Gousset and H. J. Pirner, Phys. Lett. **B 375** 349 (1996).

[48] Hermes Drafting Comitee 32: *The Deuterium of Hydrogen Cross section ratio in Inclusive Deep inelastic Scattering* (2005).

[49] J. Gomez *et al.*, Phys. Rev. **D 49** 4348 (1994).

[50] A. C. Benvenuti *et al.*, Phys. Lett. **B 189** 483 (1987).

[51] E. L. Berger, F. Coester and R. B. Wiringa, Phys. Rev. **D 29**, 398 (1984); E. L. Berger and F. Coester, Phys. Rev. **D 32** 1071 (1985).

[52] C. A. Garca Canal, E. M. Santangelo, and H. Vucetich, Phys. Rev. Lett. **53** 1430-1432 (1984).

[53] R. L. Jaffe, Phys. Rev. Lett. **50** 228 (1983).

[54] A. W. Hendry, D. B. Lichtenberg and E. Predazzi, Phys. Lett. **B 136** 433 (1984).

[55] Wang-Zheng Ben (Yunnan U.), Z. Phys. **C 46**, 293-297 (1990).

[56] E. L. Berger and J. Qiu, Phys. Lett. **B 206** 141 (1988).

[57] L. L. Frankfurt, M. I. Strikman, Phys. Rep. **76** (1981) 215.

[58] A. Brüll, *Die Strukturfunktionen des Nukleons und die Gottfried-Summe*, Habilitationsschrift, Ruprecht-Karls-Universität Heidelberg (1995).

[59] S. Stein *et al.*, Phys. Rev. 12 (1975) 1884; A. Bodek *et al.*, Phys. Rev. Lett. **30** (1973) 1087.

[60] A. W. Thomas, Phys. Lett. **B 126** 97 (1983).

[61] E. J. Eichten, I. Jinchliffe and C. Quigg, Phys. Rev. **D 45** 2269 (1992); **47** R747 (1993).

[62] A. Szczurek, A. Buchmans and A. Faessler, J. Phys. **C 22** 1741 (1996)

[63] D. A. Ross and C. T. Sachrajda, Nucl. Phys. **B 149** 497 (1979).

[64] A. D. Martin, W. J. Stirling and R. G. Roberts, Phys. Lett. **B 252** 653 (1990).

[65] A. S. Ito *et al.*, Phys. Rev. **D 23** 604 (1981).

[66] J. J. Aubert *et al.*, Phys. Lett. **B 123** 123 (1983); Nucl. Phys. **B 293** 740 (1987).

[67] A. C. Benvenuti *et al.*, Phys. Lett. **237** (1990) 599 & 592.

[68] P. Amaudruz *et al.*, Phys. Rev. Lett. **66** 2712 (1991); M. Arneodo *et al.*, Phys. Rev. **D 50** 1-3 (1994).

[69] M. R. Adams *et al.*, Phys. Rev. Lett. **75** (1955) 1466; Phys. Rev. **D 54** (1996) 3006.

[70] K. Ackerstaff *et al.*, DESY-Hermes-96-01, Dissertation, Universität Hamburg (1996).

[71] K. Ackerstaff *et al.*, Nucl. Phys. Proc. Suppl. **79** 146-148, (1999).

[72] A. Baldit *et al.*, Phys. Lett. **B 332** (1994) 244.

[73] P. E. Reimer *et al.*, AIP Conference Proceedings 412: Intersections between Particle and Nuclear Physics, T. W. Donnelly, ed., Bigsky, Montana, May 1997 (Woodbury, NY: AIP Press, 1997) p. 643.

(1991) 607.

[74] A. A. Sokolov and I. M. Ternov, Phys. Dokl. **8** 1203-1205 (1964).

[75] A. Nass *et al.*, Nucl. Instrum. Meth. **A505**, 633-644 (2003).

[76] A. Airapetian *et al.*, Phys. Rev. **D 75** (2007) 012007.

[77] W. Augustyniak, A. Miller, G. Schnell, S. Yen, P. Zupranski, *TMC - Vertex Reconstruction in the Presence of the HERMES Transverse Target Magnet*, 07-008 Internal Report.

[78] S. Kowalski and H. A. Enge, computer code RAYTRACE, unpublished (1986).

[79] F. Méot and S. Valero, *zgoubi user's guide*, DAPNIA-02-395 (2002).

[80] A. Airapetian *et al.*, DESY 98-057, Nucl. Instr. Meth. **A 417** (1998) 230.

[81] U. Elschenbroich, Diploma thesis, Heinrich-Heine-Universität Düsseldorf, 2001.

[82] W. Wander, Dissertation, University of Erlangen-Nuernberg (1996);
DESY-HERMES-96-23.

[83] J. Wendland, Dissertation (2003).

[84] J. Wendland, Particle Identification for HERMES Run I, HERMES-01-067, 2001.

[85] L. De Nardo, private communication.

[86] M. Kolstein, ACE Manual, Efficiencies
(http://www-hermes.desy.de/~machiel/ACEmanu/ACEmanu.html);
M. Kolstein, Dissertation, Vrije Universiteit te Amsterdam, 1998.

[87] http://wwwasdoc.web.cern.ch/wwwasdoc/psdir/geant/geantall.ps.gz

[88] G. Ingelman *et al.*, Comp. Phys. Comm. **101**, 108-134 (1997).

[89] H. Böttcher, I. Akushevich and D. Ryckbosch, hep-ph/9906408; Proceedings of the 'Monte Carlo Generators for HERA Physics' Workshop, Hamburg, Germany (1999).

[90] T. Sjöstrand *et al.*, Comp. Phys. Comm **82**, 74 (1994).

[91] H. Abramowicz and A. Levy, hep-ph/9712415.

[92] L.W. Whitlow *et al.*, Phys. Lett. **B 250** 193 (1990).

[93] K. Abe *et al.*, Phys. Lett. **B452** 194 (1999).

[94] P. Amaudruz et al., Nucl. Phys. **B 371** 3-31 1992, CERN-PPE-91-167, (1991).

[95] S. I. Bilenkaya *et al.* Pisma Zhetf **19** 613 (1974).

[96] G. Hohler *et al.*, Nucl. Phys. **B 114** 505 (1976).

[97] A. Miller, *Applying radiative corrections to polarization asymmetries for deeply inelastic scattering* (unpublished), 2002.

[98] A. Airapetian *et al.*, Phys. Rev D **71**, 012003 (2005), hep-ex/0407032, DESY 04-107.

[99] Erratum to: *K. Ackerstaff et al., Phys. Lett.* **B 475** *386 (2000)*, A. Airapetian *et al.*, Phys. Lett. **B 567** 339 (2003).

[100] C. Itzykson and J.-B. Zuber, Quantum Field Theory, New York, McGraw-Hill, 1985 (Equation 5.150).

[101] A. Courau and P. Kessler, Phys. Rev. **D 46**, 117-124 (1992).

[102] A. Kisselev, Studies based on the beam-finder-code.

[103] A. Brüll, *Top/Bottom Misalignment for 96-03 Data* (unpublished), 2003

[104] Z. Ye and E.-C. Aschenauer, *Misalignment Effects on the Beam-Spin and Beam-Charge Asymmetries in DVCS* (unpublished).

[105] A. Terkulov, private communication.

[106] U. Elschenbroich, HERMES Internal Note 02-013; A. Terkulov, MC simulation studies.

[107] D. Gabbert and L. De Nardo, DESY report 07-107, hep-ph/0708.3196, DIS 2007.

[108] B. Adeva *et al.*, Phys. Rev. **D 58** (2001).

[109] W.-M. Yao *et al.*, J. of Phys. **G 33** 1 (2006).

[110] M. Derrick *et al.*, Z. Phys. **C 63** 391 (1994).

[111] V. Tvaskis, *Longitudinal-Transverse Separation of Deep-Inelastic Scattering at low Q^2 on Nucleons and Nuclei*, Dissertation, Vrije Universiteit Amsterdam (2004).

[112] ZEUS, DIS 1999.

[113] H. Abramowicz *et al.*, Phys. Lett. **B 269** 465 (1991).

[114] F. James, MINUIT, Reference Manual, Version 94.1, CERN Program Library Long Writeup D506 (European Organization for Nuclear Research, Geneva, 1994).

[115] R. Wallny, *A Measurement of the Gluon Distribution in the Proton and of the Strong Coupling Constant α_s from Inclusive Deep-Inelastic Scattering*, Dissertation, Universität Zürich (2001).

[116] D. Stump *et al.*, *Uncertainties of Predictions from Parton Distribution Functions I: the Lagrange Multiplier Method, Phys. Rev.* **D 65**, 014012 (2001).

[117] D. Gabbert and L. De Nardo, *Fit on world data of inclusive proton DIS cross sections*, http://www-hermes.desy.de/users/dgabbert/SIGMATOT_PARAM.tgz, (2007).

Acknowledgements

I would like to express my sincere gratitude to Elke-Caroline Aschenauer who supervised my work and was most helpful with her extensive knowlege and experience. This work was made possible by her steady support and guidance throughout the entire time. I am also highly thankful to Wolf-Dieter Nowak for his encouragement, the trustful relation and for the role he played in the moderation of the work.

I would like to thank Lara De Nardo for the good cooperation and team work, the easy and friendly communication and the productive development of ideas and strategies. Work was so much more productive and enjoyable with her. It was a great pleasure in the first part of the time to share the office with Hayg Guler. The good time we had and the large collection of tea we enjoyed every day I will never forget. I would like to thank Caroline Riedl for the good team work on data quality. Thanks to Antje Brüll and Andy Miller for good advice and suggestions. Furthermore, Alexander Kisselev and Adel Terkulov were always there for discussions. I sincerely thank Elke-Caroline Aschenauer, Wolf-Dieter Nowak, Lara De Nardo and Joshua Rubin for proof-reading my thesis.

Last but not least, I would like to thank my parents Ilse and Wolfgang, my sister Nadja and my wife Sabrina for their love, patience and support.